ornl

**OAK RIDGE
NATIONAL
LABORATORY**

MARTIN MARIETTA

Noble Gas, Iodine, and Cesium Transport in a Postulated Loss of Decay Heat Removal Accident at Browns Ferry

R. P. Wichner
C. F. Weber
S. A. Hodge
E. C. Beahm
A. L. Wright

Chemical Technology Division
Engineering Technology Division

NOBLE GAS, IODINE, AND CESIUM TRANSPORT IN A
POSTULATED LOSS OF DECAY HEAT REMOVAL ACCIDENT
AT BROWNS FERRY

R. P. Wichner   S. A. Hodge
C. F. Weber   E. C. Beahm
A. L. Wright

Notice: This document contains information of a preliminary na-
ture. It is subject to revision or correction and therefore does
not represent a final report.

CONTENTS

v

NOBLE GAS, IODINE, AND CESIUM TRANSPORT IN A
POSTULATED LOSS OF DECAY HEAT REMOVAL ACCIDENT
AT BROWNS FERRY

R. P. Wichner   S. A. Hodge
C. F. Weber   E. C. Beahm
A. L. Wright

ABSTRACT

This report presents an analysis of the movement of noble
gas, iodine, and cesium fission products within the Mark-I
containment PWR reactor system represented by Browns Ferry
Unit 1 during a postulated accident sequence initiated by a
loss of decay heat removal capability following a scram. The
event sequence has been analyzed separately and is documented
in a companion report. The event analysis showed that this
accident could be brought under control by various means, but
the sequence with no operator action ultimately leads to con-
tainment (drywell) failure followed by loss of water from the
reactor vessel, core degradation due to overheating, and re-
actor vessel failure with attendant movement of core debris
onto the drywell floor.

The analysis of fission product transport presented in
this report is based on the no-operator-action sequence and
provides an estimate of fission product inventories, as a
function of time, within 14 control volumes outside the core,
with the atmosphere considered as the final control volume in
the transport sequence. As in the case of accident sequences
previously studied, we find small barrier for noble gas ejec-
tion to air, these gases being effectively purged from the
drywell and reactor building by steam and concrete degradation
gases. However, significant decay of krypton isotopes occurs
during the long delay times involved in this sequence. In
contrast, large degrees of holdup for iodine and cesium are
projected due to the chemical reactivity of these elements.
Only about $2 \times 10^{-4}\%$ of the initial iodine and cesium activity
are predicted to be released to the atmosphere. Principal
barriers for release are deposition on reactor vessel and con-
tainment walls. A significant amount of iodine is captured in
the water pool formed in the reactor building basement after
actuation of the fire protection system.

---

1. INTRODUCTION

1.1 Objectives and Approach

The authors of this report are primarily applied researchers in
various areas relating to fission product transport under LWR accident

conditions, and in general, work in an experimental environment within the Chemical Technology Division. It is not our purpose or inclination to produce a general purpose computer code for estimation of LWR accident consequences. Instead we have the following primary goals:

1. To provide a conduit for applying the most current research information to the methodology for computing accident consequences, and

2. To place all known fission product transport phenomena, physical and chemical, in a context that allows evaluation of their impact on the magnitude of the accident consequence.

As researchers in this field we know full well the uncertainties involved in the estimates presented in this report, dealing as it does with the transport of chemically reactive materials through regions of high temperature in complex chemical mixtures and varying gaseous compositions. With this insider's knowledge, we do not claim any specified degree of accuracy for the quantitative results on iodine and cesium release to the atmosphere. Such a claim from any source at this time would be premature in view of the number of poorly known factors involved in the transport of these materials. What we do state is that given the careful and detailed analysis of this accident sequence provided in Ref. 1.5, and by utilizing the most current information bearing on fission product transport properties, the computed release rates are as correct as possible with the information available at this time.

Since this subject is still developing, several technical areas have been identified that may have significant impact on the results. The reader is referred to Sect. 6.3 for our view of the areas of principal uncertainty. Currently, we are attempting to upgrade our calculational procedures to apply new developments in these areas as they occur.

1.2 Outline and Acknowledgements

This is the third in a series of fission product transport analyses for postulated accident sequences at a Mark-I type BWR. Specifically, Browns Ferry Unit 1 is used for the model and numerous reactor-specific details provided by the utility-owner, TVA, are utilized for the analysis of the sequence of events and fission product transport. We would like to gratefully acknowledge the cooperation of the TVA Engineering Support Offices in Chattanooga and Knoxville in providing the numerous design and control details without which these studies would be extremely difficult and much less realistic. In addition, we acknowledge the aid provided by GE reactor safety personnel who have contributed helpful comments and information throughout the course of the study. This research is sponsored by the Containment Systems Research Branch of the Division of Accident Evaluation of the NRC Office of Research.

This report presents an analysis of the fission product transport attendant to the severe accident phase of a prolonged loss of decay heat removal capability following a scram at the Browns Ferry Nuclear Plant. The postulated loss of decay heat removal capability involves

the loss of the power conversion system and both the pressure suppression pool cooling and the reactor vessel shutdown cooling modes of the residual heat removal (RHR) system. With the RHR decay heat removal capability unavailable, the reactor decay heat energy would be concentrated in the pressure suppression pool.

Earlier studies in this series have dealt with a postulated station blackout event[1.1] and a small-break LOCA outside of the containment vessel* caused by a piping failure in the control rod drive hydraulic system following scram.[1.2] Both of these accidents are predicted to lead to loss of core cooling, core collapse, and breach of the reactor vessel and containment system in the very unlikely event that operators do not intervene with appropriate corrective actions. Without effective operator action, the Loss of Decay Heat Removal Accident Sequence, which is the subject of this report, also leads to severe results with the difference that containment failure here precedes (in fact indirectly causes) loss of core cooling followed by reactor vessel failure. In all cases, the fission product transport analyses (Refs. 1.1, 1.2, and this report) are accompanied by companion reports devoted to a description of the event sequence.[1.3-1.5]

For the convenience of the reader, a brief description of the accident sequence of events is provided in Chap. 2, where we have followed our usual practice of abstracting sequence details bearing on fission product transport from the companion report which deals exclusively with the accident sequence analysis. However, a significant parameter in this event sequence has been modified so that the summary presented in Chap. 2 differs in some of the details from that in the original report.[1.5] Information obtained from Ames Laboratory after Ref. (1.5) was published pointed toward a smaller projected drywell overpressurization failure area [2 ft^2 (0.19 m^2) vs 10 ft^2 (0.93 m^2)]. Thus the temperatures, flows, and pressures vs time shown in Chap. 2 differ from those presented in Chap. 8 of Ref. (1.5) due to this alteration.

In addition, a significant aspect of the event sequence is the projected behavior of the reactor building which surrounds the containment vessel (drywell and wetwell). Description of this behavior was not provided in Ref. 1.5 and appears here in Chap. 2 and in more detail in Appendix A.

In Chap. 3, three modifications to the fission product transport analysis performed for the earlier studies are described. A brief discussion is presented regarding some recently recognized features of cesium and iodine chemistry not incorporated in this study but which may in the future significantly impact the reactor vessel transport model for these elements.

In Chap. 4 are described estimates of the amount of aerosol produced in the drywell as a result of the core/concrete interaction after reactor vessel bottom head failure and the transport of these aerosols through the drywell and reactor building. A point of departure from

---

*The following terminology is used for the reactor containment structures: <u>reactor vessel</u>, <u>containment vessel</u> including the wetwell and drywell, and <u>reactor building</u>.

previous studies is the use of CORCON/MOD 1 for predicting rubble temperatures and VANESA for aerosol production. Although CORCON is believed to be superior to the INTER subroutine of MARCH, the early version at our disposal probably contains some developmental aspects which for our case may have resulted in higher than realistic rubble bed temperatures.

Both VANESA and CORCON are developments of Sandia National Laboratory (SNL) and we gratefully acknowledge the helpful discussion with Sandia personnel regarding these codes. We are particularly indebted to Dana Powers for the VANESA results which were run at Sandia for our case.

The results of the fission product transport calculations are provided in Chap. 5. The study and the calculated results are summarized in Chap. 6, which also provides a discussion of the principal uncertainties. The thermalhydraulic conditions in the reactor building and refueling bay during the accident sequence are discussed in Appendix A. Appendix B provides the details of the calculations concerning the corium-concrete reactions on the drywell floor and the subsequent aerosol transport in the drywell and the reactor building. The acronyms and symbols used in the report are defined in Appendix C.

References for Chap. 1

1.1   R. P. Wichner et al., *Station Blackout at Browns Ferry Unit 1 — Iodine and Noble Gas Distribution and Release*, NUREG/CR-2182, Vol. 2 (August 1982).

1.2   R. P. Wichner et al., *SBLOCA Outside Containment at Browns Ferry Unit 1 Vol. 2. Iodine, Cesium, and Noble Gas Distribution and Release*, NUREG/CR-2672, Vol. 2 (September 1983).

1.3   S. A. Hodge et al., *Station Blackout at Browns Ferry Unit 1 — Accident Sequence Analysis*, NUREG/CR-2182, ORNL/TM-455 VI (November 1981).

1.4   S. A. Hodge et al., *SBLOCA Outside Containment at Browns Ferry Unit 1 — Accident Sequence Analysis*, NUREG/CR-2672, ORNL/TM-8119/V1 (November 1982).

1.5   S. A. Hodge et al., *Loss of DHR Sequences at Browns Ferry Unit 1 — Accident Sequence Analysis*, NUREG/CR-2973, ORNL/TM-8532 (May 1983).

2. ACCIDENT SEQUENCE SUMMARY

2.1 Introduction

The predicted response of Unit 1 at the Browns Ferry Nuclear Plant to a prolonged post-shutdown loss of decay heat removal capability has been analyzed and is described in detail in a companion document[2.1] to this report. In this chapter, we abstract information from that document, emphasizing the aspects that are most pertinent to fission product transport analyses. The general outline of the accident progression is provided here for the convenience of the reader. Nevertheless, Ref. 2.1 should be consulted for other important aspects of the accident sequence such as the effect of various postulated operator actions or equipment failures on the sequence of events, a detailed description of the residual heat removal system and its operational modes, and a discussion of the effect of thermal stratification in the pressure suppression pool.

The Loss of Decay Heat Removal (DHR) accident sequence has been listed among the risk-dominant accident sequences leading to core melt in every BWR probabilistic risk assessment (PRA) conducted to date.[*] It is an extremely important sequence from the standpoint of fission product transport because the containment vessel[†] is failed by overpressurization before there is a loss of injection to the reactor vessel. However, the long period (about 36 hours) between reactor shutdown and core uncovery provides partial compensation for the unavailability of primary containment when fission product releases begin.

In this study, fission product transport calculations are performed for the period from drywell failure until time 3100 min, an interval of about 17.25 h. The decision to terminate calculations at time 3100 min is somewhat arbitrary, but all major transient events of the accident sequence have occurred by this time. The following listing provides a general outline of the sequence of events:

Time (h)	Events
0	Initiating reactor trip followed by MSIV closure and failure of both the suppression pool cooling and the shutdown cooling modes of the RHR system.
0 – 34.4	Normal reactor vessel water level maintained. Monotonic heatup of pressure suppression pool by condensation of periodic reactor vessel SRV discharge. Primary containment pressure and temperature increase. SGTS

---

[*]This is the "TW" sequence first identified in the Reactor Safety Study, WASH-1400.

[†]The term containment vessel refers to the wetwell and drywell.

automatically initiated on high drywell pressure signal. Primary containment reaches failure pressure [132 psia (0.91 MPa)] at end of period and failure occurs at juncture of cylindrical and spherical sections of drywell. Drywell begins to depressurize into reactor building, and harsh environmental conditions there cause loss of reactor vessel injection capability.

34.4 - 36.7   Without injection capability, the reactor vessel undergoes a pressurized boiloff of coolant. Core uncovery begins at the end of this period.

36.7 - 41.5   Drywell blowdown into reactor building essentially complete. First cladding failures occur (38.1), melting begins for control blade sheaths (39.1), fuel assembly channel boxes (39.6), and fuel (40.1). 75% of the core becomes molten and "core slump" into the lower plenum of the reactor vessel occurs at the end of this period.

41.5 - 43.2   The fallen corium boils off the water in the reactor vessel lower plenum and attacks the reactor vessel bottom head. The bottom head fails at the end of this period and the corium mass drops onto the dry concrete floor of the drywell.

43.2 - 51.7   The corium-concrete reaction phase of the study. Calculations are terminated as of the end of this 8.5 h period (time 3100 min).

It should be noted that the information presented in Chapter 8 of Ref. 2.1, which concerns the events of the accident sequence after core uncovery, is superceded by the corresponding material presented in this report. The information presented in this report has the benefit of recent improvements to the ORNL version of the MARCH code. Also, the 2-ft^2 $(0.186\ m^2)$ area assumed here for the drywell opening upon its failure by overpressurization is believed to be more reasonable than the $10\ ft^2$ $(0.929\ m^2)$ opening assumed in Chapter 8 of Ref. 2.1.

For accident sequences that involve failure of the BWR Mark I containment vessel by overpressurization, it is necessary to assume the failure pressure, failure location, and failure size. A recent study at Ames Laboratory[2.2] provides invaluable assistance in the first two tasks, indicating that the failure would be expected to occur at a pressure of 132 psia (0.910 MPa) by yielding at the juncture of the cylindrical and spherical sections of the drywell. The Ames Laboratory study does not address the expected failure size, but in subsequent discussions, its authors have indicated that it would be expected to be less than $10\ ft^2$ $(0.929\ m^2)$. The $2\ ft^2$ $(0.186\ m^2)$ opening assumed for the fission product transport analysis discussed here is slightly larger than the minimum hole size necessary to terminate the pressure increase in the containment vessel. The assumption of a larger break opening would accelerate the depressurization of the containment vessel but would not significantly affect the fission product transport calculations since, for the Loss of Decay Heat Removal accident sequence, core uncovery does not occur until 2.2 h after drywell failure.

For this accident sequence, in which the containment vessel has already failed by the time the core becomes uncovered, it is evident that consideration of the fission product removal and holdup potential of the secondary containment is of paramount importance in the analysis of the overall fission product transport.

Section 2.2 provides a brief discussion of the sequence of events during the 34.4 h period leading up to containment failure by overpressurization and the concomitant loss of reactor vessel injection capability. Subsequent events are described in Sect. 2.3, followed in Sect. 2.4 by a detailed discussion of the progression of core melt and, after core collapse, the temperature of the debris bed in the reactor vessel lower plenum. The flows between the reactor vessel, wetwell, and drywell are described in Sect. 2.5, and Sect. 2.6 provides a discussion of the response of the secondary containment, which becomes an important part of the overall analysis immediately after drywell failure. The fission product transport pathways are discussed in Sect. 2.7, and very important considerations concerning the performance and endurance of the SGTS are discussed in Sect. 2.8.

2.2 Events Prior to Containment Failure and Loss of Injection

A detailed discussion of the events leading to failure of the primary containment in a postulated Loss of Decay Heat Removal (DHR) accident sequence at Browns Ferry Unit 1 is provided in Chapter 3 of Ref. 2.1. The reader is also referred to Appendix A of Ref. 2.1 for a detailed description of the RHR system and its potential for providing reliable pressure suppression pool cooling under accident conditions.

Table 2.1 provides a timetable and summary of events for the first 34.4 h of the Loss of DHR accident sequence, during which the primary containment remains intact. The reactor vessel is isolated by the MSIV closure that accompanies the scram and is assumed to remain isolated throughout the remainder of the accident sequence. The practical impact of this is that the main condensers of the power conversion system are not available as a decay heat removal mechanism.

With the reactor vessel isolated, the steam generated by decay heat is relieved into and condensed within the pressure suppression pool. Since the means for cooling the pool are by definition not available in this accident sequence, the pool temperature increases monotonically. Evaporation from the pool surface causes a concomitant increase in the primary containment pressure. After one hour, the primary containment pressure reaches 2 psig (0.115 MPa) causing automatic actuation of the standby gas treatment system.

Also at the 1-h point, the pressure suppression pool temperature exceeds 120°F (322 K). Plant Emergency Operating Instructions (EOIs) require the operator to depressurize the reactor vessel when this occurs, so that sufficient reserve capacity is maintained in the pressure suppression pool as necessary to absorb the discharge of a subsequent large-break LOCA without exceeding other temperature limits.

At the 2-h point, the combination of high drywell pressure and operator-induced low reactor vessel pressure causes automatic initiation of the low-pressure ECCS pumps. The high-pressure (HPCI and RCIC) injection systems also remain available, although the pressure suppression pool temperature is above the recommended maximum for their lube oil coolers.* The operator continues to have available much more reactor vessel injection capability than he needs.

Four hours after shutdown, the level of reactor decay heat has subsided to the point where all necessary reactor vessel injection can be supplied by the continuously operating control rod drive hydraulic system, which provides cooling water to the reactor control blades. At the 8.6-h point, the operator must act to reduce the control blade cooling flow to avoid excessive water levels in the reactor vessel.

Although they would not normally be needed, it is worthwhile to note the occurrence of loss of availability of the high-pressure injection systems in this very slowly developing accident sequence. The HPCI and RCIC systems would be threatened by inadequate lube oil cooling if they were used to pump pressure suppression pool water after two hours. The steam supply valves to these systems would be automatically shut at the 13-h point because of high sensed temperature [200°F (366 K)] in the respective turbine rooms. Finally, the steadily increasing primary containment pressure would reach 25 psig (0.274 MPa) at the 14-h point, thereby providing a high exhaust pressure trip signal to the RCIC turbine.

The containment vessel design pressure [56 psig (0.487 MPa)] would be exceeded after 21.5 h, but actual failure is expected to occur at a much higher pressure.[2.2] After 23.5 h, the primary containment pressure reaches 65 psig (0.550 MPa), and the reactor vessel SRVs are no longer operable in the remote-manual mode.† SRV discharge terminates and the reactor vessel begins to repressurize, reaching the 1105 psig (7.720 MPa) setpoint for automatic operation of the SRVs at 27.7 h. SRV discharge and the concomitant heatup of the pressure suppression pool resumes at this time.

At 34.4 h, the drywell pressure reaches 132 psia (0.910 MPa) and the drywell is assumed to fail by the opening of a 2 ft^2 (0.186 m^2) hole located at the juncture of the cylindrical and spherical sections of the drywell. The pressure suppression pool temperature at this time is 343°F (446 K), so a large amount of steam is generated by flashing of the water at the pool surface as the containment depressurizes. The steam escaping from the drywell creates harsh environmental conditions in the reactor building (see Appendix A), and this is assumed to cause failure of the control rod drive hydraulic system (CRDHS). Thus loss of reactor vessel injection occurs simultaneously with drywell failure.

---

*The lubricating oil for the high-pressure injection systems is cooled by the water being pumped.

†In the remote-manual mode, service air pressure on one side of a piston works against drywell pressure on the other. A differential pressure of at least 25 psi (0.172 MPa) is required for actuation.

2.3 Events Following Loss of Injection and Containment Failure

As noted earlier, conditions in the reactor vessel, wetwell, and drywell following drywell failure and subsequent loss of coolant injection at 2064 min (34.4 h) are reported here as computed by the MARCH code, assuming a 2-ft^2 (0.19-m^2) effective break area.

During the time following drywell failure, the events tabulated in Sect. 2.1 following the 34.4-h point occur. These include:

	Time	
	min	h
Vessel boiloff begins	2064	34.4
Core uncovery begins	2200	36.7
First cladding failure	2330	38.8
Core melting begins	2407	40.1
Core slump assumed at 75% of core melt	2492	41.5
Reactor vessel bottom head failure	2591	43.2
Core/concrete reaction to produce aerosols and sparge fission products	2600	43.3
Downstream SGTS HEPA filters tear	2917	48.6

Following bottom head failure, the core/structure rubble deposits on the concrete base of the drywell floor. Initially frozen, the rubble bed heats up due to decay heat, separates into molten metal and oxide layers and is sparged by gases evolving from the degrading concrete below and surrounding the bed. Rubble bed behavior is discussed in Sect. 3.2.1 and Chap. 4. Table 2.2 provides an abbreviated event timetable for the entire sequence with emphasis placed on events significant to fission product transport.

2.4 Reactor Vessel Conditions

2.4.1 Predicted core heatup progression

Core temperature distributions predicted by MARCH are listed in Tables 2.3 through 2.6. According to the highly idealized model in MARCH, each of the 100 core control volumes is presumed to "melt" when an average volume temperature of 4352°F (2400°C) is achieved. Table 2.3 shows this first occurs at time 2407 min in the 8th radial zone at the 8th axial position. Tables 2.4 to 2.6 show temperature maps at times 2428, 2461, and 2491 min, respectively, the last just prior to the projected core collapse onto the bottom head.

It is important to note from Table 2.6 that relatively cool zones in the core exist just prior to collapse. Temperatures in the bottom axial zone at this time range from 702 to 3470°F (372 to 1910°C),

reflecting the continued presence of water near this region. Also, the outer radial zones remain quite cool relative to the melt temperature due to both a lower decay heat source in this region and high radial heat losses.

According to the MARCH formulation, the core is presumed to collapse instantaneously when 75% (user-specified) of the core control volumes achieve the melting point.

The temperature map shown in Table 2.6 indicates that it is reasonable to assume that the outermost radial zone (10) remains in place following core collapse. The low temperatures in the bottom axial zones indicate that the collapsed core still contains about 10% (except for decay losses) of its original inventory of even the more volatile fission product groups. Since rubble bed temperatures in the reactor vessel bottom head are also relatively low, about 10% of the original core inventory of fission products passes to the drywell floor following reactor vessel bottom head failure, according to this temperature history.

2.4.2 Predicted corium debris temperature in the reactor vessel

Figure 2.1 illustrates the temperature history of the rubble bed in the reactor vessel as predicted by MARCH. Note, only one mass-average temperature is available, and an almost instantaneous quench from 4352°F (2400°C) is assumed to occur at the time of core collapse (2492 min). This is because the mass-average temperature decreases rapidly when the hot corium material instantaneously combines with cooler steel structures below the core and boils away the water remaining in the reactor vessel bottom head.

Bottom head failure is predicted to occur at 2590 min at which time the debris bed temperature has reheated to 3385°F (1863°C), principally due to decay heat. During most of the ~100 min time interval between core slump and reactor vessel bottom head failure, debris bed temperatures are relatively cool for fission product evolution; therefore, most of the inventory of fission products in the collapsed core is retained.

2.4.3 Reactor vessel conditions

Figures 2.2 through 2.11 illustrate some of the conditions in the reactor vessel up to the projected time of core collapse at 2492 min. Figure 2.2 shows the effect of the relief valve operation on reactor vessel pressure, which averages 1100 psia (7.58 MPa) until the time of bottom head failure. The expanded water level (which includes the projected bubble volume) in the primary vessel is shown in Fig. 2.3. Note that the top of active fuel (TAF) is uncovered at ~2200 min and that some water is projected to exist in the lower axial zone of the core throughout the period until core slump. Each relief valve opening produces a temporary increase in the two-phase water level, each time quenching some of the previously uncovered portion of the core.

Figures 2.4 and 2.5 show the projected masses of water and hydrogen in the reactor vessel up to time of core collapse. The hydrogen is produced by metal-water reactions during periods when the core cladding, channel box, or control blade material is at elevated temperature and

sufficient steam is available to feed the reaction. The average core temperature is shown in Fig. 2.6. Figure 2.7 shows the energy input from metal/water reactions. Note, about 5.6×10^7 kJ are added to core materials due to metal water reactions, primarily from the cladding. Figure 2.8 shows that even so, only about 15% of the cladding is estimated to be oxidized by the time of core collapse. During the time interval extending from initiation of the Zr/H_2O reaction at 2300 min until core collapse at 2492 min, about 30% of the thermal input is estimated to be derived from the metal/water reaction. The progression of core melting is shown in Fig. 2.9.

Figure 2.10 illustrates the MARCH-predicted variation of gas temperatures exiting from the core up until the time of core slump. The temperature generally increases with time, reaching a peak of 2642°F [~1450°C (1723 K)] just prior to core slump. The exit gas temperature from the core drops periodically to the saturation temperature corresponding to the reactor vessel pressure during periods when a safety relief valve is open.

Surface and gas temperatures in the steam separator are shown in Fig. 2.11. Following core uncovery at time 2200 min, gas temperatures are predicted to increase significantly above surface temperatures [1274°F vs 626°F (~690°C vs 330°C) at core slump]. Although not presented here, other gas and surface temperatures in the upper reactor vessel are predicted to follow the trends shown in Fig. 2.11.

2.4.4 Containment vessel conditions

Figures 2.12 to 2.15 show conditions in the wetwell and drywell from time 2000 min (prior to drywell failure) to time 3200 min, when the MARCH calculations were terminated. The drywell pressure history is shown in Fig. 2.12. Note that about 300 min are required to depressurize the drywell to atmospheric pressure through the assumed 2 ft² (0.186 m²) failure area.

The drywell atmosphere temperature history is shown in Fig. 2.13. Drywell temperatures increase significantly after failure of the reactor vessel bottom head because of the oxidation of previously unreacted steel and zirconium in the corium on the drywell floor. The necessary steam to fuel this reaction is provided by the corium-concrete reaction. The suppression pool water and wetwell airspace temperatures shown in Figs. 2.14 and 2.15 follow the saturation temperatures at the corresponding pressure fairly closely.

2.5 Predicted Flowrates Between the Reactor
Vessel, Wetwell, and Drywell

Volumetric flowrates between the reactor vessel, wetwell, drywell and reactor building are illustrated in Figs. 2.16 through 2.18. Figure 2.16 shows the flowrate from the reactor vessel into the suppression pool via the SRVs and the T-quenchers in the suppression pool. The effect of the on/off action of the SRVs is shown; peak flow into the suppression pool while one SRV is open is about 1412 ft³/min (40 M³/min).

Note the fraction of time that the SRVs are open diminishes after ~2300 min. The large flow pulse at time 2492 min of ~106,000 ft^3/min (~3000 M^3/min) is due to multi-SRV-opening at core slump into the water in the reactor vessel lower plenum, following which the reactor vessel is dry, effectively terminating flow to the suppression pool by this means.

Figure 2.17 illustrates the flow communication between the drywell and wetwell through the vent pipes. Note that after drywell failure, generally the flow direction is from the wetwell airspace to the drywell due to water boiloff from the suppression pool as the containment depressurizes, beginning at 2064 min, the time of drywell failure. Core slump at time 2492 min causes a large surge from the wetwell to the drywell, whereas the predicted effect of reactor vessel bottom head failure is initially a large volume surge from the drywell to the wetwell followed by a flow pulse in the other direction.

Figure 2.18 shows the predicted flow rates from the drywell into the reactor building due to steam boiloff from the suppression pool and generation of concrete degradation gases after reactor vessel failure. After reactor vessel bottom head failure, the solid line indicates the flowrates predicted by MARCH utilizing subroutine MACE for estimating steaming rates from the suppression pool and INTER for flows from the degrading concrete. The INTER results were not used in the present study. These were replaced by the CORCON-MOD1 flowrate estimates represented by the dashed line in Fig. 2.18, where the steaming rate from MARCH has been combined with the CORCON results for times following vessel melt-through (2590 min).

Prior to reactor vessel failure (Fig. 2.18), flow from the drywell to the reactor building is driven primarily by suppression pool boiling; hence the flow is primarily steam. These predicted steam flows are quite large, initially up to 71,000 ft^3/min (2000 M^3/min), a magnitude which effectively flushes the drywell every 2.3 min during the time interval from 2050 min to 2300 min.

The volumetric flows driven by the corium/concrete reaction as predicted by CORCON MOD/1 were used for the fission product transport calculations and are represented by the dashed line in Fig. 2.18. Note that after the initial pulse at time 2590 caused by reactor vessel failure, the predicted flowrate of gases generated by concrete degradation combined with steam from the pressure suppression pool generally equals about 6200 ft^3/min (175 M^3/min) from time 2640 to the termination of the calculation at 3100 min.

2.6 Reactor Building and Refueling Bay Response

The release of steam and gases into the reactor building begins when the drywell fails at time 2064 min (34.4 h) as shown in Fig. 2.18. Drywell pressure is 132 psia (0.910 MPa) at the time of failure, and the drywell is assumed to depressurize by blowdown into the reactor building through a 2 ft^2 (0.186 m^2) hole. This causes a rapid increase in reactor building pressure.

At first, the flow escaping from the reactor building is limited to leakage by exfiltration through its concrete walls. However, there are 300 ft^2 (27.87 m^2) of blowout panels between the reactor building and the refueling bay located above which open permanently when the differential pressure exceeds 6.93 inches of water (1.7 KPa). The subsequent flow into the refueling bay increases the pressure there until the 3200 ft^2 (297.28 m^2) of blowout panels located on the stainless steel superstructure permanently open at a differential pressure of 9.63 inches of water (2.36 KPa) to permit direct flow to the surrounding atmosphere. All of this occurs within the first 20 seconds following drywell failure.

In this accident sequence, the Standby Gas Treatment System (SGTS) is already operating at the time of drywell failure.* This system continuously removes 12,500 cfm (5.90 m^3/s) from the reactor building and an equal amount from the refueling bay as shown schematically in Fig. 2.19. (In actuality, the SGTS blowers take suction on the normal ventilation system ducting within each compartment.)

After drywell failure, the pressure in the primary containment and the flow from the drywell into the reactor building both decrease rapidly. Furthermore, the reactor building fire protection system sprays are automatically initiated by the melting of sprinkler head fusible links in the areas of the reactor building into which hot gases are released from the drywell. As a result of the reduced flow into the reactor building and the reduction of the gas temperature there, the action of the SGTS blowers is sufficient to maintain a sub-atmospheric pressure and to produce an inflow to the refueling bay and to the reactor building through the respective blowout panels, as shown schematically on Fig. 2.20. Once established, this pattern of flows is maintained throughout most of the remainder of the accident sequence.

A detailed description of the conditions within the reactor building and the refueling bay after drywell failure is provided in Appendix A. With a subatmospheric pressure in the reactor building during most of this period, the dominant wall-filtration flow is inward, i.e., from the outside atmosphere into the reactor building where it mixes with the much larger flow entering via the open blowout panels connecting to the refueling bay. This combined inflow then mixes with the effluent from the failed drywell before passing into the ventilation ductwork leading to the suction of the SGTS blowers.

Outflow (exfiltration) from the reactor building does take place during brief periods that occur after the onset of fuel melting at time 2407 min. One significant period of outflow begins at time 2492 min when an enormous quantity of steam enters the pressure suppression pool through flow distributers (termed T-quenchers) upon the occasion of "core slump" into the reactor vessel bottom head. A second significant outflow begins at time 2590 min when the reactor vessel bottom head fails. On both occasions, a large amount of steam enters the drywell

_____

*The SGTS is initiated early in the accident when the drywell pressure exceeds 2.5 psig (0.119 MPa).

and is immediately released through the break into the reactor building, causing the reactor building pressure to be greater than atmospheric in each case for about eight minutes. (See Fig. A.6.)

The hot gases exiting from the drywell are cooled by the action of the reactor building fire protection system sprays. The fusible link sprinkler heads are initiated whenever the temperature of the surrounding atmosphere exceeds 225°F (380 K) and continue to spray throughout the remainder of the accident sequence. The average reactor building temperature consequently remains quite low during the accident sequence [between 225°F and 85°F (380 K and 303 K)]. The action of the sprays also causes the accumulation of a large amount of water in the reactor building basement, at the rate of about 500 GPM ($0.032 \text{ m}^3/\text{s}$).

Flow from the reactor building into the refueling bay only occurs during the period immediately following drywell failure, when there are no fission products in the drywell, and during the brief periods of positive pressure in the reactor building after "core slump" and after failure of the reactor vessel bottom head. As a result, there will be almost no fission products in the refueling bay during this accident sequence, and the conditions in the refueling bay will be almost atmospheric.

The predicted mixed-mean temperature at the inlet to the SGTS is shown in Fig. 2.21. The sharp drop immediately after the initial rise is caused by actuation of the reactor building sprinkler systems. At no time during the accident sequence is the inlet temperature high enough to damage the organic components of the SGTS or to preclude the dehumidifiers at the inlet to the filter trains from performing their function.

2.7 Fission Product Transport Pathways

Figures 2.22 and 2.23 illustrate the principal transport pathways prior to and following failure of the reactor vessel, respectively. Dominant features are the early failure of the drywell (at 2064 min) and actuation of the fire protection sprays in the reactor building (at 2080 min), events which occur long before the first cladding failure at ~2330 min.

The main pathways prior to reactor vessel failure are shown in Fig. 2.22. Material evolved from the overheated core enters the reactor vessel gas space from where it is convected upward by steam/H_2 flow as long as the boiling pool exists below the core. As it flows upward, fission product vapors may condense on or react with available solid surfaces, e.g., aerosols or steel surfaces. Gases and aerosols in the reactor vessel upper gas space would leak through the shut MSIVs to the condenser system or would pass into the suppression pool via the T-quencher devices at times when the SRV opens due to excess pressure. Fission products leaking through the MSIVs are assumed to accumulate in the main condenser. The volatile fission products Xe, Kr, and I also collect in the pressure suppression pool and are assumed to equilibrate with the wetwell gas space from where they may pass into the drywell with steam from the boiling suppression pool through the vacuum breakers. Fission products in the drywell airspace, as vapors or as

material condensed on aerosols, may either deposit on drywell surfaces or, after drywell failure at 2064 min, pass into the reactor building with the same steam flow from the suppression pool.

Flows in the reactor building are dominated by the SGTS blowers which operate throughout the sequence and maintain the building under negative pressure at all times, except momentarily at core slump (2492 min) and drywell failure (2064 min). At all other times, reactor building flows are inward from the refueling bay and drywell and outward into the SGTS, as shown.

Aerosols containing fission products may settle in the reactor building and by the action of the fire protection system sprays, wash into the pool collecting in the basement. In addition, fission product vapors, mainly I_2 and Org-I, are assumed to equilibrate with the reactor building water inventory. There is a potential water pathway to the liquid radwaste systems, but the sump pumps required to transfer water from the reactor building basement are assumed to experience motor failure by flooding early in the sequence.

Flow patterns change following reactor vessel failure, as shown in Fig. 2.23. After reactor vessel failure at 2950 min and a brief period of pressure equilization, the principal flow path develops from gases evolving from degrading concrete into the reactor building through the failure in the drywell liner. Flows to or from the wetwell and to the condenser essentially stop after vessel failure. As reactor vessel surfaces heat up due to deposited fission products, gas expansion causes flow from the reactor vessel into the drywell, as shown in Fig. 2.23.

2.8 Standby Gas Treatment System (SGTS) Behavior

Blowers drawing air into the SGTS filters from the reactor building and refueling bay are actuated early in the sequence and continue to operate throughout. Ar estimated 12,500 ft^3/min (5.90 m^3/s) are drawn from each control volume from various distribution locations using the normal air handling ducting system. Complete descriptions of the HEPA and charcoal filters within the SGTS are provided in earlier reports.[2.3,2.4]

The principal difference for the current case relative to the two earlier accident sequence studies relates to the use of CORCON-Mod 1 for estimation of rubble bed temperatures and concrete-gas production rates and VANESA for estimation of the amount of concrete-based aerosols produced in the drywell. The previous study estimates were based on the INTER subroutine in MARCH. By comparison, CORCON-Mod 1 yields significantly higher oxide-layer temperatures and concrete degradation rates. Hence, VANESA currently yields higher aerosol production rates than would be anticipated, based on earlier cases.

The significance is that current estimates of drywell aerosol production rates would probably cause the HEPA filters to plug (see Chap. 4 for further detail). As discussed in earlier reports,[2.3,2.4] the following event sequence is believed to occur in the SGTS when it is exposed to an excess amount of aerosols: (a) the front HEPA bank plugs and tears immediately on deposit of 178.6 lbs (81 kg) of aerosols;

(b) the rear filter bank plugs and tears on deposit of 178.6 lbs (81 kg) of aerosols; and (c) since air flow is therefore unimpeded, charcoal filter efficiencies for I_2 and Org-I are assumed to be unaffected by the tearing of the HEPA filters.

As noted in an earlier report,[2,4] SGTS behavior during any sequence in which it is operational undoubtedly has a profound effect on the calculated accident consequence. The above-described failure mode is to our best current judgement the manner in which it would fail when exposed to an excess amount of aerosols. We should note that other failure modes are possible, even reasonable, that would lead to a higher calculated consequence. For example, if the HEPA filters plug but do not tear, the flows to the charcoal bed would greatly diminish resulting in heatup of the bed with possible evolution of the previously adsorbed iodine. Pressure in the secondary containment would be slightly above atmospheric and direct leakage to the atmosphere would occur. However, our current best judgement is that the filters would tear when plugged.

The SGTS HEPA filters are designed to remove particulates 0.3 micron in size and larger with an efficiency of up to 99.97% and the Browns Ferry Technical Specifications require that the filters demonstrate >99% DOP removal during periodic testing. The charcoal filters are required to demonstrate >99% removal of halogenated hydrocarbons and >90% removal of methyl iodide. The following filtration and charcoal bed efficiencies are assumed for the Loss of DHR accident sequence:

Prior to upstream HEPA plugging (At times to 2768 min)

Aerosol filtration efficiency	99.99%
I_2-removal efficiency (gas)	99.9%
Org-I removal efficiency (gas)	95%

Following upstream HEPA bank plugging and tearing (2768 to 2880)

Aerosol filtration efficiency	99.0%
I_2-removal efficiency (gas)	99.9%
Org-I removal efficiency (gas)	95%

Following plugging and tearing of both HEPA banks (time > 2880 min)

Aerosol filtration efficiency	0%
I_2-removal efficiency (gas)	99.9%
Org-I removal effiency (gas)	95%

References for Chapter 2

2.1 S. A. Hodge, et al., *Loss of DHR Sequences at Browns Ferry Unit One — Accident Sequence Analysis*, NUREG/CR-2973, ORNL/TM-8532 (May 1983)

2.2 L. C. Greimann, et al., *Reliability Analysis of Steel Containment Strength*, NUREG/CR-2442 (June 1982)

2.3 R. P. Wichner et al., *Station Blackout of Browns Ferry Unit One — Iodine and Noble Gas Distribution and Release*, NUREG/CR-2182, Vol. 2 (August 1982)

2.4 R. P. Wichner et al., *SBLOCA Outside Containment at Browns Ferry Unit One Volume 2. Iodine, Cesium, and Noble Gas Distribution and Release*, NUREG/CR-2672, Vol. 2 (September 1983).

Table 2.1. Timetable and summary of events preceding
containment vessel failure and loss of injection

Time (h)	Event
0	Initiating reactor scram followed by MSIV closure and failure of both pressure suppression pool cooling and reactor vessel shutdown cooling modes of the RHR system.
1	Drywell pressure reaches scram setpoint of 2 psig (0.115 MPa), causing automatic initiation of diesel generators and the SGTS and actuation of Groups 2, 6, and 8 of the Primary Containment Isolation System. Simultaneously, pressure suppression pool temperature exceeds 120°F (322 K) and operators begin a controlled depressurization of the reactor vessel.
2	LPECCS initiation signal on combination of high drywell pressure and low reactor vessel pressure. Pressure suppression pool temperature exceeds the maximum recommended temperature for cooling of HPCI and RCIC system lube oil.
4	All necessary reactor vessel injection can be supplied by the CRDHS.
8.6	Operators begin to throttle the CRD pump discharge to avoid overfilling the reactor vessel.
13	HPCI and RCIC steam supply line isolation.
14	RCIC turbine trip on high exhaust pressure.
21.5	Primary containment pressure exceeds its design value of 56 psig (0.49 MPa).
23.5	SRVs become inoperative in remote-manual mode because of high drywell pressure.
34.4	Drywell fails on high internal pressure of 117 psig (0.91 MPa). Pressure suppression pool temperature is 343°F (446 K).

Table 2.2. Abbreviated sequence of events relevant
to fission product transport

	Time	
	Min	Hour
Reactor trip, MSIV closure, RHR fails	0	0
SGTS on	60	1
.	.	.
.	.	.
.	.	.
Suppression pool temperature = 338°F (~170°C)	2060	34
Containment fails and water boiloff begins	2064	34.4
Reactor building sprays on	~2080	34.7
Core uncovery begins	2200	36.7
First cladding failure	2330	38.8
Core melting begins	2407	40.1
Core slump assumed at 75% of fuel melt	2492	41.5
Reactor vessel bottom head failure	2590	43.2
Core/concrete reaction, drywell aerosol production	~2600	~43.3
Downstream HEPA filter in SGTS tears	2917	48.6
Calculations terminated	3100	51.7

Table 2.3. Core temperature map (°C); time
2407.3 min; % core melted = 1.0

Top										
10	1221	1327	1332	1354	1271	1327	1277	1354	1210	654
9	1966	2093	2160	2160	2166	2160	2127	2316	1860	899
8	2099	2232	2243	2238	2271	2260	2227	Melt	1993	904
7	1716	1854	1871	1866	1866	1871	1871	1916	1593	799
6	1510	1677	1671	1693	1682	1677	1727	1777	1454	766
5	1543	1549	1482	1582	1560	1560	1582	1577	1410	727
4	1471	1621	1488	1627	1638	1643	1482	1666	1416	677
3	1677	1877	1993	1882	1882	1882	1727	1977	1788	638
2	1099	1204	1216	1221	1221	1221	1204	1282	1038	560
1	292	293	293	293	293	293	293	293	292	292
Bottom	1	2	3	4	5	6	7	8	9	10

Center   Edge

Table 2.4. Core temperature map (°C); time
2428.3 min; % core melted = 33.0

Top										
10	1632	1699	1810	1777	1699	1710	1710	1721	1632	743
9	Melt	Melt	Melt	Melt	Melt	Melt	Melt	Melt	Melt	1060
8	Melt	Melt	Melt	Melt	Melt	Melt	Melt	Melt	Melt	1071
7	2260	Melt	Melt	Melt	Melt	Melt	Melt	Melt	1943	916
6	1866	2132	2082	2160	2027	2093	1849	Melt	1810	749
5	1854	1927	1810	1960	2027	1949	1938	2010	1649	821
4	1893	2071	1660	2143	2116	2093	1849	2266	1810	749
3	2321	Melt	Melt	Melt	Melt	Melt	2338	Melt	Melt	688
2	1532	1693	1710	1749	1604	1721	1688	1854	1721	610
1	291	291	291	291	291	291	291	291	291	290
Bottom	1	2	3	4	5	6	7	8	9	10

Center   Edge

Table 2.5. Core temperature map (°C); time
2461.3 min; % core melted = 54.0

Top										
10	1721	1799	1893	1860	1799	1810	1810	1821	1716	816
9	Melt	Melt	Melt	Melt	Melt	Melt	Melt	Melt	Melt	1166
8	Melt	Melt	Melt	Melt	Melt	Metl	Melt	Melt	Melt	1193
7	Melt	Melt	Melt	Melt	Melt	Melt	Melt	Melt	2316	1027
6	2177	Melt	Melt	Melt	Melt	Melt	Melt	Melt	1932	977
5	2154	Melt	Melt	Melt	Melt	Melt	Melt	Melt	1893	927
4	2210	Melt	1943	Melt	Melt	Melt	2154	Melt	2082	849
3	Melt	Melt	Melt	Melt	Melt	Melt	Melt	Melt	Melt	804
2	1866	2071	2049	2143	1938	2099	2021	2266	2243	732
1	426	434	437	437	436	434	434	441	421	343
Bottom	1	2	3	4	5	6	7	8	9	10

Center   Edge

Table 2.6. Core temperature map (°C) at time of postulated
collapse; time 2491.3 min; % core melted = 74.0

Top										
10	Melt	2077	Melt	2249	2110	2066	2382	2093	2354	1032
9	Melt	Melt	Melt	Melt	Melt	Melt	Melt	Melt	Melt	1404
8	Melt	Melt	Melt	Melt	Melt	Melt	Melt	Melt	Melt	1410
7	Melt	Melt	Melt	Melt	Melt	Melt	Melt	Melt	Melt	1227
6	Melt	Melt	Melt	Melt	Melt	Melt	Melt	Melt	Melt	1160
5	Melt	Melt	Melt	Melt	Melt	Melt	Melt	Melt	Melt	1093
4	Melt	Melt	Melt	Melt	Melt	Melt	Melt	Melt	Melt	949
3	Melt	Melt	Melt	Melt	Melt	Melt	Melt	Melt	Melt	916
2	Melt	Melt	Melt	Melt	Melt	Melt	Melt	Melt	Melt	843
1	743	971	1127	1116	1093	1060	582	1910	649	372
Bottom	1	2	3	4	5	6	7	8	9	10
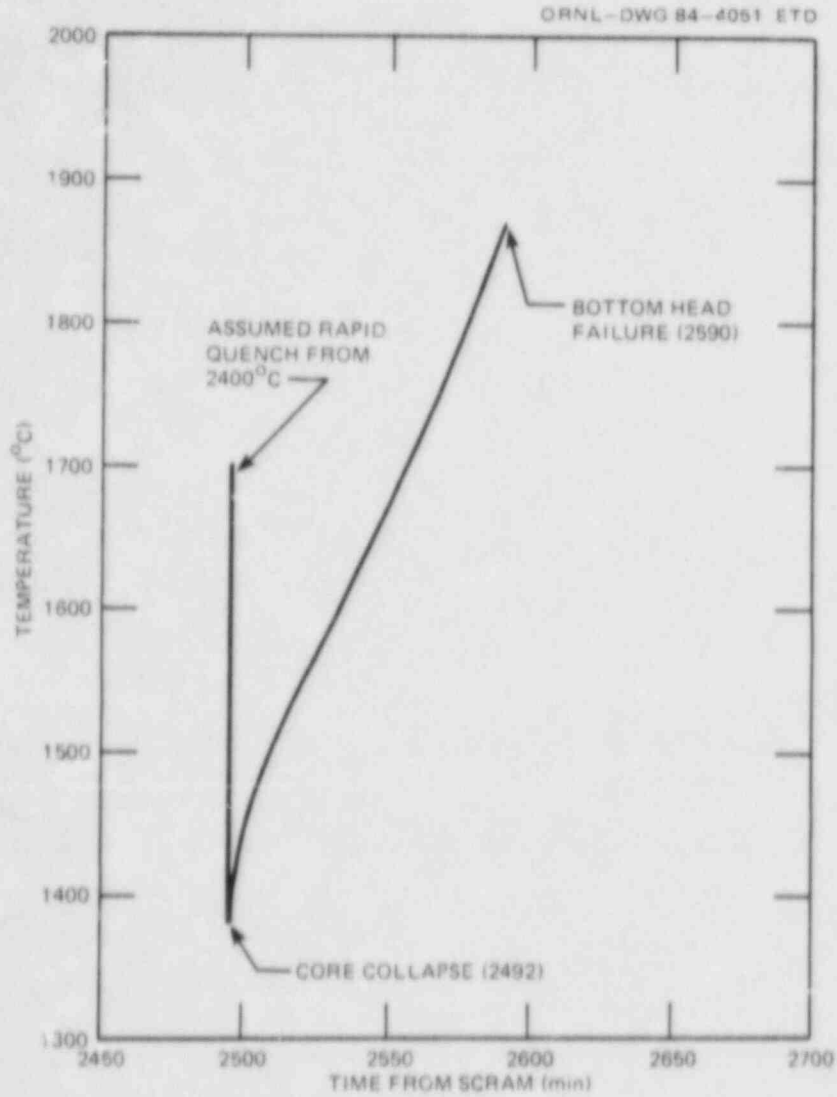
Center   Edge

Fig. 2.1. Core debris temperature in the reactor vessel as predicted by MARCH.

PRIMARY SYSTEM PRESSURE (PA)   *10⁸

0.0   1.8   3.6   5.4   7.2   9.0

PRIMARY SYSTEM PRESSURE (PSIA)

0.0   260.0   520.0   780.0   1040.0   1300.0

2000   2100   2200   2300   2400   2500

TIME — MINUTES

INITIAL CLADDING FAILURE

CORE SLUMP
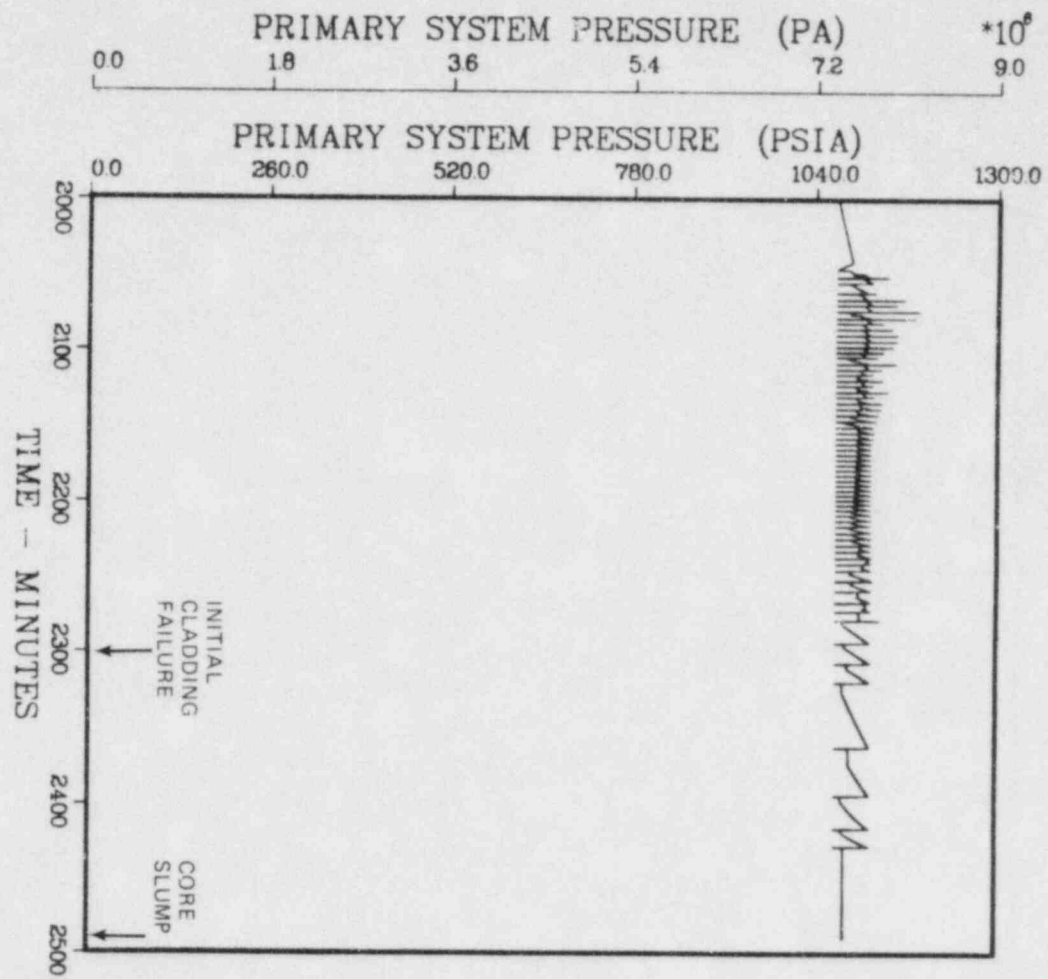
Fig. 2.2. Primary system pressure.

23

ORNL—DWG 84—5709 ETD

24
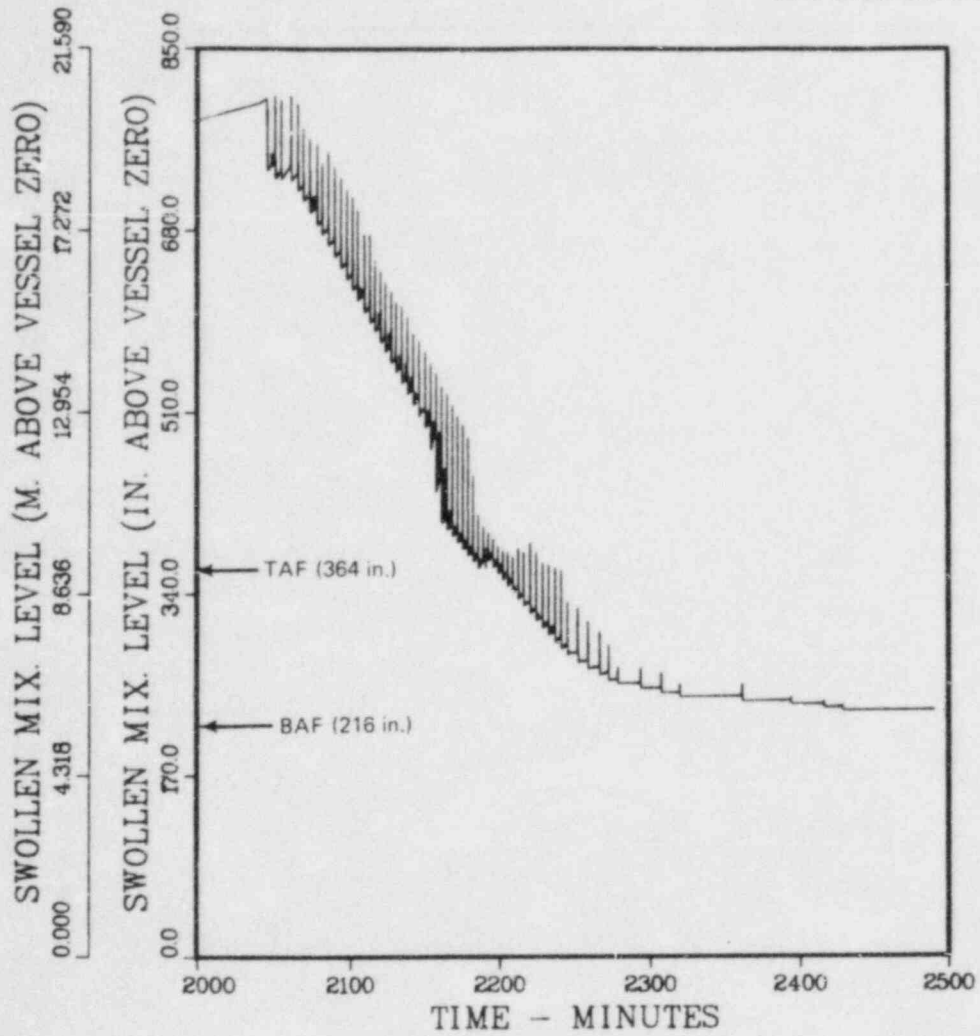
Fig. 2.3. Expanded liquid level in the reactor vessel.

MASS OF WATER IN PRIMARY (KG)   *10⁴

0.0   5.2   10.3   15.5   20.7   25.9

MASS OF WATER IN PRIMARY (LB)   *10⁵

0.0   1.1   2.3   3.4   4.6   5.7

Fig. 2.4. Mass of water in the reactor vessel.

TIME — MINUTES

2000   2100   2200   2300   2400   2500

25
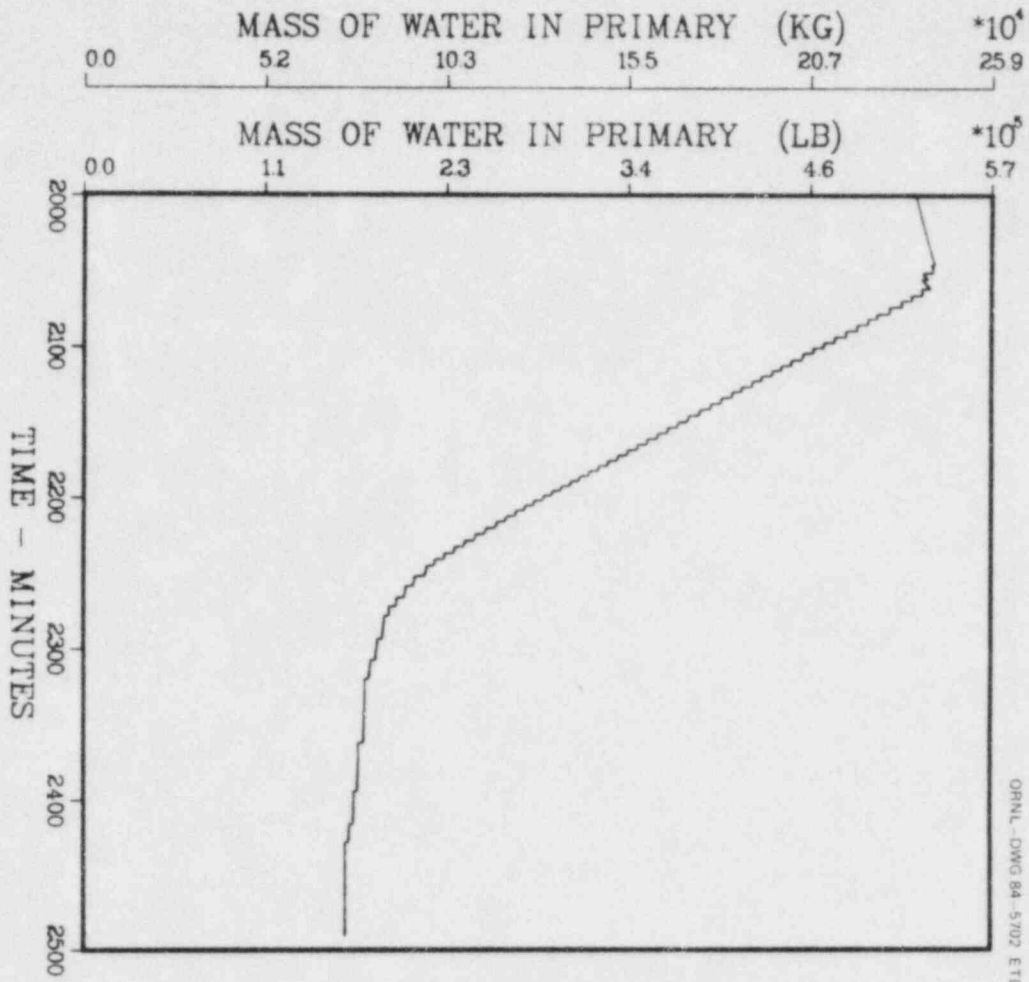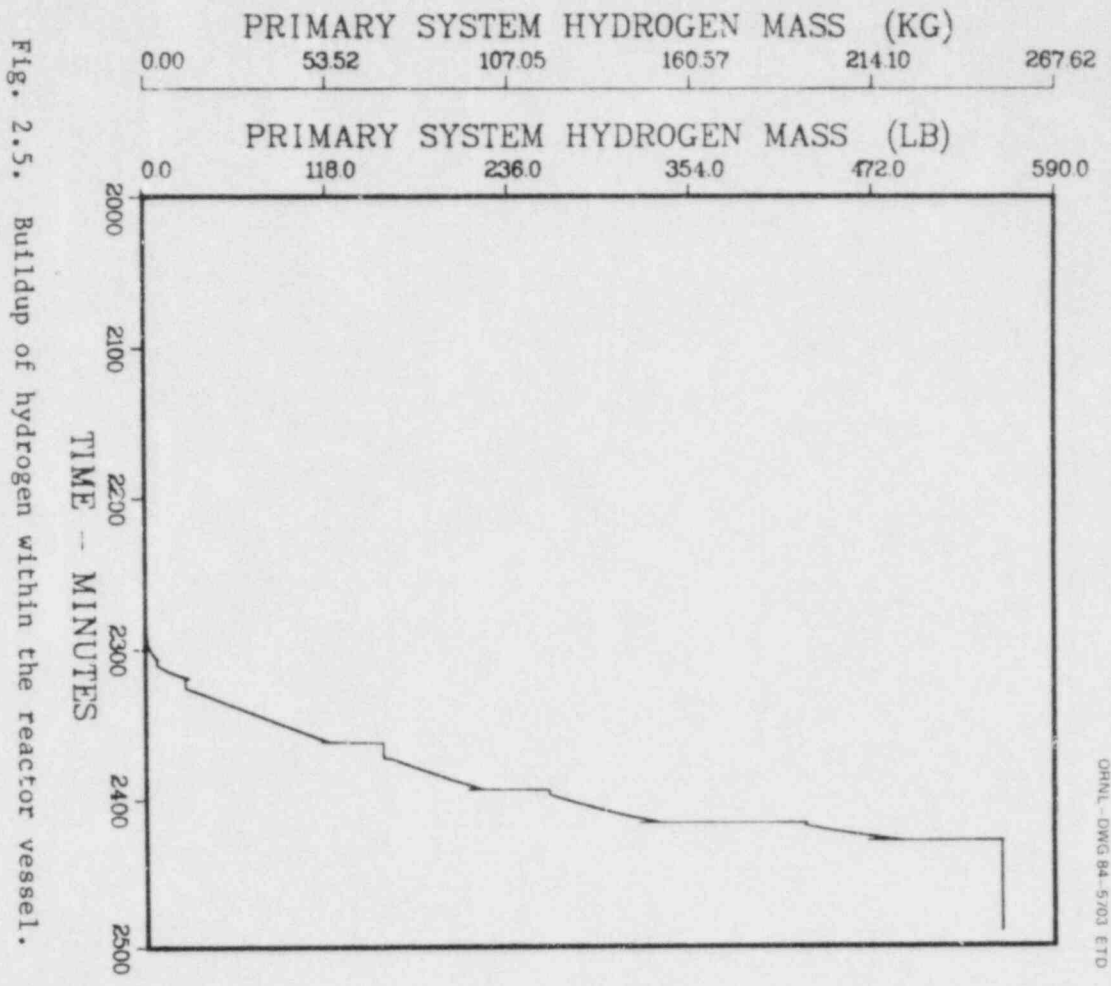
ORNL-DWG 84-5702 ETD

Fig. 2.5. Buildup of hydrogen within the reactor vessel.

ORNL—DWG 84-5/03 ETD
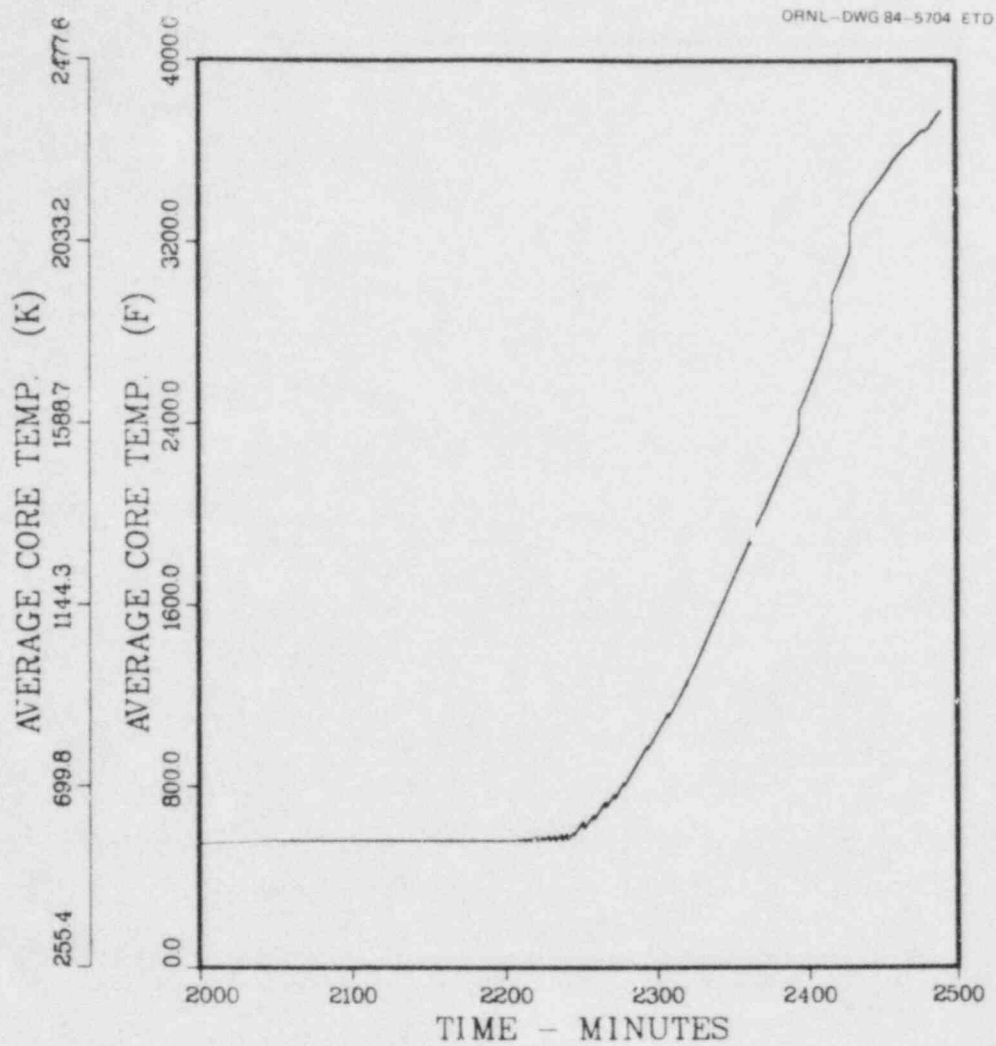
ORNL-DWG 84-5704 ETD

Fig. 2.6. Average core temperature.
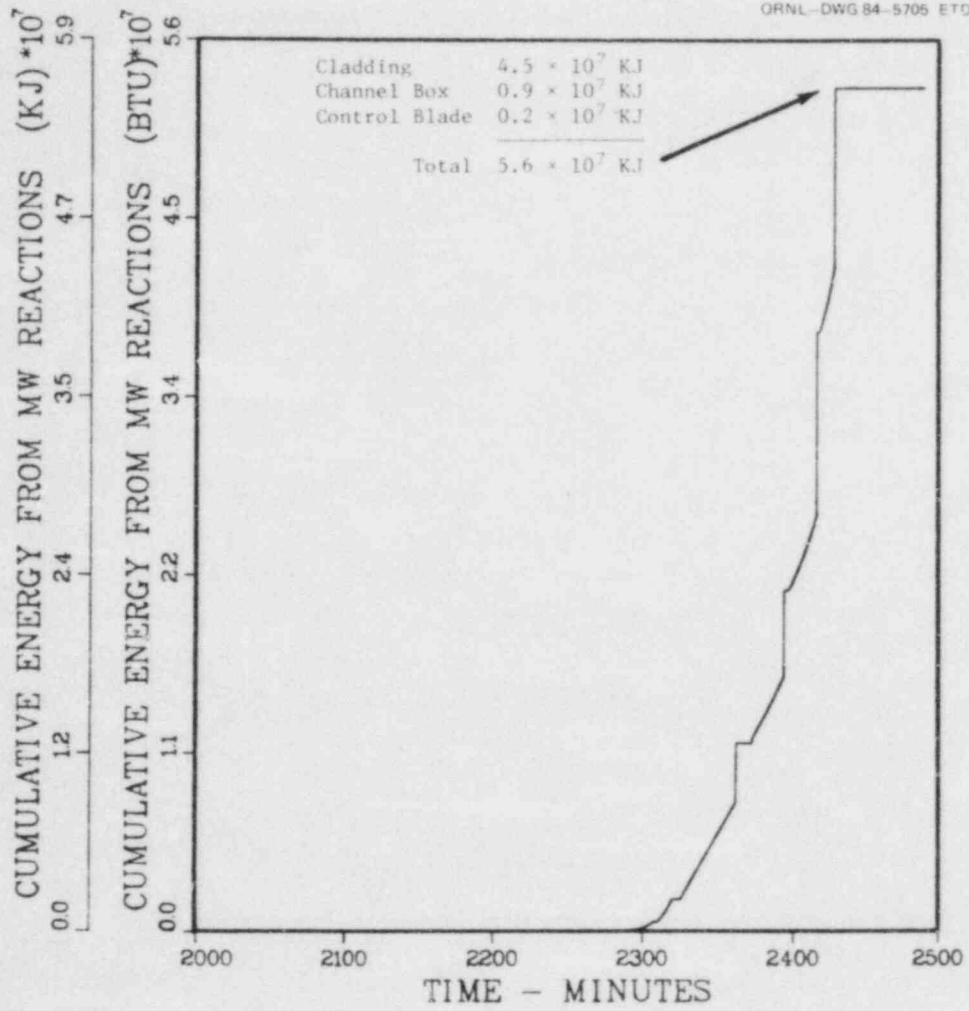
Fig. 2.7. Cumulative energy input from metal-water reactions.
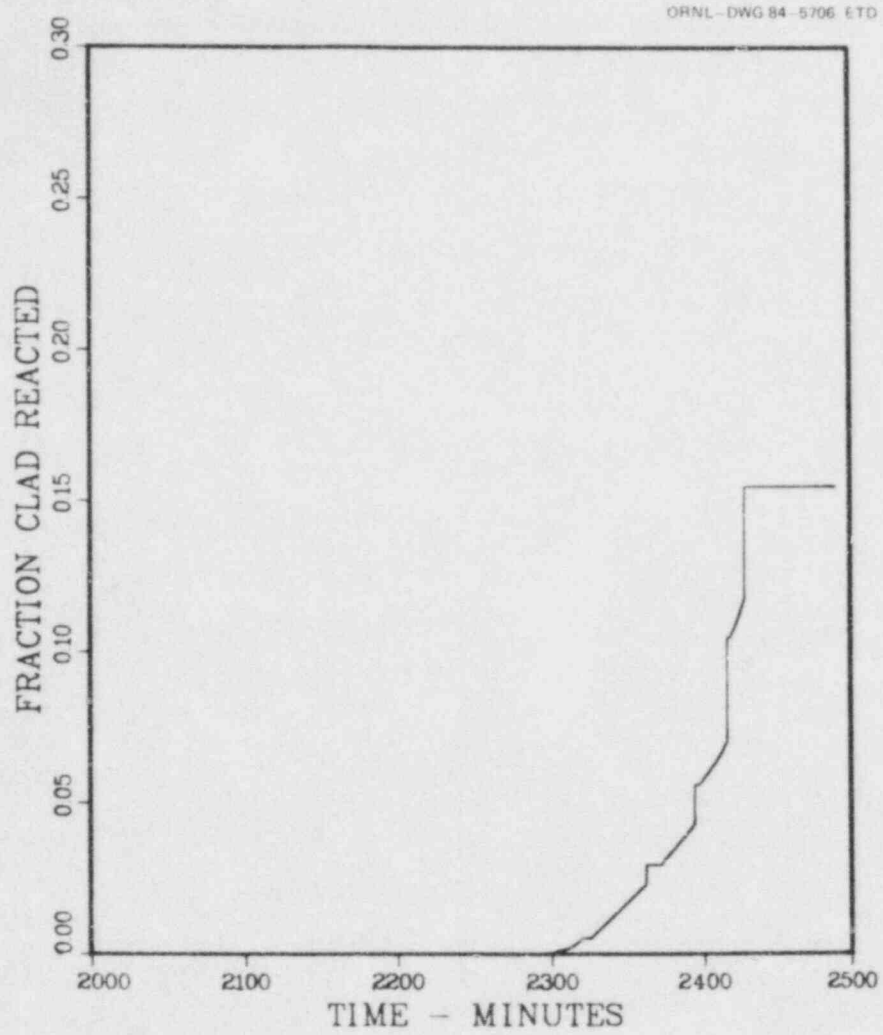
Fig. 2.8. Fraction of cladding reacted.
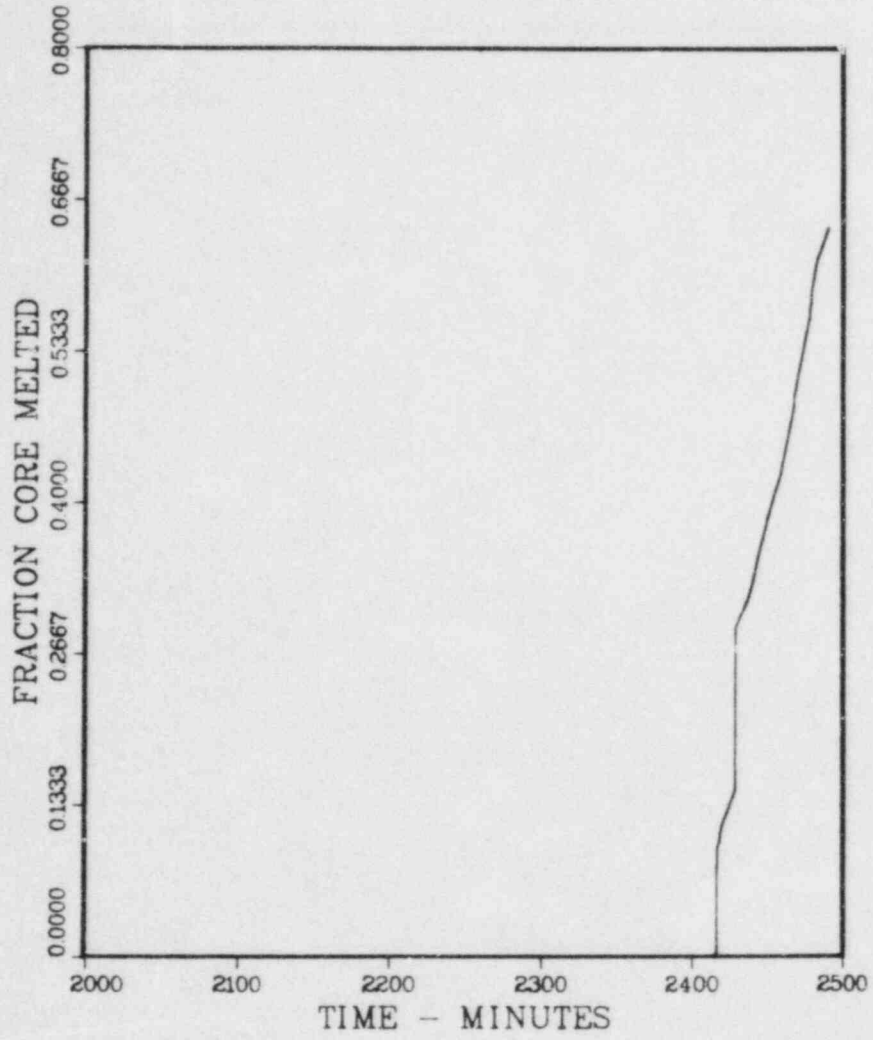
Fig. 2.9. Fraction of core melted.
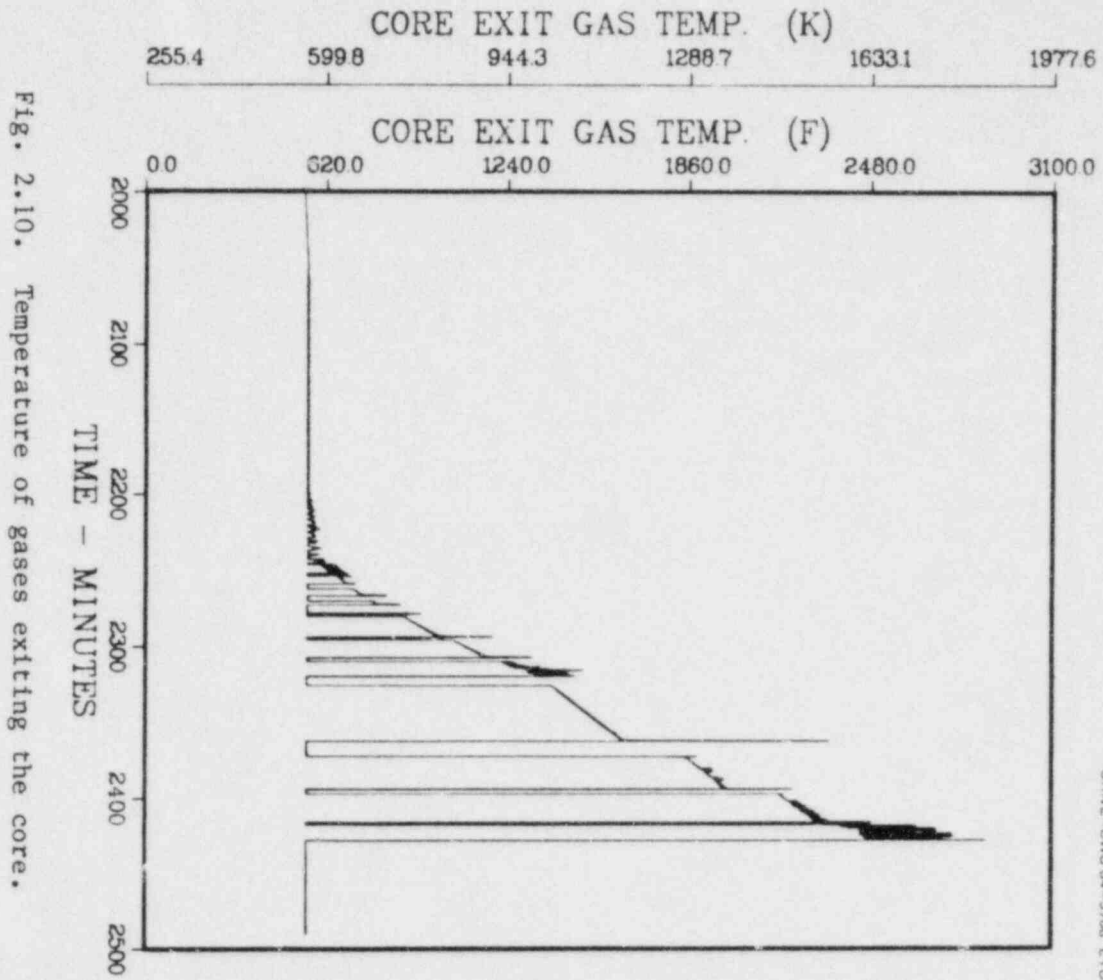
Fig. 2.10. Temperature of gases exiting the core.

CORE EXIT GAS TEMP. (K)

| 255.4 | 599.8 | 944.3 | 1288.7 | 1633.1 | 1977.6 |

CORE EXIT GAS TEMP. (F)

| 0.0 | 620.0 | 1240.0 | 1860.0 | 2480.0 | 3100.0 |

TIME — MINUTES

31
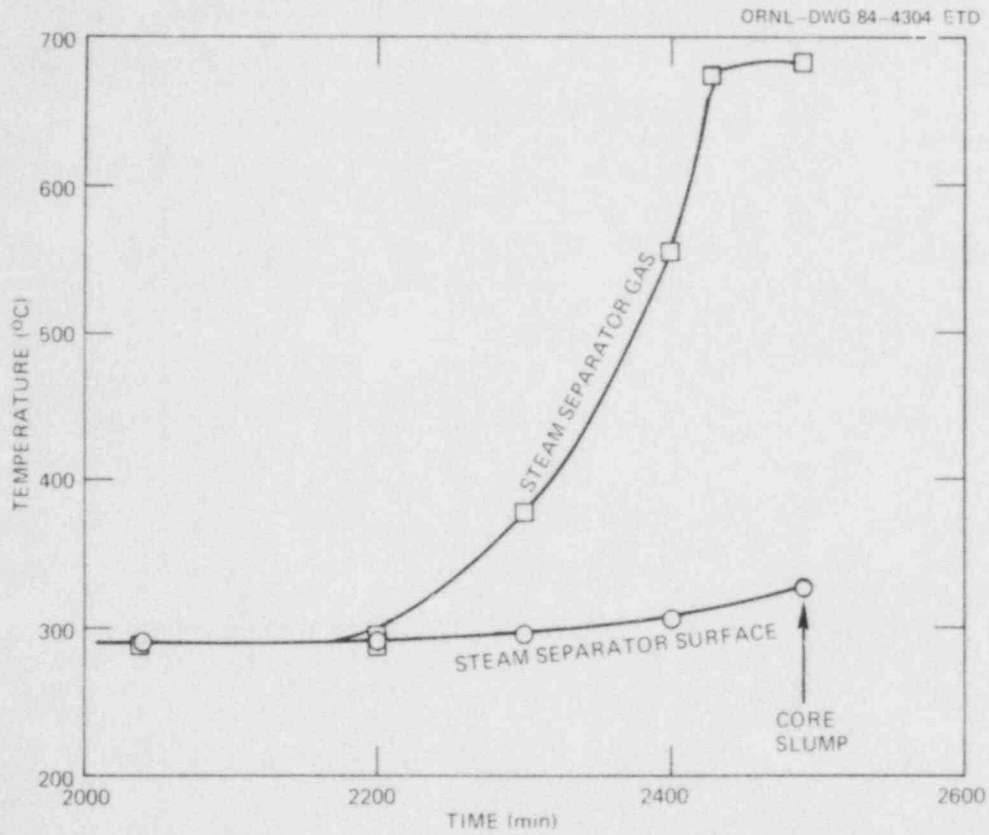
Fig. 2.11. Reactor vessel gas and surface temperatures at the steam separator.
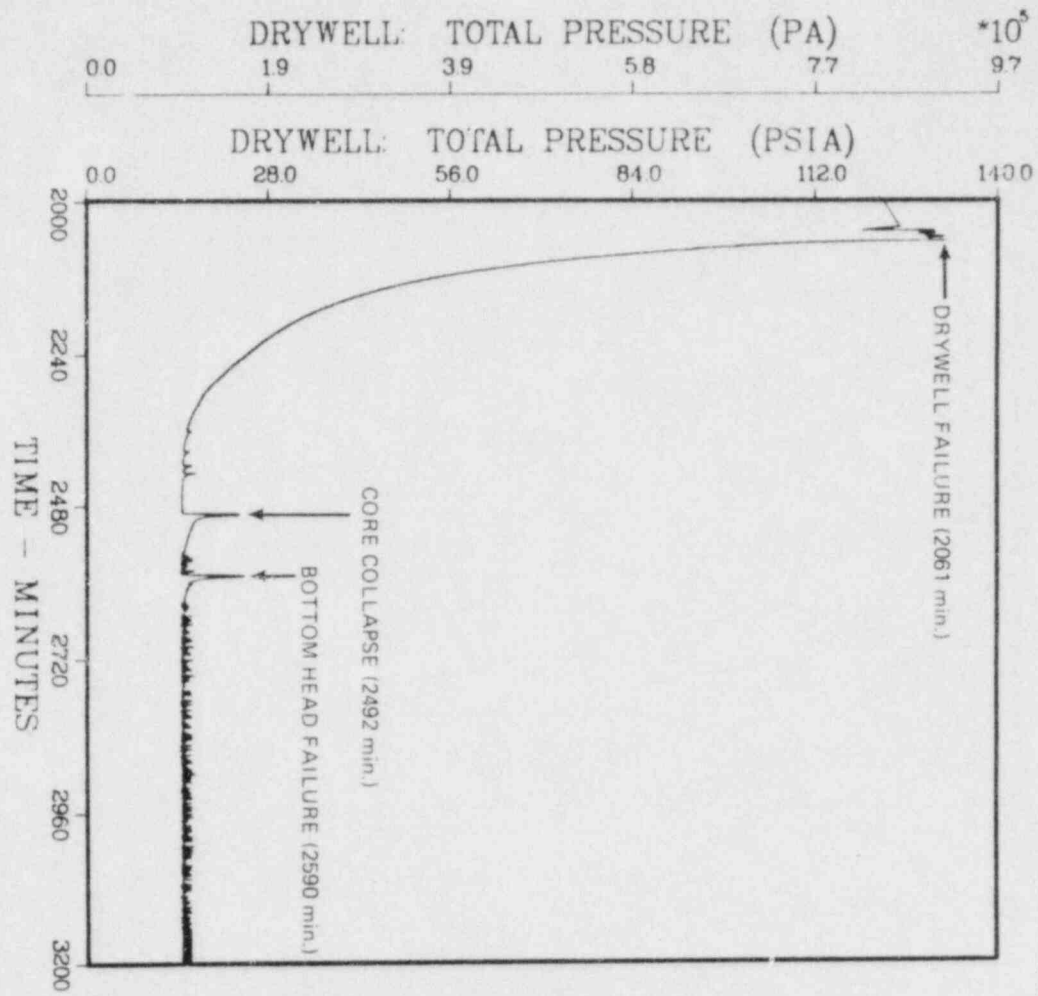
Fig. 2.12. Drywell pressure.

33

ORNL-DWG 84-5711 ETD
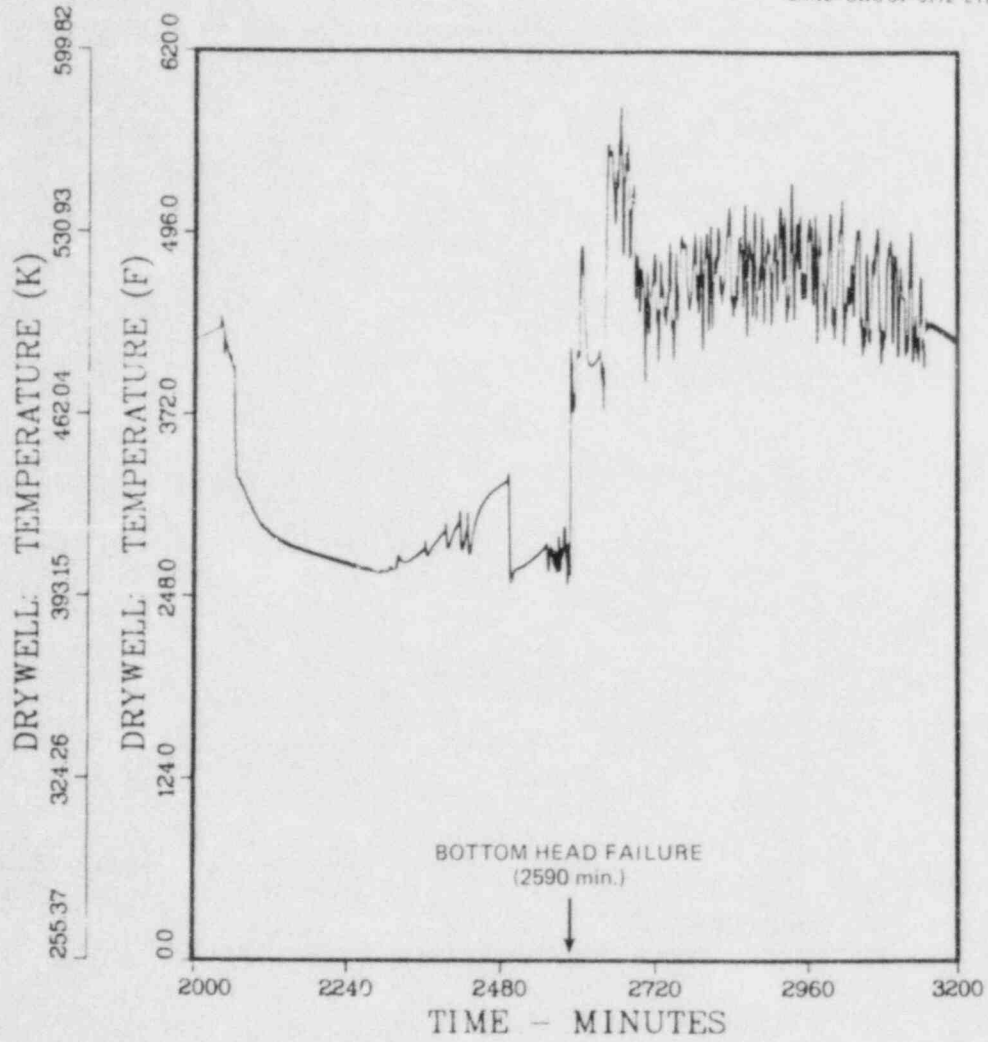
Fig. 2.13. Drywell ambient temperature.

Fig. 2.14. Pressure suppression pool water temperature.

ORNL-DWG 84-5714 ETD
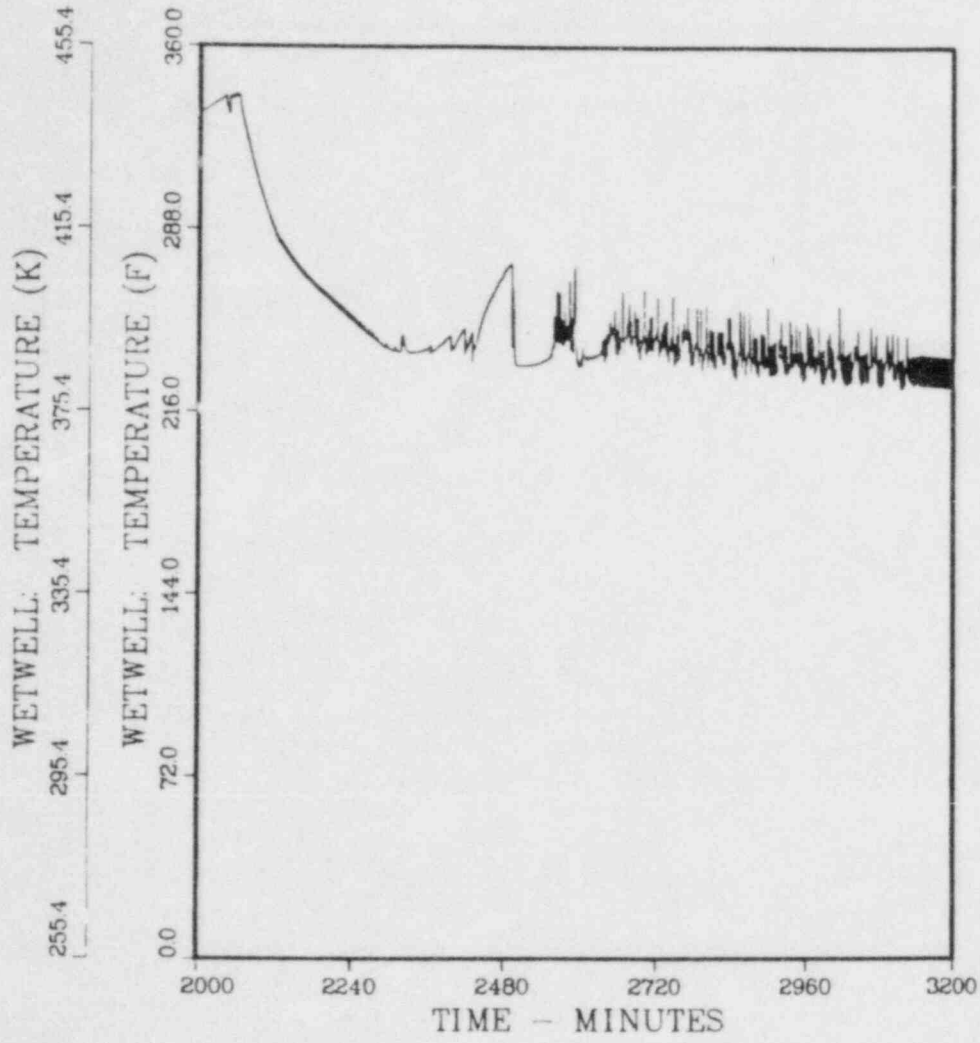
Fig. 2.15. Wetwell airspace temperature.
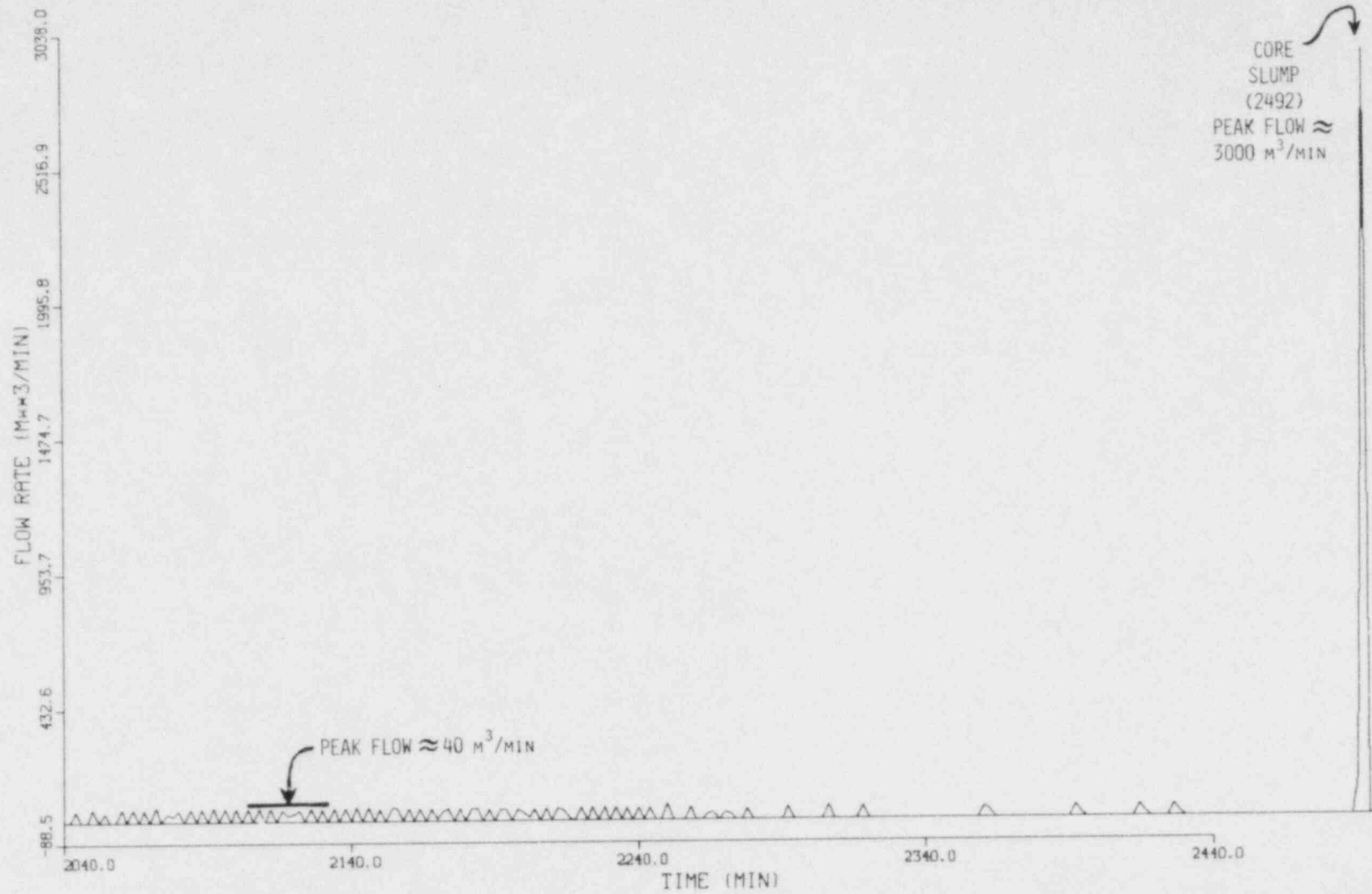
Fig. 2.16. Volumetric flow from reactor vessel to suppression pool through safety relief valves.
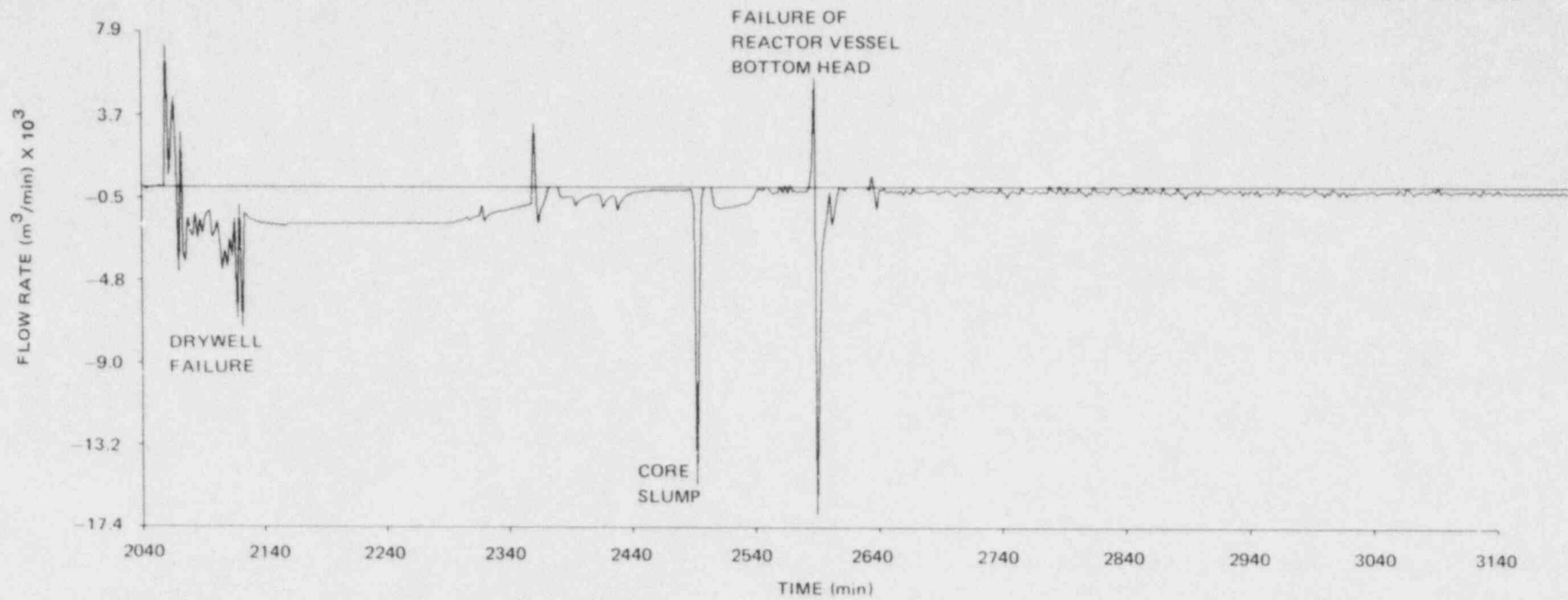
Fig. 2.17. Volumetric flow between the drywell and wetwell through the vent pipes. Negative flows are from the wetwell to the drywell.
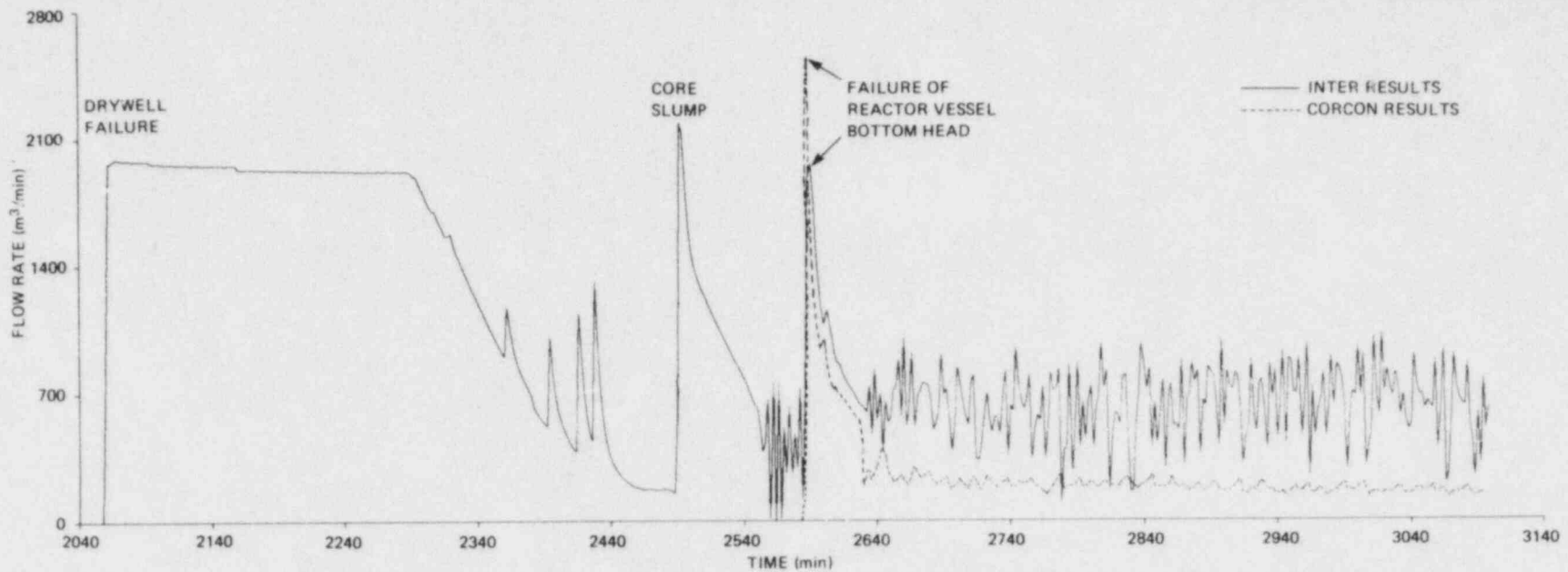
Fig. 2.18. Volumetric flow from the drywell to the reactor building as calculated by MARCH subroutine MACE. The depicted flows after reactor vessel bottom head failure include both the effect of the high corium-concrete reaction gas generation rates predicted by MARCH subroutine INTER (solid line) and the CORCON-predicted gas generation rates (dashed line).

ORNL–DWG 84-5716 ETD
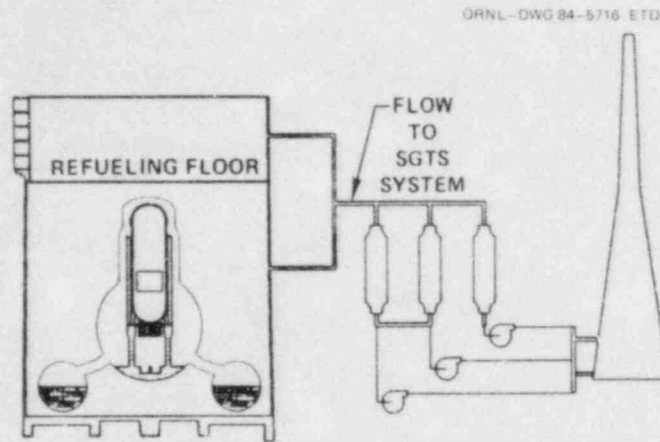
Fig. 2.19. The SGTS filters the exhaust from the secondary containment under accident conditions.

ORNL–DWG 84-5717 ETD
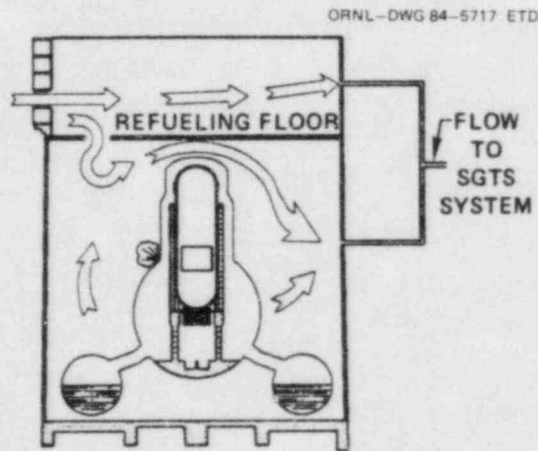
Fig. 2.20. The SGTS blowers have sufficient capacity to maintain a vacuum in the secondary containment after partial drywell blowdown; flow through the blowout panels is into the refueling bay and reactor building.
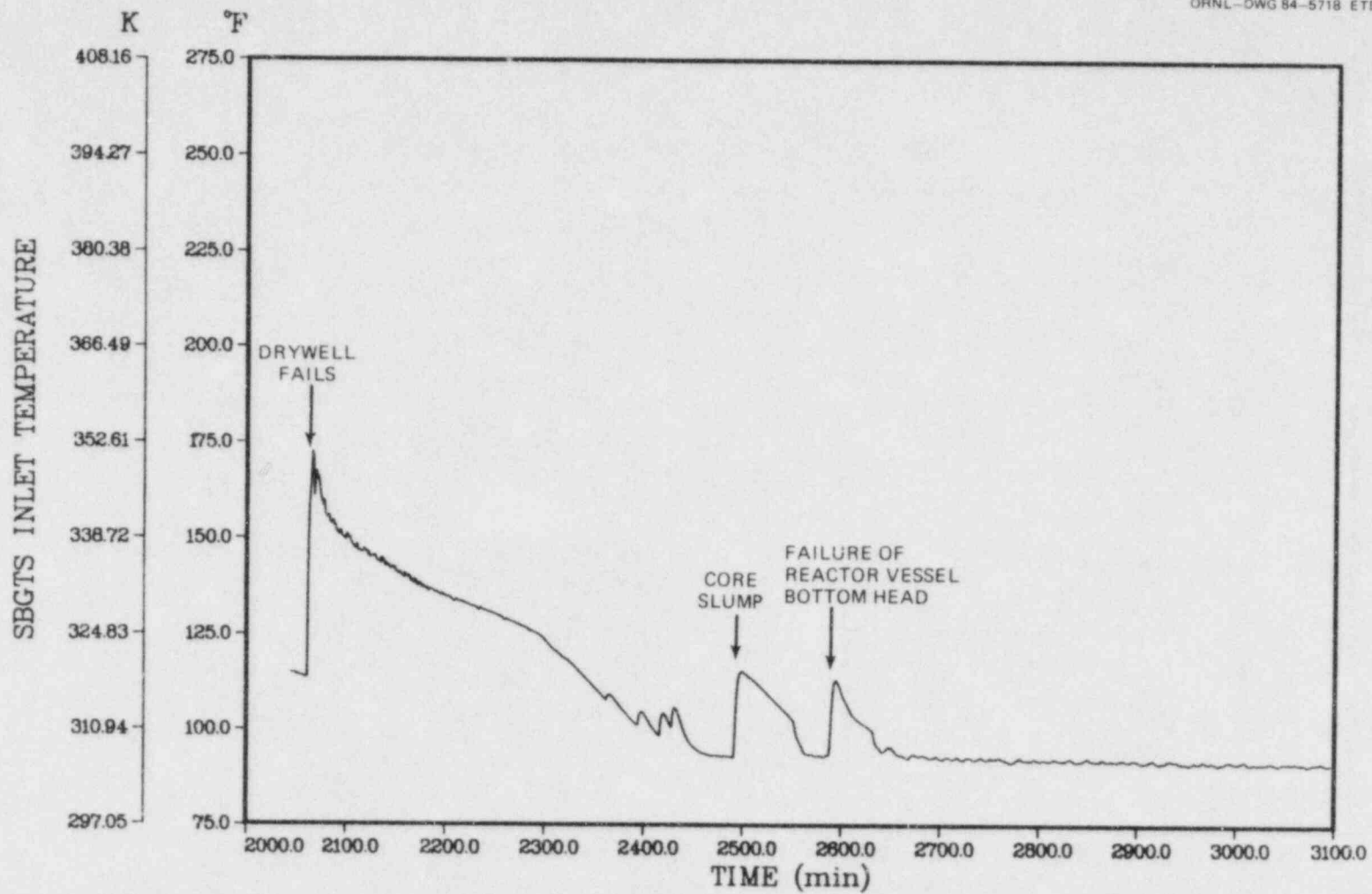
Fig. 2.21. Temperature at inlet to the standby gas treatment system.
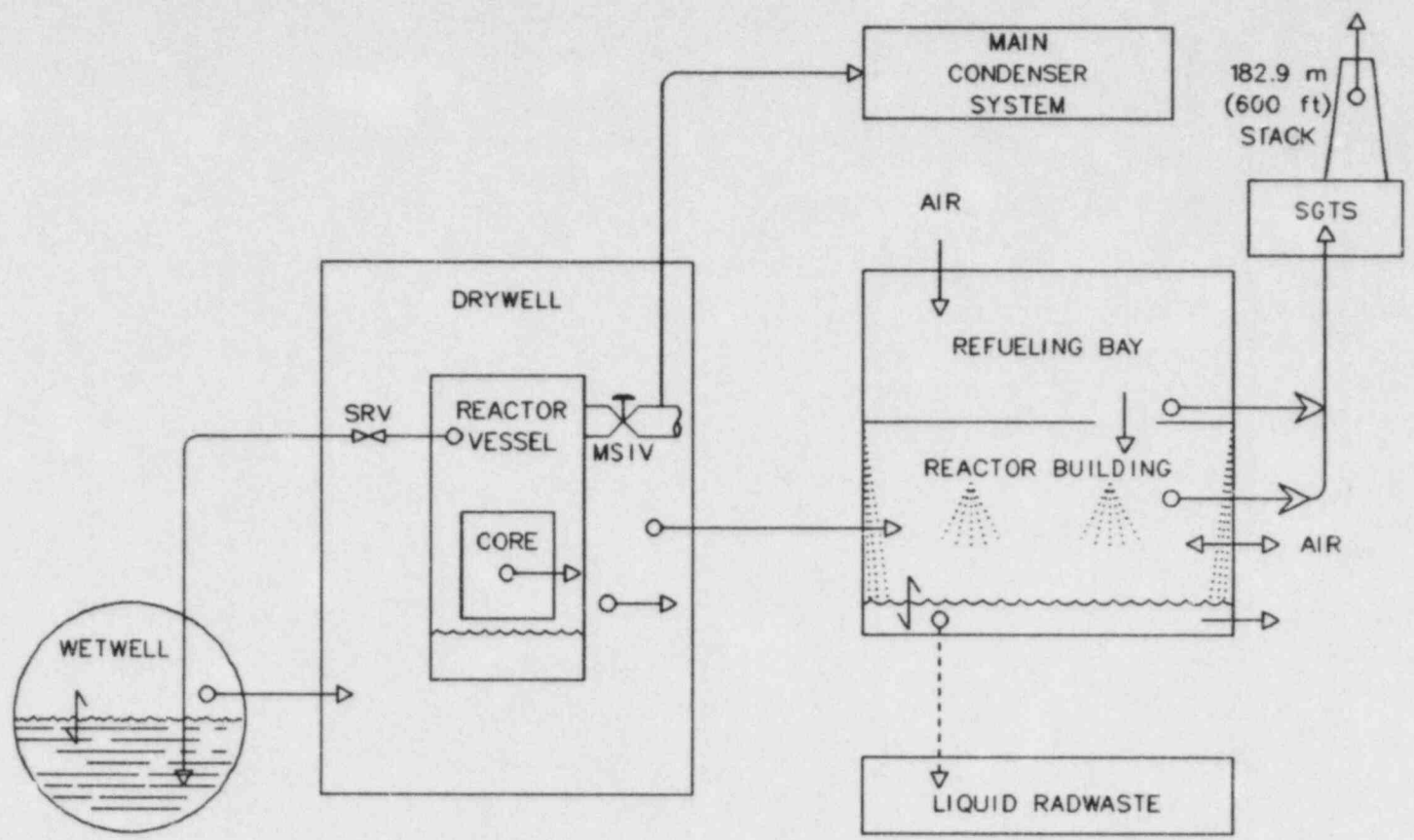
Fig. 2.22. Principal fission product pathways prior to time of reactor vessel bottom head failure (2590 min).
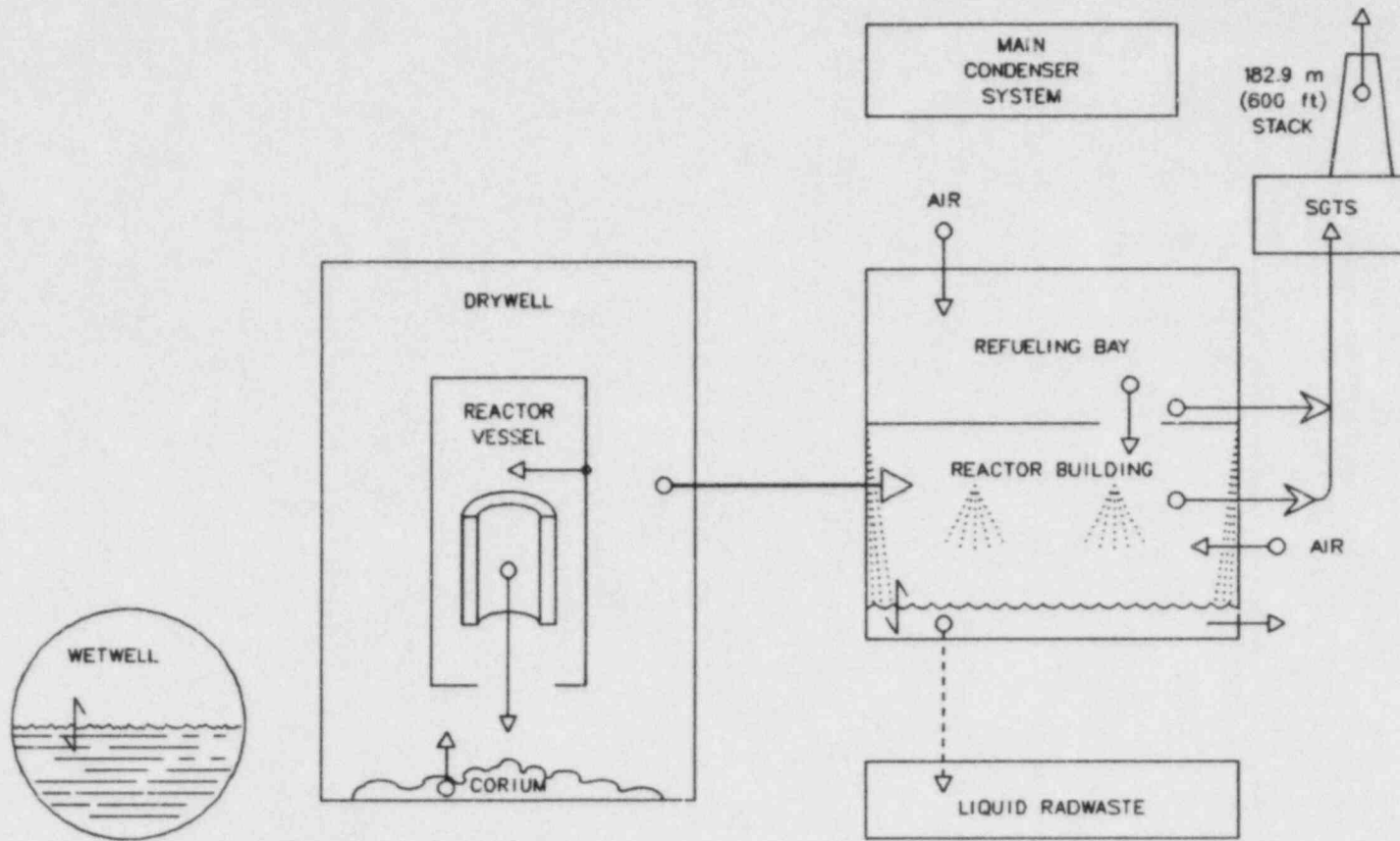
Fig. 2.23. Principal fission product pathways after time of reactor vessel bottom head failure (2590 min).

3. FISSION PRODUCT TRANSPORT ASSUMPTIONS

3.1 Introduction

Models and assumptions used for estimation of (1) fission product release from fuel, (2) chemical forms in the reactor vessel and in the primary containment, (3) interaction of gaseous species with aerosols, (4) deposition of gaseous forms onto solid surfaces, (5) volatility over water, (6) rates of formation of organic iodides, and (7) aerosol formation rates in the reactor vessel and in the drywell have been outlined in previous reports.[3.1,3.2] There is admittedly considerable room for improvement of many of these models and we are continually reexamining them as new information being developed by NRC research programs becomes available.

In this chapter are described three modifications to the earlier models used in previous studies. The new models are the result of recently developed information and are described in Sects. 3.2.1 through 3.2.3. In addition, Sect. 3.2.4 describes some new insights regarding the chemical behavior of cesium and iodine which have not been incorporated into this study but may at some future time alter transport model assumptions for these two elements.

3.2 Changes in Iodine and Cesium Transport Assumptions

3.2.1 Estimated release from drywell rubble

Estimates of the rate of fission product release from the core/concrete debris bed on the drywell floor could be a critical factor in the overall transport pathway. Materials evolving from this source location bypass the suppression pool, entering directly into the drywell atmosphere.

Earlier estimates of release rates from this inventory location were based on use of the conventional fuel release rate factor, multiplied by a surface-to-volume ratio factor to account intuitively for the smaller surface per unit volume ratio of the drywell debris bed relative to that of the fuel element geometry on which the experimental values were based. For the drywell rubble bed, a surface area factor of 25 was employed; i.e., release rate coefficients obtained for the calculated bed temperature were divided by 25 to account for its smaller surface to volume ratio. Bed temperatures were obtained from the INTER subroutine of the MARCH program.

The above procedure was always considered to be an interim method. In particular, it excludes consideration of the sparging action caused by gases evolving from the concrete which should significantly accelerate the fission product evolution rate.

For this study, we have replaced this interim procedure by employing directly results obtained using the VANESA code.[3.3,3.4] This computational procedure, developed at Sandia National Laboratory, can be

characterized as follows:

1.   VANESA employs the CORCON code to develop the thermal-hydraulics of the drywell rubble bed. Due to the differing densities, the rubble bed is predicted to divide into metal and oxide layers and the CORCON results include predictions of metal and oxide layer temperatures, CO_2 and H_2 evolution rates from the degrading concrete, and determination of the melt geometry.

2.   An important feature of CORCON used by VANESA is the determination of the melt layer locations relative to the gases evolving from overheated concrete. This feature is essential for determination of realistic sparging rates and estimation of the degree of availability of CO_2 and H_2 for reaction with the more reactive elements in the metallic layer; i.e., there occurs various degrees of bypassing of gas flow.

3.   The degree of reaction of H_2O and CO_2 with metals to produce H_2 and CO is then estimated. The principal reactive metal is Zr and when available, Zr is oxidized to ZrO_2 (which transfers to the oxide layer), CO_2 reduces to elemental C, and H_2O reduces to H_2.

4.   Fission product compounds are assumed to be distributed in solution between the oxide and metal phases. Cesium is assumed to be principally Cs_2O, iodine is assumed to be CsI, and both are assumed to be dissolved in the oxide phase. Vapor pressures of dissolved materials are estimated to determine the driving force for transfer into the sparging gas flow. Raoult's Law is used to determine the vapor pressure of each fission product compound dissolved in either the oxide or liquid metal phase, a method strictly suitable only for ideal solutions. VANESA, in its current simple form, presumes complete liquifaction of all core/concrete phases, even when CORCON predicts otherwise.

5.   VANESA then calculates the amount and composition of aerosol material which forms by subsequent condensation of compounds in the sparge gas. (These results are discussed in Chap. 4.)

Results of the CORCON/VANESA calculation for the loss-of-DHR accident sequence are illustrated in Figs. 3.1 and 3.2.[*] Figure 3.1 illustrates the predicted oxide and metal layer temperatures. Note that most of the decay heat is assumed deposited in the oxide layer causing much higher temperatures relative to the metallic layer. Interface heat transfer resistance is evidently estimated to be extremely high, resulting in predicted temperature differences in excess of ~750°C in the oxide layer relative to the metal layer.

The level portion of the oxide layer temperature curve is evidently due to melting of this layer during the time period, ~2620 min to ~2850 min; i.e., prior to 2620 min, the oxide layer is completely solid and later than 2850 it is completely liquid. For this case, the oxide layer is predicted to be more dense than the metal layer and thus is the lower layer. In addition to these two principal phases, oxide crusts form above and below the metallic layer. Further description of CORCON results is provided in Chap. 4 in connection with aerosol transport estimates.

The resulting evolution of cesium and iodine as computed by VANESA is illustrated in Fig. 3.2 and compared with estimates based on our earlier model. Note that VANESA predicts far more rapid evolution rates, as would be anticipated by the inclusion of the sparging effect. The higher evolution rate of cesium relative to iodine results solely from the higher estimated vapor pressure for Cs_2O relative to CsI. Note, all of the cesium is predicted to evolve within 40 min after reactor vessel bottom head failure and during the period when the oxide phase is predicted by CORCON to be still frozen. This is currently an unrealistic feature of the CORCON-MOD1/VANESA results.

We will use directly the predicted rate of cesium and iodine release from the drywell rubble bed in our current transport rate estimate. Although no estimate of noble gas release is provided, it will be assumed that it is at least as rapid as the predicted cesium evolution rates. This is formally accomplished in our computational procedure by assuming the following values for release rate coefficients from the drywell rubble:

<div align="center">

Release rate coefficients to approximate
VANESA predictions

Noble gases	$0.046 \ min^{-1}$
Cesium	$0.046 \ min^{-1}$
Iodine	$0.011 \ min^{-1}$

</div>

3.2.2 Organic iodide production rate

Organic iodides [principally methyl iodide (CH_3I)], which form to a small degree under containment vessel and reactor building conditions, possess far lower chemical reactivity than does molecular iodine (I_2), which is the principal vapor form outside the reactor vessel, and have a far higher volatility than any metal iodide vapors that might exist. Therefore, organic iodides will deposit more weakly on all surfaces (structure and aerosol), are less soluble in water, and are less absorbent in the SGTS charcoal beds than other iodine forms. The potential for release to the atmosphere is therefore significantly greater for organic iodides relative to other iodine vapor forms.

In order to determine the amount of iodine present as organic iodides, a rate of formation equation is needed to calculate the rate at which I_2 is converted to organic iodides. Since the principal mechanisms of formation are not known, a well-founded rate equation cannot be developed. In available reviews on the subject of organic iodide formation, the rate of formation was mostly ignored and only equilibrium levels were considered. Since the formation rate and not the equilibrium level is needed, an estimate must be made from the data available.

In earlier reports,[3.1,3.2] the formation rate was estimated by using the equilibrium equation presented by Postma and Zavodski[3.5] to predict equilibrium levels of organic iodides, and by assuming that these levels are achieved in 4 h. These assumptions yielded a formation rate:

conversion rate of I-vapor to organic iodine, $\%/h = 0.05 \times C^{-0.26}$ (3.1)

where C is the iodine concentration in the vapor in mg/m^3. This equation predicts a formation rate of 0.015%/h for a "typical" I_2 concentration of 100 mg/m^3. In more conventional units, the predicted equilibrium level of organic iodide in the atmosphere of a control volume may be expressed as

$$C_o^* = 8.11 \times 10^{-6} \, Cg^{0.74} \, , \tag{3.2}$$

where

C* = equilibrium level of organic iodide, ($gmol/cm^3$),
Cg_o = initial concentration of I_2 in the atmosphere, $gmol/cm^3$.

We now will assume an exponential formation rate approaching C_o^* asymptotically,

$$\frac{dC_o}{dt} = \alpha(C_o^* - C_o) \, , \tag{3.3}$$

where C_o = the concentration ($gmol/cm^3$) of organic iodine at time t(s). The integrated form of Eq. (3.3) is:

$$C_o(t) = C_o^* (1 - e^{-\alpha t}) + C_o(0)e^{-\alpha t} \, . \tag{3.4}$$

The factor α was determined by using the equilibrium results given by Postma[3.5] and by assuming 4 h is required to reach equilibrium; i.e., if 99% of the equilibrium value is reached in 4 h and assuming no organic iodine was present initially, the constant α becomes equal to 3.2 × 10^{-4} s^{-1}.

Organic iodides will be removed from the vapor phase by absorption, decomposition, and by chemical reaction. Data from the Containment Systems Experiment (CSE)[3.6] were used to derive an equation for organic iodide removal as a function of time and temperature. Currently we will assume that the removal rate of organic iodide can be expressed as a first order process:

$$\frac{dCo}{dt} = -\gamma Co \, , \tag{3.5}$$

where

$$\gamma = \gamma(T) = \exp[a - b/T] \, . \tag{3.6}$$

The CSE data indicate that the value of γ is relatively independent of C_o. At temperatures of 358 K and 395 K, values of 3 × 10^{-6} and

10^{-5} sec^{-1} respectively are estimated, yielding values of $a = 0.14$, $b = 4.6 \times 10^3$ for the constants in Eq. (3.6).

The complete organic iodide formation/destruction equation may thus be written:

$$\frac{dCo}{dt} = \alpha(C_o^* - C_o) - \gamma C_o \ , \tag{3.7}$$

whose solution is

$$C_o(t) = \frac{\alpha C_o^*}{\alpha + \gamma} \ [\ 1 - e^{-(\alpha+\gamma)t}] + C_o(0)e^{-(\alpha+\gamma)t} \ . \tag{3.8}$$

It must be recognized that the principal mechanisms for the formation and removal of organic iodine are not known, and the equations presented above are estimates developed from the experimental data available. In this regard, it should also be noted that factors other than iodine gas phase concentration might affect the formation rate of organic iodine. These factors include the type of paint used on the vessel walls and the amount of oxygen, moisture, and radiation present. While it seems fairly well established that moisture and radiation can increase the formation of organic iodides and the presence of oxygen decreases its formation, there is still some doubt on the effect of different types of paint. For example, Bennett et al.[3.7] suggests that the presence of organic paint on the walls increases the formation of organic iodides, but this would suggest a surface reaction while most researchers feel that the main mechanism is reaction with airborne organics.

3.2.3 Iodine volatility

Iodine volatilities are usually expressed in terms of a partition coefficient defined by:

$$\text{partition coefficient (PC)} = \frac{\text{concentration of iodine in aqueous solution}}{\text{concentration of iodine in gas phase}} \ .$$

The aqueous-to-gas phase iodine partitioning is partly determined by the rate and degree of iodine hydrolysis and the effect of radiolysis on iodine solutions. The classical representation of iodine hydrolysis is expressed in two successive reactions:

$$I_2 + H_2O \rightleftharpoons HOI + I^- + H^+ \tag{3.9}$$

$$3HOI \rightleftharpoons IO_3^- + 2I^- + 3H^+ \ .$$
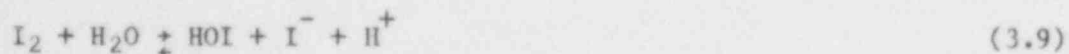
For purposes of evaluating volatility only, the molecular (un-ionized) iodine forms need to be considered. Because of the polar nature of water and electrostatic effects, ions are not expected to vaporize directly. The final products of iodine hydrolysis are I^-, IO_3^-, and H^+. Since these products are ionic, parameters such as high pH and high temperature that favor their formation reduce iodine volatility.

Radiolysis of iodine solutions results in the interaction of iodine species with radiolysis products from the solvent water. Thus, the chemistry is concerned with the interaction of water radiolysis products $OH\cdot$, e_{aq}^-, $H\cdot$, H_2O_2, O_2^-, and HO_2 with iodine species such as I_2, I_3^-, I^-, and IO_3^-.

The basic aspects of aqueous iodine chemistry and radiolysis have been studied for many decades and are still not well understood. However, there are a number of experimental measurements of iodine partition coefficients which yield information that can be used to evaluate aqueous/gaseous iodine partitioning in nuclear reactor accidents. In a series of four tests at the Containment Systems Experiment,[3.6] a partition coefficient of $6.2 \times 10^3 \pm 1.9 \times 10^3$ is given. These tests were conducted with a vapor temperature of either 358 K or 398 K and sump temperatures between 303 K and 317 K, and initial iodine vapor concentrations from 1.17 to 165 mg/m^3.

In addition, there have been a number of laboratory scale studies of iodine partitioning. In carrying out measurements of iodine partition coefficients, it is far easier to accurately measure low values (high volatility) rather than high values. This is due to the nature of the tests whereby large values mean that very little iodine appears in the gas phase. Also anomalous chemical behavior of low concentrations ($<\sim 10^{-6}$ $g\cdot mol/L$) of radioiodine has been observed for many years.[3.8] The difficulty in measuring large partition coefficients and the anomalous behavior of radioiodine at low concentrations indicate that many laboratory scale volatility measurements will be system dependent. That is, factors such as interaction with container materials and impurities could dominate the experimentally reported volatility. It is a paradox that such measurements may still be the best guideposts that can be expected because nuclear reactor accidents do not occur in "hypothetically pure" systems.

Lin[3.9] reports that for iodine concentrations less than $\sim 10^{-6}$ $g\cdot mol/L$, partition coefficients tend toward a value of $\sim 9 \times 10^3$ and become relatively insensitive to concentration. Kelly[3.10] reports values somewhat lower than this; at 7.9×10^{-7} $g\cdot mol/L$ and 303 K, a value of 8.5×10^2 is given. At this same temperature and a concentration of 7.9×10^{-10} $g\cdot mol/L$, Kelly lists a value of 2.1×10^3. Pelletier and Hemphill[3.11] report results at concentrations as low as 7.9×10^{-14} $g\cdot mol/L$. The partition coefficients at this extremely low concentration are $\sim 8 \times 10^3$ and thus substantiate the value given by Lin.

At Oak Ridge National Laboratory, both calculations[3.12] and experimental measurements[3.13] have emphasized the importance of concentration, pH, temperature, and mixing time in determining iodine partition coefficients. Values in the range 10^2 to 7×10^4 have been measured under widely varying conditions.

In general then, values of iodine partition coefficients measured in the laboratory and in the large Containment Systems Experiment yield

values in the range 10^3 to 10^4. For this accident sequence, an iodine partition coefficient of 5×10^3 will be used. This is close to the value found in the Containment Systems Experiment and is in line with values measured in the laboratory. It is a factor of 10 lower (factor of 10 <u>higher volatility</u>) than assumed for our earlier studies.

It is recognized that radiolysis of iodine solutions could alter the results obtained from tests involving iodine hydrolysis alone. The influence of pH on the radiolysis is quite complex. In acid solution, I^- can be oxidized by OH or H_2O_2 to give I_2. Conversely, in alkaline solutions I_2 can be reduced by H_2O_2 to form I^-. Until the complexities of radiolysis of iodine solutions are better understood, it appears necessary to use partition coefficients based on hydrolysis.

3.2.4 Cesium and iodine chemical behavior

In earlier reports[3.1],[3.2] it was noted that cesium compounds CsOH and CsI may react with a number of available metal oxides, such as Cr_2O_3, Al_2O_3, $Al_2O_3 \cdot SiO_2$, to form stable cesium compounds. The net effect of these reactions would be to sequester cesium and liberate iodine from CsI. The degree to which these reactions proceed depends principally on the temperature and oxygen potential. Most are predicted to proceed at relatively high oxygen potentials ($H_2/H_2O \ll 1$), but some are predicted to proceed at least partially under reducing conditions expected in the reactor vessel prior to failure, i.e., $H_2/H_2O > 0.1$.

It has also been noted that the major portion of the iodine liberated from CsI by reaction with metal oxides would not long remain as gaseous I_2, but would likely chemisorb on available surfaces such as oxidic or metallic aerosols and metallic structural surfaces.

We now note that in addition, control rod material, B_4C, will likely hydrolyze in a steam environment to form a number of relatively volatile compounds such as HBO_2, $H_3B_3O_6$, B_2O_3, which are predicted to have a high thermodynamic driving force for formation of cesium metaborate ($CsBO_2$) or dicesium tetraborate ($Cs_2B_4O_7$).

We have performed equilibrium thermochemic calculations for the hydrolysis reaction of B_4C with steam and subsequent reaction with CsOH and CsI for hydrogen to water ratios of 0.0, 0.1, 1.0, and 10, at temperatures of 1000, 1200, 1400, 1600, 1800, and at 2000 K and 70 atm total pressure. At 1800 K and all hydrogen to water ratios, more than 90% of the cesium was calculated to be in the form of $CsBO_2$ and $Cs_2B_4O_7$. Also at this temperature and for hydrogen to water ratios of 0.0, 0.1, or 1.0, more than 70% of the iodine was in the form of HI + I. As noted earlier, HI or I released due to stripping of cesium from cesium iodide would likely not be permanently gaseous species. They are quite reactive and are likely to combine with other available metal forming another iodide or attach via chemisorption to virtually any available solid surface.

A more complete description of the predicted degree of B_4C hydrolysis at various H_2/H_2O atmospheres and the subsequent reactions to form cesium borates is presented by E.C. Beahm and R. P. Wichner[3.14].

References for Chapter 3

3.1   R. P. Wichner et al., *Station Blackout at Browns Ferry Unit One — Iodine and Noble Gas Distribution and Release*, NUREG/CR-2182, Vol. 2 (August 1982), Chapters 3 and 4.

3.2   R. P. Wichner et al., *SBLOCA Outside Containment at Browns Ferry Unit One Volume 2. Iodine, Cesium, and Noble Gas Distribution and Release*, NUREG/CR-2672, Vol. 2 (September 1983), Chaps. 3 and 4.

3.3   D. A. Powers and J. E. Brockmann, *Status of VANESA Validation* (Sandia report, to be published).

3.4   D. A. Powers and J. E. Brockmann, *Release of Fission Products and Generation of Aerosols Outside the Primary System* (Sandia report, to be published).

3.5   A. K. Postma and R. N. Zavodski, *Review of Organic Iodine Formation*, WASH-1233 (1972)

3.6   R. K. Hilliard and L. F. Coleman, *Natural Transport Effects on Fission Product Behavior in the Containment Systems Experiment*, BNWL-1457, 1970.

3.7   R. L. Bennett et al., *Reactions of I-Vapor with Paints*, ORNL/TM-2760, 1970.

3.8   M. Kahn and J. Kleenberg, *Radiochemistry of Iodine*, NAS-NS-3062, 1977.

3.9   C. C. Lin, "Volatility of Iodine in Dilute Aqueous Solutions," *J. Inorg. Nucl. Chem. 43*, 3229 (1981).

3.10 J. L. Kelly, C. J. Babad, and R. U. Mulder, *Study of Iodine Partition Coefficients*, Report No. UVA/532256/NEEP 81/101, 1981.

3.11 C. A. Pelletier and R. T. Hemphill, *Nuclear Power Plant Related Iodine Partition Coefficients*, EPRI NP-1271, 1979.

3.12 J. T. Bell, M. H. Lietzke, and D. A. Palmer, *Predicted Rates of Formation of Iodine Hydrolysis. Species at pH Levels, Concentrations and Temperature Anticipated in LWR Accidents.* NUREG/CR-2900 (ORNL-5876), 1982.

3.13 E. C. Beahm, private communication, 1983.

3.14 E. C. Beahm and R. P. Wichner, *Survey of Chemical Reactions of Cesium, Iodine, and Tellurium Which May Occur in LWR Accidents*, (to be published).

ORNL—DWG 84—4218 ETD
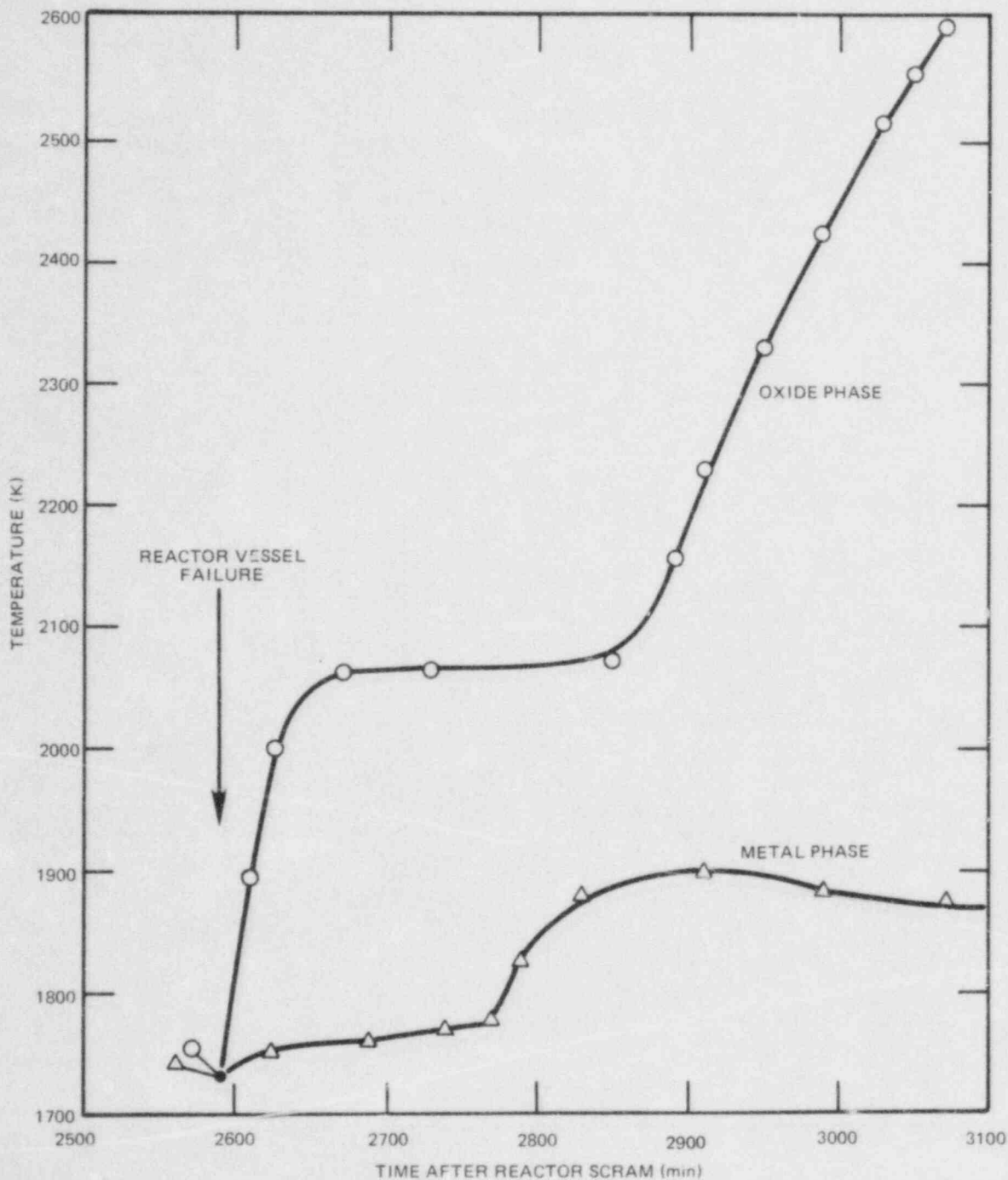
Fig. 3.1. Drywell rubble bed temperatures predicted by CORCON.
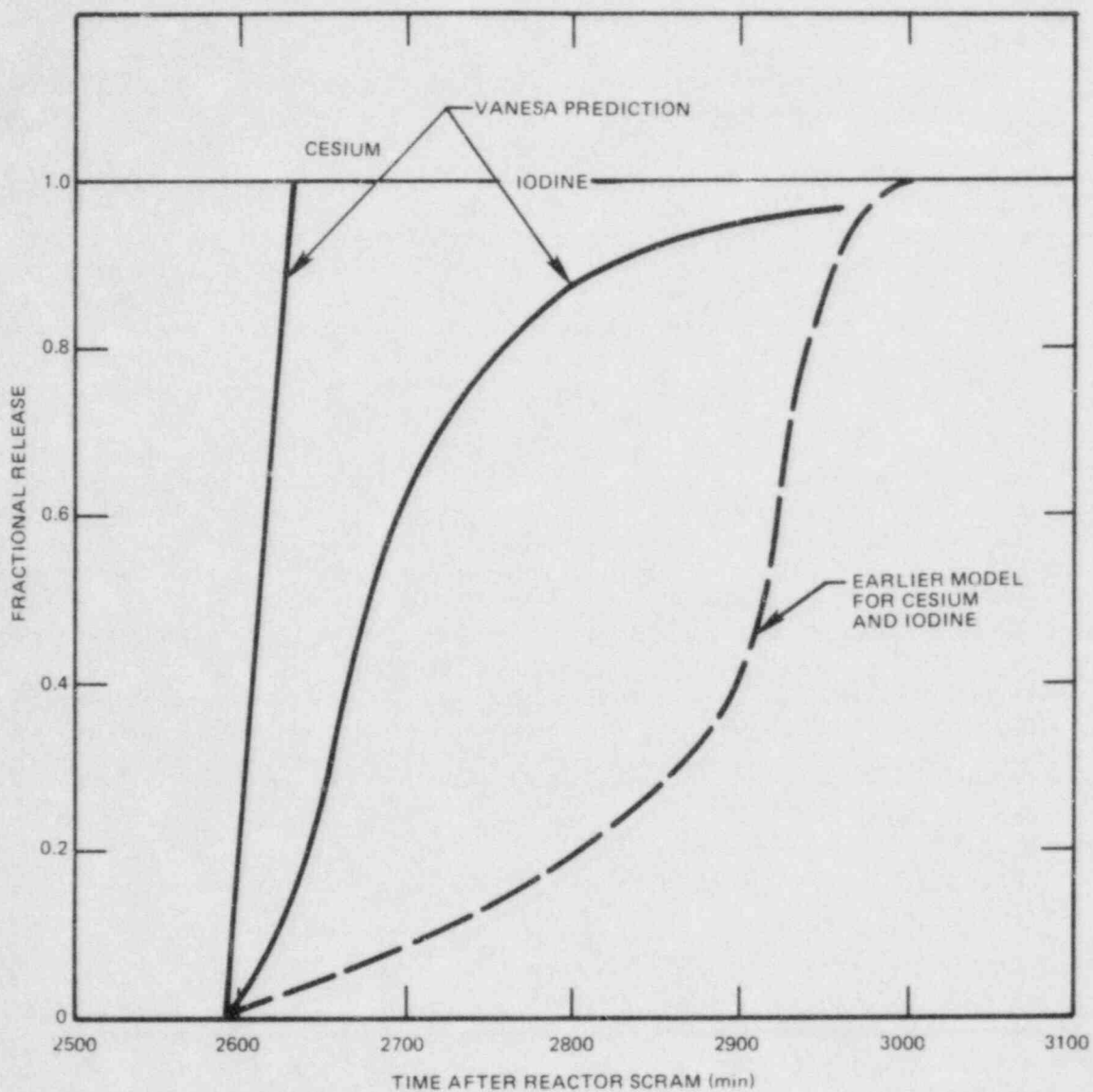
Fig. 3.2. Comparison of the VANESA-predicted cesium and iodine releases from the drywell rubble bed with the releases predicted by a previous model.

4. AEROSOL PRODUCTION AND TRANSPORT

4.1 Introduction

After reactor vessel melt-through, molten fuel comes into contact with the concrete basemat in the drywell, and the heat from the molten fuel produces concrete decomposition, gas evolution, and evolution of "core-concrete" aerosols. Evaluation of the transport and deposition of these aerosols is an important factor for determining fission product transport rates. This is so because volatile fission products can adsorb or condense on the aerosols and some fission product species may themselves form aerosols. In either case, aerosol transport behavior may largely determine fission product transport behavior.

The calculational procedures used in this study to determine core-concrete interaction phenomena, core-concrete aerosol production rates, and aerosol transport in the drywell and reactor building are different from those used in the previous two Browns Ferry accident sequence studies[4.1],[4.2] The differences in calculational procedures include the following:

1. In the previous studies, core-concrete rubble temperatures and gas evolution rates from the decomposing concrete were estimated using the results from the MARCH subroutine INTER. In this study, the CORCON-MOD1 code, developed at Sandia National Laboratories,[4.3] is used for this purpose.
2. Core-concrete aerosol production rates were estimated in the previous studies using a simple correlation based on experiments performed at Sandia.[4.4] In this study, the VANESA code, developed by Dana Powers at Sandia,[4.5] is used to determine aerosol production rates.
3. The HAARM-3 aerosol transport code was previously used to determine aerosol transport in the drywell, reactor building, and refueling bay. In this study, the QUICK aerosol transport code, developed at Battelle-Columbus Laboratories,[4.6] is used to calculate aerosol transport.

A summary of the results from the series of calculations used to estimate aerosol transport in the LDHR accident sequence is presented in this chapter; the details of these calculations are presented in Appendix B. Also presented in Appendix B are results from a group of sensitivity calculations performed using the MARCH subroutine INTER, the CORCON-MOD1 code, and the VANESA code.

4.2 Drywell Debris Bed Behavior

Calculation of the gas evolution rates and core material temperatures produced due to core-concrete interactions in the drywell is

important for the following reasons:

1. The rates of release of volatile fission products and structural aerosols from the core material-concrete mixture are a strong function of the core-concrete temperatures and gas evolution rates.
2. The rates of gas evolution from the core-concrete mixture largely determine the thermal-hydraulic conditions existing in the drywell, reactor building, and refueling bay; these thermal-hydraulic conditions influence aerosol and fission product deposition in these compartments.

In analyses performed for the previous two Browns Ferry accident sequences, results from the MARCH subroutine INTER were used to estimate the time history of core material temperatures and gas evolution rates due to the interaction of the molten core with the concrete basemat. For the present LDHR study, the CORCON-MOD1 code[4.3] was made operational at ORNL and used to estimate gas evolution rates and core material temperatures due to core-concrete interactions. In this section we present results from the CORCON and the INTER calculations to illustrate how they differ for this accident sequence (more details on these calculations are presented in Appendix B).

Table 4.1 presents a summary of the core-debris initial conditions, as calculated by the MARCH code. Figure 2.8 shows that about 15% of the zircaloy fuel-rod cladding is estimated to be oxidized prior to reactor vessel melt-through. The table also shows that the calculated core material temperature prior to the start of core-concrete interaction is 1737 K. Since the estimated initial solidus temperature for the oxide portion of the melt, as calculated by CORCON, is roughly 2100 K, at least some portion of the time the oxide portion of the melt is projected to be solid. Since the CORCON-MOD1 code was not designed to model a solidified melt, results for early times with low oxide layer temperatures may be unrealistic.

The CORCON and INTER calculations were performed to model a period of 8 h after the start of the time of core-concrete interaction for the LDHR accident sequence (the start of core-concrete interaction was calculated to occur 2590 min after reactor scram was initiated). Table 4.2 presents a summary of the total amounts of CO, CO_2, H_2, and H_2O evolved due to core-concrete interaction, based on the CORCON and INTER calculations (the "base-case" CORCON calculation used in the accident sequence analysis is noted as "CORCON1"). Figures 4.1 and 4.2 present the oxide and metal layer temperatures calculated using the CORCON and INTER codes. The results of the comparison of the calculated CORCON and INTER results can be summarized as follows:

1. The amounts of gases evolved from the melt projected by INTER is significantly greater than predicted by CORCON. The largest difference occurs for CO; INTER predicts that about 10,000 times more CO is evolved for the LDHR accident sequence than does CORCON. The low CO release in the CORCON calculation is, based on discussions with members of the Sandia staff,[4.7] due to "coking," or the reduction of CO in the CORCON calculation to elemental carbon. As is illustrated

in calculations presented in Appendix B, coking is predicted to occur when there is a large amount of un-oxidized zircaloy in the core melt (this is the situation predicted for the LDHR sequence). For the "base-case" CORCON calculation summarized in this section, 755 kg of elemental carbon was calculated to have been produced due to coking.

2. As illustrated in Figs. 4.1 and 4.2, CORCON predicts significantly higher metal and oxide layer temperatures than does INTER. The calculated CORCON metal layer temperatures are roughly 300 K higher than the INTER temperatures. The calculated CORCON oxide layer temperatures are roughly 400 to 500 K higher than the INTER temperatures for the first 5.5 h after the start of core-concrete interaction; however, at 8 h, the CORCON oxide temperature is roughly 1000 K higher than that calculated with INTER. CORCON predicts that the oxide portion of the melt does not begin to melt until 3 h after the start of the core-concrete interaction, and that the oxide remains heavier than the metal layer for the entire 8 hours of the calculation. In contrast, INTER predicts that the oxide layer becomes molten almost immediately after the start of the core-concrete interaction, and that the metal layer becomes more dense than the oxide layer roughly 1 hour after the start of the calculation. Even when melting of the oxide layer in bulk is predicted, a detailed look at the output shows that the interfaces between the oxide, metal, and concrete layers are below the solidus temperature. Since the heat-transfer correlations in CORCON-MOD1 are not designed to model this situation, we suspect that the high oxide temperatures predicted near the end of the 8-hour calculation are not realistic.

4.3 Aerosol Production Rates in the Drywell

For the previous Browns Ferry accident sequence studies, an empirical correlation developed based on experiments performed at Sandia[4.4] was used to estimate aerosol production rates resulting from core-concrete interactions. More recently a mechanistic model, VANESA, has been developed to predict aerosol generation and fission product release during core-concrete interactions.[4.5] VANESA results related to volatile fission product release rates are discussed in Section 3.2 of this report; in this section we will discuss the aerosol generation rate results obtained using the VANESA model.

The VANESA model was developed at Sandia by Dana Powers who performed the VANESA calculations summarized in this section and in Appendix B. VANESA includes models for aerosol formation due to evaporation from the melt, sparging of the melt by gaseous products of concrete decomposition, reactive vaporization of melt components, and mechanical formation when gas bubbles burst at the melt surface.

Inputs required to run VANESA include the initial composition of the core debris, the concrete composition, the melt temperatures (metal and oxide) during core-concrete interaction, the rate of gas evolution from the melt, and the geometric top surface area of the molten pool. This input was supplied to Sandia from the CORCON1 and INTER calculations discussed in the previous section.

The aerosol generation rates predicted by VANESA for the CORCON1 thermal data are summarized in Fig. 4.3 and Table 4.3. VANESA predicts that a total of 973 kg of core-concrete aerosol would be produced. As illustrated in Table 4.3, the majority (roughly 94%) of this aerosol is made up of SiO_2, CaO, K_2O, FeO, Al_2O_3, Na_2O, and MnO_2. Details of the VANESA results obtained based on inputs from the INTER data and from three other CORCON runs are presented in Appendix B. It should be mentioned that the calculated amount of aerosol produced based on INTER was roughly a factor of 2 higher than that based on the CORCON1 thermal data.

4.4 Aerosol Transport in the Drywell

Aerosols are produced in the drywell due to core-concrete interaction phenomena that start roughly 2590 minutes after reactor scram. Prior to the start of core-concrete interaction the drywell is calculated to have failed due to over-pressurization (see Sect. 2.2). After drywell failure, aerosols produced by core-concrete interaction can be transported from the drywell to the reactor building; the gases that would transport the aerosols out of the drywell are those produced by the core-concrete interaction.

The QUICK aerosol transport code[4.6] was used to calculate aerosol behavior and transport in the drywell. Input requirements for QUICK include the time dependence of the rate of gas leakage from the drywell (obtained from the CORCON1 gas evolution data), the rate of aerosol production in the drywell (obtained from VANESA) and parameters related to the sizes of the aerosols produced due to core-concrete interactions. QUICK code outputs include the aerosol concentration and size distribution in the drywell, the aerosol deposition on horizontal surfaces by settling, and the aerosol leakage from the drywell; all of these were determined as a function of time. Detailed results are presented in Appendix B.

A summary of the results for the QUICK drywell calculations for the LDHR sequence is presented in Table 4.4 and Figs. 4.4-4.6. Table 4.4 lists the amounts of aerosol predicted to have settled in the drywell, leaked out of the drywell, and to have remained airborne in the drywell at 3070 min, or 8 h after the start of core-concrete interaction. Roughly 82% of the aerosol produced in the drywell is predicted to be transported to the reactor building, and about 14% of the aerosol produced settles on the drywell horizontal surfaces. These results are somewhat different from those produced in the SBLOCA analysis;[4.2] in that case, 93% of the aerosol produced was transported to the reactor building while only 0.9% of the aerosol mass settled to the floor. The differences in the LDHR and SBLOCA results are due to two major factors. First, the LDHR drywell leak rates are lower than those used in the SBLOCA sequence; because of this, aerosols would reside in the drywell longer in the LDHR sequence. Secondly, the projected aerosol mass produced in the LDHR sequence is roughly 5 times that predicted in the SBLOCA sequence; because of this and the lower leak rates, aerosols would be expected to grow to larger sizes and settle faster under LDHR accident conditions.

The time variation of the suspended aerosol concentration predicted in the drywell is shown in Fig. 4.4. The concentration peaks at about 13.2 g/m^3 at 2832 min, roughly 4 h after the start of the core-concrete interaction. The concentration airborne at 3070 min remains high and has a value of 9.2 g/m^3. Figures 4.5 and 4.6 illustrate, respectively, the time variation of the leaked and settled mass between 2590 min and 3070 min.

4.5 Aerosol Transport in the Reactor Building

As discussed in Sect. 4.4, roughly 82%, or 848 kg, of the core-concrete aerosol produced in the drywell is predicted to be released into the reactor building. The aerosol transport pathways in the reactor building and refueling bay for the LDHR accident sequence are somewhat different than those produced in the SBLOCA accident sequence. For the LDHR sequence, the gas flow rates into the reactor building from the drywell are somewhat smaller than those produced in the SBLOCA sequence; this is largely due to the fact that CORCON-MOD1 was used instead of INTER for the present sequence. Because of the lower flow rates to the building, the Standby Gas Treatment System (SGTS) is able to maintain a slightly negative pressure in the building continuously for the 8-h period after the start of the core-concrete interaction. This means that, except for a short period of time after 2590 min, all of the gases flowing into the reactor building go through the SGTS, and there is only a short period of time where there is flow to the refueling bay or direct exfiltration to the environment from the reactor building. The reactor building thermal-hydraulic response is described in more detail in Sect. 2.6 and Appendix A.

Because of the flow conditions in the reactor building, the main pathway for aerosol transport to the environment is through the SGTS after the HEPA filters in the SGTS rupture. The SGTS has two banks of HEPA filters; based on analyses performed for the SBLOCA sequence,[4.2] each of the banks may be loaded with ~81 kg of aerosols before failure by tearing. Thus according to this assessed failure mode, both HEPA filters would tear following transport of 162 kg to the SGTS after which there would be a direct aerosol transport path through the SGTS to the environment.

The QUICK code was used to calculate aerosol behavior and transport in the reactor building. The rates of aerosol input to the reactor building were determined from the drywell results. Gas leak rates from the reactor building were determined from calculations performed with the secondary containment thermal-hydraulics model (see Appendix A). QUICK code outputs were of the same type as those produced for the drywell calculations. Aerosol leakage results from the reactor building determine the times when the SGTS filters would rupture. Details of the QUICK reactor building calculations are presented in Appendix B.

A summary of the reactor building calculations is presented in Table 4.5 and Figures 4.7-4.9. Table 4.5 lists the amounts of aerosol predicted to have settled in the reactor building, remained airborne in the reactor building, and leaked to the SGTS. Also listed are the

amount of aerosol deposited on the SGTS filters, the predicted times for SGTS filter rupture, and the amount of aerosol that leaks through the SGTS after filter rupture. Table 4.5 illustrates that aerosol settling is the major deposition mechanism; roughly 67% of the aerosols transported to the building deposit there by settling. The table also illustrates that the second filter bank is predicted to rupture at 2880.5 min. roughly 290.5 min after the start of the core-concrete interaction. Prior to filter rupture, 162 kg, or 17.9% of the aerosol transported to the reactor building from the drywell, was deposited on the SGTS filters. The amount of aerosol transported to the SGTS after filter rupture, 87.3 kg or 9.6% of the aerosol in the reactor building, is predicted to be released to the environment.

It should be noted that the LDHR reactor building results differ from those for the SBLOCA sequence in that SGTS filter rupture was not predicted in the SBLOCA sequence. This difference is due to the fact that the predicted aerosol source for the LDHR sequence is almost 5 times higher than the source for the SBLOCA sequence.

The time variation of the suspended aerosol concentration predicted in the reactor building is shown in Figure 4.7. The concentration peaks at about 2.1 g/m^3 at 2836 min, roughly 246 min after the start of the core-concrete interaction. Figures 4.8 and 4.9 illustrate, respectively, the time variation of the leaked and settled mass between 2590 min and 3070 min.

4.6 Summary of Aerosol Transport Results

The overall results from the QUICK calculations indicate that all aerosol release to the environment for the LDHR accident sequence occurs by transport through the SGTS after filter rupture. The predicted amount of aerosol release through the ruptured SGTS filters is 87.3 kg; this represents 9% of the total mass of aerosol predicted to be produced in the drywell (973.3 kg).

The main uncertainties in the aerosol transport calculations for the LDHR accident sequence are summarized below:

1. The temperature of the core material "melt" predicted by MARCH at the time of the start of core-concrete interaction was 1737 K; at this temperature none of the core material would actually be molten. Uncertainties in this initial melt temperature would influence both the CORCON and the VANESA results.

2. The CORCON-MOD1 code was used in this analysis to calculate gas evolution rates and core material temperatures resulting from core-concrete interactions. Although we believe that using CORCON for such calculations is an improvement over using the results obtained from MARCH-INTER calculations, the CORCON-MOD1 code is not designed to model conditions where a portion of the core material is frozen. Because of this, the predicted core material oxide temperatures based on the CORCON calculations are believed to be too high. It should be noted that a new version of CORCON, called CORCON-MOD2, is being developed and should be available in 1984;

this version is designed to handle situations where portions of the melt are frozen.

3. The aerosol generation rates calculated by VANESA are dependent on the CORCON results; therefore there is an uncertainty in the aerosol generation rates used for the LDHR calculations. For the calculations presented here, the aerosol generation rates are important largely because they influence the time when SGTS filter rupture could occur, if at all.

4. It was determined that the reactor building fire protection sprays would be operating during the time when core-concrete aerosols would be produced. The QUICK code does not include models to account for the influence of the sprays on aerosol behavior in the reactor building. The sprays would be expected to increase the rate of aerosol deposition in the reactor building; however, the fire-protection sprays are not designed for aerosol washout. A more careful assessment of the effect of these sprays on aerosol transport is highly desirable.

References for Chapter 4

4.1 R. P. Wichner et al., *Station Blackout at Browns Perry Unit One - Iodine and Noble Gas Distribution and Release*, NUREG/CR-2182, ORNL/TM-455/V2 (August 1982).

4.2 R. P. Wichner et al., *SBLOCA Outside Containment at Browns Perry Unit One, Volume 2. Iodine, Cesium, and Noble Gas Distribution and Release*, NUREG/CR-2672, Vol. 2, ORNL/TM-8119/V2 (September 1983).

4.3 J. F. Muir, R. K. Cole, Jr., M. L. Corradini, M. A. Ellis, *CORCON-MOD1: An Improved Model for Molten Core/Concrete Interactions*, NUREG/CR-2142, SAND 80-2415 (February 1982).

4.4 D. A. Powers, "Containment Safety Studies," Appendix 5A, Empirical Description of the Rate of Aerosol Generation During Melt/Concrete Interactions, in *Report of the Zion/Indian Point Study: Vol. 1*, prepared by W. R. Murfin, Sandia Laboratories, NUREG/CR-1410, SAND80-0617/1 (August 1980).

4.5 D. A. Powers and J. E. Brockman, "Status of VANESA Validation," in *Report of the Status of Validation of the Computer Codes Used in the NRC Accident Source Term Reassessment Study* (BMI-2104), prepared by T. S. Kress, ORNL/TM-8842 (to be published).

4.6 H. Jordan, P. M. Schumacher, and J. A. Gieseke, *QUICK Users Manual*, NUREG/CR-2015, BMI-2082 (April 1981).

4.7 Personal communication, R. K. Cole, Jr., Sandia National Laboratories, August 1983.

Table 4.1. Summary of core debris, concrete conditions
prior to start of core-concrete interaction

---

1. Initial Temperature of Core Materials

   Oxides and Metals - 1737 K

2. Core Material Metal Phase Composition:[a]

   Cr : 18,820 kg
   Ni : 10,450 kg
   Fe : 120,100 kg for INTER
        116,100 kg for CORCON[b]

3. Core Material Oxide Phase Composition:[a]

   JO_2 : 159,400 kg
   FeO : 0 for INTER, 5150 kg for CORCON[b]

4. Concrete Composition:

   $CaCO_3$: 45.5%
   $Ca(OH)_2$: 7.0%
   $Si\ O_2$: 38.8%
   H_2O (free) : 4.8%
   Rebar   : 0.135 kg - Fe/kg - concrete

5. Initial cavity radius: 3.23 m for INTER, 3.09 m for CORCON

---

[a]Quantities of Z_r and Z_rO_2 in the melt were varied as shown in Table B.1.

[b]MARCH predicted no FeO in the core melt, about 5000 kg was added for CORCON runs based on discussions with Sandia staff.[4.7]

Table 4.2. Comparison of
cumulative evolution of
CO, CO2, H2, and H2O
for "CORCON1" and
INTER calculations,
at 3070 min[a]

Gas	Total release, CORCON1 (kg)	Total release INTER (kg)
CO	0.9	13300
CO_2	6456.0	20240
H_2	100.5	757
H_2O	2098.0	6575

[a]"CORCON1" was the base-case CORCON calculation done for the LDHR sequence.

Table 4.3. Core-concrete
aerosol composition pre-
dicted by VANESA (using
CORCON1 input data), at
3070 min

Material	Total aerosol (%)
SiO_2	26.6
CaO	20.4
K_2O	13.0
FeO	12.4
Al_2O_3	7.32
Na_2O	7.22
MnO_2	7.11
La_2O_3	1.87
CeO_2	1.08
All other materials	3.0

Table 4.4. Summary of QUICK drywell results
for LDHR sequence, at 3070 min

	Mass (kg)	Total mass[a] (%)
1. Mass settled on floor	145.6	14.1
2. Mass leaked to reactor building	848.1	81.9
3. Mass airborne in drywell	41.5	4.0
Total[a]	1035.2	

[a]Percent of total based on total mass from QUICK
calculation = 1035.2 kg; this is 6.4% higher than the
973.3 kg input amount based on the VANESA data.

Table 4.5. Summary of QUICK reactor building
results for LDHR sequence, at 3070 min

	Mass (kg)	Precent of total mass to building[a]
1. Mass settled on floor	602.5	66.6
2. Total mass leaked to SGTS	249.3	27.6
3. Mass deposited on SGTS filters	162.0	17.9
4. Mass leaked through SGTS after SGTS filter rupture[b]	87.3	9.6
5. Mass airborne in drywell	53.1	5.8
6. Mass transported through building leaks and to refueling bay	0	0
Total:[a]	904.9	

[a]The percent of total mass to the building was based on the total mass to the building from the QUICK calculation = 904.9 kg; this is 6.7% higher than the 848.1 kg to the building based on QUICK drywell results.

[b]Time for rupture of first SGTS filter bank (81 kg to SGTS) = 2768 min; time for rupture of second SGTS bank (162 kg to filters) = 2880.5 min.
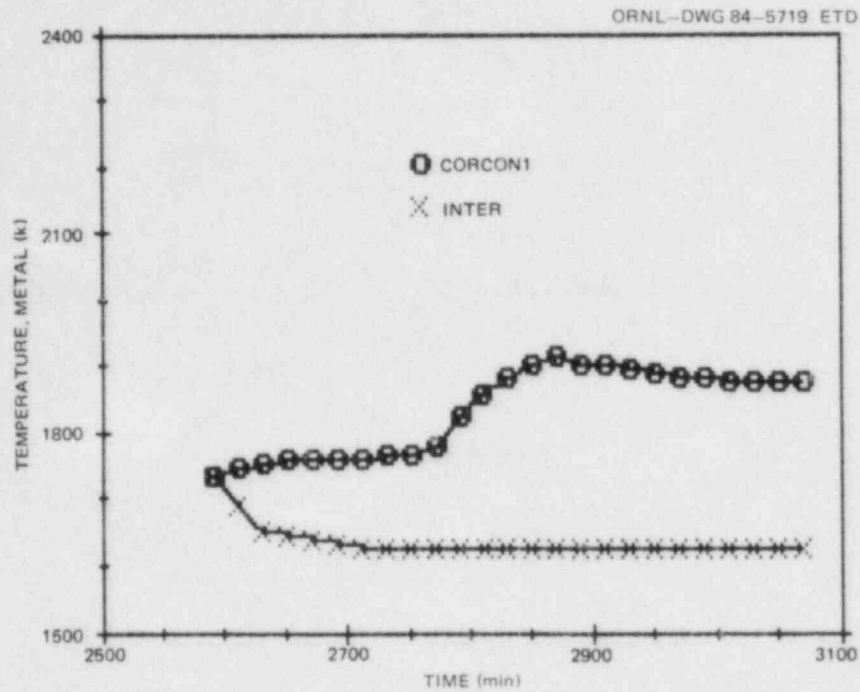
Fig. 4.1. Core debris metal layer temperatures predicted by "CORCON1" and INTER.
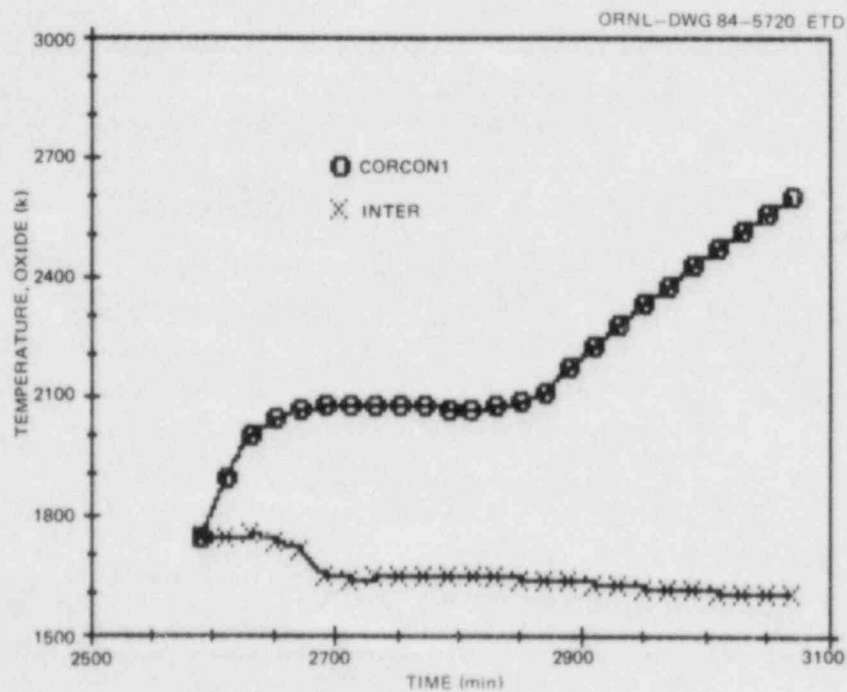
Fig. 4.2. Core debris oxide layer temperatures predicted by "CORCON1" and INTER.
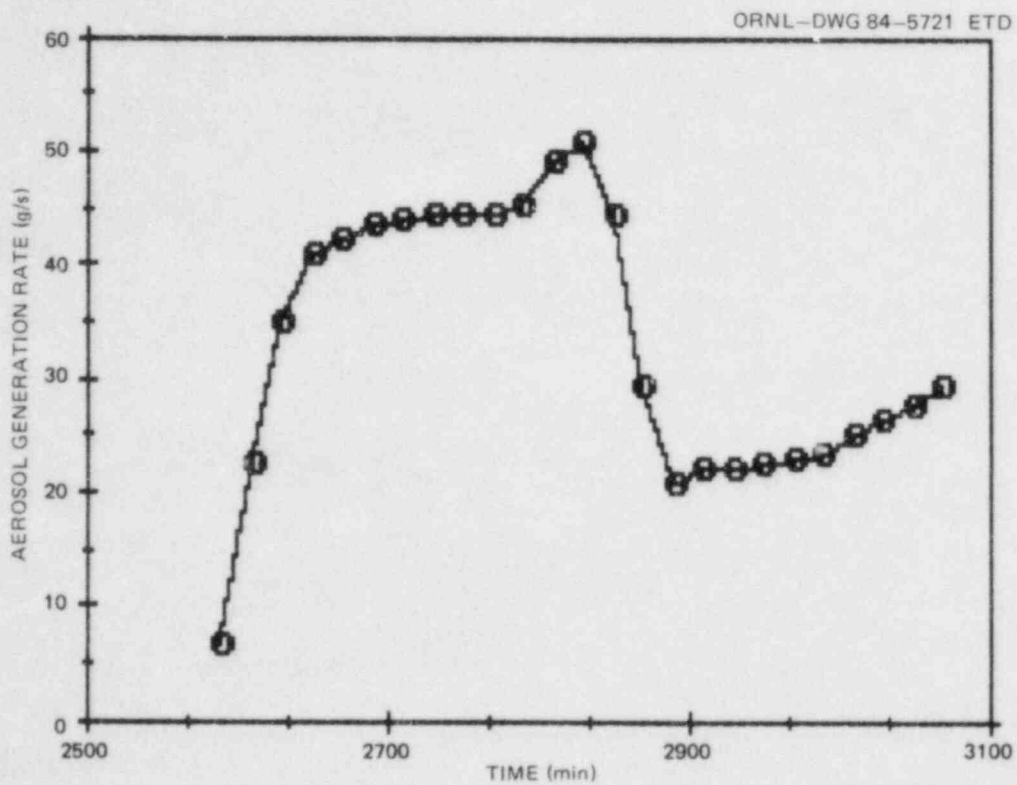
Fig. 4.3. Core-concrete aerosol generation rates predicted by VANESSA, based on "CORCON1" data.
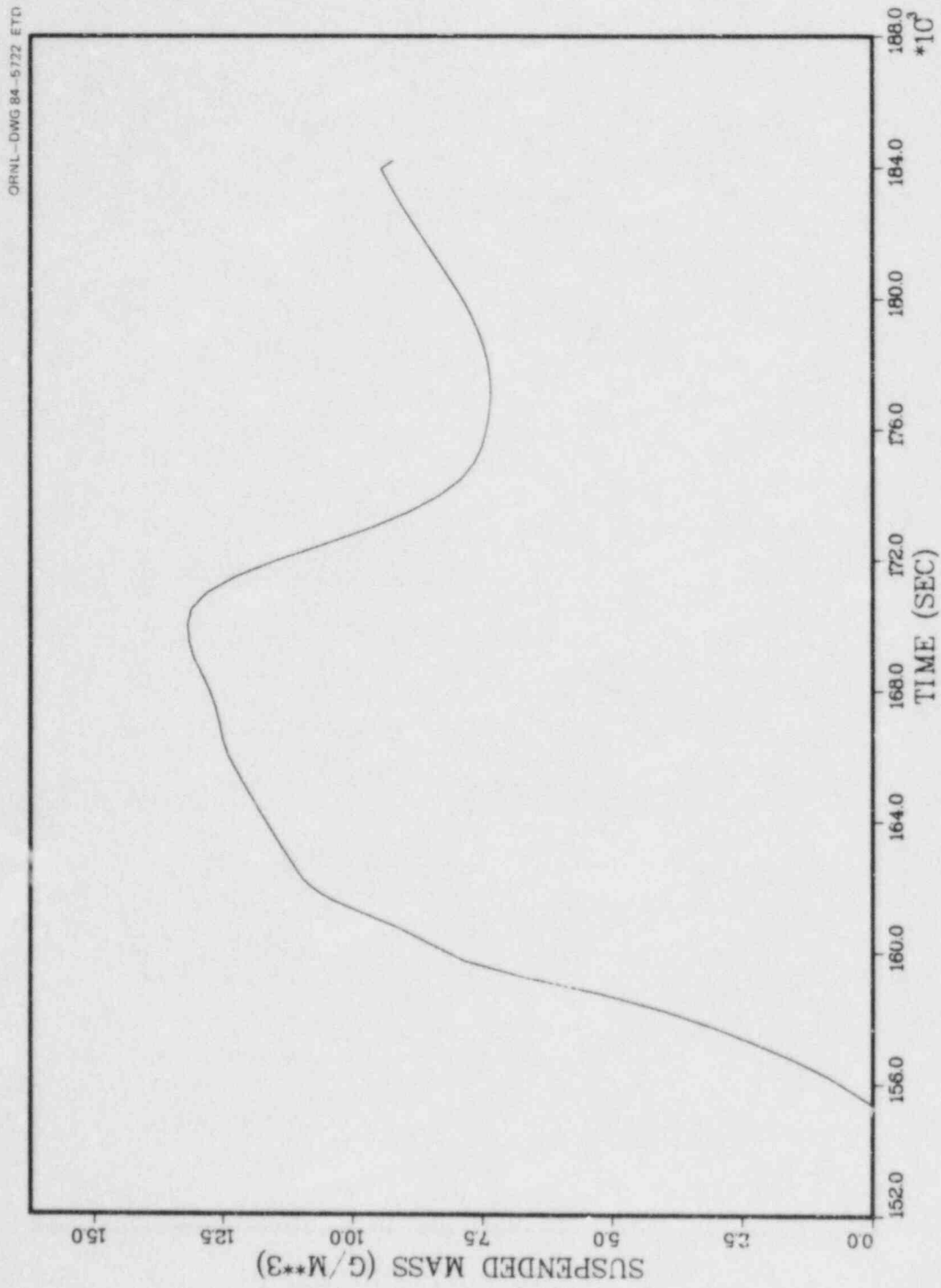
Fig. 4.4. Drywell aerosol concentration vs. time.
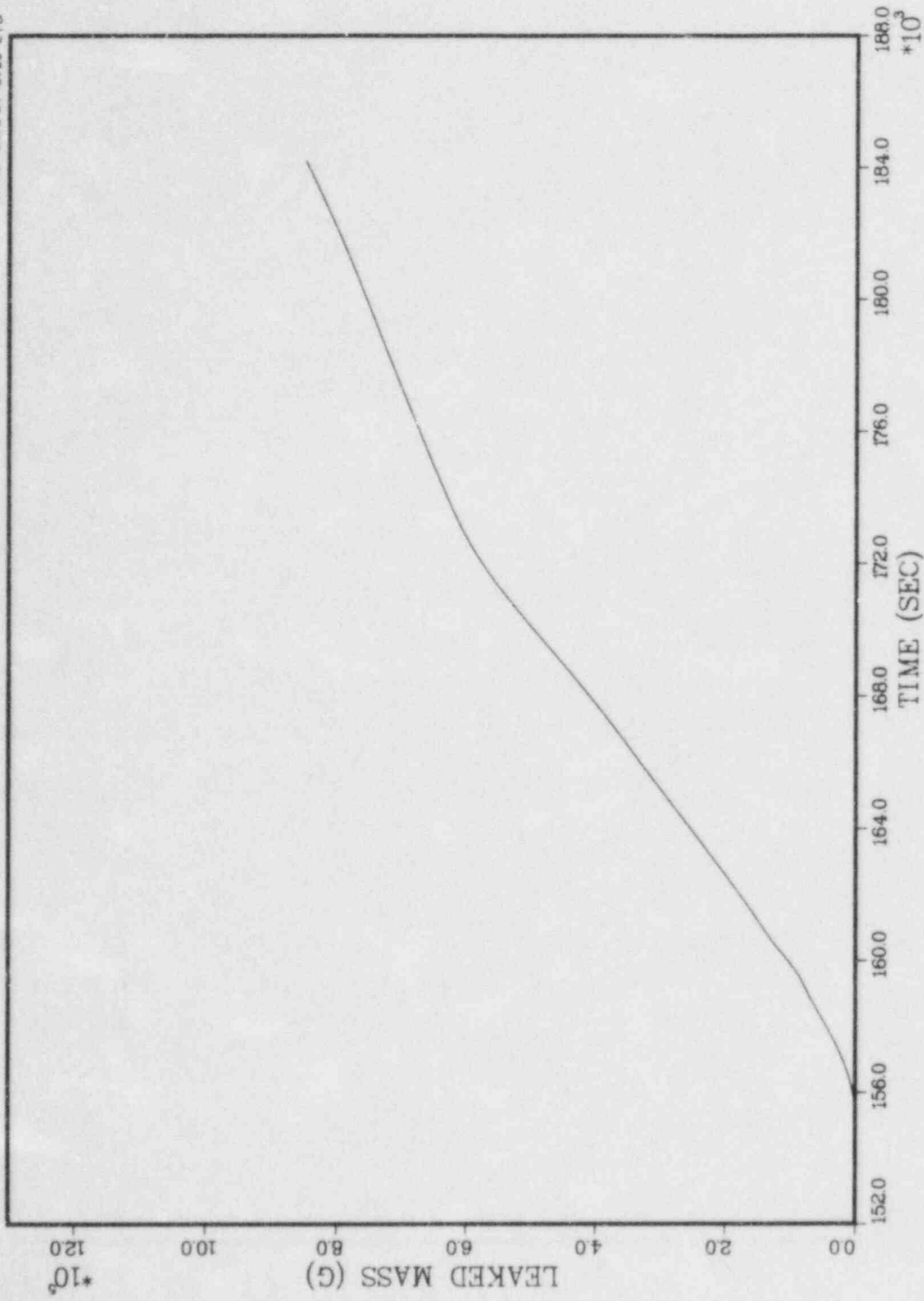
Fig. 4.5. Drywell leaked mass vs. time.
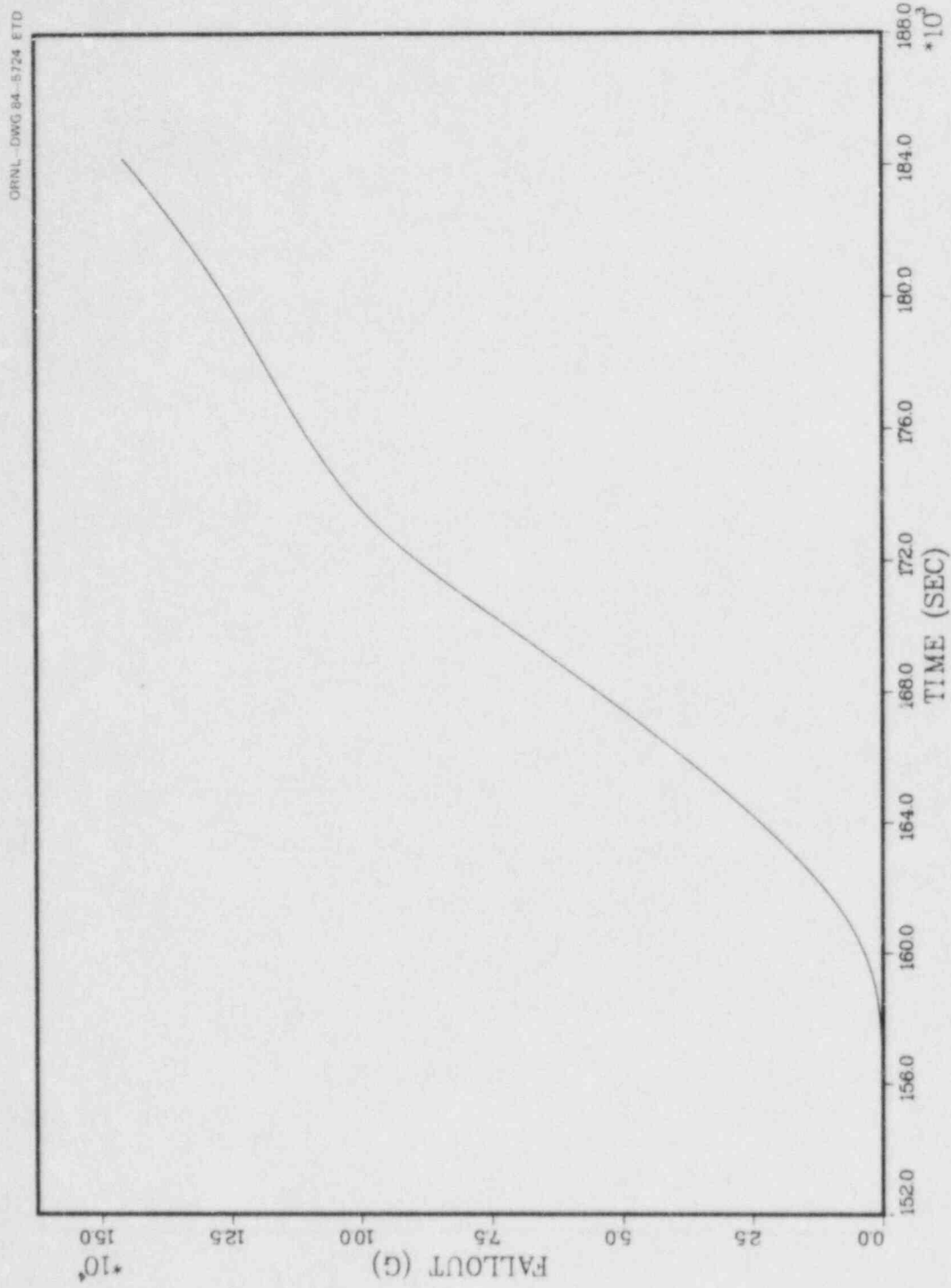
Fig. 4.6. Drywell settled mass vs. time.
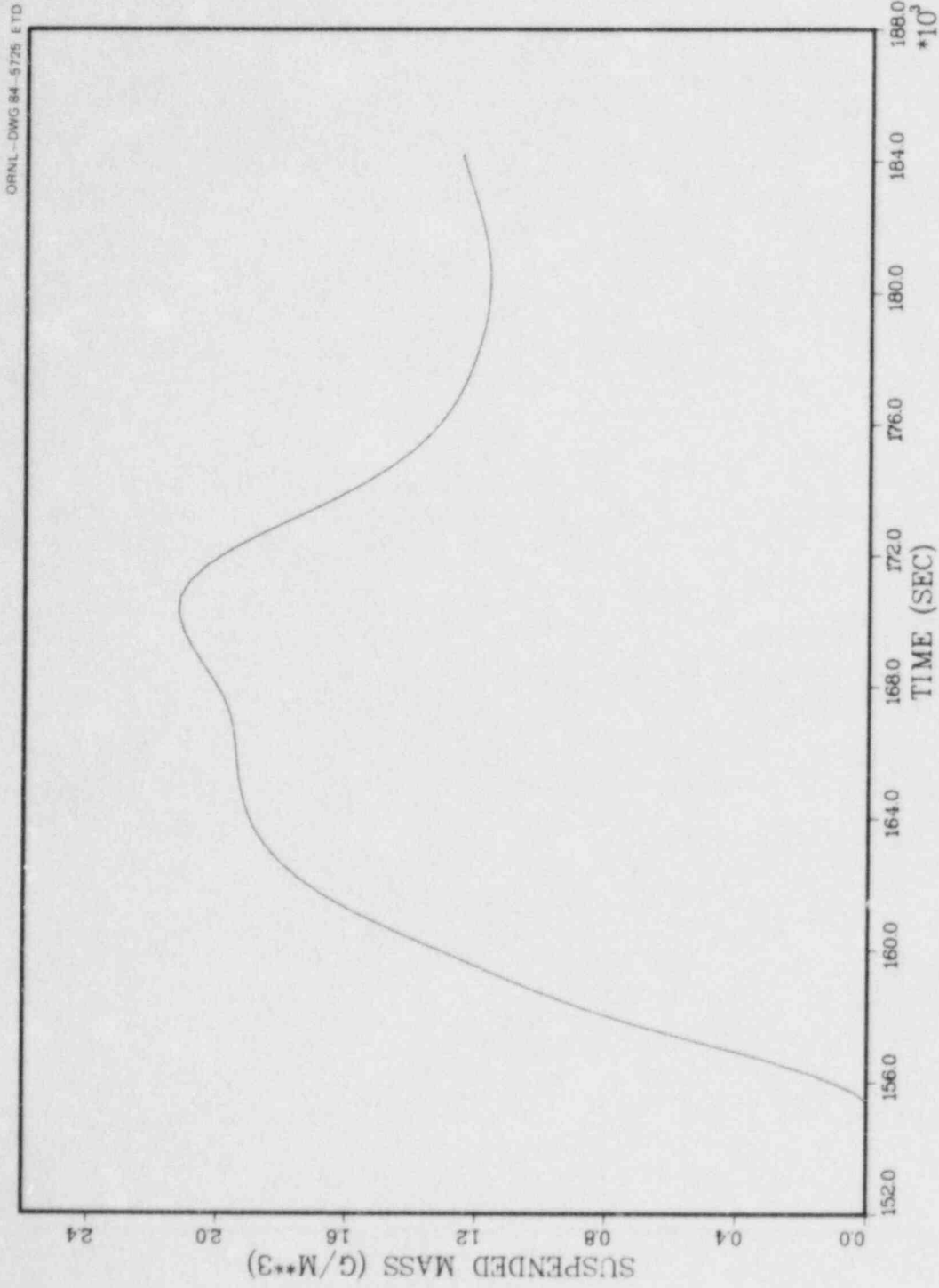
Fig. 4.7. Reactor building aerosol concentration vs. time.
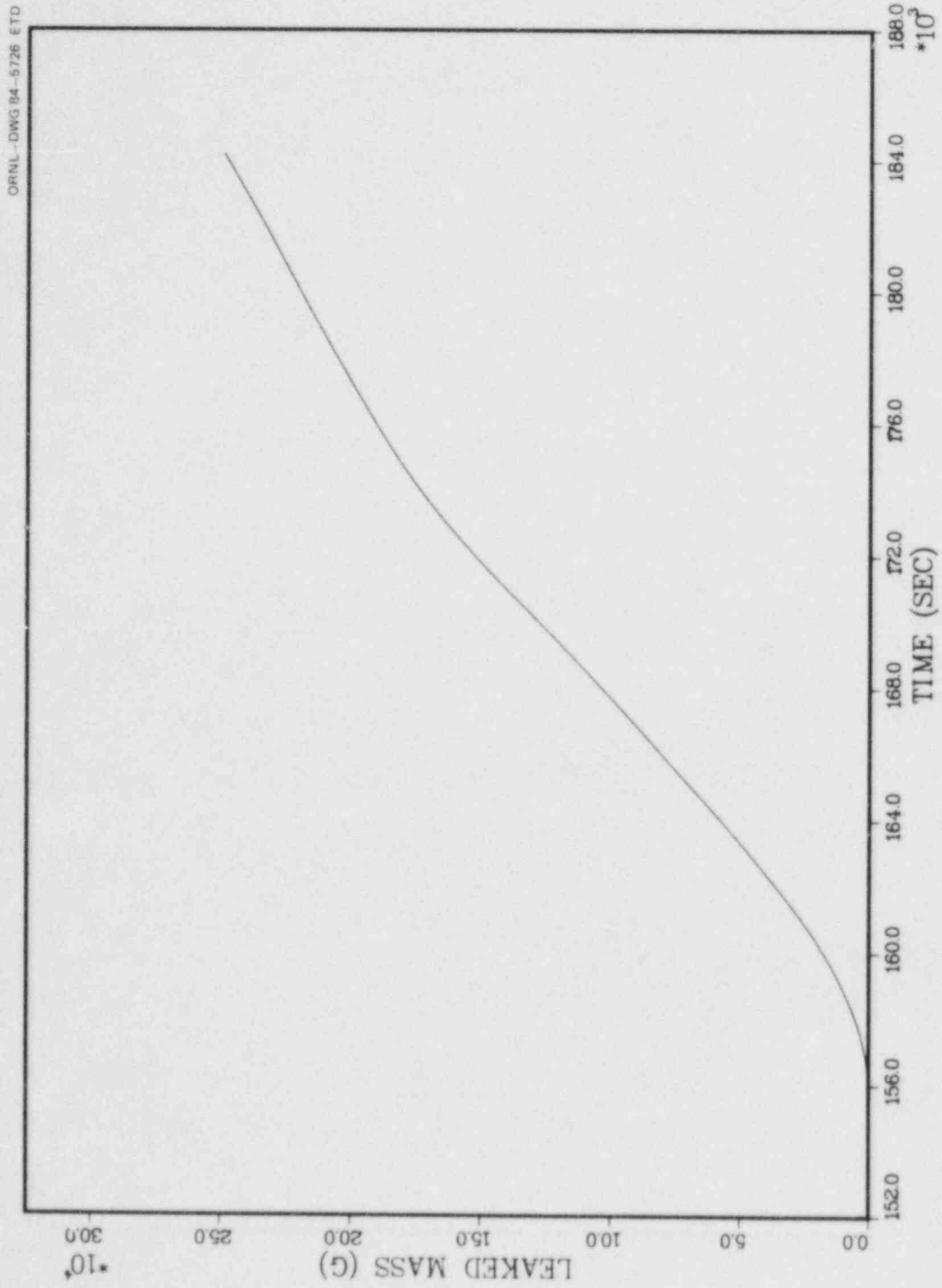
Fig. 4.8. Reactor building leaked mass vs. time.
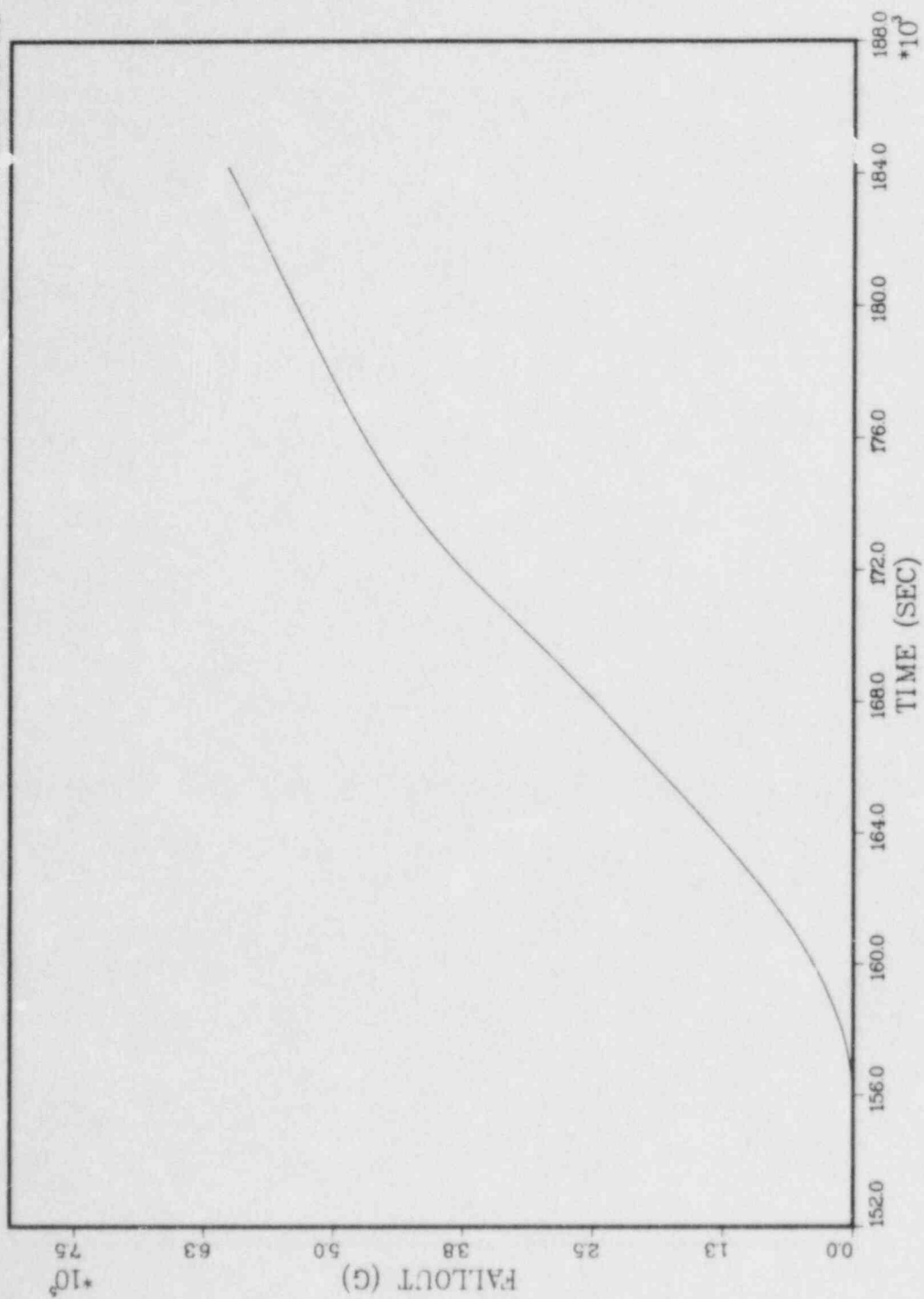
Fig. 4.9. Reactor building settled mass vs. time.

73

5. FISSION PRODUCT TRANSPORT CALCULATIONS AND RESULTS

5.1 Initial Nuclide Inventories

Estimates for the initial inventories of Kr, Xe, I, and Cs nuclides in the core are identical with those employed in the two previous studies,[5.1,5.2] and are described in detail in Sect. 5.2 of the station blackout study.[5.1] The initial fuel loading (in 1973), the refueling schedule and the power history to the eleventh month of the fourth refueling cycle were used with the ORIGEN2 code[5.3] to calculate nuclide inventories at shutdown.

In determining the particular nuclides to be included in the study, both mass and radioactivity contributions were considered. The total mass of each element, which determines transport and chemical activity, is comprised mostly of stable isotopes, although the calculations do account for the small mass contributions of all radioactive nuclides. The calculations do not currently account for the specific behavior of Te or Br; both were treated as isotopes of I in transport and chemical activity.* With the exception of the tellurium precursors of iodine, the calculations do include the behavior of precursors.

The nuclides currently included in the calculation are listed in Table 5.1, which also lists their half-lives and amounts present at the time of shutdown. As shown in the table, all stable isotopes of each element are considered as a single nuclide in the transport calculation. The total masses and activities for the elements Kr, Xe, I, and Cs are listed in Table 5.2 for selected times during the accident sequence. The table entries indicate that significant quantities of Kr, I, and Cs decay before the severe portion of the accident (after 2040 min) is reached.

It is important to note that, as for the previous two studies,[5.1,5.2] included here are only those nuclides with half-lives greater than 30 min. For these three cases, shorter-lived nuclides would have no significant impact on either the transport characteristics within the reactor or on the amount of activity ultimately released to the atmosphere. The curves presenting fission product inventory vs time discussed in Sects. 5.5 through 5.7 are all normalized with respect to the initial total elemental activities listed in Table 5.2.

Decay chains accounted for in the fission product transport calculations used for this study are listed below:†

---

*Te transport models are currently being developed for use in the next study.

†^{131m}Xe, ^{133m}Xe, and ^{135m}Xe are simply added to the masses of ^{131}Xe, ^{133}Xe, and ^{135}Xe, respectively. This appears to adequately approximate the actual decay chains.

$$^{130}I \longrightarrow {}^{130}Xe$$

$$^{131}I \longrightarrow {}^{131}Xe$$

$$^{132}Te \longrightarrow {}^{132}I \longrightarrow {}^{132}Xe$$

$$^{133}I \longrightarrow {}^{133}Xe \longrightarrow {}^{133}Cs$$

$$^{134}Te \longrightarrow {}^{134}I \longrightarrow {}^{134}Xe \qquad {}^{134}Cs \longrightarrow$$

$$^{135}I \longrightarrow {}^{135}Xe \longrightarrow {}^{135}Cs$$

$$^{136}Cs \longrightarrow$$

$$^{137}Cs \longrightarrow$$

$$^{138}Cs \longrightarrow$$
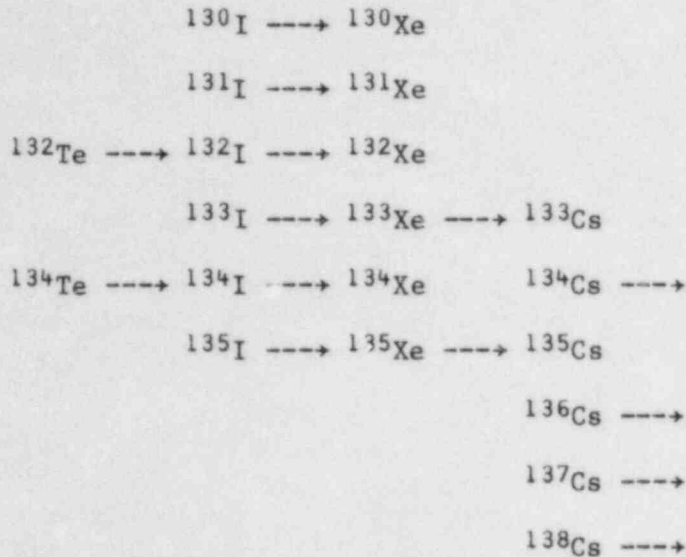
5.2 Control Volume Characteristics

For fission product transport calculations, the entire nuclear plant is divided into two basic regions, each of which is then sub-divided into control volumes corresponding to distinct, physically separate zones. The first region includes the reactor vessel and steam lines, i.e., all parts of the primary system that remain pressurized after the reactor scram. The second region contains various containment or building areas and basically any volume or system not included in the first region. Calculational procedures for different control volumes of each region are similar, although the actual models used may vary considerably among control volumes of a region. The individual control volumes are the smallest subdivision for flow and chemical activity calculations, in that the distribution of nuclide species in each control volume is assumed to be uniform.

5.2.1 Primary system volumes

The primary system is subdivided into eight control volumes, which represent specific portions of the reactor vessel internal structure and connecting steam lines. These volumes are listed in Table 5.3 along with their deposition surface areas and free volumes; their locations and interrelationships are illustrated in Fig. 5.1.

Although the core region is assumed to be a typical well-mixed control volume in calculating inflow and outflow, it is subdivided into 10 radial and 10 axial zones for the calculation of fission product releases from intact fuel. (The first radial zone is the center of the core, the tenth is the outer portion; the first axial zone is at the bottom of the core, the tenth is at the top.) These 100 core nodes have equal volumes, but do not have equal fission product inventories or temperatures. As shown in Table 5.4, decay power is higher in the central regions of the core. Nevertheless, core loading patterns provide that

the longer-lived isotopes are concentrated in the lower-power, long-burnup fuel assemblies that are located near the perimeter. (Details of the core loading pattern can be found in Ref. 5.1.) The nodal fuel temperatures also vary considerably in different areas of the core, with generally lower values at the extreme perimeter (9th and 10th radial zones) and in the lower regions. Because the fission product release rates depend upon both the temperature and fuel inventories, this nodalization produces a much more accurate description than would core-averaged quantities.

5.2.2 Containment and building control volumes

Because all portions of the plant outside the primary system are considered as parts of this general region, there will be many differences in the characteristics and modeling of fission product behavior in the different control volumes. The particular volumes used in this study are listed in Table 5.5 with their surface areas and free volumes, and include such diverse entries as the reactor building, standby gas treatment system, and wetwell. The physical locations and inter-relationship of the different control volumes are shown in Figs. 2.19, 2.20, 2.22 and 2.23 of Chap. 2. The main steam lines (downstream from the MSIVs) and the SRV tailpipes are included here, since they are not at primary system pressure and therefore are not subject to the same fission product behavior.

As discussed in Sect. 2.2, the drywell fails prior to core uncovery; hence, there is extensive venting from the drywell to the reactor building during the later stages of the accident. The drywell-wetwell and drywell-reactor building flows are major fission product transport pathways and are illustrated in Figs. 2.17 and 2.18. Except for a few brief instances, the SGTS operation is successful in maintaining negative pressure in the reactor building and refueling bay during the accident. As a result, very little flow from reactor building to refueling bay occurs, and thus fission products have very little opportunity to enter the refueling bay, or the atmosphere except through the filters of the SGTS.

5.3 Calculational Procedure

The movement and activity of released nuclides in the various reactor control volumes are determined primarily by the flows between the volumes and the temperatures of structures and fluids within the volumes. Additional information is required in certain volumes (e.g., the mole ratios H/O and I/H$_2$O are used in the reactor vessel to determine the distribution of iodine species.)

Flow and temperature information are obtained from the output of four different computer codes, whose contributions are as follows:

1. The MARCH code, as improved at ORNL for BWR analyses, furnishes all data for the core and pressure vessel, and most temperatures and flow rates for the wetwell and drywell.

2. The ORNL-developed secondary containment model (described in Appendix A of Ref. 5.2) provides necessary flow and temperature information for the reactor building, refueling bay, SGTS, and atmosphere.
3. The QUICK[5.4] code is used to determine aerosol concentration, plating, settling, and leakage in the drywell and reactor building.
4. Gas release rates from the corium-concrete reaction after reactor vessel failure are calculated by the CORCON-MOD1[5.5] code.

All data from the above sources are input to a special input processing routine that interpolates and integral-averages all quantities, outputting a single data set at standardized 2-min intervals. This data set then becomes the principal input to the main fission product transport computations. The time steps for the transport calculations are generally smaller than the times between data input, requiring interpolation of the data.

At each new time step, the transport calculation progresses through the following stages of computation:

1. DATA: Input of new temperature and flow data, if needed.
2. RADIOACTIVE DECAY: Isotope inventories are revised according to the exact solution of the coupled decay differential equations.
3. RELEASE FROM FUEL: Using current temperature data and isotope concentrations, the release of nuclides from fuel to gas is calculated.
4. TRANSPORT: The movement of nuclides between control volumes (based on flow rates between connected volumes) is done explicitly (i.e., using only the concentrations from the previous time).
5. CHEMISTRY: Chemical activity (e.g., plating, dissolution, I species distribution) is calculated using updated concentrations in each control volume. Aerosol settling and plating in each volume is done after the calculation of deposition or condensation of nuclides onto aerosols.
6. OUTPUT: Done every 2 min after the beginning of calculations (2040 min).

5.4 Aerosols in the Reactor Vessel

The term aerosol is here restricted to materials originally incorporated in the steel structures of the reactor vessel or the Zircaloy cladding and channel boxes of the core. These materials are of sufficiently low volatility that the aerosols can be considered to form by condensation in all of the reactor vessel control volumes outside of the core. The degree to which the fission product species CsI and CsOH add to the aerosol mass depends on the amount of condensation permitted by the local temperatures.

5.4.1 Production and deposition rates

Figure 5.2 shows the amount of structural aerosols produced in the reactor vessel as a function of time during the course of the severe accident. The figure also shows the plated and suspended aerosol masses

for a base case that assumed 80% aerosol deposition by the time of vessel failure (2590 min). Because of the uncertainty in certain deposition rate parameters, two other cases were also investigated; these cases assumed a degree of aerosol deposition at vessel failure of 60% and 95% of the total produced. Suspended mass at vessel failure was 3.1, 1.9, and 0.4 kg for the cases of 60, 80, and 95% deposition, respectively.

5.4.2 Aerosol effects on fission product transport

As described in the previous section, aerosol deposition was treated parametrically by consideration of cases with 60, 80, and 95% plating of all structural aerosols produced. The degree of aerosol trapping would have no effect on the Kr and Xe releases since no interactions between these elements and aerosols are postulated. Overall releases of I and Cs to the atmosphere are almost identical in each of the three cases, although the behavior of these elements in certain control volumes was affected by the aerosol deposition fraction in the early stages of the accident.

The major differences in I behavior occurred in the reactor vessel before failure of the bottom head at 2590 min. As shown in Fig. 5.3, the suspended I activity (including I in the gas phase and plated on airborne aerosols) varies somewhat, but the values for the three cases are very close at vessel failure. Figure 5.4 shows the effects of aerosol deposition fraction on the total amount of I that deposits in the reactor vessel (including I plateout from condensation directly onto surfaces and I plated onto deposited aerosols). Both figures indicate that amounts of plated or suspended I at the time of vessel failure are largely independent of the aerosol deposition fraction, although these amounts vary at earlier times. The reason for this is that in the case of 60% deposition, more aerosols remain airborne and available for I deposition. Consequently, when these aerosols do finally deposit, they carry larger amounts of I with them. It is also important to note that both plated and suspended I activity depend not only on aerosol trapping but on I plateout directly to fixed surfaces and gas flows from the vessel during periods of SRV actuation.

The effect of aerosol trapping on the release of I to the environment is illustrated in Fig. 5.5, which shows that the degree of aerosol deposition in the reactor vessel is significant only in the early stages of the accident (before vessel failure at 2590 min). The only release pathway available prior to this time is by leakage from the wetwell airspace to the reactor building; hence, this figure is also a good indication of the variance in the amounts of I in the wetwell atmosphere due to SRV operation. It is important to note that the releases from fuel rubble on the drywell floor in the later portion of the accident <u>completely overshadow the early releases</u>, thus rendering inconsequential the variation during the early stages due to aerosol deposition fraction in the vessel.

The effect of aerosol deposition upon the behavior of Cs resembles that of I and will not be described in great detail. The activity of Cs suspended and plated in the reactor vessel is similar to that of I as

depicted in Figs. 5.3 and 5.4. Also, similar to Fig. 5.5 for I, the release of Cs to the atmosphere shows essentially no variation between the three parametric cases. Due to the lack of Cs evaporation and venting from the wetwell airspace, atmospheric release of Cs occurs only after the vessel fails at 2590 min.

Because of the similarities noted above for various aerosol deposition fractions, it is concluded that this parameter is not of great importance in assessing the overall consequence of this accident, i.e., the release to the atmosphere. Rather than overload the reader with an excessive number of tables and figures, only a base case with the aerosol deposition of 80% will be used for reporting results in the following sections.

5.5 Noble Gas Transport Results

Calculated Kr and Xe activity inventories (PBq) in several key control volumes during the course of the accident sequence are listed in Tables 5.6 and 5.7. The only noticeable differences in the behavior of these two noble gases are due to the much higher effective decay rate for Kr and the somewhat higher solubility of Xe. Both gases are evolved from the fuel in large quantities and effectively flushed through the plant systems by steam in the reactor vessel and concrete degradation gases in the drywell.

As seen from Table 5.6, less than 1% of the initial Kr inventory (given in Tables 5.1 and 5.2) is projected to be released to the atmosphere. This low value is due to the rapid decay of Kr nuclides relative to the holdup time involved in this accident sequence. On a mass basis, the released Kr at time 3100 min represents about 76% of the initial inventory.

Physically, Xe behaves in a similar way. However, Xe nuclides decay more slowly, and significant amounts build-in due to precursor decay. Thus there is less decay loss in the 3100 min spanned by this study. As seen in Table 5.7, about 60% of the initial Xe activity is projected to be present in the atmosphere at sequence termination.

Tables 5.6 and 5.7 show that the major repositories for noble gases within the reactor complex at time 3100 min are the in-place fuel, the reactor building atmosphere, and the main condenser.

Figures 5.6 through 5.10 show the time-variation of Kr activity, normalized to the activity at time 0, in the fuel material, reactor vessel, wetwell water and air, drywell, reactor building air and water, and the main condenser. Figure 5.11 shows the timing of the release to the surrounding environment, also normalized to the initial activity. As seen in figures 5.8 through 5.11, virtually all of the movement of Kr before vessel failure is governed by SRV actuations (cf. Fig. 2.16), which induce flow not only from the reactor vessel to the pressure suppression pool, but also from the wetwell airspace to the drywell and from the drywell to the reactor building. The major releases to the environment result from these SRV actuations and from the burst of activity occurring at reactor vessel failure. As noted above, less than 1% of the initial Kr activity is projected to be present in the

environment at the termination of the sequence, most of which release occurs after vessel failure at 2590 min.

Similarly, Figs. 5.12 through 5.17 show the time variation of the normalized Xe activity in key control volume locations, the last one (Fig. 5.17) referring to the timing of the release to the atmosphere. As noted above, the major differences in the results for Xe and Kr are attributable to the much slower rate of Xe decay.

5.6   Iodine Transport Results

Estimated iodine activities (in PBq) are listed in Table 5.8 for times up to 3100 min following event initiation for the following inventory locations: (1) in fuel within the original locations in the core, (2) in fuel material slumped onto the reactor vessel bottom head and later located on the drywell floor, (3) plated on the reactor vessel surfaces in all forms (e.g., condensed CsI, deposited aerosols carrying some iodine form), (4) suspended in the reactor vessel (gaseous plus on suspended aerosols), (5) dissolved in the reactor vessel water, (6) plated on drywell walls, (7) gaseous plus suspended in the drywell air, (8) wetwell water, (9) wetwell air space, (10) reactor building water, (11) reactor building air, (12) in the main condenser, (13) on the HEPA filters, (14) absorbed on charcoal in the SGTS, and (15) in the atmosphere.

Interpretation of the iodine inventory estimates given in Table 5.8 may be aided by viewing Figs. 5.18 through 5.27, which illustrate the time-dependence of these quantities, and by reviewing the descriptions of the leakage pathways shown in Figs. 2.22 and 2.23.

As seen in Table 5.8, the largest iodine repository at time 3100 min is the reactor vessel. Of the total 6854 PBq available at this time, about 400 PBq is in the tenth (outer) radial region of fuel, which remains intact throughout the accident, and about 6000 PBq is deposited on interior vessel surfaces. Concerning the latter, Fig. 5.20 indicates that the dominant mechanism is plating of iodine-laden aerosol particles, accounting for 60% of the vessel iodine. Other iodine remaining in the reactor vessel is due to CsI condensation or HI deposition directly onto vessel structures. This second mechanism is augmented at the time of core slump (2492 min) by the rapid boiloff of water in the bottom head, leaving previously dissolved iodine deposited on lower vessel surfaces. It is interesting to note that in a previous study,[5.2] most of the iodine remaining in the vessel resulted from direct plating, since high gas temperatures inhibited plating onto aerosol particles. However, in the current accident sequence, gas temperatures are much lower, permitting more extensive plating onto aerosols.

Another major repository is the water in the reactor building basement pool, which contains 239 PBq of dissolved iodine at 3100 min. As in the SBLOCA accident sequence,[5.2] the reactor building fire protection system sprays are assumed to continually flush surfaces in the vicinity of the drywell rupture. Iodine in the reactor building atmosphere is assumed to equilibrate with and partly dissolve in water on floors or walls, and be washed into the basement pool.   The calculational

mechanism used is equilibration with a partition coefficient of 5000. This calculational mechanism is a great simplification. The assumption of gas/water equilibration is reasonable, but the partition coefficient would in fact vary with location (local water temperature, pH, and iodine concentration) and with time of contact in a way that might be unique for iodine. That is, the effective volatility diminishes with time as the dissolved I_2 reacts with the water to produce the nonvolatile I^- and IO_3^- forms. Therefore, short-term contacts such as with building sprays can exhibit higher effective iodine volatility than the long-standing basement pool. The selection of a single value of 5000 for the iodine partition coefficient applicable to the air-water contact in the reactor building may lead to over-estimation of the iodine dissolution in the sprays and also to a compensating underestimation of the retention in the basement pool.

The other location involving major iodine activity is the drywell, where 178 PBq remain plated at 3100 min. Most of this plating occurred shortly after reactor vessel failure, resulting from I_2 deposition directly onto drywell surfaces.

Although the wetwell is not a significant iodine repository, it is interesting to note the timing of I transport to this control volume. As can be seen in Fig. 5.21, the presence of I is governed by SRV actuation before the reactor vessel fails and by drywell venting afterward. Because the only release pathway before reactor vessel failure is through the wetwell, the early releases to the other containment volumes also reflect this dependence on SRV operation, as seen in Figs. 5.22—5.27.

The great preponderance of iodine in the reactor building and the primary containment volumes occurs as gaseous I_2. However, the formation of a small amount of organic iodide is calculated, according to the model described in Sect. 3.2.2. As shown in Figs. 5.24—5.27, the presence of this species does not appear to be a significant factor in the overall transport of I through the reactor or to the environment according to current modeling estimates.

The total atmospheric inventory of radioactive iodine shown in Table 5.8 represents a cumulative total. The release of 0.05 PBq at 3100 min is a very small fraction of the initial inventory. Gaseous I is the dominant form, and results mostly from the fraction (1% of I_2, 5% of organic iodide) that is not absorbed in the SGTS charcoal. Smaller contributions released directly from the reactor building occur during brief moments of positive building pressure at core slump (2492 min) and vessel failure (2590 min), as noted in Fig. 5.27. Also evident in the figure is the increased release of I_2 on suspended aerosols after tearing of the upstream and downstream HEPA filter banks (occurring at 2768 and 2880 min).

The iodine release to the surrounding atmosphere in this report is an estimate that depends strongly on the assumptions regarding the operation of the SGTS and the effects of the fire-protection system sprinklers in the reactor building. Without the SGTS, releases from the reactor building directly to the environment would be much higher. However, the timing of HEPA filter failure is not particularly important for I release, since most I occurs in the gas, not plated on suspended aerosols. The reactor building sprays are the mechanism for removing a

large amount of iodine from the gas in the reactor building, although no effect on aerosol particles is assumed. Therefore, any degree of aerosol washout that would be affected by the sprays would reduce the release estimates provided in this report.

5.7 Cesium Transport

The activity of cesium nuclides at various locations is listed in Table 5.9 for selected times during the accident sequence. The normalized (relative to activity at time 0) inventories for many locations are plotted as functions of time in Figs. 5.28 through 5.35.

The behavior of cesium resembles that of iodine in many respects. Table 5.9 indicates that most of the Cs at 3100 min is deposited in the reactor vessel. Figure 5.30 reveals that the strongest mechanism for fission product removal is again aerosol deposition. Direct condensation of CsOH onto fixed surfaces also plays an important role, augmented by the Cs remaining in the lower vessel, (previously dissolved) after the boiloff of water at core slump (2492 min).

As is the case with iodine, a significant inventory of cesium is plated on the drywell walls at 3100 min. The mechanism here is predominately the direct condensation onto surfaces. Unlike the situation in the reactor vessel, condensation onto aerosol particles that subsequently settle or deposit is not a significant factor here.

The third major repository for Cs is that remaining in the intact outer ring of the core. This inventory is about 10% of the total Cs activity at 3100 min.

Differences in Cs and I behavior are evident from several of the control volume inventories shown in Tables 5.8 and 5.9. Very little Cs dissolves in the reactor building basement pool because no equilibration is assumed between the liquid and gas phases, and because most Cs in the reactor building is in aerosol particles. The quantity of Cs in the reactor building water depends on the degree of aerosol deposition predicted for that control volume. This latter situation is also responsible for the greater trapping of Cs in the HEPA filters of the SGTS. Although the SGTS charcoal was arbitrarily assumed to retain 90% of the gaseous Cs, the very small gaseous inventory rendered this assumption almost inconsequential. Perhaps the most significant difference in I and Cs behavior is the sparging release from fuel rubble in the drywell, illustrated by the dashed lines in Figs. 5.18 and 5.28. Since Cs is assumed to be released from fuel rubble by sparging at a much faster rate than iodine, it is not surprising that the fraction of Cs released to the environment is about ten times that of I at the end of computations.

From Table 5.9, the Cs released to the atmosphere at 3100 min is 0.04 PBq, less than 0.01% of the total remaining inventory at that time. Figure 5.35 illustrates the timing and form of this release. Since no Cs volatility is assumed, all Cs entering the pressure suppression pool during the reactor vessel blowdown remains there; hence, there is no pathway for early releases to the environment, as was the case with iodine (Fig. 5.27). Thus, the appearance of Cs in the atmosphere begins only after vessel failure at 2590 min., largely in the form of

aerosol particles, with negligible amounts released in the gas phase. The solid curve in Fig. 5.35 illustrates the dramatic increase in Cs release at the failures of each HEPA filter bank (at 2768 and 2880 min), indicating that the timing and amount of Cs released to the environment is very dependent on assumptions regarding SGTS operation.

83

References for Chap. 5

5.1 R. P. Wichner et al., *Station Blackout at Browns Ferry Unit One — Iodine and Noble Gas Distribution and Release*, NUREG/CR-2182, Vol. 2, ORNL/TM-455, Vol. 2 (August 1982).

5.2 R. P. Wichner et al., *SBLOCA Outside Containment at Browns Ferry Unit One*, NUREG/CR-2672, Vol. 2, ORNL/TM-8119/V2 (September 1983).

5.3 A. G. Croff, *ORIGEN2 — A Revised and Updated Version of the Oak Ridge Isotope Generation and Depletion Code*, ORNL-5621 (July 1980).

5.4 H. Jordan, P. M. Schumacher, and J. A. Gieseke, *QUICK Users Manual*, NUREG/CR-2015, BMI-2082 (April 1981).

5.5 J. F. Muir, R. K. Cole, Jr., M. L. Corradini, M. A. Ellis, *CORCON-MOD1: An Improved Model for Molten Core/Concrete Interactions*, NUREG/CR-2142, SAND 80-2415 (February 1982).

Table 5.1. Nuclides of Kr, Xe, I, Cs,
and Te represented in the
transport calculation[a]

Nuclide	Half-life	Initial Inventory	
		(gmol)	(PBq)[b]
Kr 83 + 84 + 86	∞	277.9	0
85 m	4.4 h	0.0333	879.9
85	10.7 year	20.1	24.7
87	1.3 h	0.0182	1,666.0
88	2.8 h	0.0572	2,368.0
Xe 131 + 132 + 134 + 136	∞	2,803.0	0
133	5.3 d	6.862	6,289.0
135	9.2 h	0.138	1,739.0
Cs 133 + 135	∞	837.0	0
134	2.1 year	45.0	290.5
136	13.0 d	0.316	117.4
137	30.2 year	624.2	273.3
138	32.2 min	0.093	20,093.0
I 127 + 129 + Br81	∞	147.3	0
130	12.4 h	0.0086	81.0
131	8.0 d	5.304	3,175.0
132	2.3 h	0.0915	4,612.0
133	20.8 h	1.177	6,529.0
134	52.0 min	0.0545	7,293.0
135	6.7 h	0.350	6,058.0
Te 132	78.0 h	3.064	4,553.0
134	0.700 h	0.0378	6,262.1

[a] Includes nuclides with half-lives greater than 30 min.

[b] Petabecquerel ≡ 10^{15} Bq = 27,027 curies.

Table 5.2. Total mass (gmol) and activity
(PBq) of fission product elements
at selected times[a]

Element	Time after shutdown (min)				
	0	2,040	2,500	2,800	3,100
Kr					
gmol	298	297.9	297.9	297.9	297.9
PBq	4,939	29.3	26.0	25.2	24.9
Xe					
gmol	2,810	2,811	2,811	2,810	2,810
PBq	8,028	6,786	6,280	6,012	5,784
I[b]					
gmol	154.3	152.5	152.3	152.1	152.0
PBq	27,748	8,636	7,747	7,268	6,854
Cs					
gmol	1,508	1,508	1,508	1,508	1,508
PBq	20,774	672.7	670.7	669.4	668.2

[a] 1 Petabecquerel ≡ 10^{15} Bq = 27,027 curies.

[b] Includes Br 81.

Table 5.3. Reactor vessel control volumes

Control volume	Surface area (m^2)	Volume (m^3)	Interconnecting regions
1 Core	1.28×10^4	45.1	(2) (3)
2 Lower plenum	1.00×10^3	90.7	(1)
3 Upper plenum	34.8	27.8	(1) (4)
4 Steam separator	6.4×10^2	38.0	(3) (5)
5 Downcomer	1.26×10^3	183.0	(4) (6)
6 Steam drier	2.95×10^3	64.4	(5) (7)
7 Upper head	1.98×10^2	89.0	(6) (8)
8 Steam lines (4)	3.34×10^2	55.1	(7) (MST)[a] (TP)[b]

[a] Main steam lines, downstream from MSIVs.

[b] Safety relief valve tailpipes.

Table 5.4. Decay power in core control volumes, 2.4 h after shutdown (kW)

Axial node		Center				Radial zone					Edge
		1	2	3	4	5	6	7	8	9	10
Top	10	149	136	144	132	146	145	114	112	96	80
	9	277	260	269	253	276	267	241	232	190	141
	8	361	341	351	334	362	352	330	311	256	185
	7	407	387	397	381	412	400	384	358	297	213
	6	431	412	422	407	438	425	417	387	322	230
	5	444	428	436	423	453	440	440	406	339	240
	4	452	436	444	431	462	448	456	418	345	237
	3	452	436	444	433	465	449	467	423	346	226
	2	426	411	417	410	440	423	448	400	322	198
Bottom	1	245	231	241	229	251	246	230	210	172	117

Table 5.5. Primary containment and reactor
building control volumes

Control volume	Surface area (m^2)	Volume (m^3)	Connecting regions
1 Steam lines^a (4)	10^3	1.65×10^2	(STL)^b (9)
2 Tailpipes (13)		2.0	(STL)^b (3)
3 Wetwell water		3.83×10^3	(4) (2) (5)
4 Wetwell air	3.53×10^3	3.66×10^3	(3) (5) (6)
5 Drywell	5.20×10^3	4.50×10^3	(4) (6)
6 Reactor building	2.43×10^4	4.25×10^4	(7) (8) (10) (4) (5)
7 Refueling floor	1.56×10^4	7.48×10^4	(6) (8) (10)
8 SGTS			(6) (7) (10)
9 Condenser		1.52×10^2	(1)
10 Atmosphere			(6) (7) (8)

^{a}Downstream from MSIVs.

^{b}Steam lines between reactor vessel and MSIVs.

Table 5.6. Krypton inventories and release to atmosphere (PBq)[a]

Time	Fuel		PV gas	DW gas	Wetwell		Reactor building		Condenser	Atmosphere	Total
	Core	Rubble			Gas	Water	Air	Water			
0	4939.00										4939.00
2332[b]	26.47	0	0.27	0	0	0	0	0	0	0	26.75
2488[c]	4.53	0	20.05	0.031	0.57	2×10^{-4}	0.32	2×10^{-4}	0.357	0.15	26.02
2590[d]	2.88	1.62	16.91	2×10^{-10}	1.25	0	0.75	5×10^{-4}	1.19	1.09	25.69
2768[e]	2.85	9×10^{-4}	0	4×10^{-4}	1×10^{-6}	5×10^{-8}	4.79	0.005	1.19	16.46	25.30
2917[f]	2.85	8×10^{-6}	0	3×10^{-6}	1×10^{-7}	5×10^{-9}	1.81	0.003	1.17	19.30	25.13
3100	2.84	8×10^{-10}	0	4×10^{-10}	1×10^{-4}	5×10^{-6}	0.27	5×10^{-4}	1.15	20.67	24.92

[a]1 Petabecquerel $\equiv 10^{15}$ Bq = 27,027 curies.

[b]Soon after initial cladding failure.

[c]Just prior to core slump.

[d]Directly following reactor vessel failure.

[e]First bank of HEPA filters fail.

[f]Second bank of HEPA filters fail.

Table 5.7. Xenon inventories and release to atmosphere (PBq)[a]

Time	Fuel		PV gas	DW gas	Wetwell		Reactor building		Condenser	Atmosphere	Total
	Core	Rubble			Gas	Water	Air	Water			
0	8028										8028
2332[b]	6443	0	7.3	0							6450
2488[c]	778.2	0	5326	0.031	78.5	0.02	27.6	0.02	65.7	12.8	6292
2590[d]	356.7	405.7	4520	2×10^{-10}	317.7	0	128.0	0.12	291.0	175.5	6195
2768[e]	347	0.22	0	4×10^{-4}	3×10^{-4}	2×10^{-5}	1233.0	2.2	292.0	4164	6038
2917[f]	341	0.002	0	3×10^{-6}	3×10^{-5}	2×10^{-6}	461.0	1.04	287.4	4856	5947
3100	331	2×10^{-7}	0	3×10^{-12}	2×10^{-3}	5×10^{-6}	68.1	0.22	279.3	5105	5784

[a]1 Petabecquerel $\equiv 10^{15}$ Bq = 27,027 curies.

[b]Soon after initial cladding failure.

[c]Just prior to core slump.

[d]Directly following reactor vessel failure.

[e]First bank of HEPA filters fail.

[f]Second bank of HEPA filters fail.

Table 5.8. Iodine inventories and release to atmosphere (PBq)[a]

Time (min)	Fuel		Reactor vessel			Wetwell		Drywell		Reactor building		Condenser	SGTS		Atmosphere	Total
	Core	Rubble	Plated	Gas or suspended	Water	Water	Gas	Gas or suspended	Plated	Gas or suspended	Water		Charcoal	HEPA		
0[b]	27,748															27,748
2,332[c]	8,047	0	0	0	0	0	0	0	0	0	0	0	0	0	0	8,047
2,488[d]	928	0	4,122	80.8	2,637	0.02	4×10^{-6}	4×10^{-6}	0	2×10^{-10}	1×10^{-5}	0.088	7×10^{-8}	0	7×10^{-10}	7,768
2,590[e]	436	468	6,686	5.853	0	0.23	4×10^{-5}	4×10^{-5}	0	6×10^{-7}	5×10^{-4}	0.092	3×10^{-6}	0	1×10^{-7}	7,596
2,768[f]	420	65.1	6,439	0	0	3.3	6×10^{-4}	2.9	182.6	1.4	200	0.088	1.6	0.0011	0.016	7,316
2,917	410	18.6	6,293	0	0	3.5	7×10^{-4}	1.5	198.7	1.3	221	0.086	2.8	0.0014	0.029	7,151
3,100	393	1.7	6,032	0	0	3.4	7×10^{-4}	0.68	178.1	1.1	239	0.083	4.9	0.0014	0.050	6,854

[a] 1 Petabecquerel ≡ 10^{15} Bq = 27,027 curies.

[b] Soon after initial cladding failure.

[c] Just prior to core slump.

[d] Directly following reactor vessel failure.

[e] First bank of HEPA filters fail.

[f] Second bank of HEPA filters fail.

89

Table 5.9. Cesium inventories and release to atmosphere (PBq)[a]

Time (min)	Fuel		Reactor vessel			Wetwell		Drywell		Reactor building		Condenser	SGTS		Atmosphere	Total
	Core	Rubble	Plated	Gas or suspended	Water	Water	Gas	Gas or suspended	Plated	Gas or suspended	Water		Charcoal	HEPA		
0	20,774															20,774
2,332[b]	671.5	0	0	0	0	0	0	0	0	0	0	0	0	0	0	671.5
2,488[c]	105.7	0	325.4	26.2	213.2	0.11	0	0	0	0	0	0.054	0	0	0	670.7
2,590[d]	66.3	39.0	561.2	3.4	0	0.46	0	0	0	0	0	0.059	0	0	0	670.3
2,768[e]	66.3	0.023	560.5	0	0	0.46	0	0.004	42.1	0.020	0.12	0.059	10^{-9}	0.052	5×10^{-6}	669.5
2,917[f]	66.2	2×10^{-4}	560.1	0	0	0.46	0	0.002	42.0	0.019	0.17	0.058	10^{-9}	0.068	2×10^{-4}	669.1
3,100	66.2	2×10^{-8}	559.3	0	0	0.46	0	0.004	41.9	0.022	0.25	0.058	2×10^{-9}	0.068	0.04	668.2

[a] 1 Petabecquerel $\equiv 10^{15}$ Bq = 27,027 curies.

[b] Soon after initial cladding failure.

[c] Just prior to core slump.

[d] Directly following reactor vessel failure.

[e] First bank of HEPA filters fail.

[f] Second bank of HEPA filters fail.
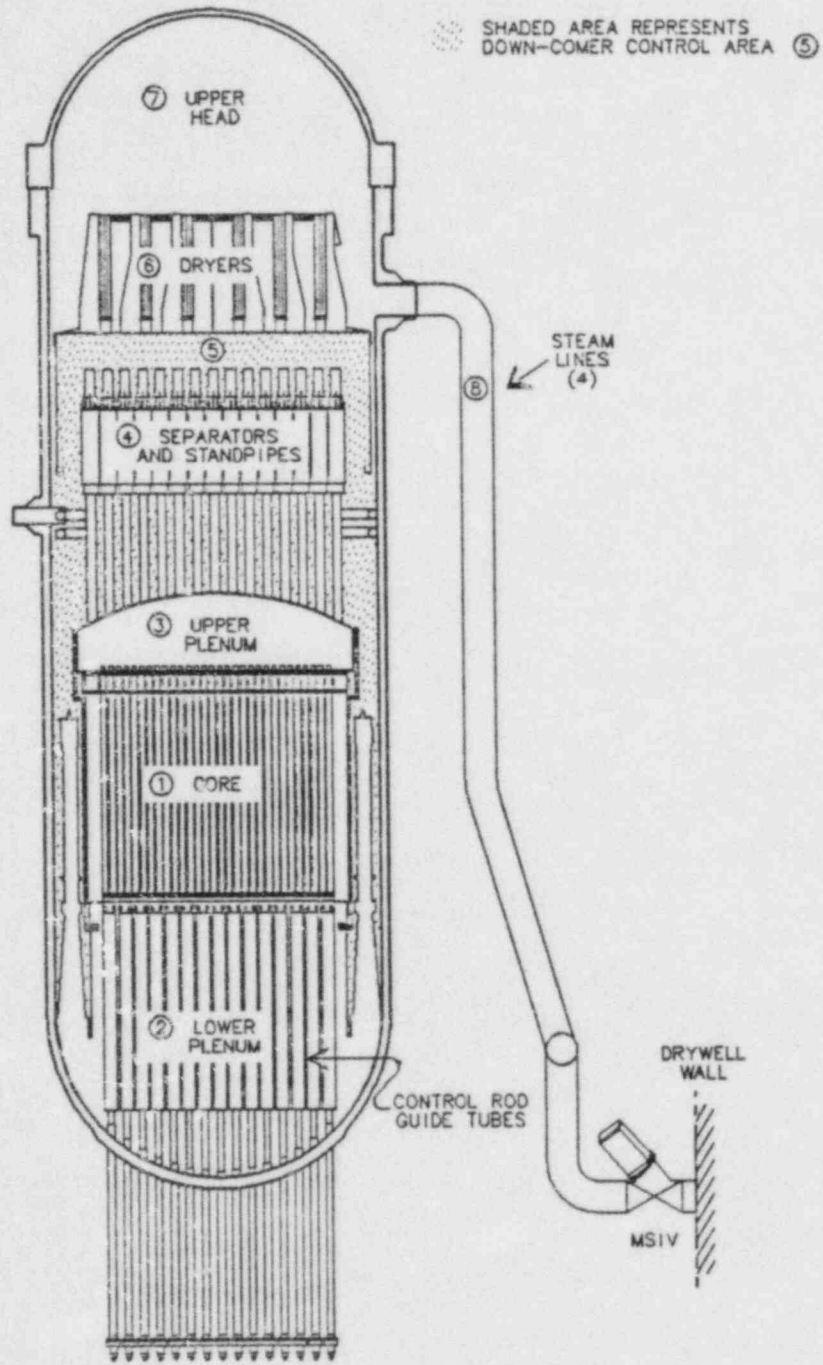
Fig. 5.1. Reactor vessel control volumes.
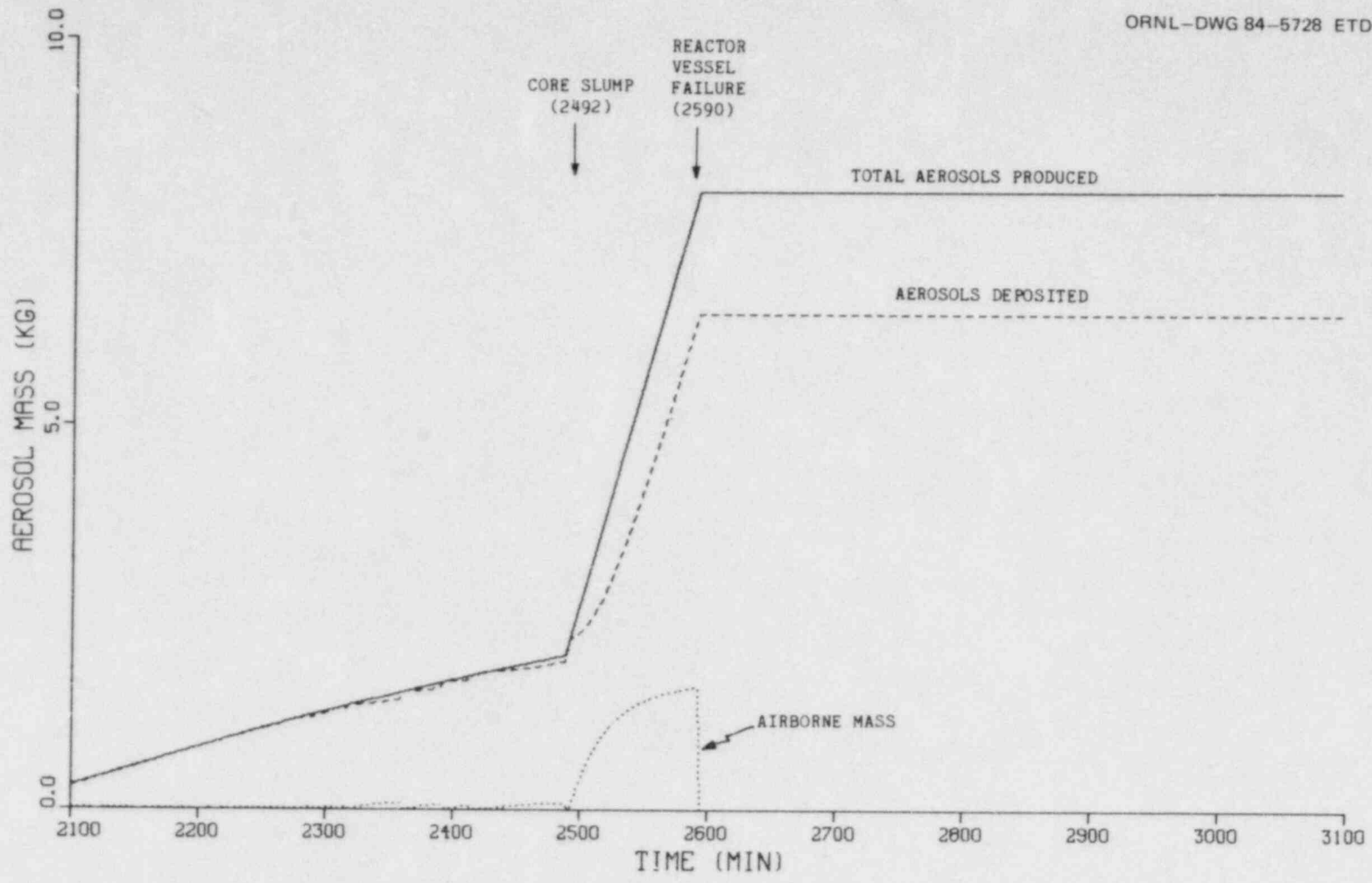
Fig. 5.2. Aerosols produced in reactor vessel; base case, 80% deposition.
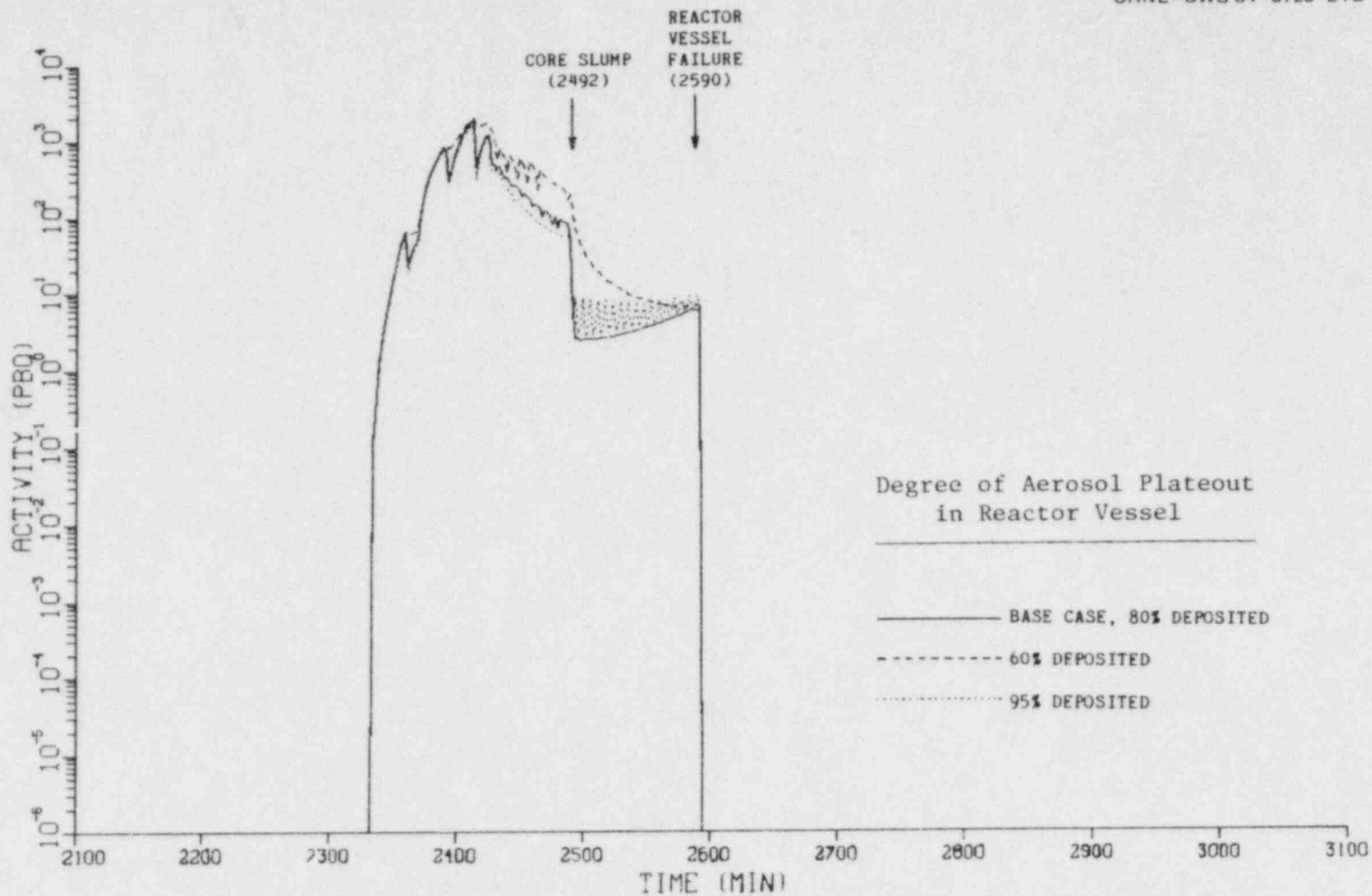
Fig. 5.3. Predicted airborne (gas plus suspended) iodine activity in the reactor vessel as a function of assumed degree of aerosol deposition.
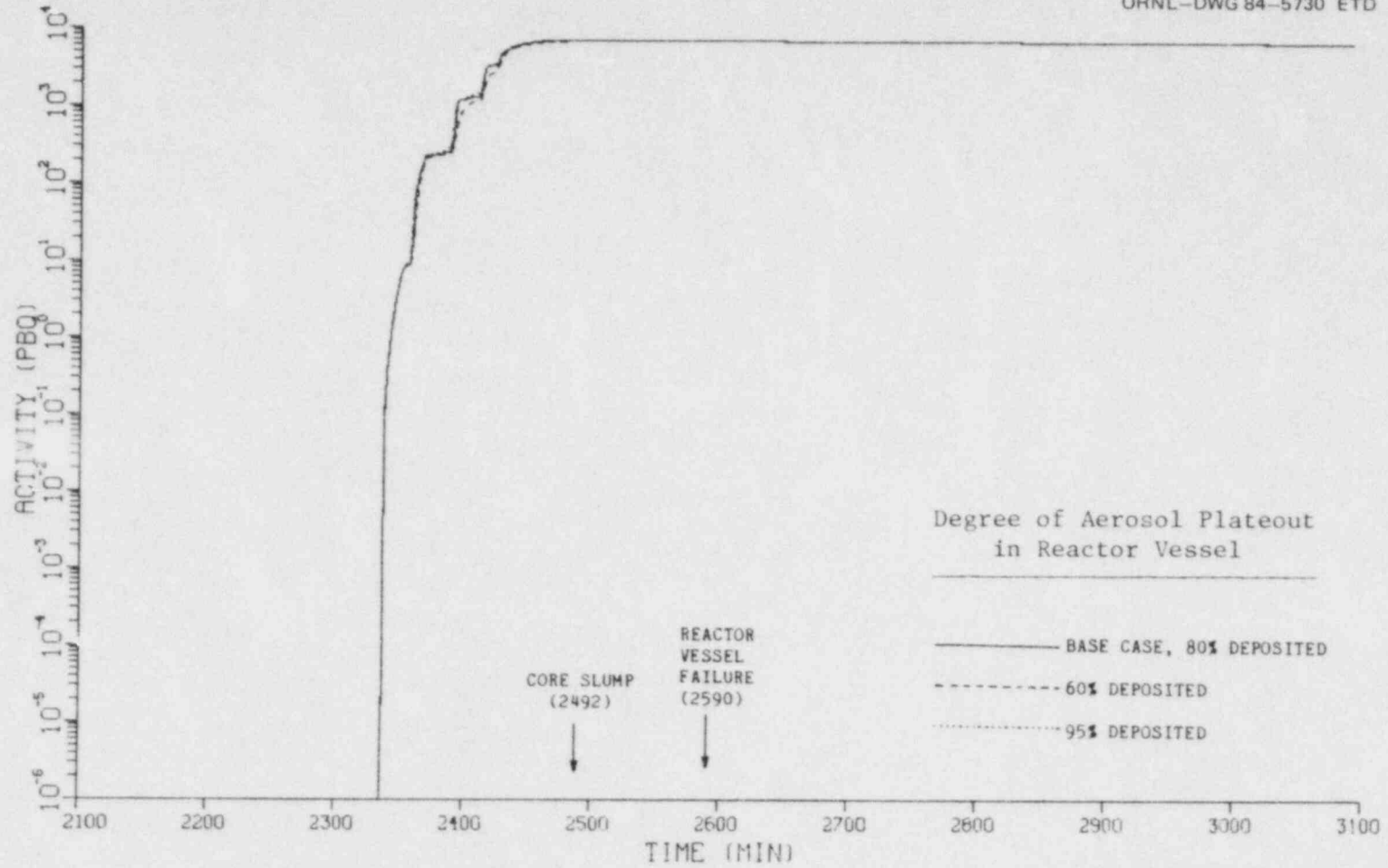
Fig. 5.4. Predicted iodine activity plated in the reactor vessel, as a function of the degree of aerosol plateout.
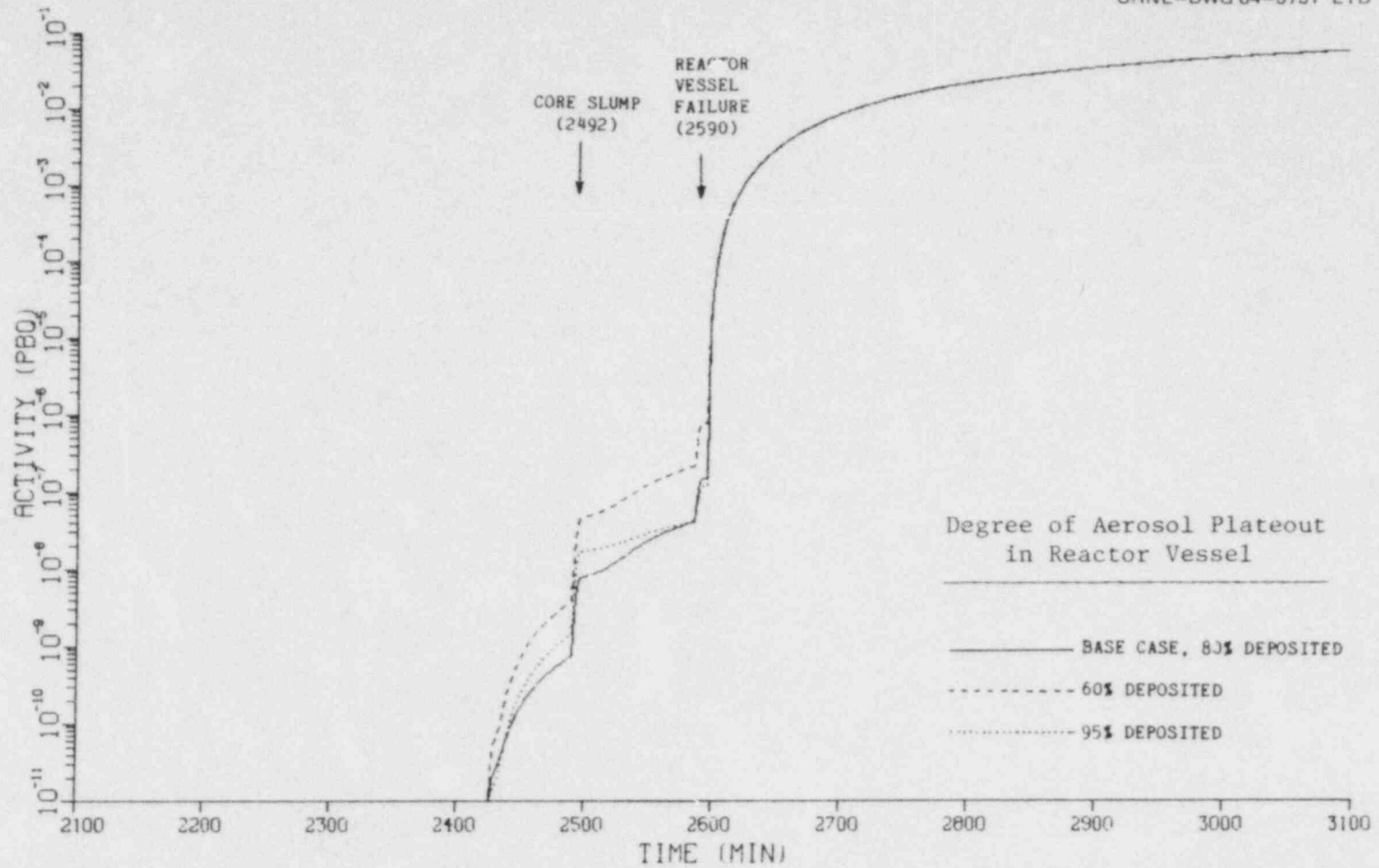
Fig. 5.5. Predicted iodine release to environment as a function of assumed degree of aerosol plateout in the reactor vessel.
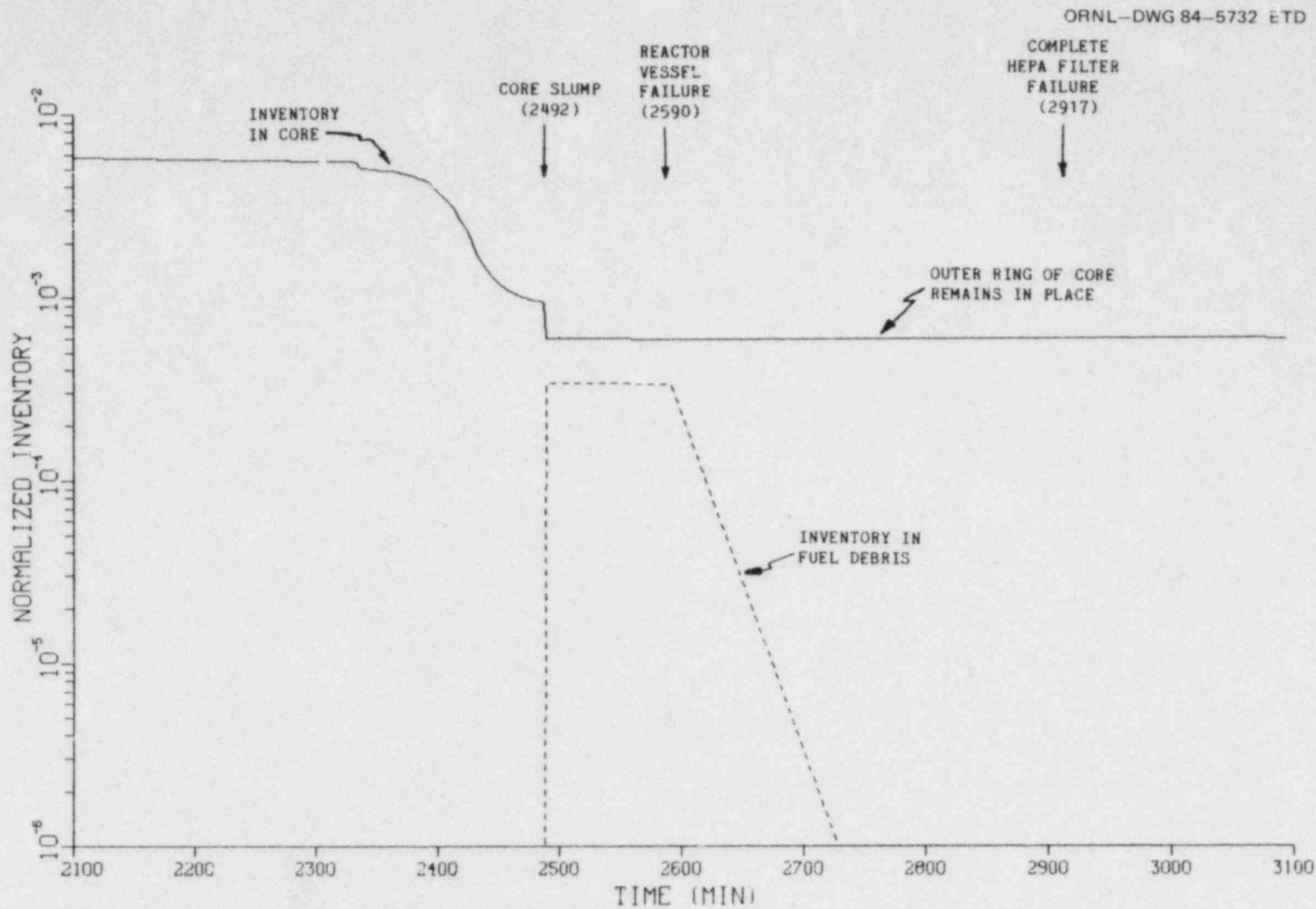
Fig. 5.6. Normalized krypton activity in fuel material. The activity is normalized to the initial activity level for nuclides with half-lives greater than 30 min. This normalization is also used for the results presented in Figs. 5.7 through 5.35.

ORNL–DWG 84–5733 ETD

REACTOR
VESSEL
FAILURE
(2590)

CORE SLUMP
(2492)

KRYPTON IN GAS SPACE
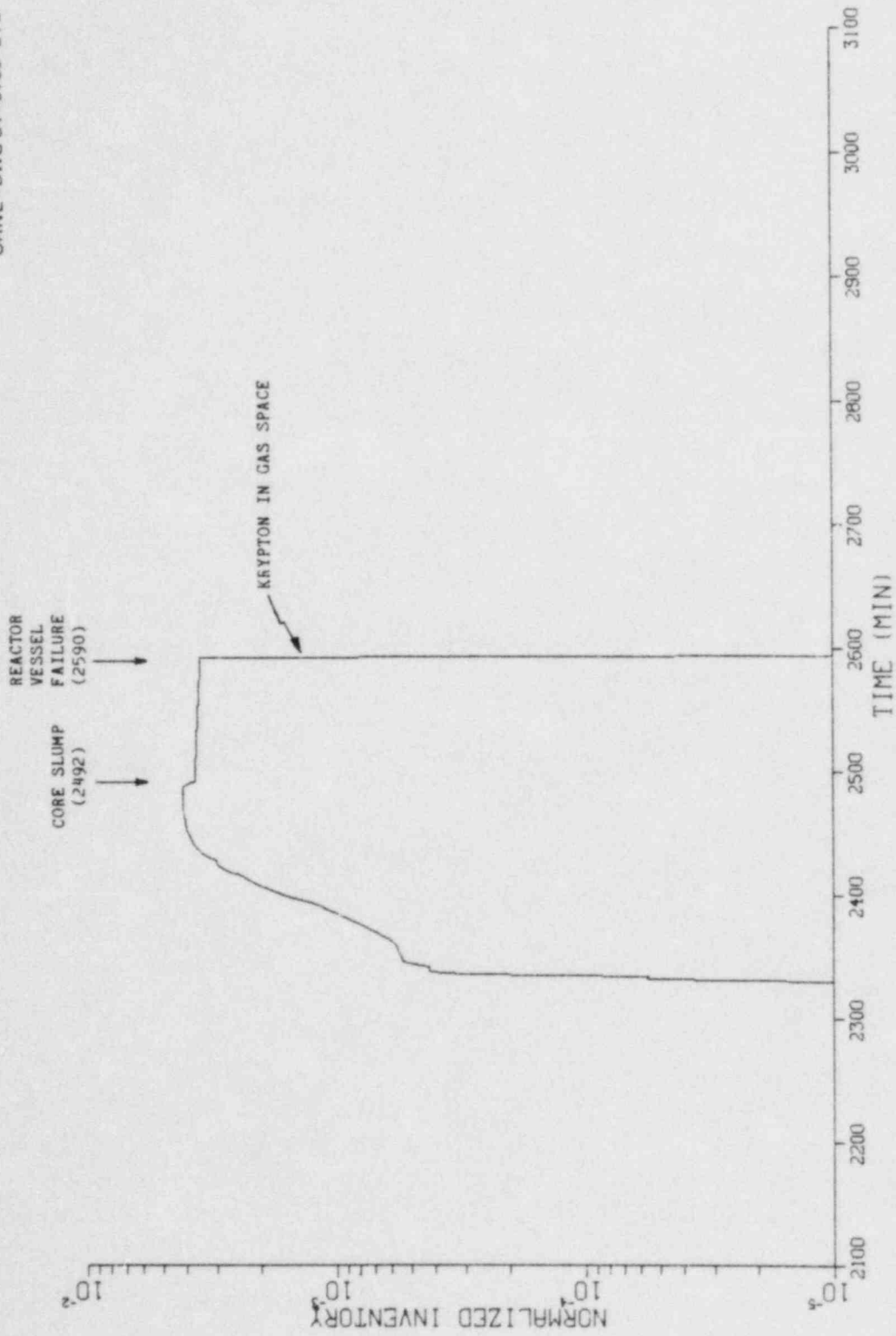
Fig. 5.7. Normalized krypton activity in reactor vessel gas space.
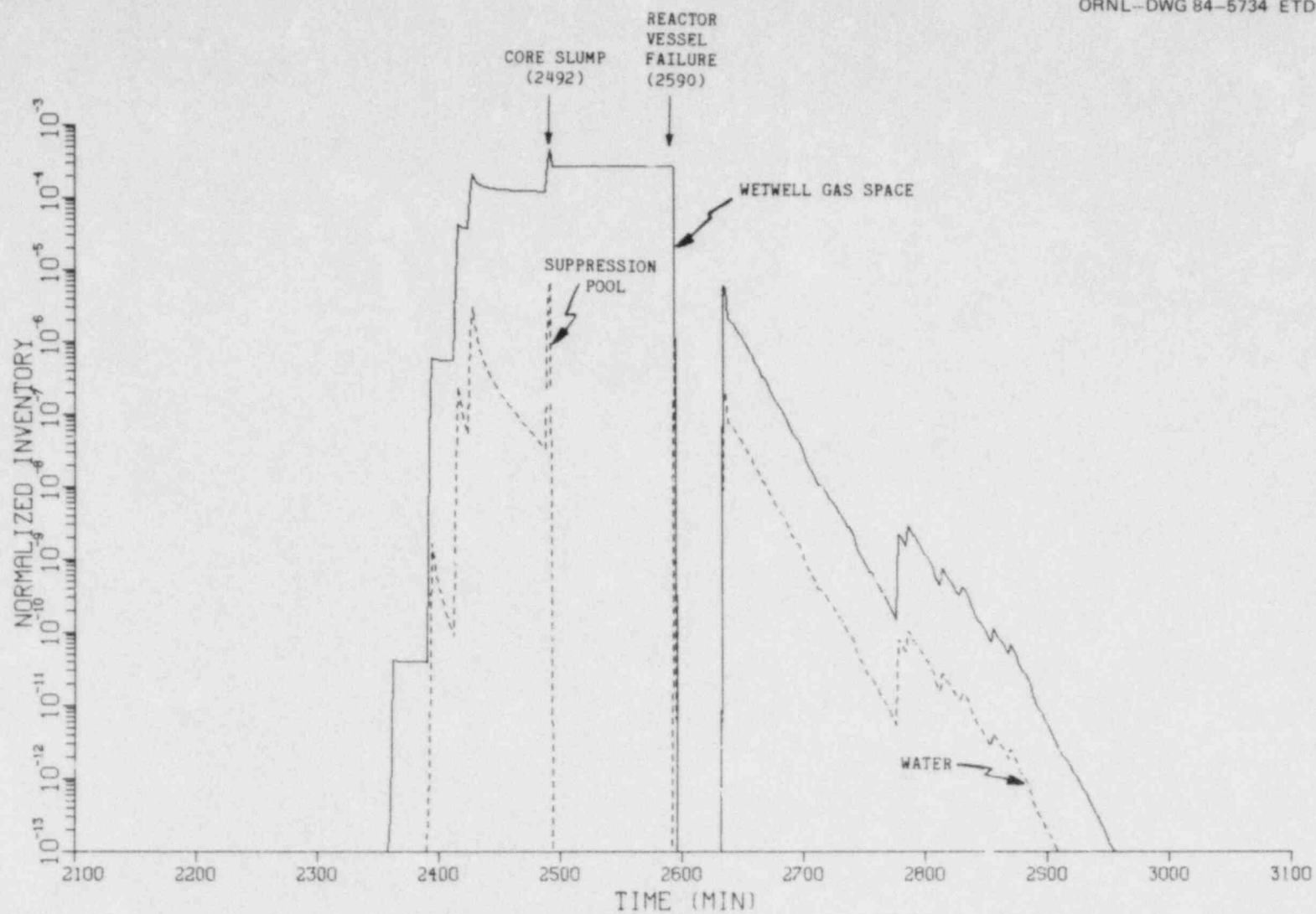
Fig. 5.8. Normalized krypton activity in the wetwell water and gas space.

ORNL-DWG 84-5735 ETD
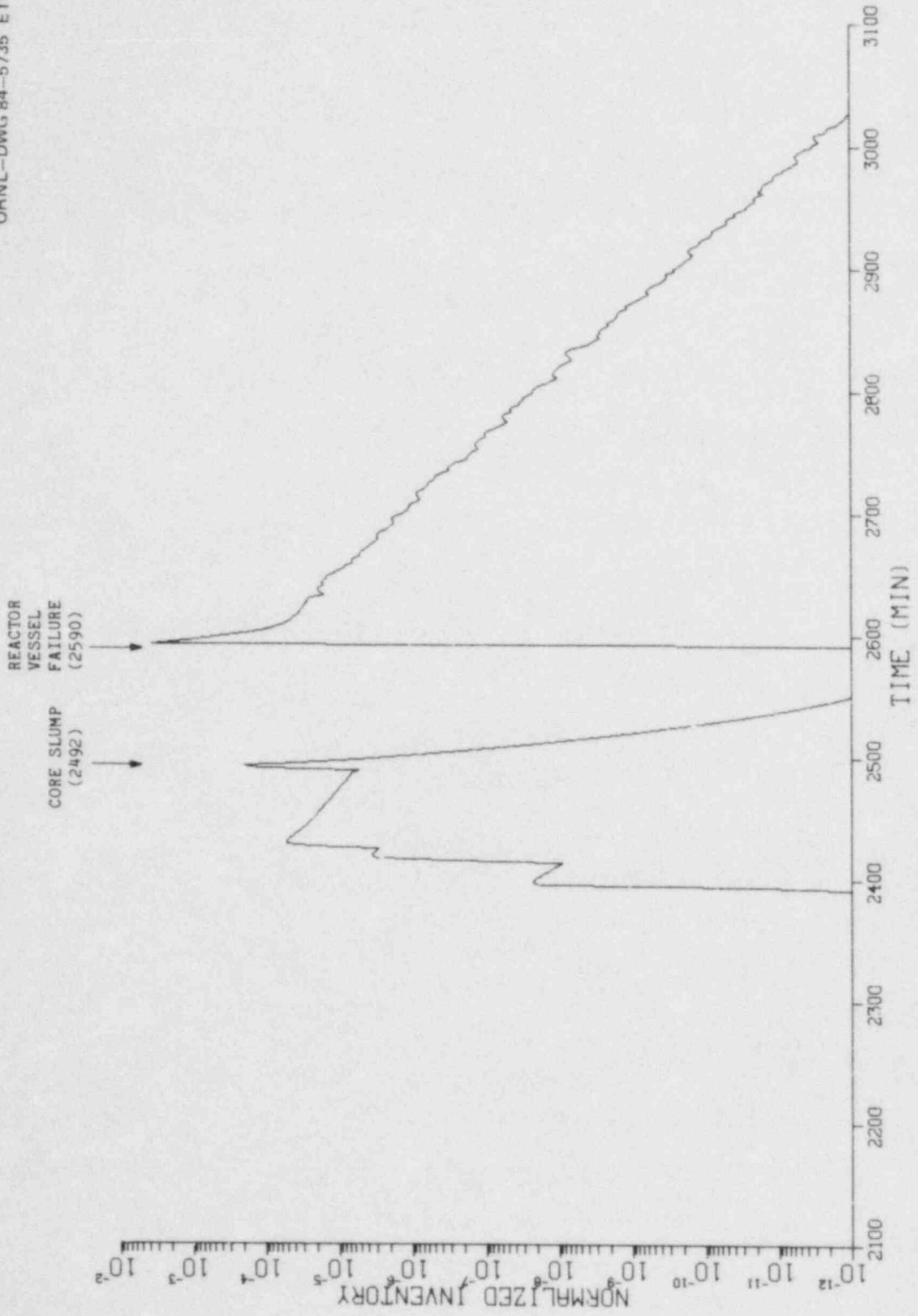
Fig. 5.9. Normalized krypton activity in the drywell.
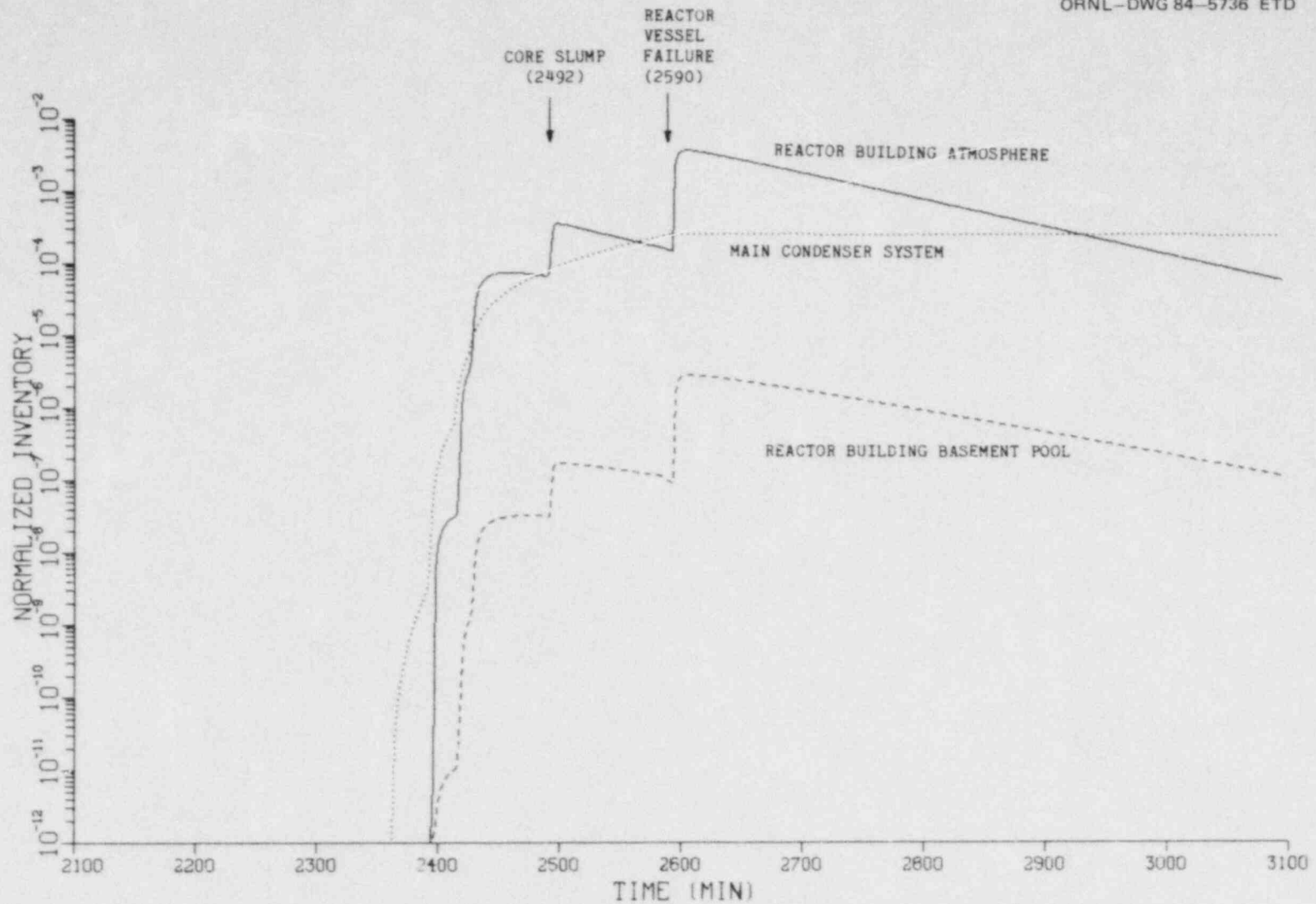
Fig. 5.10. Normalized krypton activity in the reactor building atmosphere and basement pool, and in the main condenser system in the turbine building.
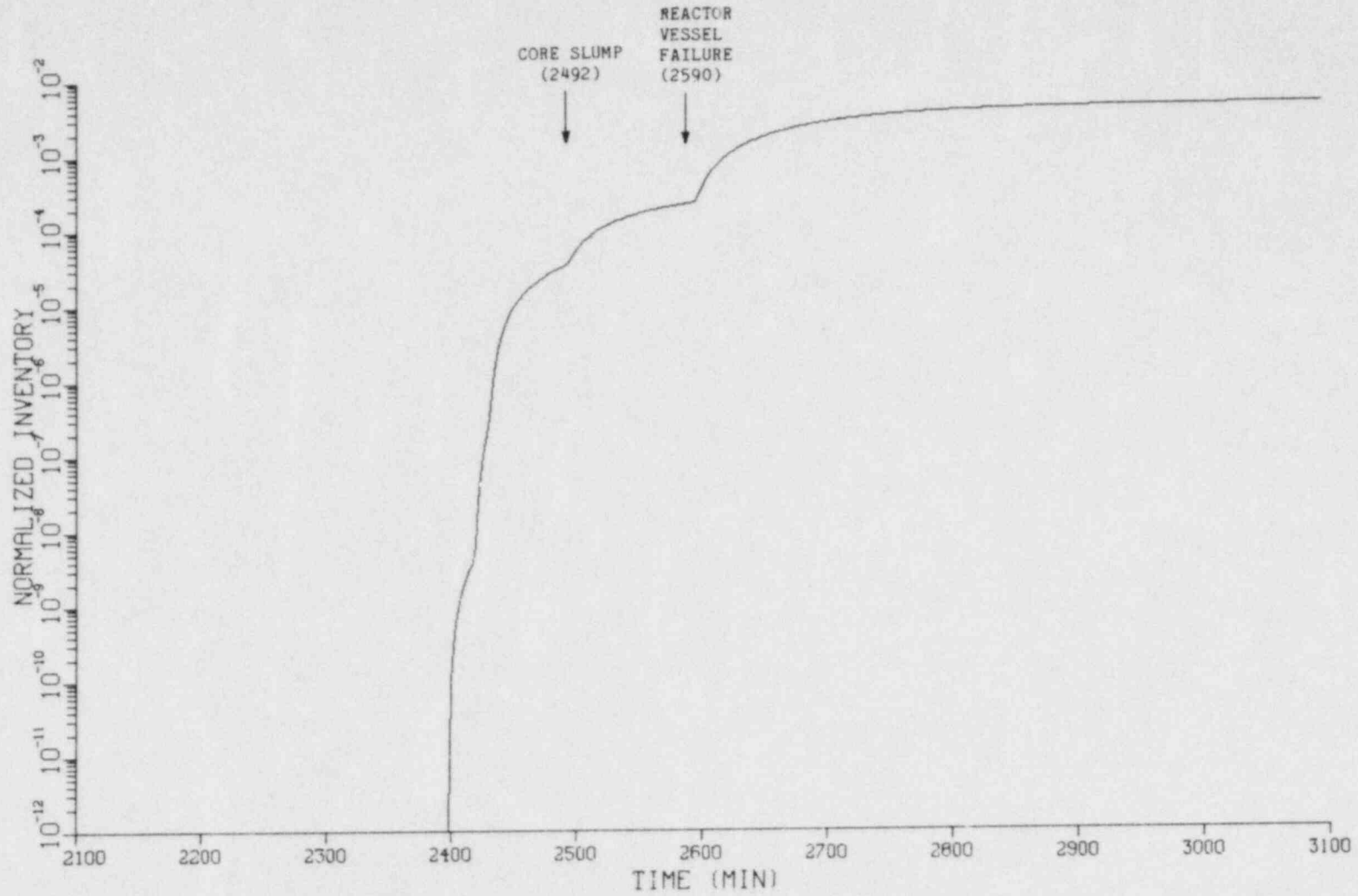
Fig. 5.11. Normalized krypton activity released to the outside atmosphere.
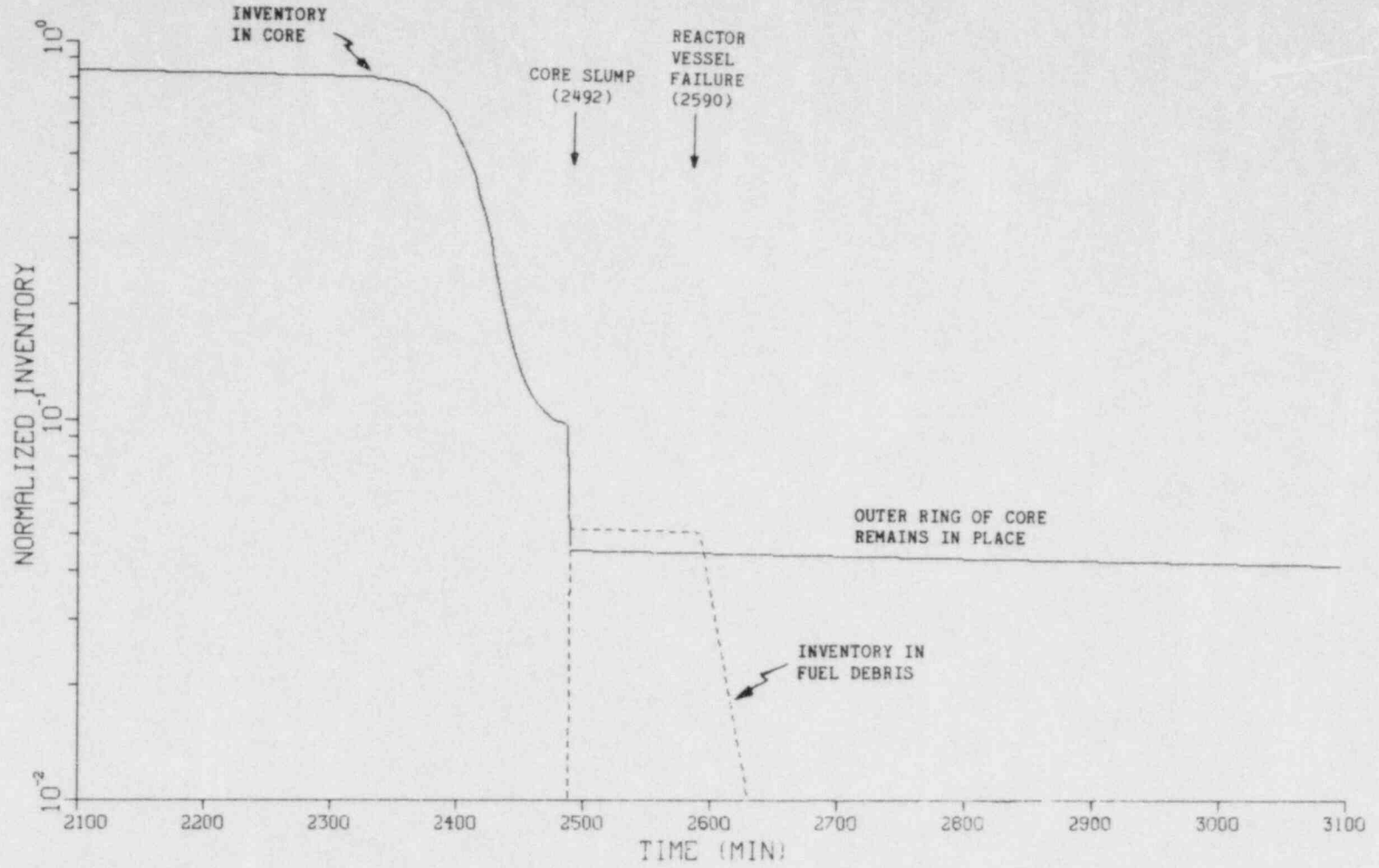
Fig. 5.12. Normalized xenon activity in fuel material.
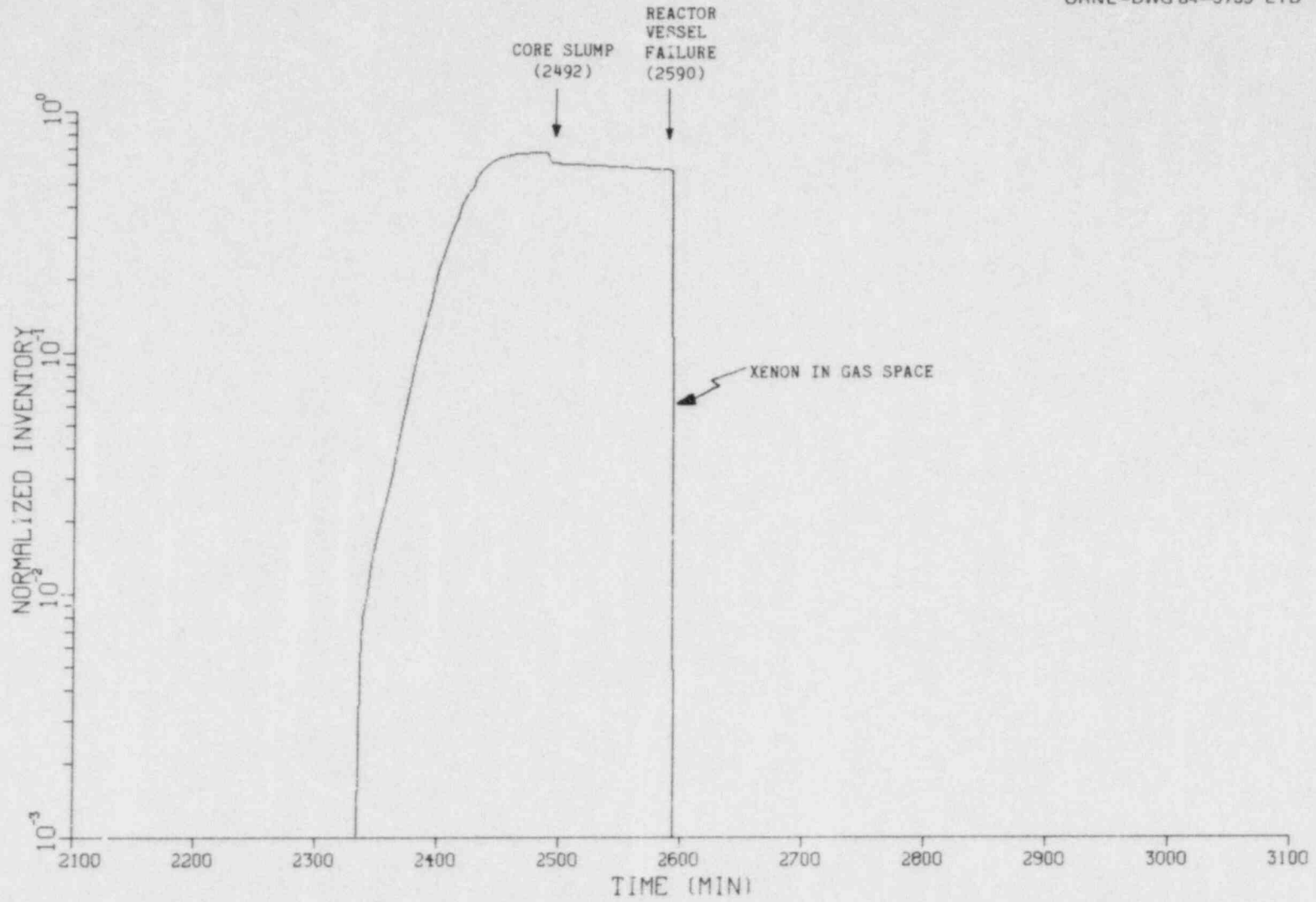
Fig. 5.13. Normalized xenon activity in reactor vessel gas space.
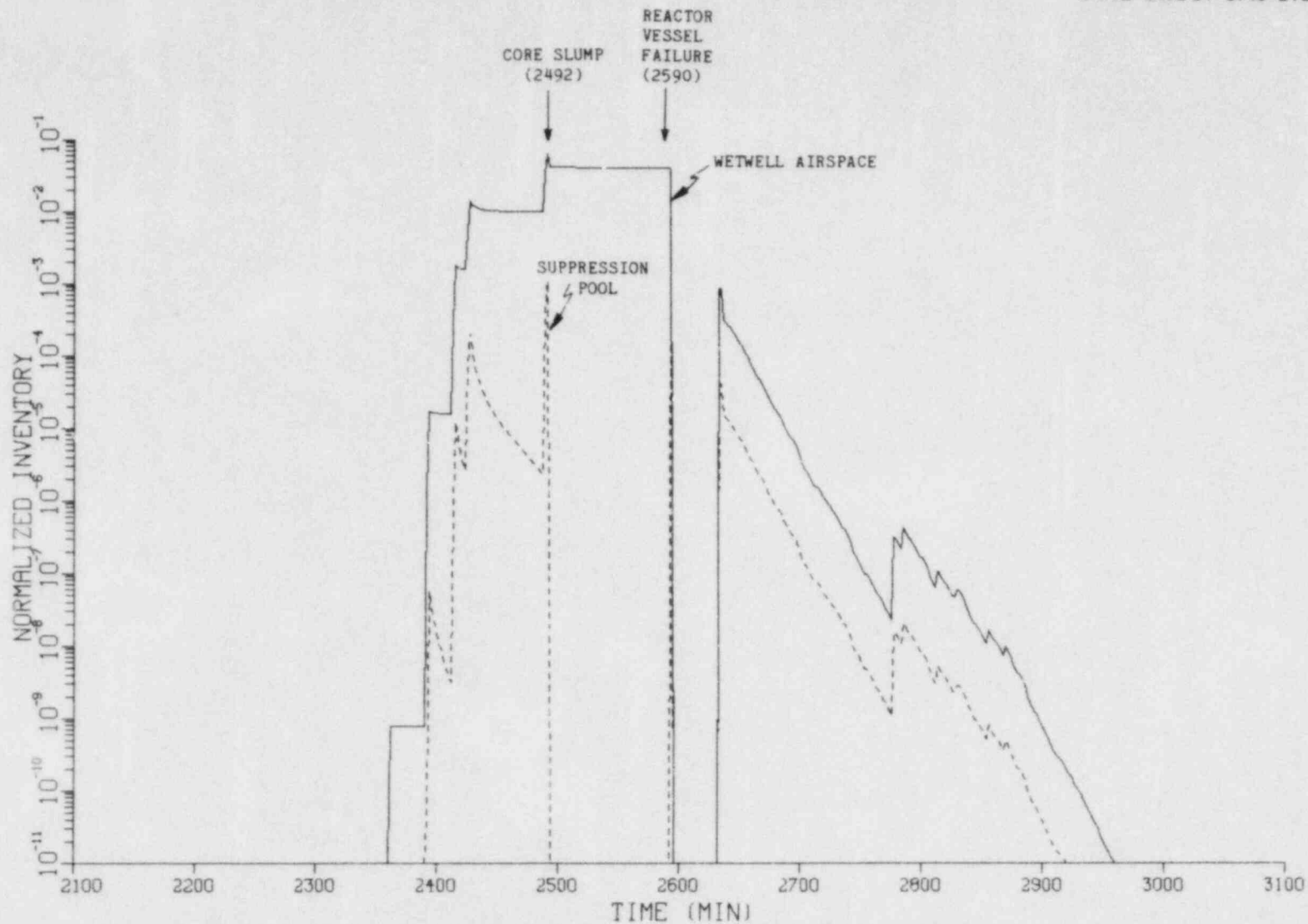
Fig. 5.14. Normalized xenon activity in the wetwell water and air-space.

ORNL–DWG 84–5741 ETD
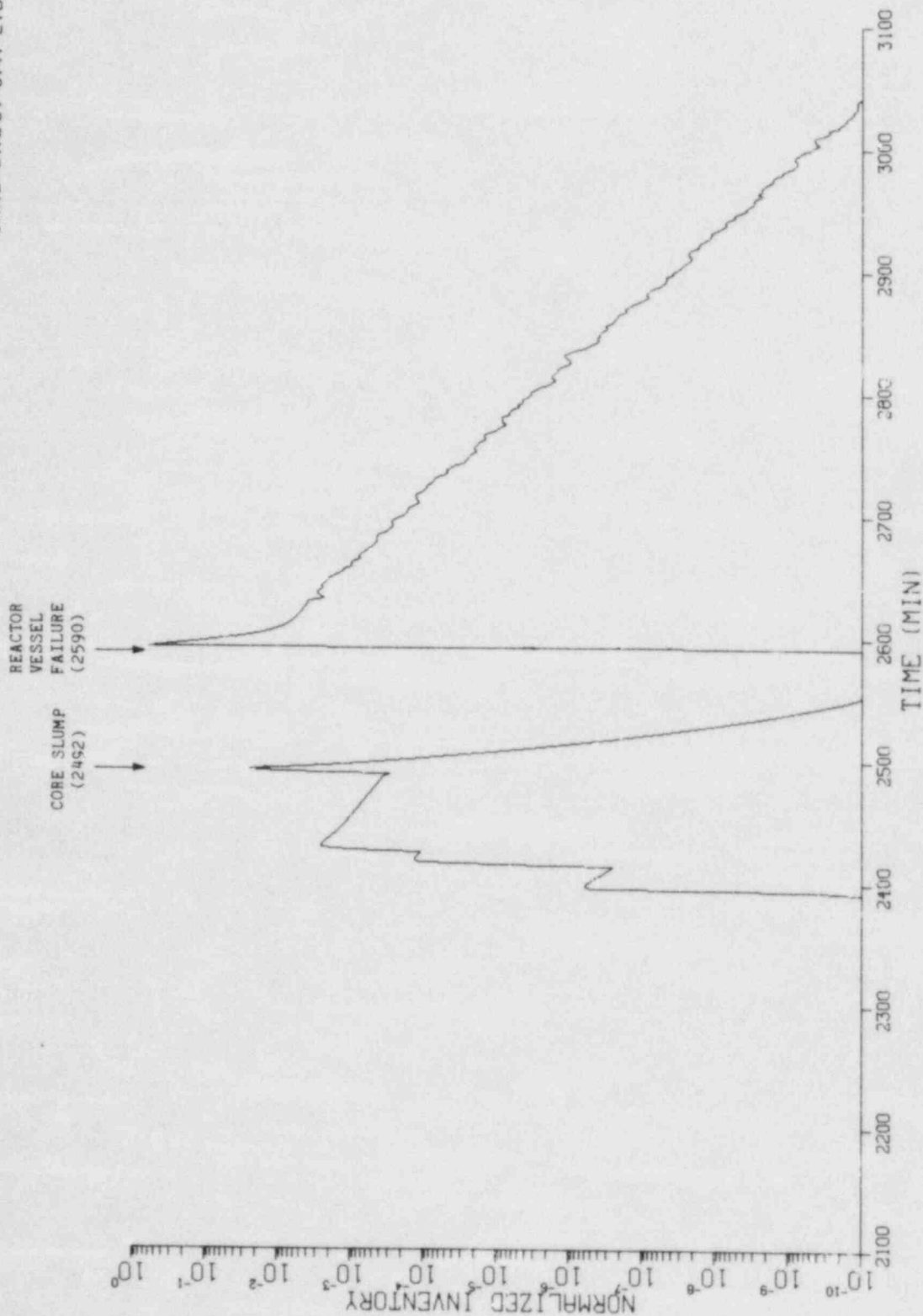
Fig. 5.15. Normalized xenon activity in the drywell.
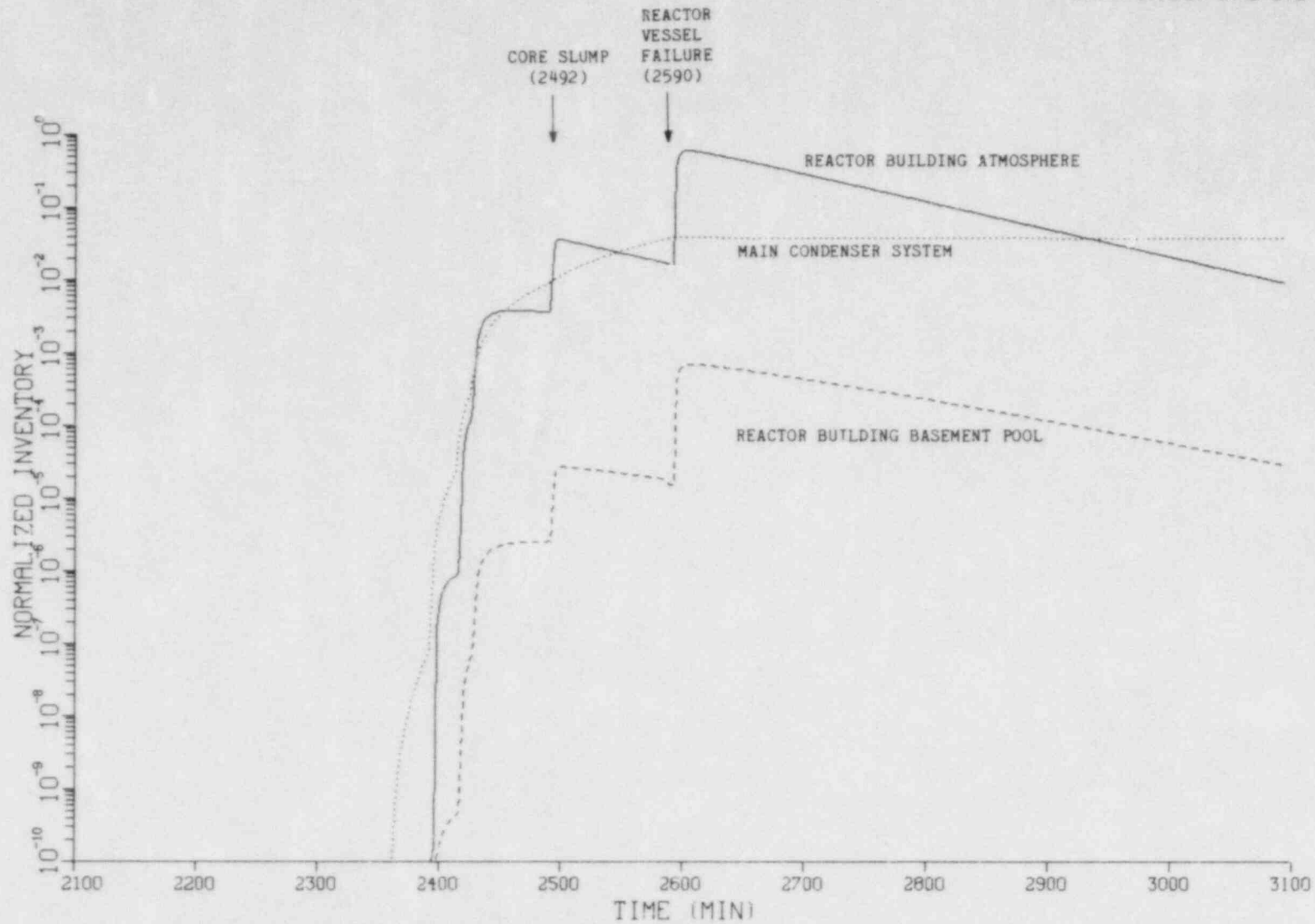
Fig. 5.16. Normalized xenon activity in the reactor building atmosphere and basement pool, and in the main condenser system in the turbine building.
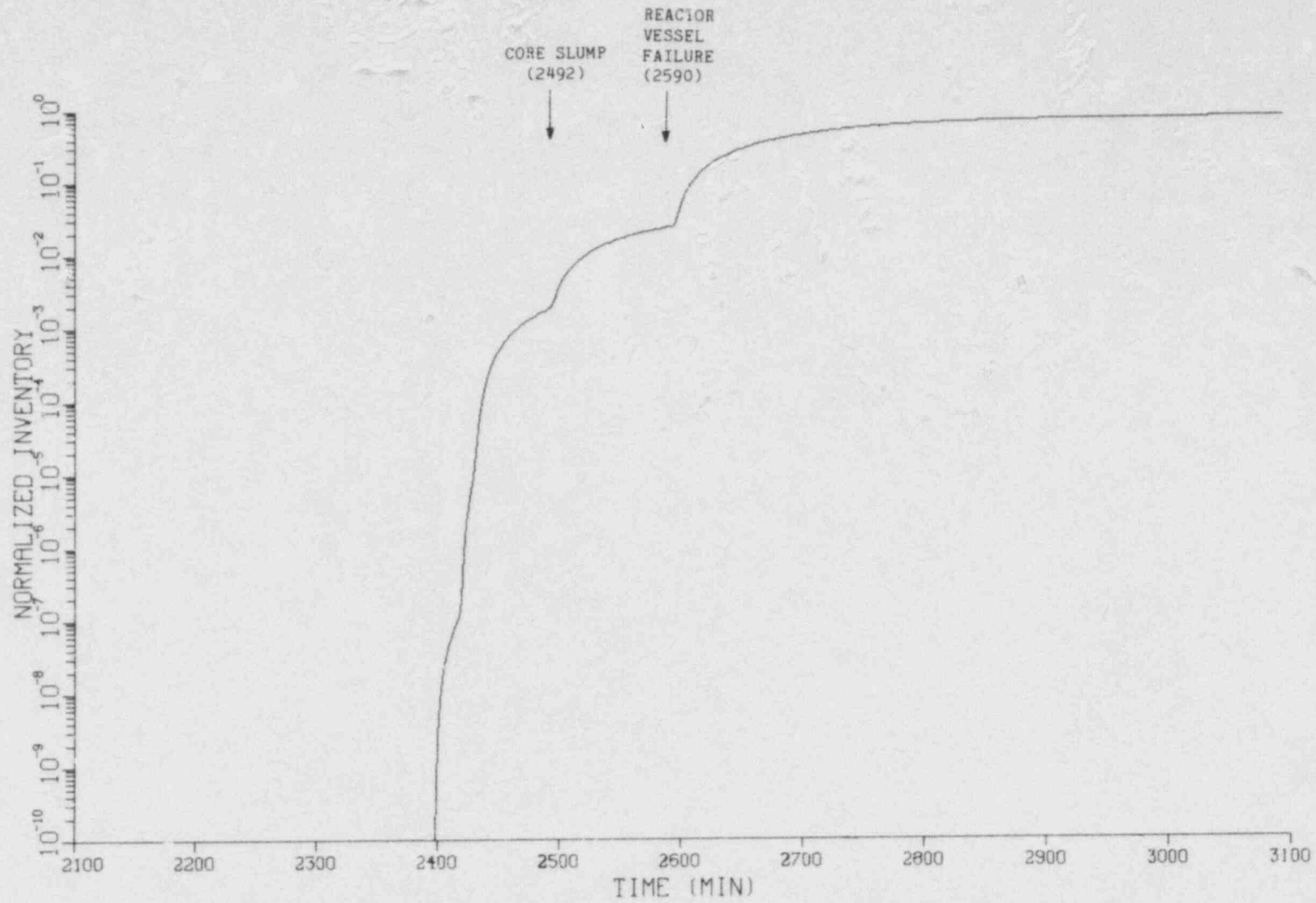
Fig. 5.17. Normalized xenon activity released to the outside atmosphere.
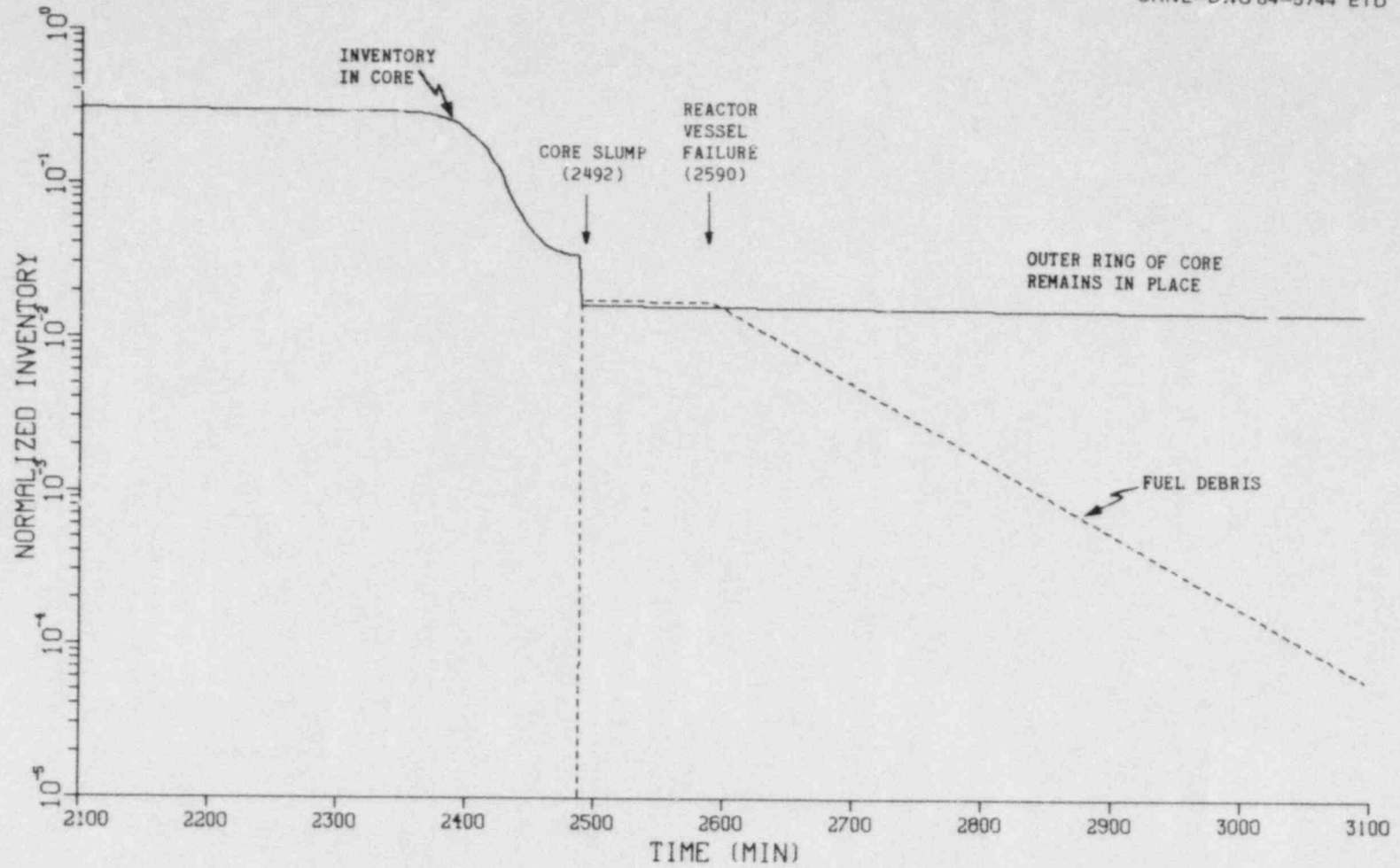
Fig. 5.18. Normalized iodine activity in fuel material.
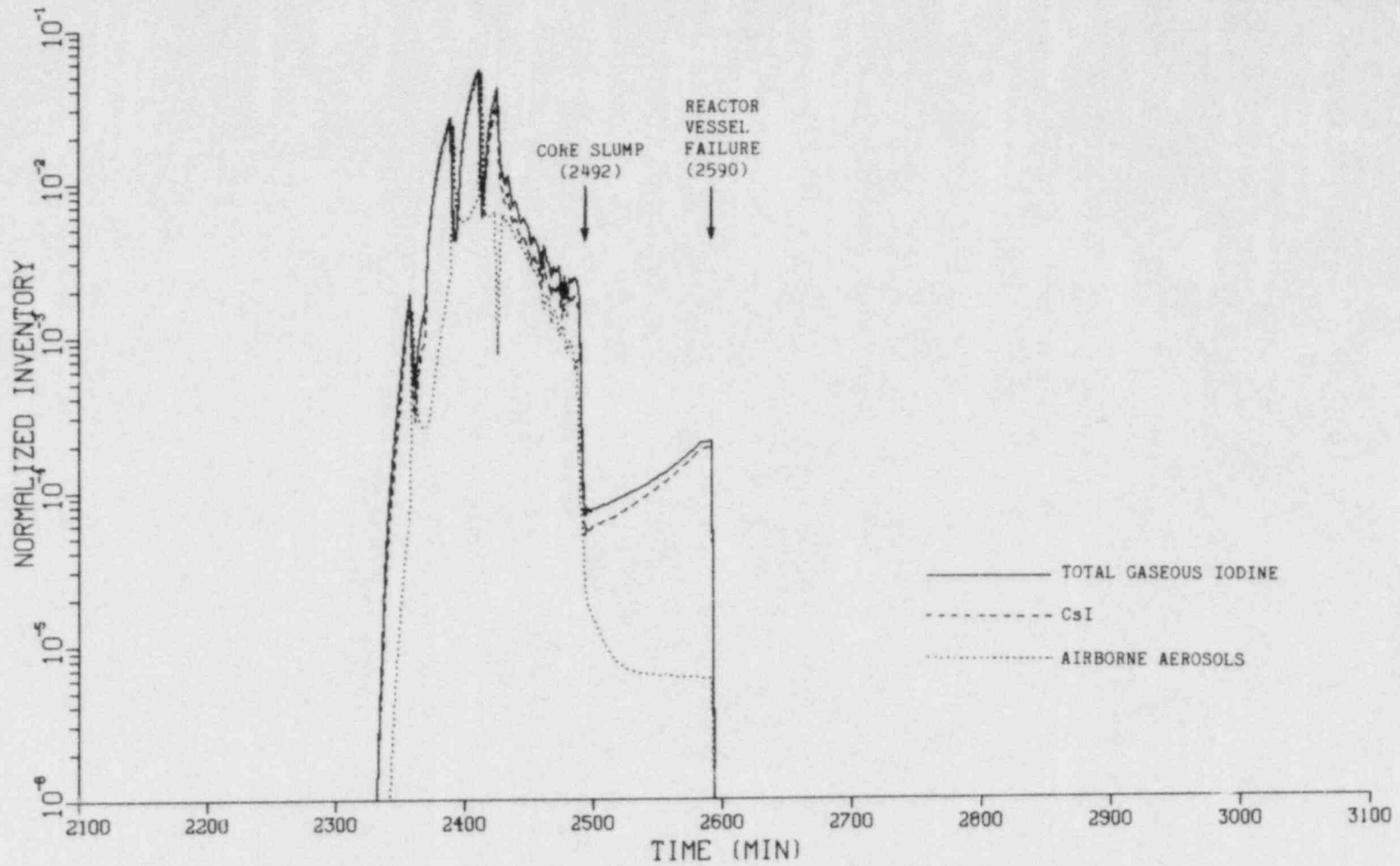
Fig. 5.19. Normalized iodine activity suspended in the reactor vessel. Iodine produced near the time of core melt is rapidly adsorbed on aerosols.
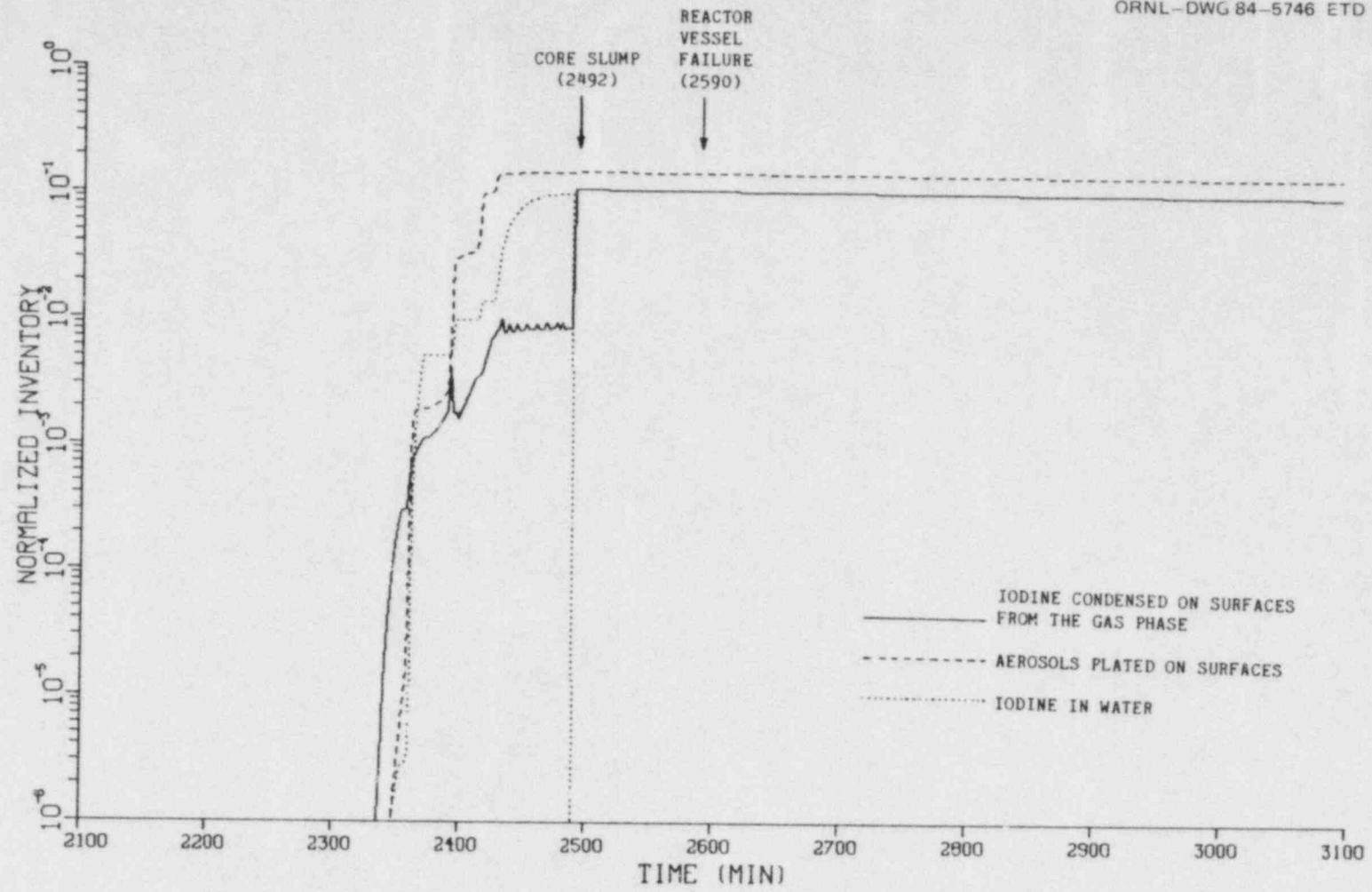
Fig. 5.20. Normalized iodine activity in the reactor vessel water and plated on interior reactor vessel surfaces.
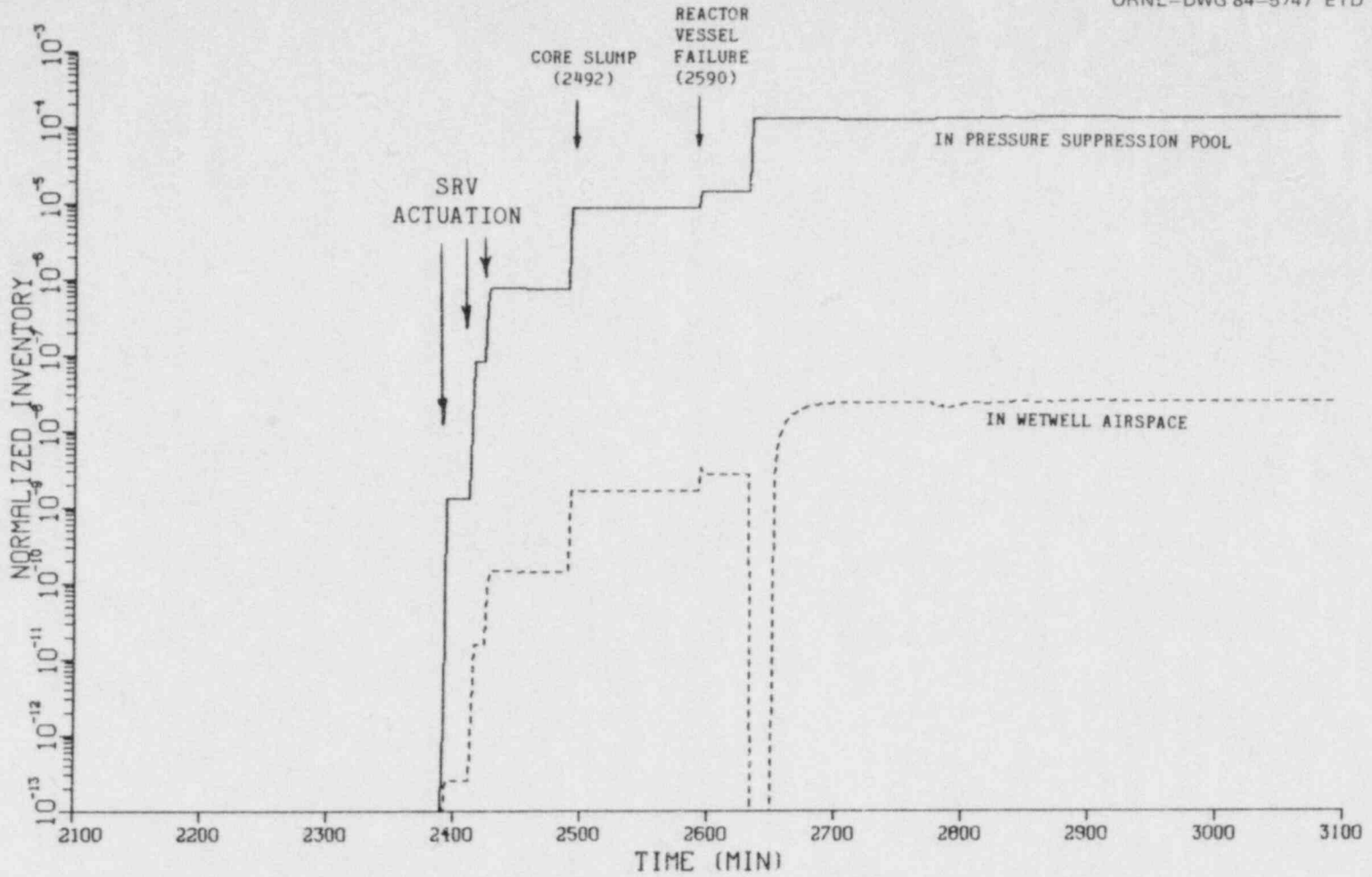
Fig. 5.21. Normalized iodine activity in the wetwell water and airspace.
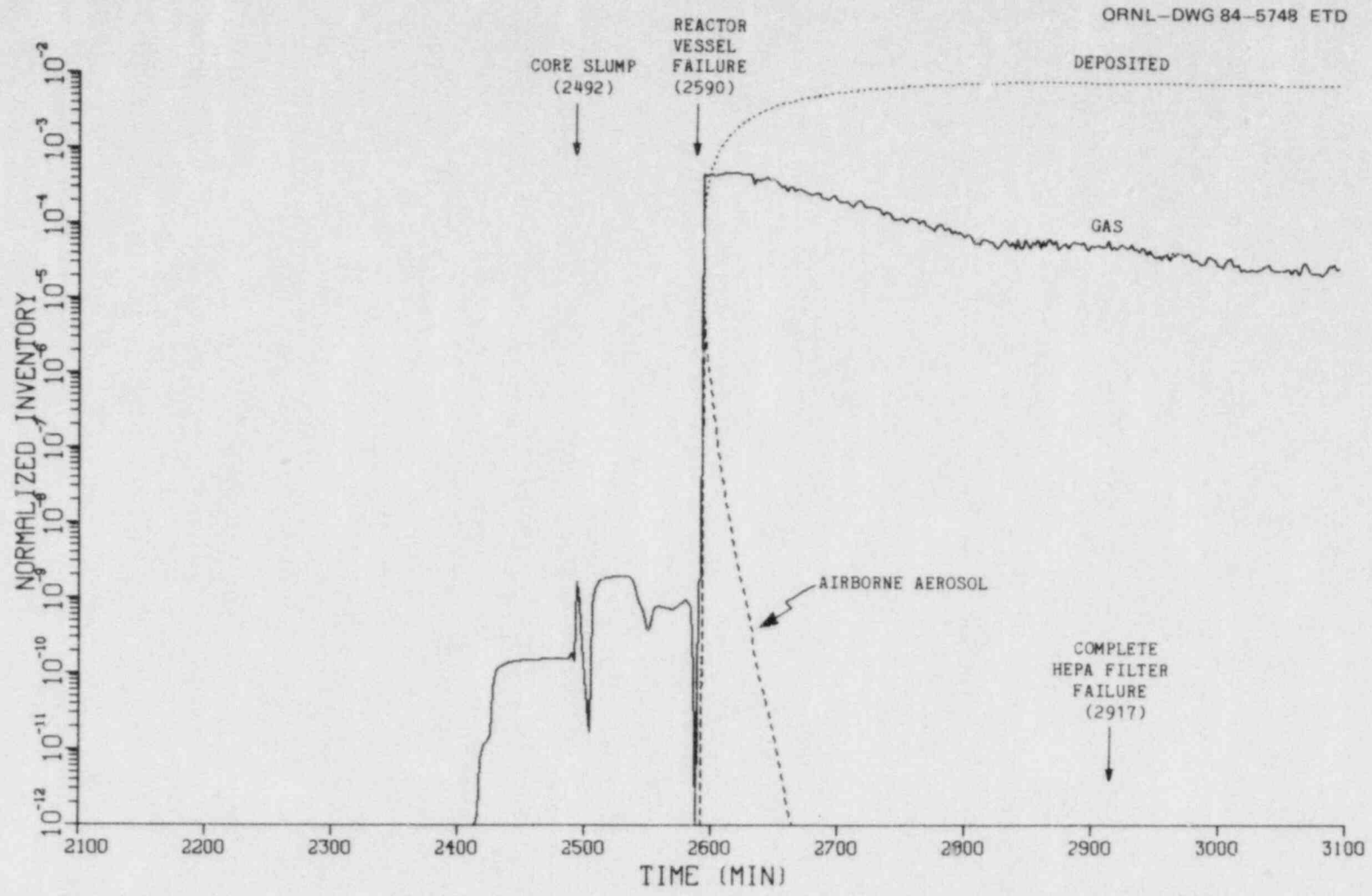
Fig. 5.22. Normalized iodine activity in the drywell.

112
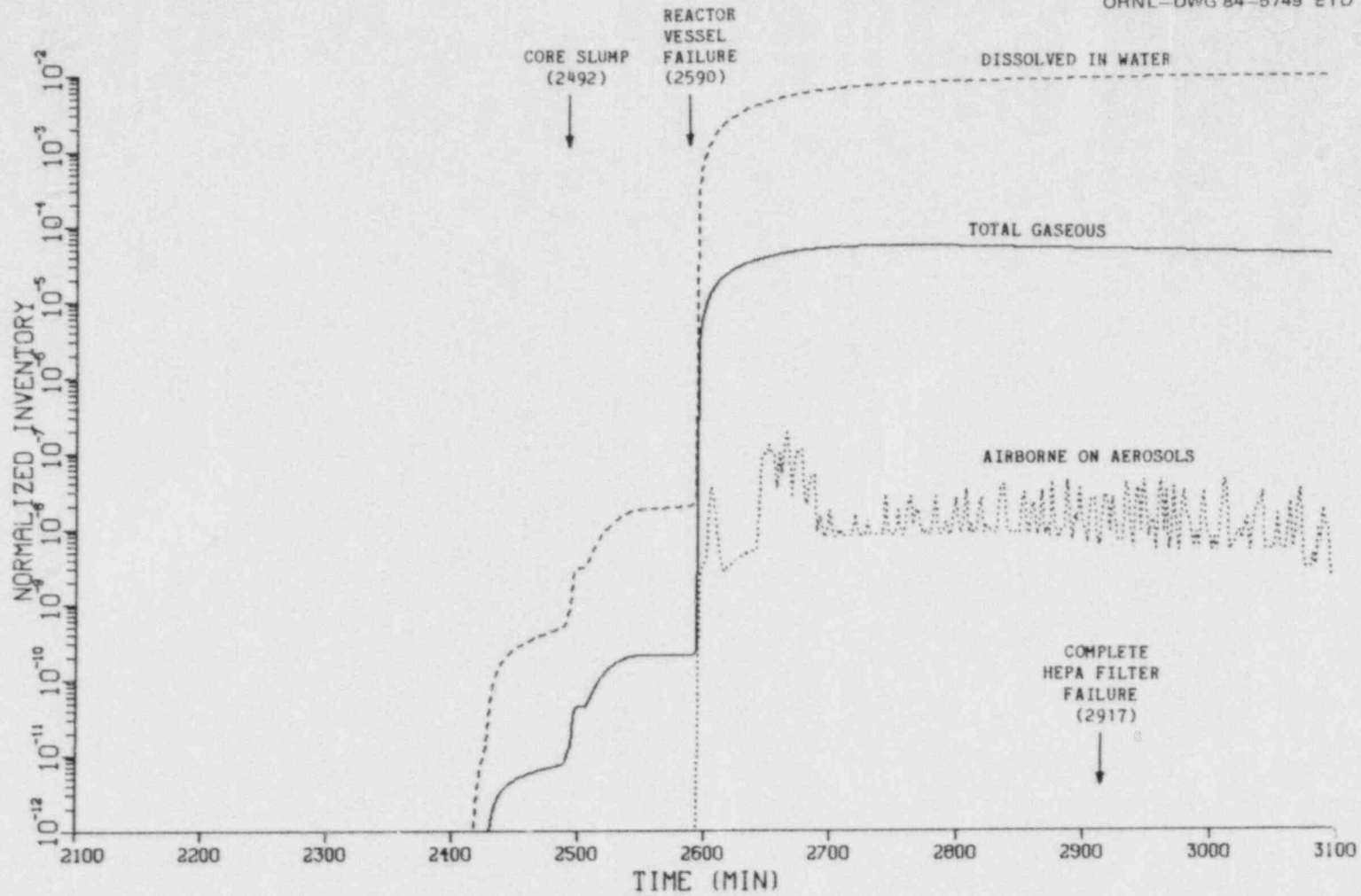
Fig. 5.23. Normalized iodine activity in the reactor building: dissolved in water, on airborne aerosols, and total gaseous.
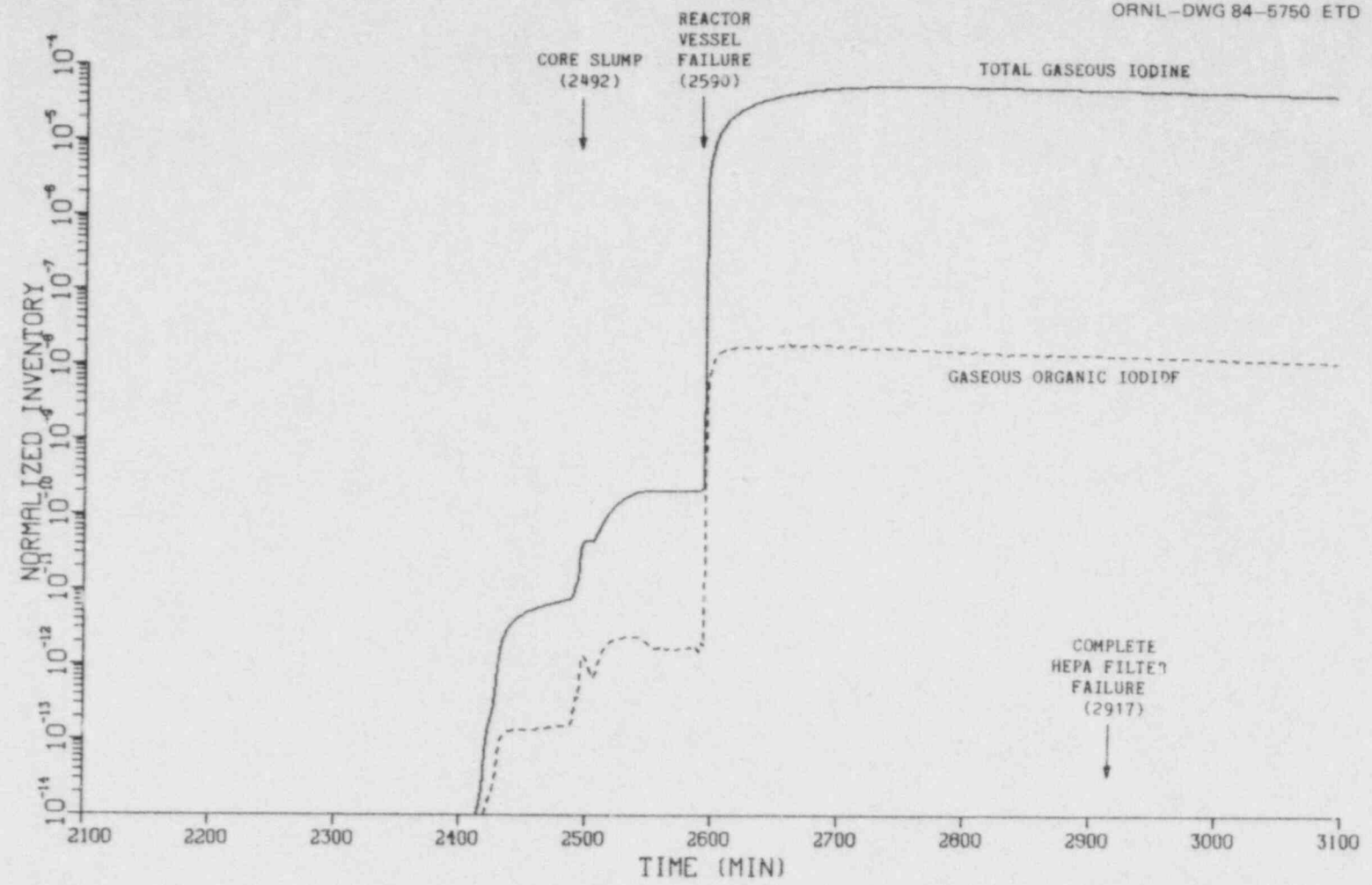
Fig. 5.24. Normalized gaseous iodine activity (total and portion as organic iodide) in the reactor building.
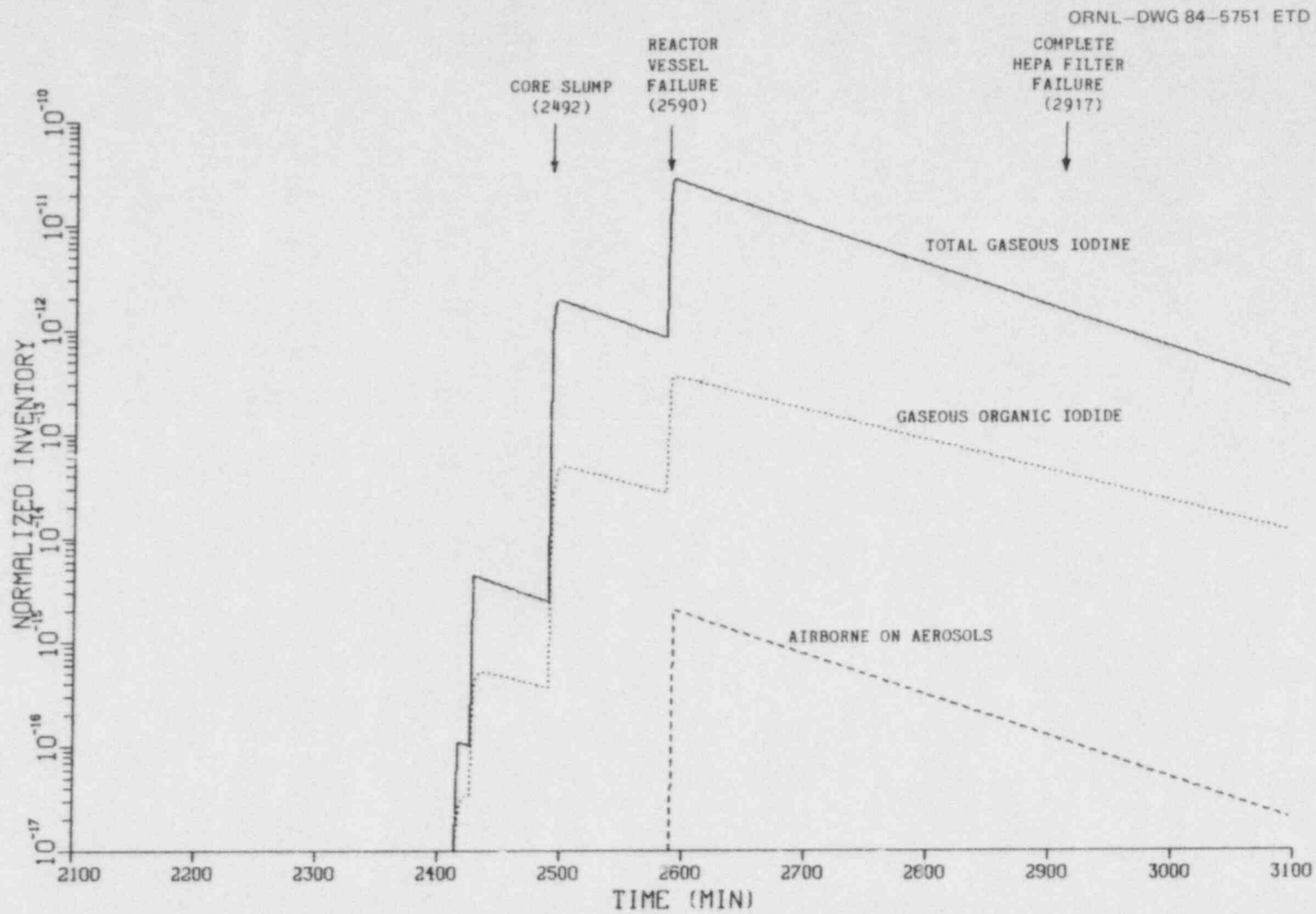
Fig. 5.25. Normalized iodine activity in the refueling bay.

115
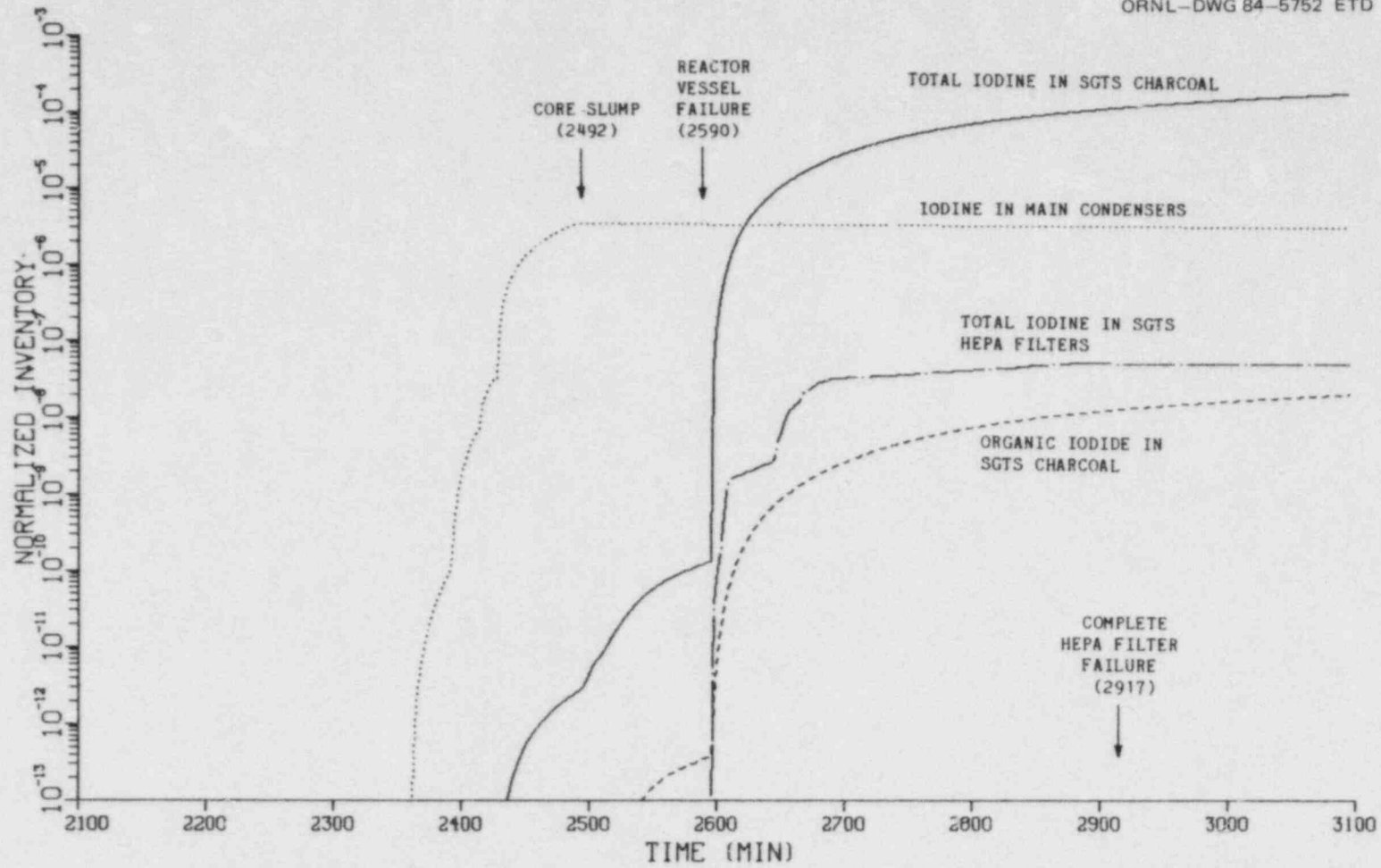
Fig. 5.26. Normalized iodine activity in components of the SGTS trains and in the main condenser system in the turbine building.

117
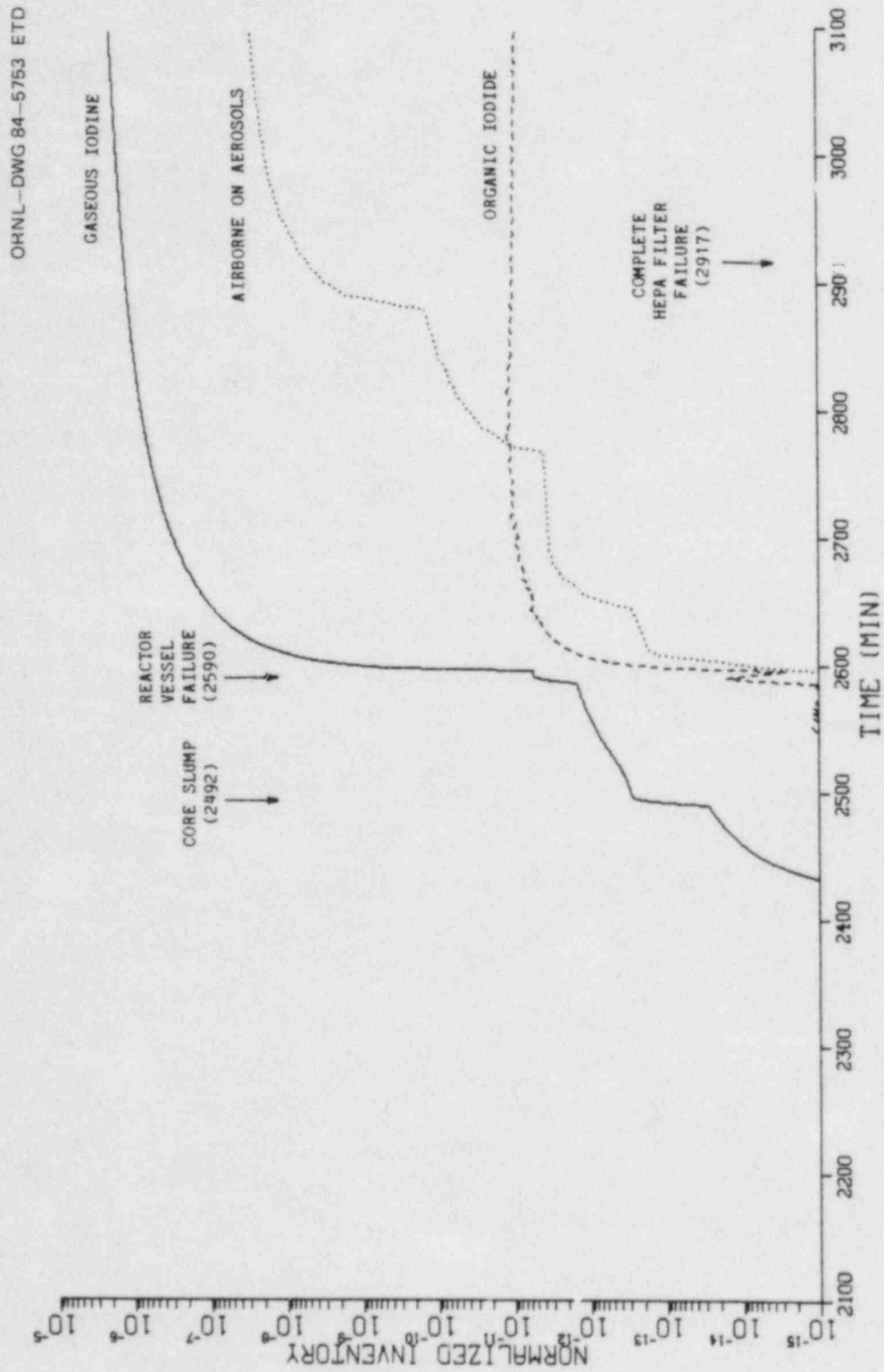
Fig. 5.27. Normalized iodine activity released to the outside atmosphere.
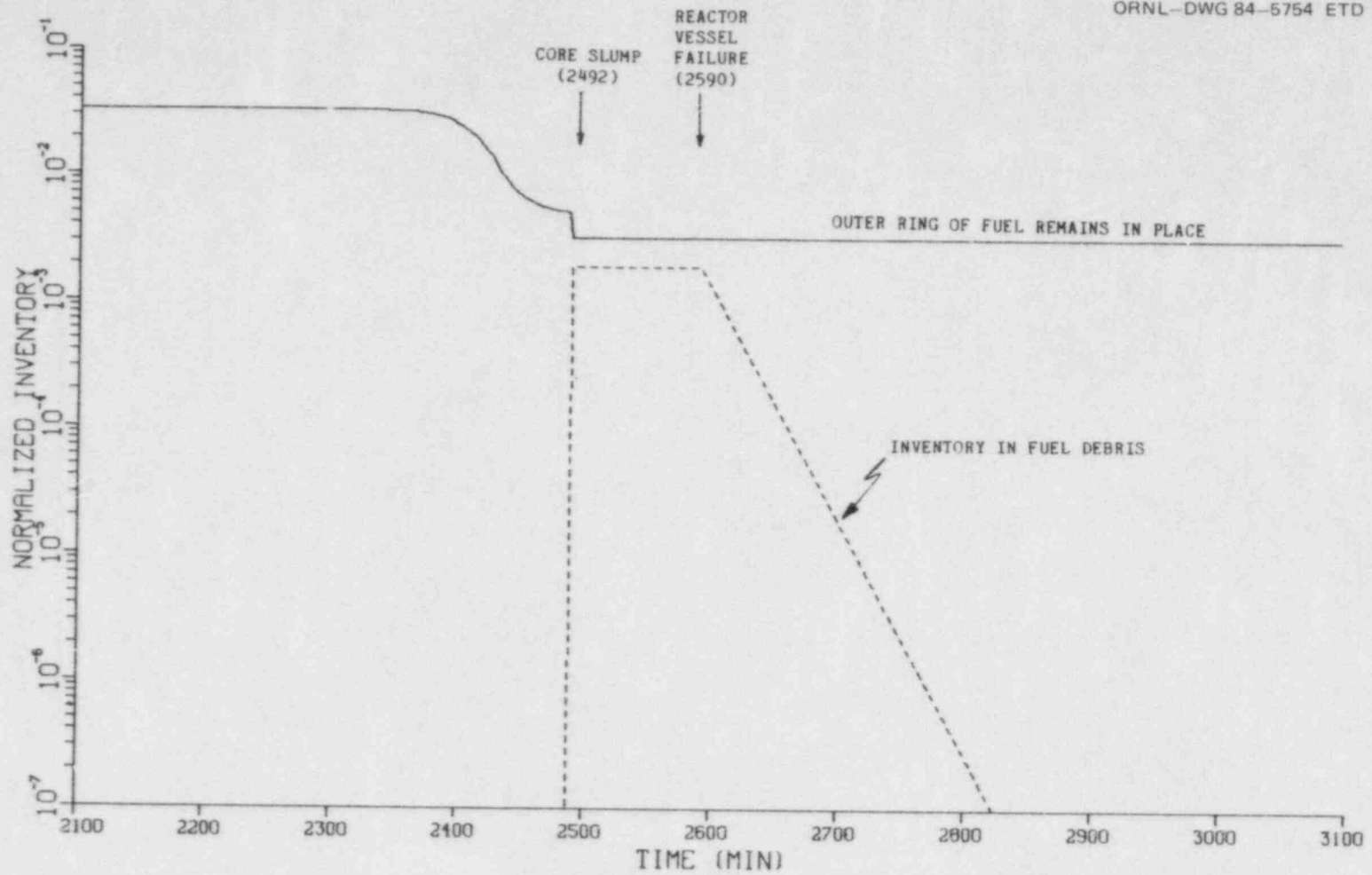
Fig. 5.28. Normalized cesium activity in fuel material.
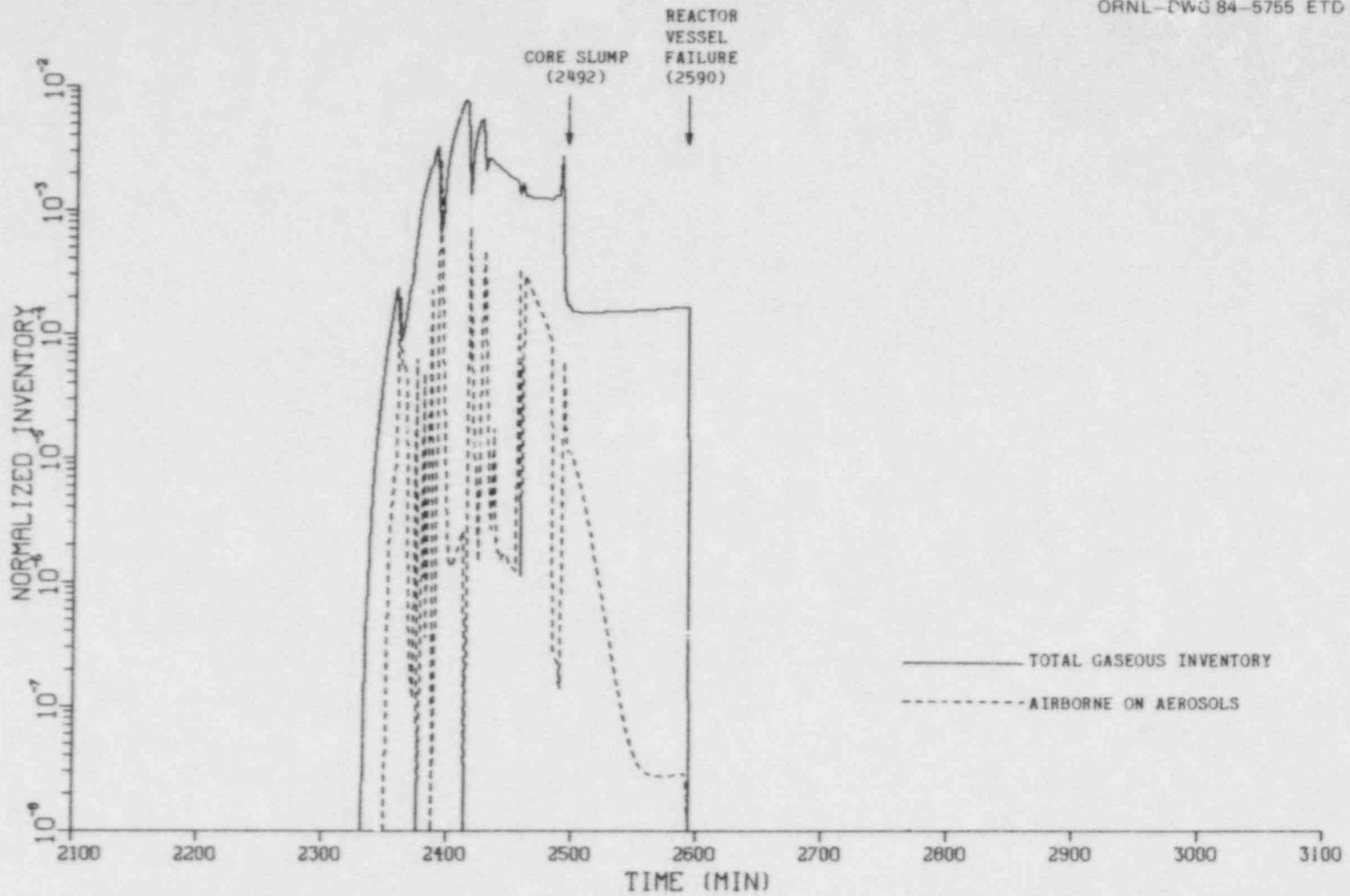
Fig. 5.29. Normalized cesium activity suspended in the reactor vessel.
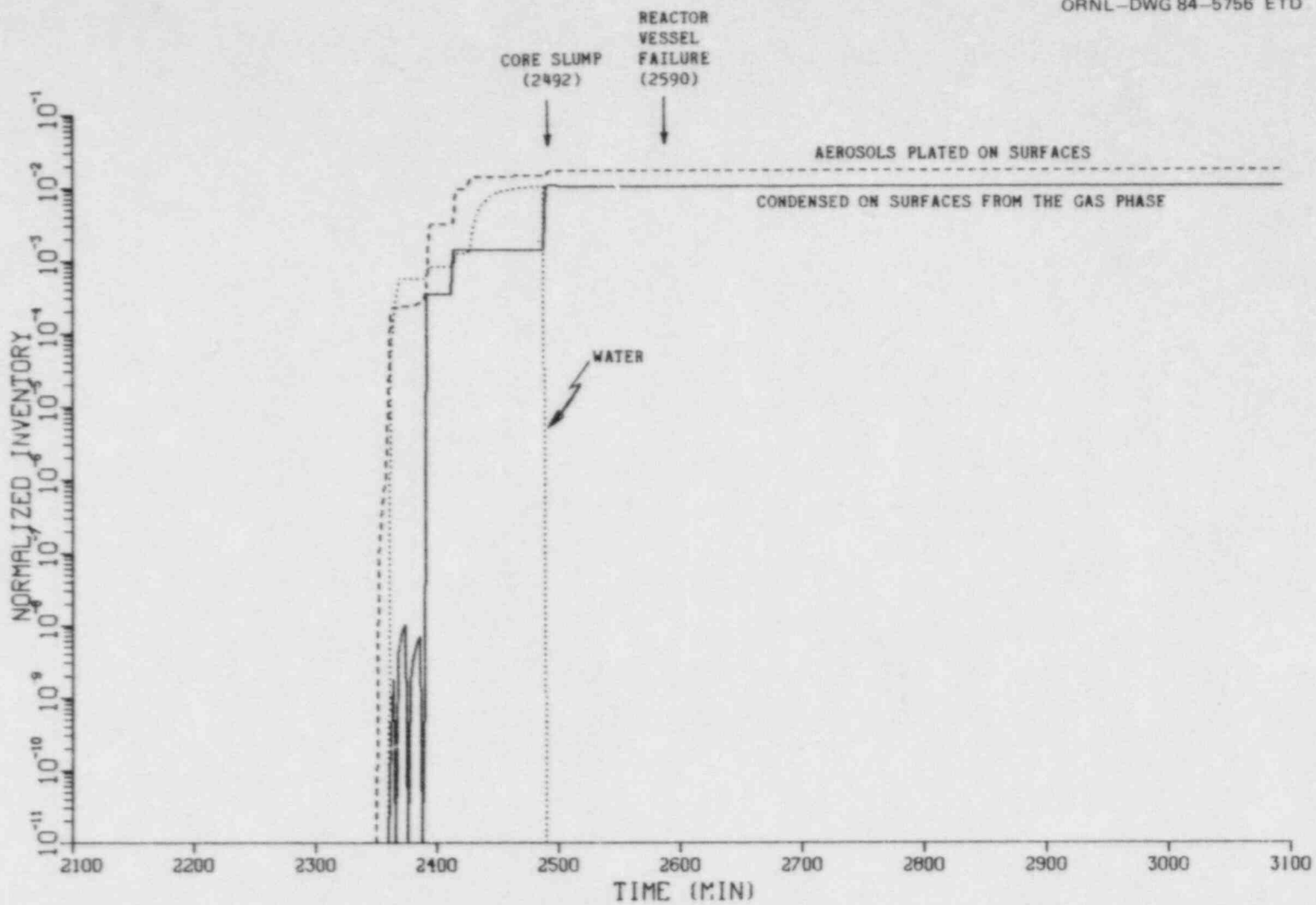
Fig. 5.30. Normalized cesium activity in the reactor vessel water
and plated on interior reactor vessel surfaces.
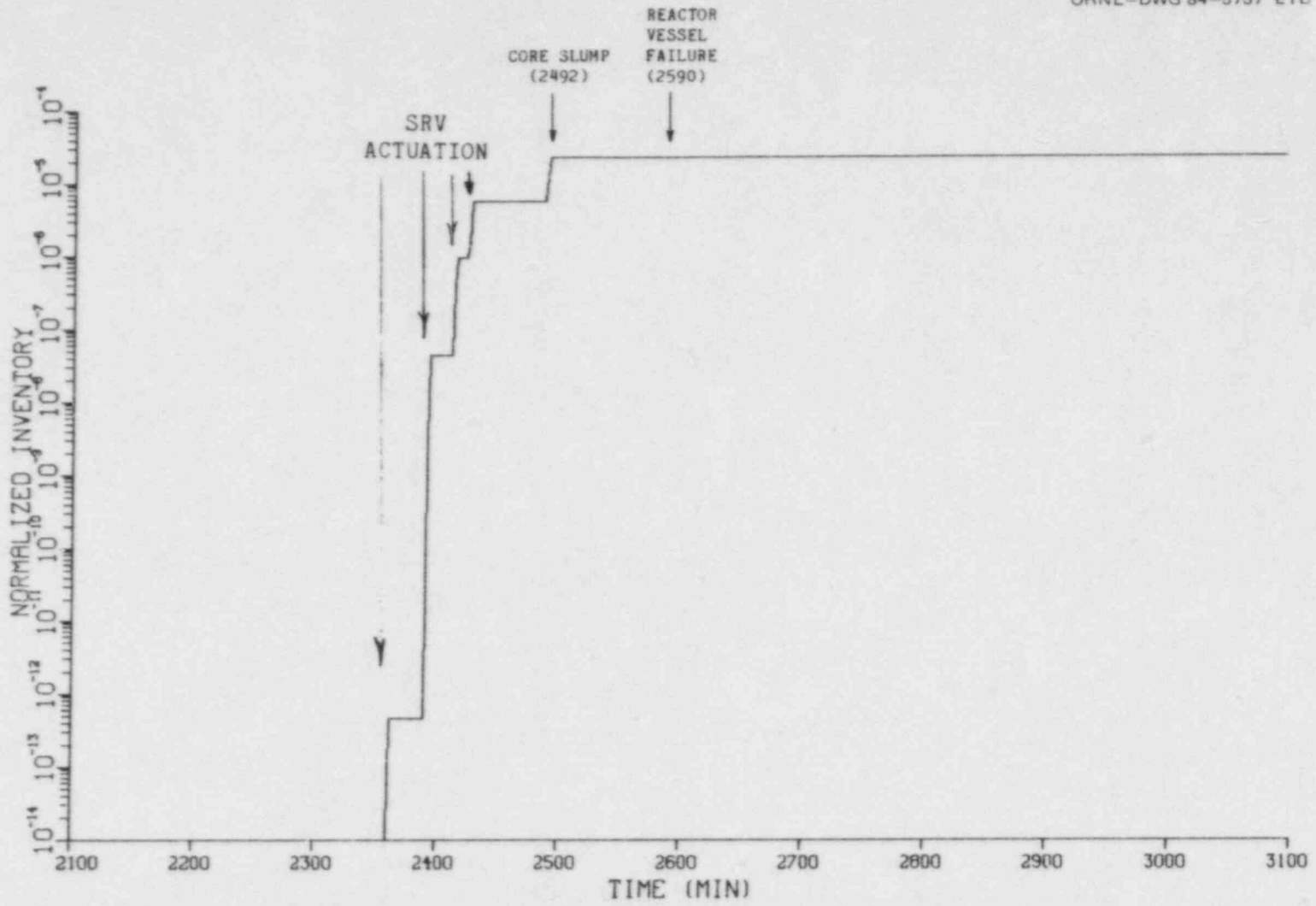
Fig. 5.31. Normalized cesium activity in the pressure suppression pool.
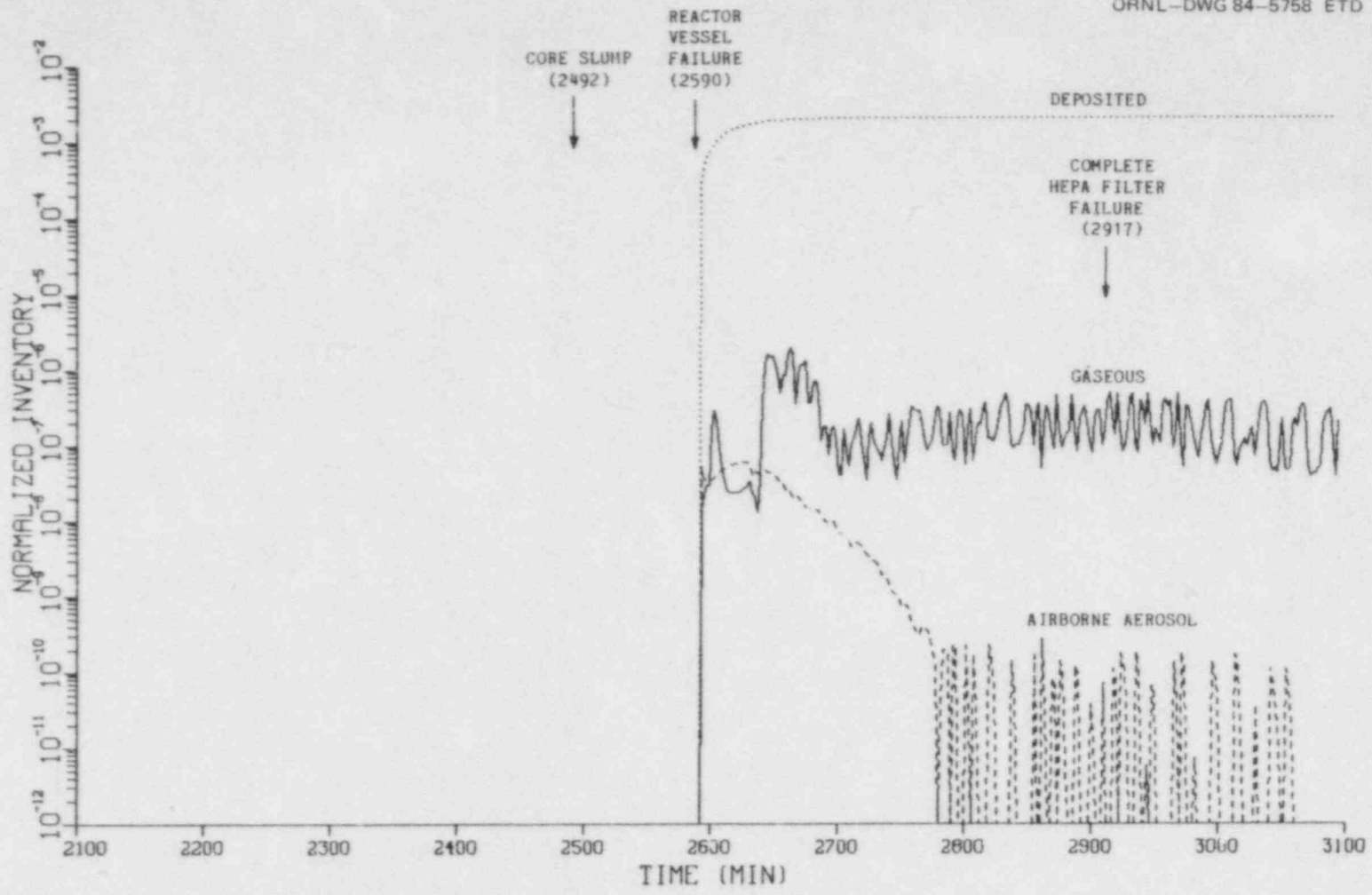
Fig. 5.32. Normalized cesium activity in the drywell.
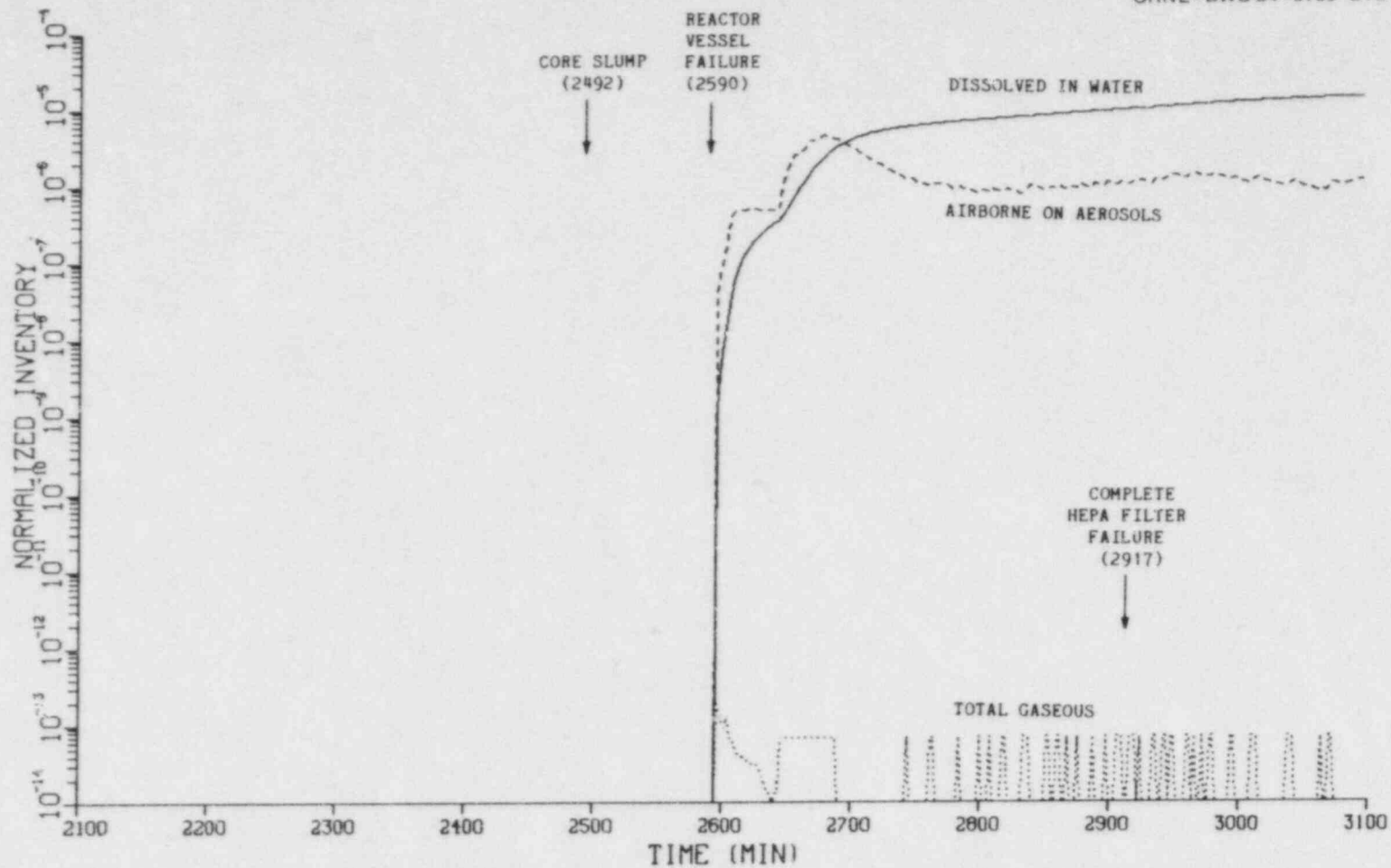
Fig. 5.33. Normalized cesium activity in the reactor building: dissolved in water, and on airborne aerosols.

CORE SLUMP
(2492)

REACTOR
VESSEL
FAILURE
(2590)

COMPLETE
HEPA FILTER
FAILURE
(2917)

NORMALIZED INVENTORY

TIME (MIN)

———————— MAIN CONDENSER SYSTEM

- - - - - - - SGTS HEPA FILTERS

.... CESIUM COLLECTED ON
SGTS CHARCOAL
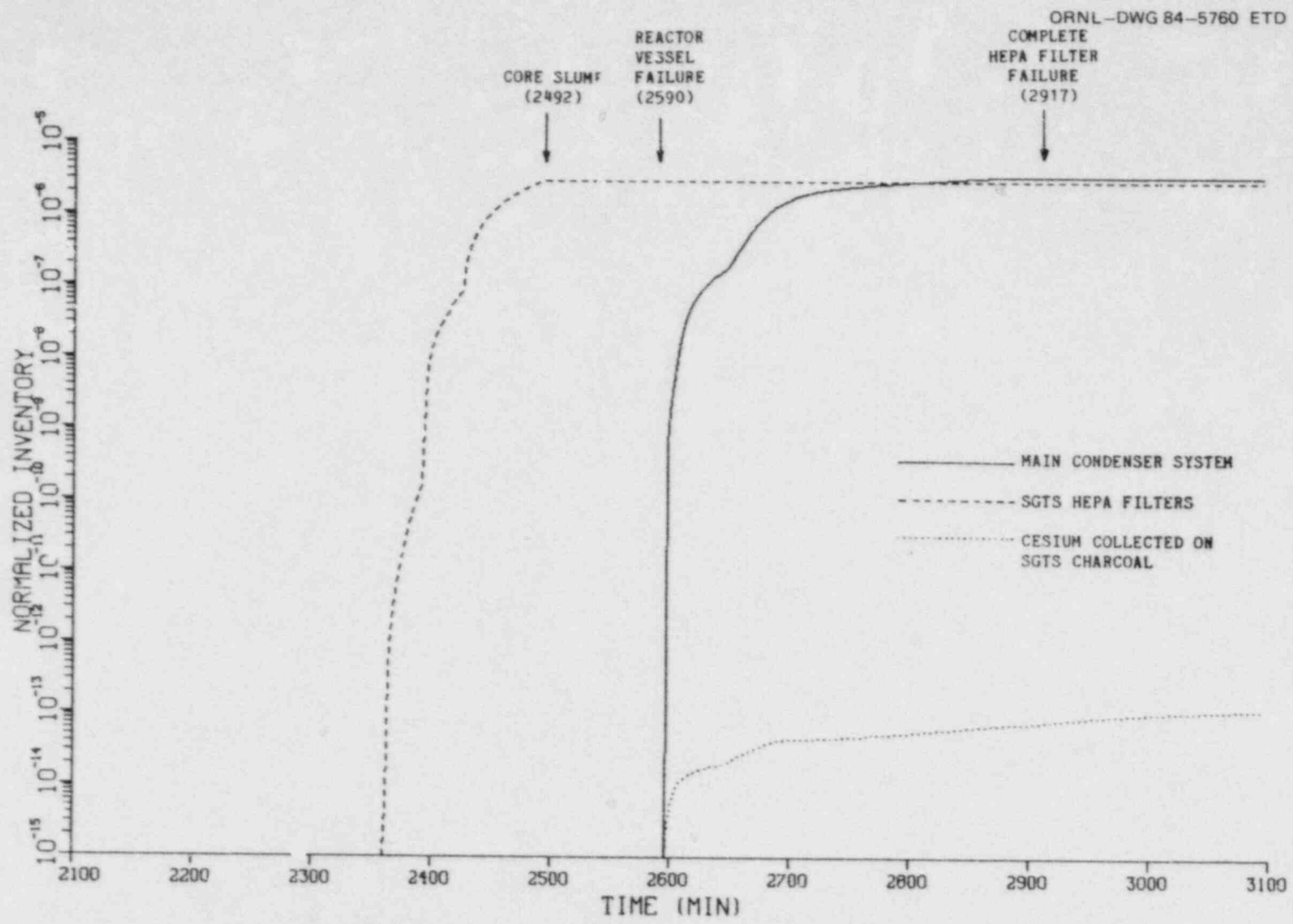
Fig. 5.34. Normalized cesium activity in components of the SGTS
train and in the main condenser system in the turbine building.
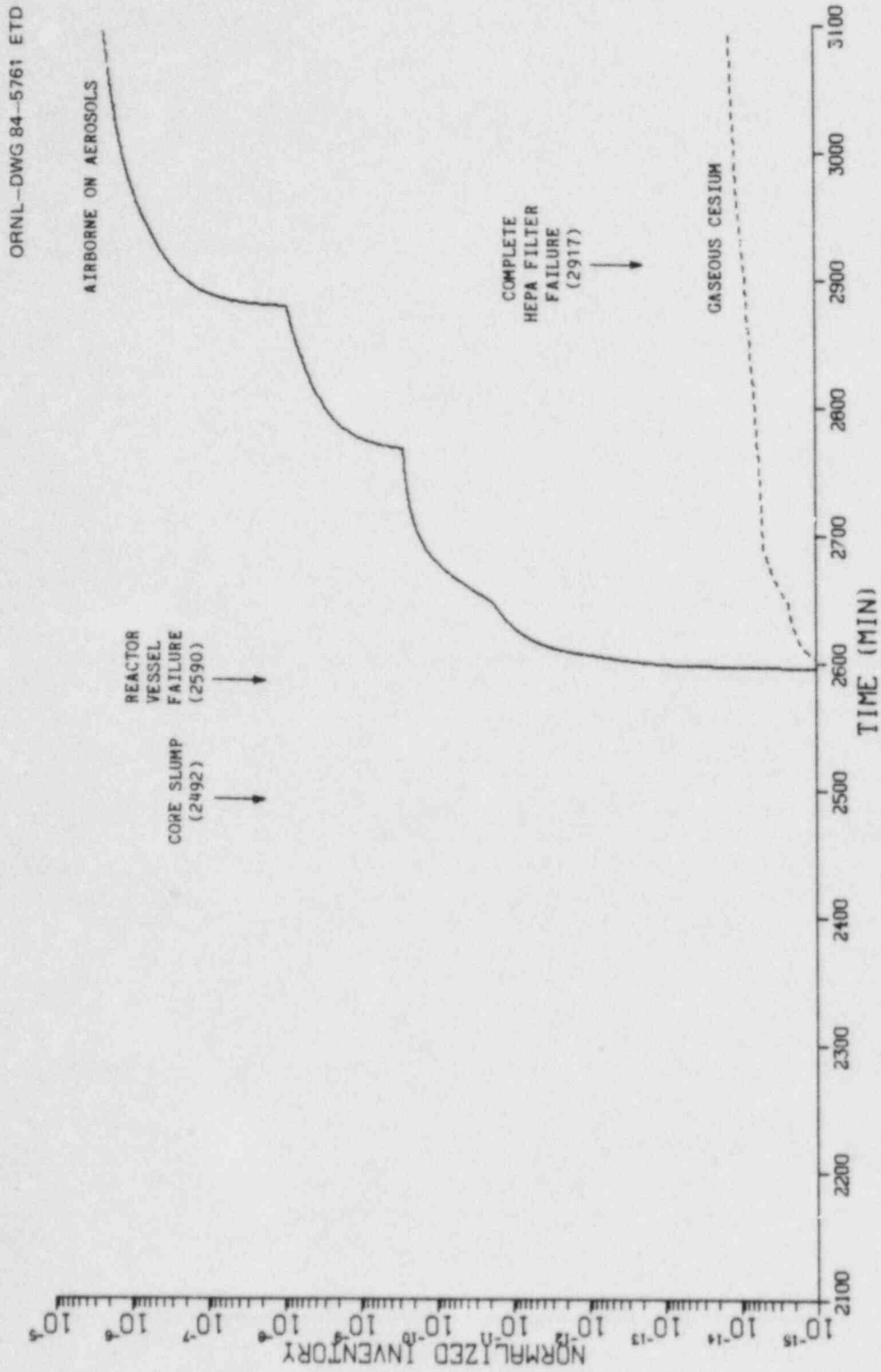
Fig. 5.35. Normalized cesium activity released to the outside at-
mosphere.

6. SUMMARY AND CONCLUSIONS

6.1 Summary of the Work Performed

1. Sequence parameters (temperatures, pressures, flow rates, etc.) were recalculated, again using the ORNL version of the MARCH code, but employing a smaller drywell failure size based on the assumption that overpressure failure of the drywell would create a 2 ft^2 (0.186 m^2) failure zone instead of 10 ft^2 (0.929 m^2) as had been assumed in the companion study. As explained in Sect. 2.1, this is believed to have an insignificant effect on the fission product transport results.

2. Conditions in the reactor building were estimated for the projected drywell leakage rates using the ORNL-developed Browns Ferry secondary containment model. Flows, temperatures and pressures in the reactor building are given in Chapt. 2 and Appendix A.

3. Some fission product transport model assumptions were altered based on new information developed from NRC-sponsored research programs: (a) A revised estimate of iodine volatility over water was adopted based on recent measurements conducted in a radiation field. The new volatility is ten times higher (partition coefficient one-tenth) than originally assumed. (b) The manner in which drywell rubble temperatures and fission product evolution from the drywell rubble are estimated was changed. The newer method employs CORCON/MOD 1 for estimating rubble temperatures and VANESA for estimating evolution from the rubble due to sparging. (c) Similarly, CORCON/MOD-1 and VANESA are used for estimating the rate and amount of aerosol produced from the core/concrete interaction on the drywell floor replacing an older procedure based on the INTER subroutine of MARCH and an unpublished correlation. (d) A modified form of the organic iodide production rate model has been developed.

4. Some newly-recognized features of iodine and cesium chemistry under reactor vessel conditions have been noted which in the future may impact transport assumptions for these materials in the reactor vessel.

5. The transport characteristics in the drywell and reactor building of aerosols produced by the corium-concrete reaction on the drywell floor were estimated using the QUICK code. These results are presented in Chap. 4 and Appendix B.

6. The transport of krypton, xenon, iodine and cesium throughout the reactor system and to the atmosphere was estimated based on (1) a fission product transport model for these elements, (2) postulated SGTS equipment and reactor vessel failure modes, and (3) flow and temperature conditions predicted in the reactor vessel, wetwell, drywell, and reactor building. These results are presented in Chap. 5.

6.2 Summary of Results and Conclusions

1. Krypton transport characteristics are presented in Table 5.6 and Figs. 5.6 through 5.11. As expected from previous studies, there is

little barrier for krypton movement through the reactor system. Steam evolution from the reactor vessel and suppression pool and concrete degradation gases evolved in the drywell effectively flush krypton from the primary and secondary contaiuments. However, significant decay of krypton radioactivity occurs due to the long delay time in this sequence. Of the 4939 PBq present at scram, only ~20 PBq of krypton are projected to enter the atmosphere, principally due to radioactive decay. This amount of krypton activity at time 3100 min represents 82% of the total krypton activity at that time.

2. Xenon transport results, presented in Table 5.7 and Figs. 5.12 through 5.17, parallel those for krypton except for a smaller degree of radioactive decay. In addition, an appreciable degree of Xe radioactivity builds in from decay of iodine precursors. About 5100 PBq of Xe are projected to be released to air by time 3100 min, which represents ~88% of the Xe activity at that time. The remainder resides principally in the fuel elements remaining in place, the reactor building air space and dissolved in water leaked into the main condenser through the shut MSIVs.

3. The computed distributions of iodine at various locations are presented in Table 5.8 in terms of total radioactivity (PBq) and in Figs. 5.18 through 5.27 in terms of relative activity normalized to the initial level (i.e., at reactor scram). We note that a far smaller degree of iodine is predicted to enter the atmosphere than noble gas because of the chemical reactivity of iodine. As shown in Table 5.8, about 0.05 PBq of iodine are predicted to be in the atmosphere at time 3100 min, which represents 7.3×10^{-4}% of the iodine activity existing at that time and 1.8×10^{-4}% of the amount existing at reactor scram.

4. The principal repositories of iodine at time 3100 min are predicted to be plateout on reactor vessel surfaces (88%), retention in unfailed fuel (5.7%), as dissolved material in the reactor building water pool (3.5%), and plateout on drywell surfaces (2.6%).

5. The principal iodine pathway to the atmosphere employing the current modeling assumptions is the following: (a) retention in the fuel during core degradation and passage with fuel rubble onto the drywell floor, (b) sparging release from the core debris on the drywell floor, (c) convective transport through the drywell and reactor building, both as gaseous iodine and as chemisorbed iodine on aerosols, due to the convection and aerosols produced by the core/concrete reaction, and (d) passage through the SGTS filter/absorber system.

6. The pressure suppression pool does not capture a large share of the iodine evolved from fuel because the reactor vessel surfaces are predicted to capture most of the iodine via plateout (of various types) during the time span when the suppression pool is in the direct path, i.e., times prior to reactor vessel failure at time 2590 min. Following time 2590 min, the suppression pool is bypassed.

7. According to current models, the principal form of iodine captured by reactor vessel surfaces is CsI condensed on aerosol particles that subsequently deposit, accounting for about 60% of the total deposition.

8. Even though about 60% of the iodine deposited in the reactor vessel is due to plateout of aerosols, Fig. 5.5 shows that the assumed

degree of aerosol trapping in the reactor vessel does not greatly affect the calculated iodine release. This is because sparging release from core rubble on the drywell floor (at time > 2590 min) overwhelms any release range created by varying assumptions on aerosol trapping in the reactor vessel.

9. Iodine transport behavior in the reactor vessel and pressure suppression pool could be significantly altered by possible revisions in assumed chemical forms currently being considered (see Sect. 3.2.4). It is possible that reactions with boron compounds evolving from overheated control rods (and other materials) could destabilize CsI. The net result would likely be a smaller degree of iodine deposition on aerosols, a smaller degree of capture in the reactor vessel and a correspondingly larger degree of capture in the suppression pool prior to vessel failure.

10. Only a minute fraction of the iodine released to air occurs as organic iodide (0.001%) according to current net production rate estimates. This is admittedly highly preliminary and is not in accord with estimates presented by German analysts for an approximately equivalent event sequence.

11. Estimated cesium inventories (in PBq) at various times and several key locations are presented in Table 5.9. Figures 5.28 through 5.35 illustrate the time variation of the cesium inventory, normalized to the initial activity level, for a number of locations. As shown in Table 5.9, an estimated 0.04 PBq of cesium activity is projected to enter the atmosphere by the end of the sequence; this represents about $1.9 \times 10^{-4}\%$ of the initial core inventory. Virtually all of this release is predicted to occur after time 2917 min, the estimated time for HEPA filter failure in the SGTS.

12. The principal cesium pathway differs somewhat from that of iodine due to its much lower volatility in the drywell and reactor building. Cesium transport in these areas occurs almost exclusively as material condensed on aerosols whereas iodine transport is projected to occur both as a gas and associated with aerosols. Hence, the critical factor in cesium release to air is the time for HEPA filter failure; virtually all of the cesium release is predicted to occur following this event. Summarizing the principal cesium pathway: (a) retention in the fuel and passage onto the drywell floor with the core rubble, (b) sparging release from the core debris on the drywell floor, (c) transport through the drywell and reactor building associated with aerosol particles generated by the core/concrete reaction, and (d) passage through the SGTS to the atmosphere following HEPA filter failure.

13. The principal cesium repositories at the end of the sequence are in order of importance: (a) plated material on the reactor vessel upper surfaces, both as condensed CsOH and cesium associated with deposited aerosols (2.7%); (b) in the portion of the original fuel elements that is predicted to remain intact (0.32%); and (c) plated on drywell walls (0.20%). Very little cesium appears in the suppression pool $(2.2 \times 10^{-3}\%)$ due to the effective trapping on reactor vessel surfaces of condensible materials. About half this amount $(1.2 \times 10^{-3}\%)$ is predicted to reside in the reactor building water pool collecting in the basement at the end of the sequence due to aerosol settling in the building and washdown by the fire-protection system spray water. (The

above percentages are activity levels referred to the core activity
level at scram.)

14. Expressing cesium releases as percentages normalized to the
activity of nuclides with half-lives greater than 30 min at scram shows
high degrees of radioactive decay mainly because most of the original
cesium activity (96.7%) is due to Cs138, which has a 32.2 min half-
life. (Nuclides with half-lives less than 30 min are assumed to be
completely decayed prior to cladding failure.)

6.3 Principal Uncertainties

Though no formal sensitivity analysis was performed, the results
indicate fairly clearly the areas of greatest uncertainty, given below
in approximate order of importance:

(1) The SGTS failure model, including the HEPA filter loading
causing failure, the type of HEPA filter failure and the functioning of
the charcoal beds under the projected environment at the bed inlet. The
SGTS failure model assumes prime importance because the SGTS is the last
barrier to the atmosphere in this accident sequence.

(2) Iodine volatility over water. The degree of iodine capture in
the thoroughly-wetted reactor building depends directly on the effective
solubility of iodine in water under those conditions. The reactor
building water pool is the second-from-last barrier to the atmosphere
for iodine.

(3) Capture in the reactor vessel by aerosol plateout and con-
densation. The current modeling assumptions project the largest reposi-
tory for cesium and iodine at the end of the event sequence to be plated
material on the reactor vessel walls, principally associated with plated
aerosols (60%) and as condensed CsOH and CsI. All factors affecting
this calculated result bear heavily on the computed distributions of
iodine and cesium throughout the reactor systems and consequently on the
predicted release to air. The major factors that affect this computed
result are: (a) the presumed chemical form of cesium and iodine gas in
the reactor vessel on which the driving force for condensation on aero-
sols and walls directly depends; (b) the surface temperatures, particu-
larly late in the sequence when revaporized deposits can pass directly
into the drywell space following reactor vessel failure, and (c) the na-
ture and rate of interaction between fission product vapor and aerosols.

(4) Rate of "sparging" release. Because cesium and iodine evolved
from the core rubble on the drywell floor bypass the suppression pool,
this transport step assumes a high significance. The rate of sparging
release depends on both the projected rubble temperatures, currently
predicted by CORCON MOD 1, and the manner of equilibration of fission
product species with the sparge gas flow as predicted by VANESA. At
this time it seems that currently estimated rubble temperatures (of the
oxide phase) calculated by CORCON MOD 1 are much too high, causing a
higher than realistic release rate from the rubble.

(5) The supporting thermal-hydraulic calculations. A major diffi-
culty lies in the use of the MARCH code to develop the thermal-hydraulic
conditions in the primary system and the drywell during the accident

sequence. For example, the core meltdown and slump into the reactor vessel bottom head as modeled in MARCH does not reflect the actual BWR under-core structure of control rod guide tubes and is therefore not realistic for such application. Of equal concern is the inadequate modeling of the heatup of the BWR steam separators and driers, whose temperature during the accident sequence is a major factor in fission product transport. For these reasons, the degraded core and containment response analysis must be considered to be no more than a reasonable approximation to the events and event timing that would occur after core uncovery in this accident sequence. Since the fission product transport analysis presented in this volume is derived from the accident sequence analysis, this also can be no more than a reasonable approximation.

6.4 Significance of the Study

The elements iodine and cesium have a complex chemistry, and their passage through the containment structures is correspondingly complicated. They evolve from fuel as a gas, partially condense upon aerosol particles or reactor structures, only to be re-evolved if the prevailing temperatures and chemical environments so favor. They can react chemically to form bonds with other elements and then, if conditions permit, break those bonds to form compounds with quite different transport properties. These effects must be considered in each control volume of the calculation. Thus the determination of the transport of cesium and iodine is not straightforward, and the results presented in this report for the transport of these materials cannot be considered to be more than reasonable estimates.

The authors of this report do not believe that the principal value of this work lies in the calculated numbers for fission product transport to the containment boundaries. Rather, the report is intended to identify the weaknesses in the state-of-the-art methodology and to provide user feedback to the code developers and to show where future experimental work is needed. At ORNL, the Chemical Technology Division SASA team members who participate in these fission product transport calculations are all part time on this effort; the remainder of their time is spent on applied research related to advancement of the understanding of fission product transport. Thus their association with the SASA program calculations provides an avenue for transmitting the most recently developed research information to the methodology for estimating LWR accident consequences.

Appendix A

REACTOR BUILDING AND REFUELING BAY CALCULATIONS

The purpose of this appendix is to describe the results of calculations performed with the ORNL-developed Browns Ferry secondary containment model for the Loss of Decay Heat Removal accident sequence. The computer code employed for these calculations is essentially the same as that described in Appendix A of Ref. A.1. Modifications were made to improve the model for condensation and evaporation and to provide for calculation of the temperature of the pool that forms in the reactor building basement as a result of the actuation of the fire protection system sprays.

A.1 Introduction

Calculations have been performed for the Loss of Decay Heat Removal accident sequence, both for the case with reactor building sprays, and for the case without sprays. In an actual accident sequence, the elevated temperatures in the reactor building after drywell failure would cause actuation of the sprays and this case is described in Sect. A.2.

Combustible gases are released during the accident, both from the metal-water reactions in-vessel and ex-vessel, and by the corium-concrete interaction on the drywell floor. Combustion is not of concern within the primary containment because it has an inerted atmosphere. On the other hand, the concentration of oxygen in the secondary containment during the course of the accident varies as a function of the relative amounts of infiltration and exfiltration. The resulting combustible concentrations in the reactor building and refueling floor are discussed in Sect. A.3.

The accident mitigating effect of the reactor building fire protection system sprays can best be demonstrated by contrast with the case without sprays; the latter is described in Sect. A.4.

A.2 Results for the Loss of Decay Heat Removal
Accident Sequence

The steam and gas flows included in the secondary containment model during the period after the refueling bay blowout panels have lifted are shown in Fig. A.1. Flow through the refueling bay blowout panels is calculated after they have lifted. The reactor building basement pool shown in Fig. A.1 is formed by the accumulation of the water from the fire protecting system sprays. The design and operation of the reactor building fire protection system is described in Appendix B of Ref. A.1. There are no sprays on the refueling floor.

The inleakage to the reactor building from the 2 ft^2 (0.186 m^2) hole in the drywell wall is provided as input to the reactor building model. The rate of mass inleakage of steam is taken directly from the

MARCH code output and is shown in Fig. A.2. Most of the steam entering the reactor building is evolved from flashing of the water in the pressure suppression pool during the depressurization of the primary containment. Additional steam sources are created in the drywell when a large quantity of water is vaporized in the reactor vessel lower plenum upon "core slump", and later upon blowdown of the reactor vessel into the drywell when the vessel bottom head fails. After this, the corium-concrete reaction begins, and concrete decomposition provides a steady source of steam to the drywell which is continuously released to the reactor building.

The rate of mass leakage of hot dry gas from the drywell into the reactor building is shown in Fig. A.3. The large release at the time of drywell failure is nitrogen plus the small amount of oxygen in the inerted primary containment; these gases are flushed from the drywell by the large steam flow during the initial phase of the blowdown. There is a continuous release of hydrogen from the drywell after the metal-water reactions begin within the reactor vessel at about time 2250 min. This leakage is too small to be discernible, but the sudden flushing of all hydrogen from the reactor vessel at the time of "core slump" results in a pulse of gas flow into the reactor building at about time 2492 min.

The corium falls onto the dry concrete floor of the drywell upon failure of the reactor vessel bottom head at time 2590 min, and the corium-concrete reaction begins shortly thereafter. Steam released from the concrete permits oxidation of the previously unreacted zirconium in the corium, releasing hydrogen. Carbon monoxide and dioxide are released by the direct concrete heating. The result is a continuous release of hot dry gases from the drywell into the reactor building during the later phase of the accident sequence as shown on Fig. A.3.*

The total inleakage to the reactor building is shown in Fig. A.4 and the mixed-mean MARCH-computed temperature at the (drywell) source is shown in Fig. A.5. The temperature increases significantly after reactor vessel bottom head failure due to oxidation of the previously unreacted zirconium in the corium mass on the drywell floor.

The reactor building and refueling bay response during the period from 2000 to 3100 min after inception of the Loss of Decay Heat Removal accident sequence has been calculated by the secondary containment model developed at ORNL for use with the inleakage flows and temperatures derived from the output of the MARCH code. Core uncovery, cladding failure, the onset of fuel melting, "core slump," reactor vessel bottom head failure, and the subsequent continuous corium-concrete reaction all occur during this period. The ORNL model, although still crude, permits a much more refined analysis than would be possible if the reactor building and refueling bay were simulated by use of the existing containment models in the MARCH code.

---

*It should be noted that CORCON MOD 1 predicted gas generation rates for H_2, CO, and CO_2 were used in lieu of MARCH subroutine INTER results for this analysis. The rates predicted by CORCON are believed to be more accurate and are much lower.

The calculated response of the reactor building is shown in Figs. A.6 through A.12. As shown on Fig. A.6, the pressure variations are small. The standby gas treatment system (SBGTS) maintains a slight negative pressure in the building during most of the period after drywell failure, but positive pressure spikes occur at the time of "core slump" and at failure of the reactor vessel bottom head.

The reactor building ambient temperature is shown in Fig. A.7. The temperature increases rapidly at the time of drywell failure because of the entry of steam and hot gases from the drywell at a temperature of about 425°F (490 K). The reactor building sprinkler system is automatically actuated when the building temperature reaches 225°F (380 K); this causes a sudden decrease in building temperature just after drywell failure as shown in Fig. A.7. The reactor building temperature continues to decrease as the leakage flow from the drywell falls off (see Fig. A.4), and the sprinklers continue to operate. Increases in building temperature occur in conjunction with the temporary increases in inleakage from the drywell occasioned by "core slump" and reactor vessel bottom head failure.

The reactor building fire protection system directly cools the building atmosphere and simultaneously increases its heat capacity by raising the water vapor content to saturation and by introducing suspended water droplets into the atmosphere. The sprays also promote turbulent mixing so that all surfaces in the vicinity would be completely wetted. The water falling onto the intermediate floors of the building would flow through drains and down walls and stairways to collect in a pool in the reactor building basement.

The mass flow to the SBGTS is shown in Fig. A.8. As modeled, the volumetric flow from the reactor building to the SBGTS is constant at 12,500 ft^3/min (5.90 m^3/s)* so the variations shown in Fig. A.8 are caused by density changes in the reactor building atmosphere. The temperature at the inlet to the SBGTS filter trains is shown in Fig. 2.21.

The volumetric infiltration flow to the reactor building is shown in Fig. A.9. This is the flow of air through leakage pathways in the building walls and through the building vacuum breakers. Infiltration occurs during most of the period after drywell failure because of the negative pressure maintained in the reactor building by the SBGTS. As shown in Fig. A.6, the reactor building pressure becomes greater than atmospheric for brief periods just after core slump and just after failure of the reactor vessel bottom head; infiltration ceases during these periods.

Whenever the pressure in the reactor building exceeds atmospheric, there is an exfiltration flow through the leakage pathways in the building walls directly to the outside environment. The volumetric rate of exfiltration is shown in Fig. A.10. No exfiltration occurs after time 2600 min because the reactor building pressure is subatmospheric throughout this period.

The relative humidity of the reactor building atmosphere is shown in Fig. A.11. The relative humidity decreases rapidly immediately after

---

*An equal amount flows to the SBGTS from the refueling floor.

drywell failure as the reactor building atmosphere is heated. Shortly thereafter, actuation of the reactor building sprays lowers the ambient temperature and increases the relative humidity to 100%. Since the sprays continue to function throughout the remainder of the accident sequence, the building relative humidity remains at 100%. (It should be noted that the calculational procedure permits relative humidities slightly in excess of 100% as seen in Fig. A.11. This slight departure from realism is accepted to avoid the use of extremely small timesteps in the calculations.)

As discussed in Sect. 2.6, the blowout panels between the Unit 1 reactor building and refueling bay are predicted to relieve almost immediately after drywell failure. This provides a large flow area between these two control volumes; the calculated inter-volume flows are shown in Fig. A.12. Except for the period immediately after drywell failure, and for brief periods immediately after core slump, and after failure of the reactor vessel bottom head, the flow is from the refueling bay to the drywell. Since fission product release from the fuel does not begin until well after drywell failure (about time 2330 min), few fission products will be transported to the refueling bay during this accident sequence.

The calculated response of the refueling bay to the flows to or from the reactor building through the blowout panels is shown on Figs. A.13 through A.18. As indicated on Fig. A.13, the refueling bay pressure is very close to atmospheric during the accident sequence. Except for brief periods at drywell failure, core slump, and reactor vessel lower head failure, the refueling bay pressure remains slightly below atmospheric.

The refueling bay atmosphere temperature is shown in Fig. A.14. Since the refueling bay responds to the inflow from the reactor building, it is reasonable that the refueling bay temperature trends follow those of the reactor building shown in Fig. A.7. However, the refueling bay free volume is about 1.76 times that of the Unit 1 reactor building and its temperature remains significantly lower throughout the accident sequence.

The mass flow from the refueling bay to the SBGTS is shown in Fig. A.15. As in the case of the reactor building, the volumetric flow from the refueling bay to the SBGTS is constant at 12,500 ft^2/min (5.90 m^3/s).

The infiltration of air to the refueling bay is shown in Fig. A.16. Infiltration occurs whenever the pressure in the refueling bay is below atmospheric so that outside air enters through leakage pathways in the superstructure, through the refueling bay vacuum breakers, or through the blowout panels (if previously opened). Exfiltration, which occurs during the brief periods when the refueling bay pressure is above atmospheric, is shown in Fig. A.17.

A large amount of water vapor is carried into the relatively cool refueling bay with the initial flow from the reactor building at the time of drywell failure. Consequently, the relative humidity in the refueling bay is predicted to be 100% for about four hours following drywell failure as shown in Fig. A.18. Subsequently, the relative humidity is reduced by the continued infiltration of cool, dry air from the outside.

A.3 Combustible Gas Concentrations in the Secondary Containment Atmosphere

Combustible gases would be present in the drywell atmosphere under the conditions of a Severe Accident. These include hydrogen gas formed by metal-water reactions both inside the reactor vessel and subsequently within the corium mass on the drywell floor and carbon monoxide, formed by the corium-concrete reaction. The combustible gases within the drywell would be released into the reactor building after drywell failure, and it is necessary to consider whether or not the conditions required for deflagration would be reached within the secondary containment at any time during the accident sequence.*

The mole fractions of steam, carbon dioxide, carbon monoxide, hydrogen, nitrogen, and oxygen in the reactor building and refueling bay are computed throughout the accident sequence by the secondary containment model. The model assumes perfect mixing of the gases which is a reasonable assumption given the turbulence created by the drywell blowdown and the action of the fire protection system sprays.

Based on information supplied by F. E. Haskin of Sandia National Laboratories (Ref. A.2), deflagration would be expected to occur in the secondary containment atmosphere if the following conditions are met:
1. The sum of the hydrogen mole fraction and 60% of the carbon monoxide mole fraction exceeds 0.090.
2. The oxygen mole fraction is greater than 0.05.
3. The sum of the mole fractions of the inerting gases steam and carbon dioxide is not greater than 0.55.

The results of the secondary containment model calculations indicate that these conditions are never met. The closest approach occurs in the reactor building during the 5 min period from 2502 to 2507 min when the combustible gas mole fraction ($H_2 + 0.60$ CO) has reached 0.088, the oxygen mole fraction is 0.16, and the inerting gas mole fraction is also 0.16. After this time, the combustible gas mole fraction falls off rapidly, being only 0.003 at the end of the calculation. Even if deflagration were to occur in the reactor building, its effects would be minimized by action of the continuously operating sprays.

As discussed in Sect. A.2, flow from the reactor building into the refueling bay occurs only during a few very brief periods in the Loss of Decay Heat Removal accident sequence. The predicted combustible gas mole fractions in the refueling bay never exceed 0.004; accordingly, deflagration would not occur there.

A.4 Secondary Containment Response Without Sprays

As discussed in Sect. A.2, the automatic actuation of the reactor building fire protection sprinkler system plays a major role in determining the reactor building response to the inleakage after drywell failure in the Loss of Decay Heat Removal accident sequence. For this

---

*It is known that this would not occur in the primary containment, which is inerted.

study, it has been assumed that the sprinkler system is actuated when the average building temperature reaches 225°F (380 K), producing a continuous spray of 500 gpm (0.032 m^3/s) of water at 100°F (311 K) into the reactor building atmosphere. This occurs when the reactor building temperature increases immediately after drywell failure.

The reactor building response without the sprinkler system sprays will be briefly discussed in this section. The reactor building temperature is shown in Fig. A.19. As can be seen by comparison with Fig. A.7, the temperatures within the reactor building are significantly higher for the case without sprays. With the sprays, the temperature decreases immediately and remains well below 200°F (366 K) for the rest of the accident sequence. Without the sprays, the temperature reaches a maximum of 235°F (386 K), and then remains in the vicinity of 200°F (366 K) for about five hours.

The reactor building pressure response without sprays is shown in Fig. A.20. Comparison with Fig. A.6 shows that the reactor building pressure is higher for the case without sprays, as would be expected. The higher reactor building pressure results in more exfiltration through the building walls and more flow into the refueling bay through the blowout panels. Thus, more fission products would be expected in the refueling bay during the latter part of the accident sequence for the case without sprays.

The combustible gas concentrations in the secondary containment were calculated for the case without sprays to determine the potential for deflagration. Deflagration is not predicted to occur in either the reactor building, or the refueling bay. The closest approach occurs during a two-minute period (time 2500 to 2502 min) in the reactor building when the combustible gas mole fraction (H_2 + 0.60 CO) is 0.086, the oxygen mole fraction is 0.10, and the inert gas (H_2O + CO_2) mole fraction is 0.41. The combustible gas mole fraction subsequently decreases rapidly. The highest combustible gas mole fraction reached in the refueling bay is 0.012, at time 2515 min.

References for Appendix A

A.1. R. P. Wichner, et al., *SBLOCA Outside Containment at Browns Ferry Unit One, Volume 2. Iodine, Cesium, and Noble Gas Distribution and Release*, NUREG/CR-2672, Vol. 2, ORNL/TM-8119/V2 (September 1983).

A.2. Private communication, F. E. Haskin letter of September 14, 1982 to S. A. Hodge.
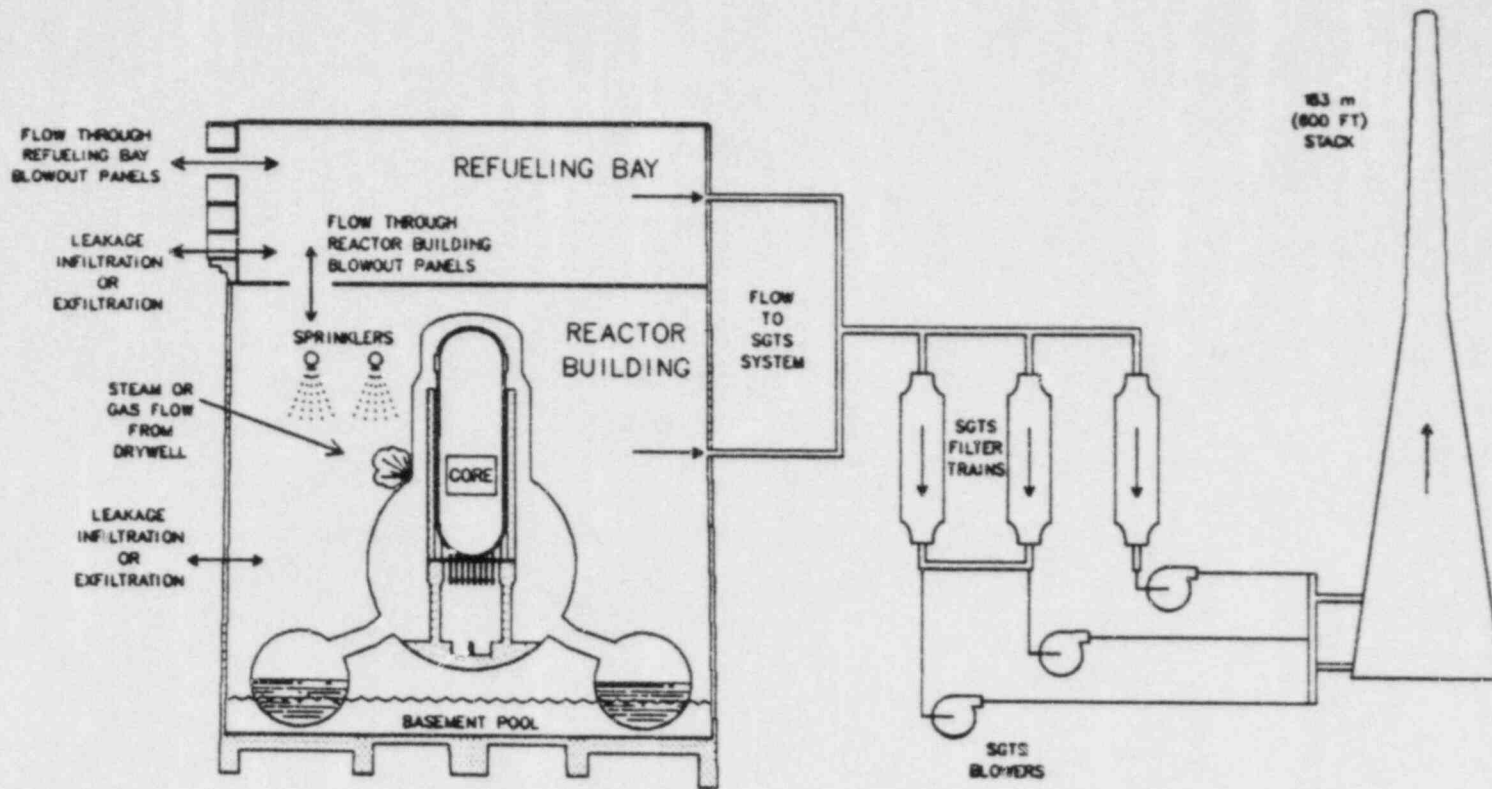
Fig. A.1. Flows included in the reactor building model after rupture of the refueling bay blowout panels.

139
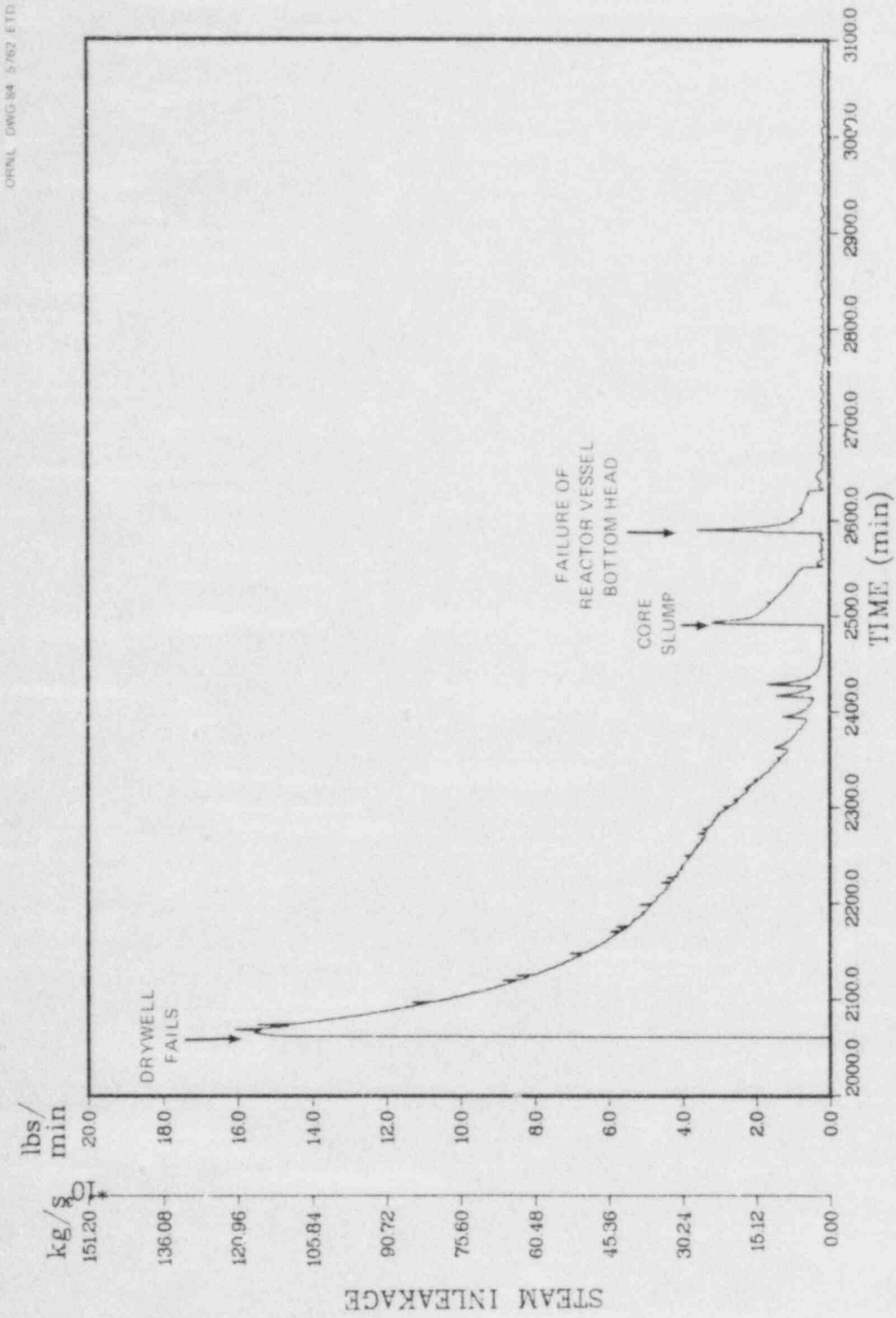
Fig. A.2. Leakage of steam from the drywell into the reactor building.
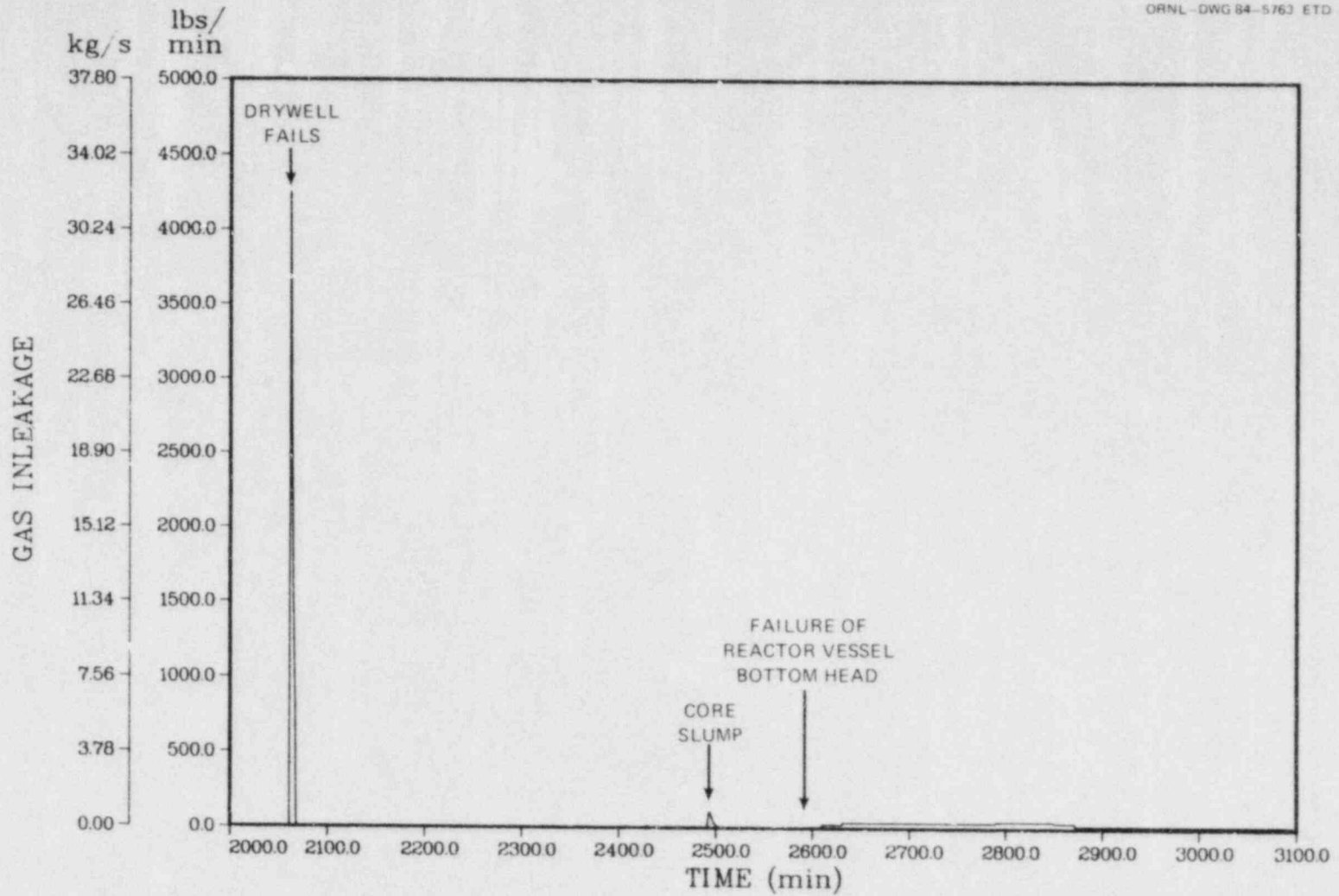
Fig. A.3. Leakage of hot dry gas from the drywell into the reactor building.
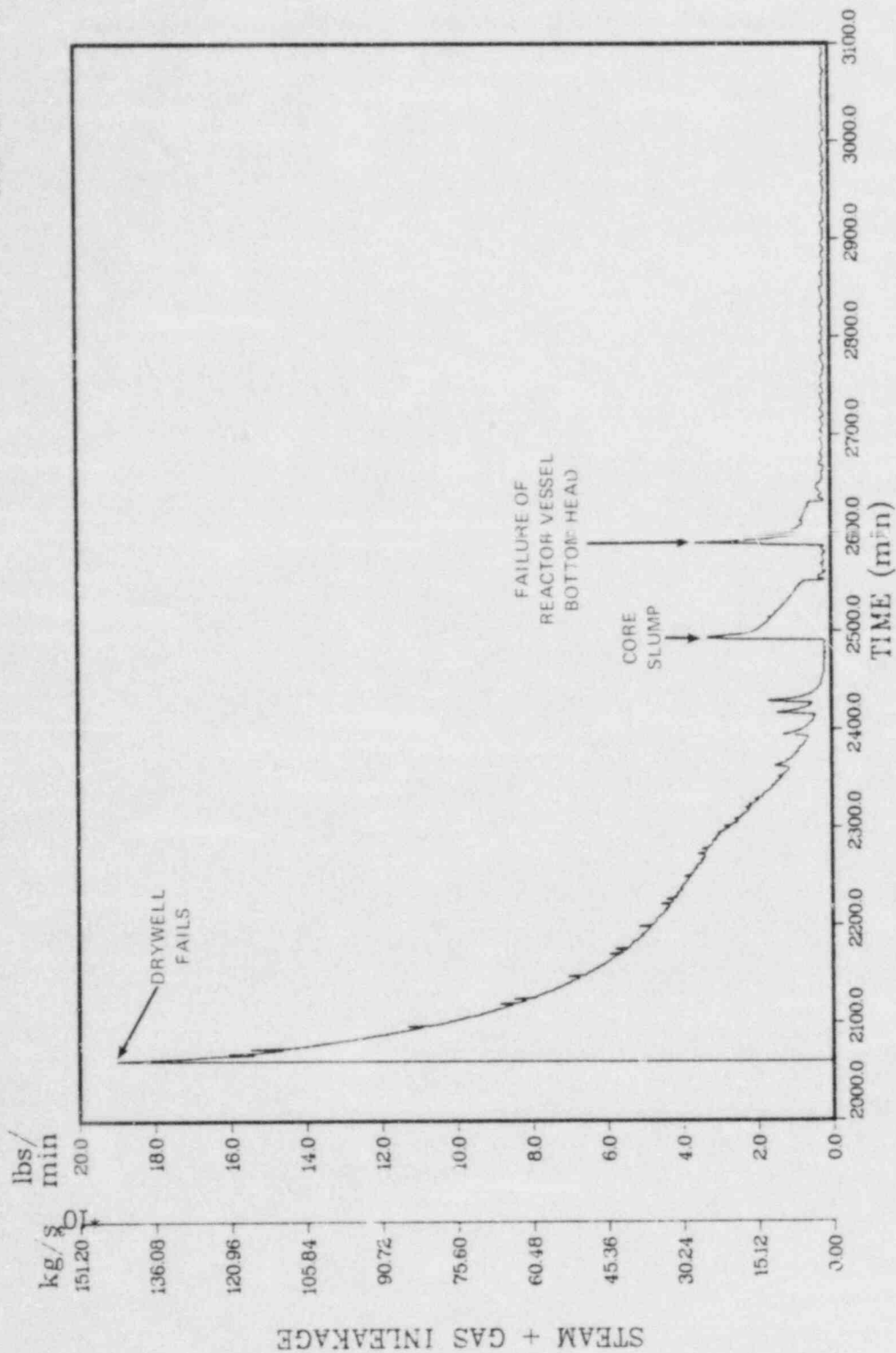
Fig. A.4. Total leakage from the drywell into the reactor build-
ing.
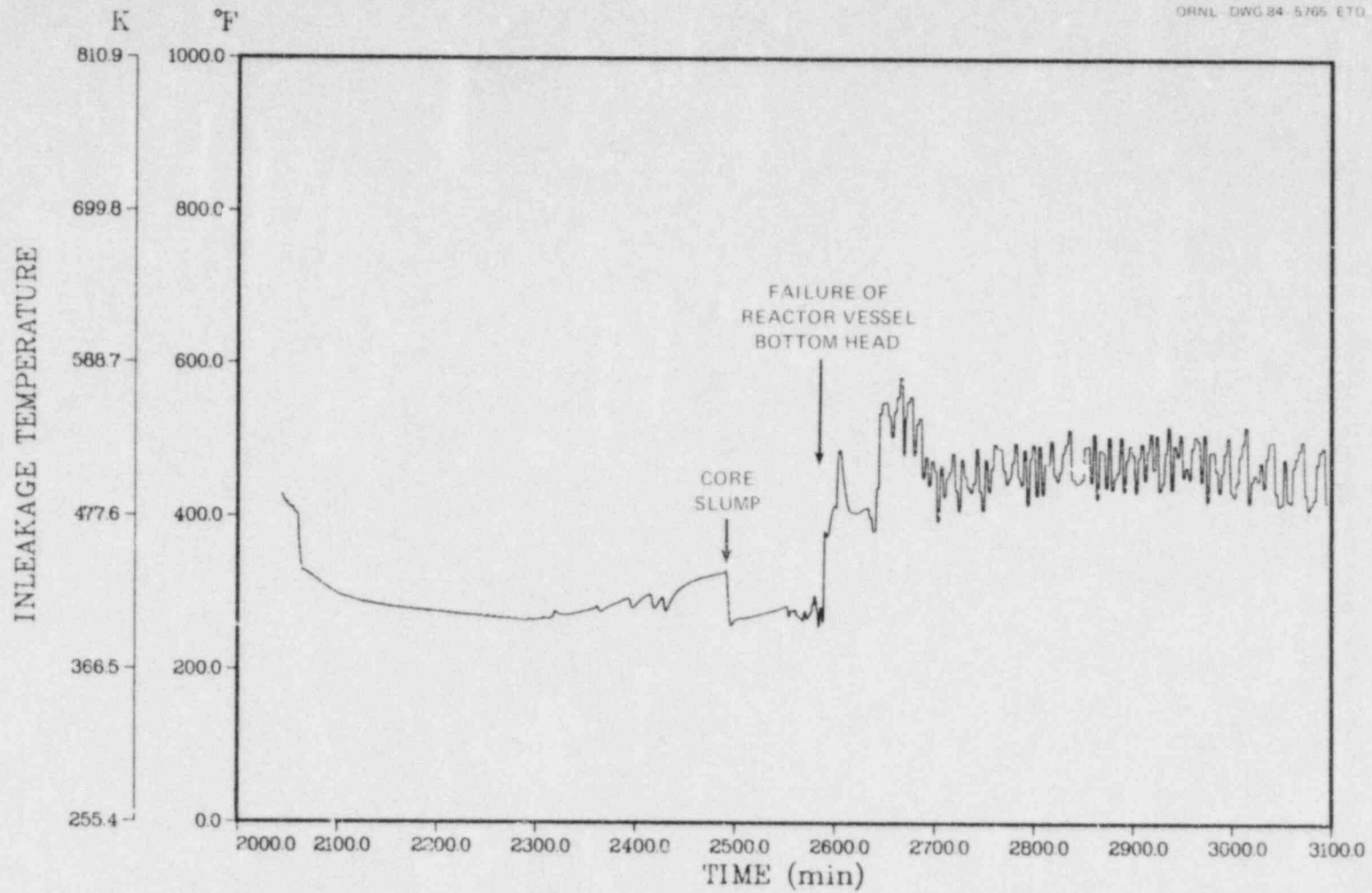
Fig. A.5. Mixed-mean temperature of drywell atmosphere.
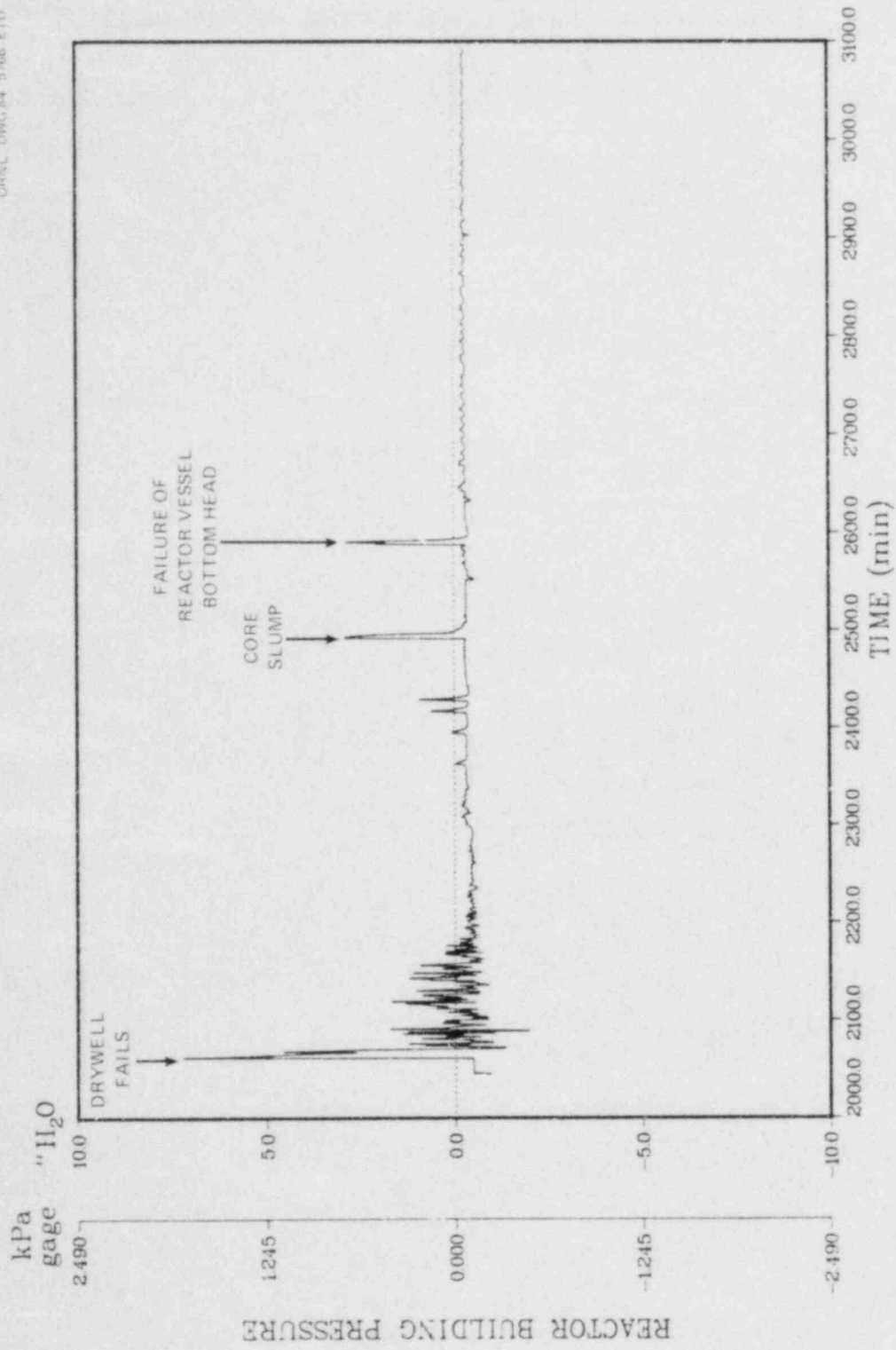
Fig. A.6. Reactor building pressure.
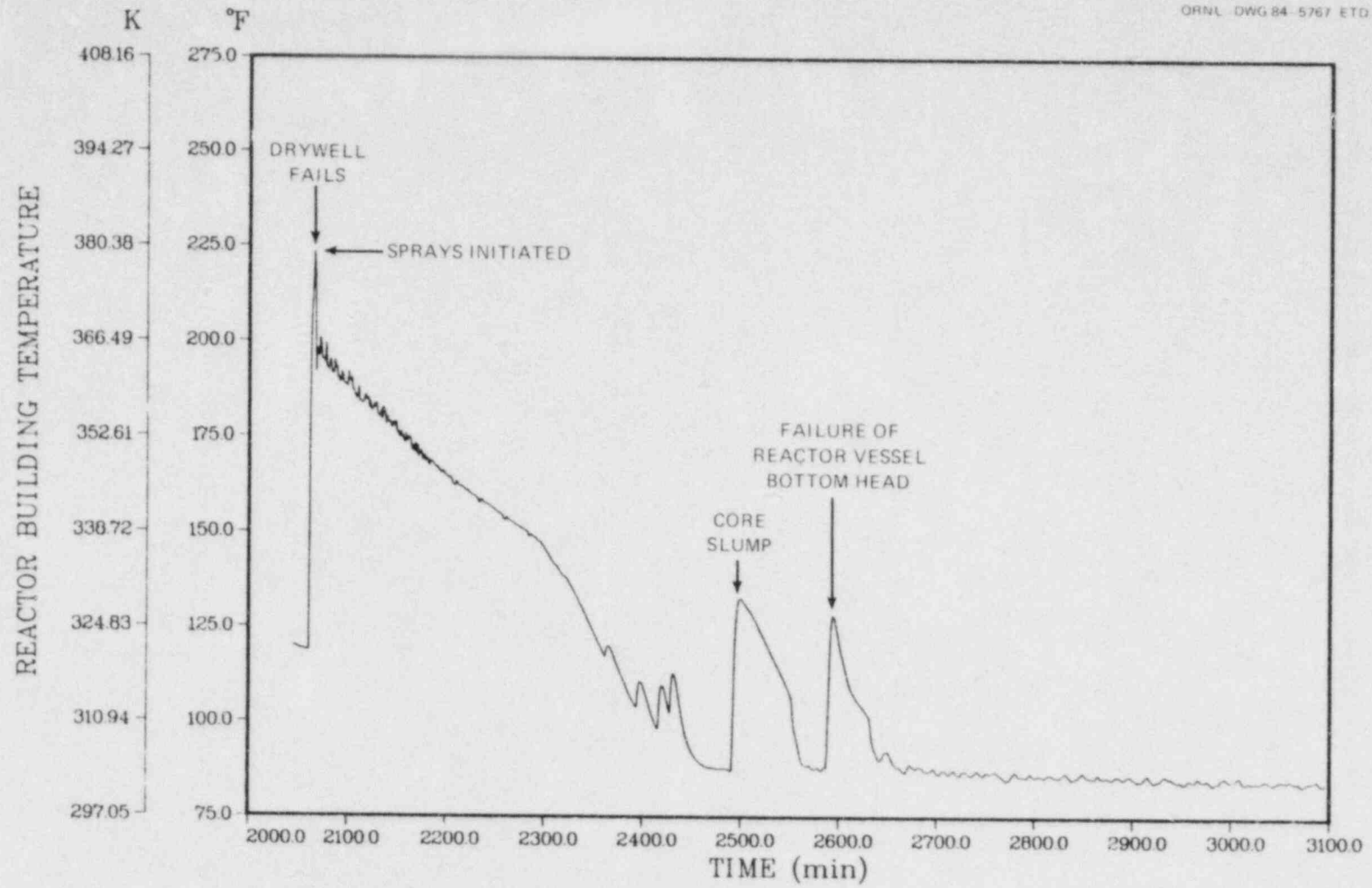
Fig. A.7. Reactor building temperature.
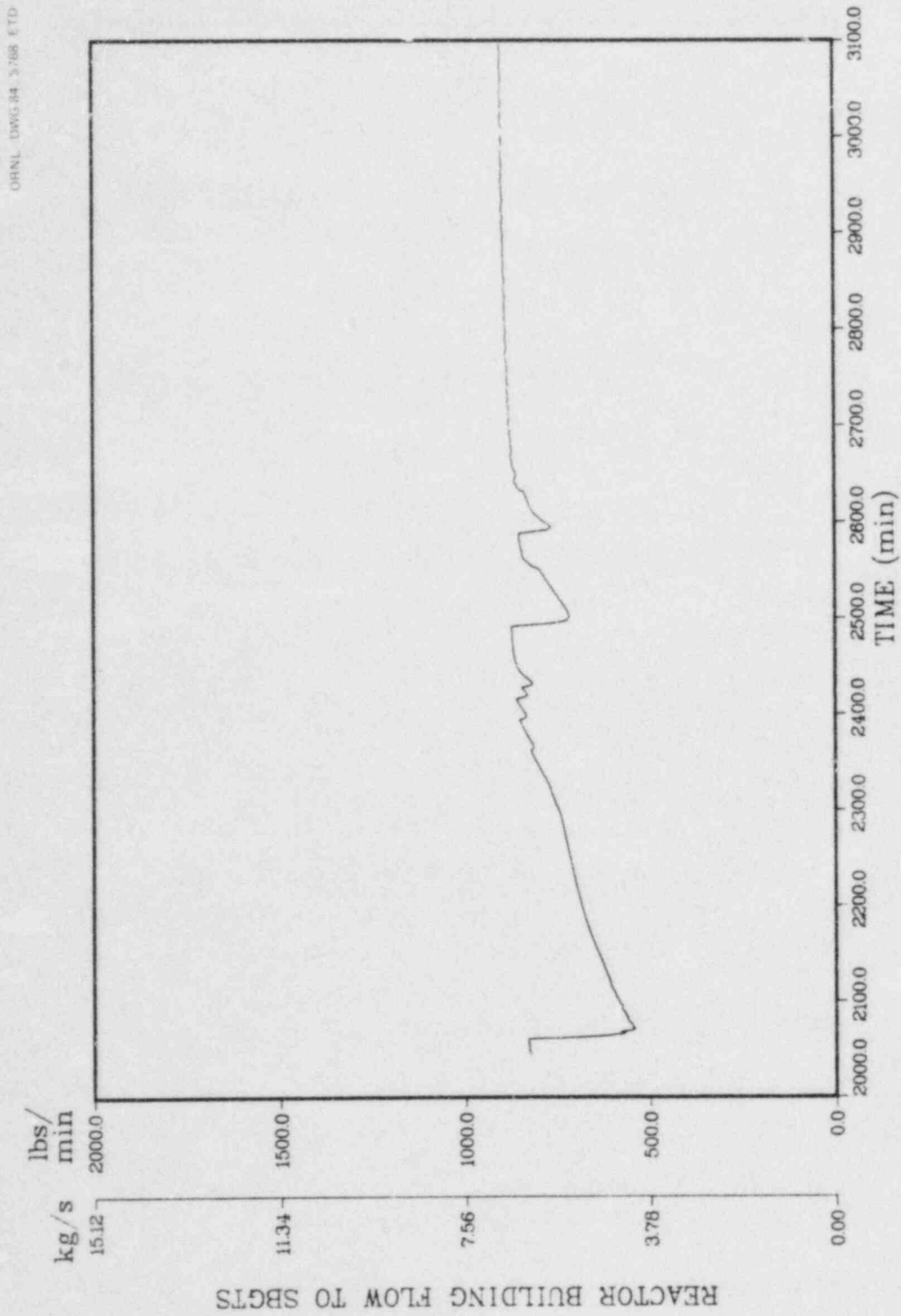
Fig. A.8. Mass flow from the reactor building to the standby gas treatment system.
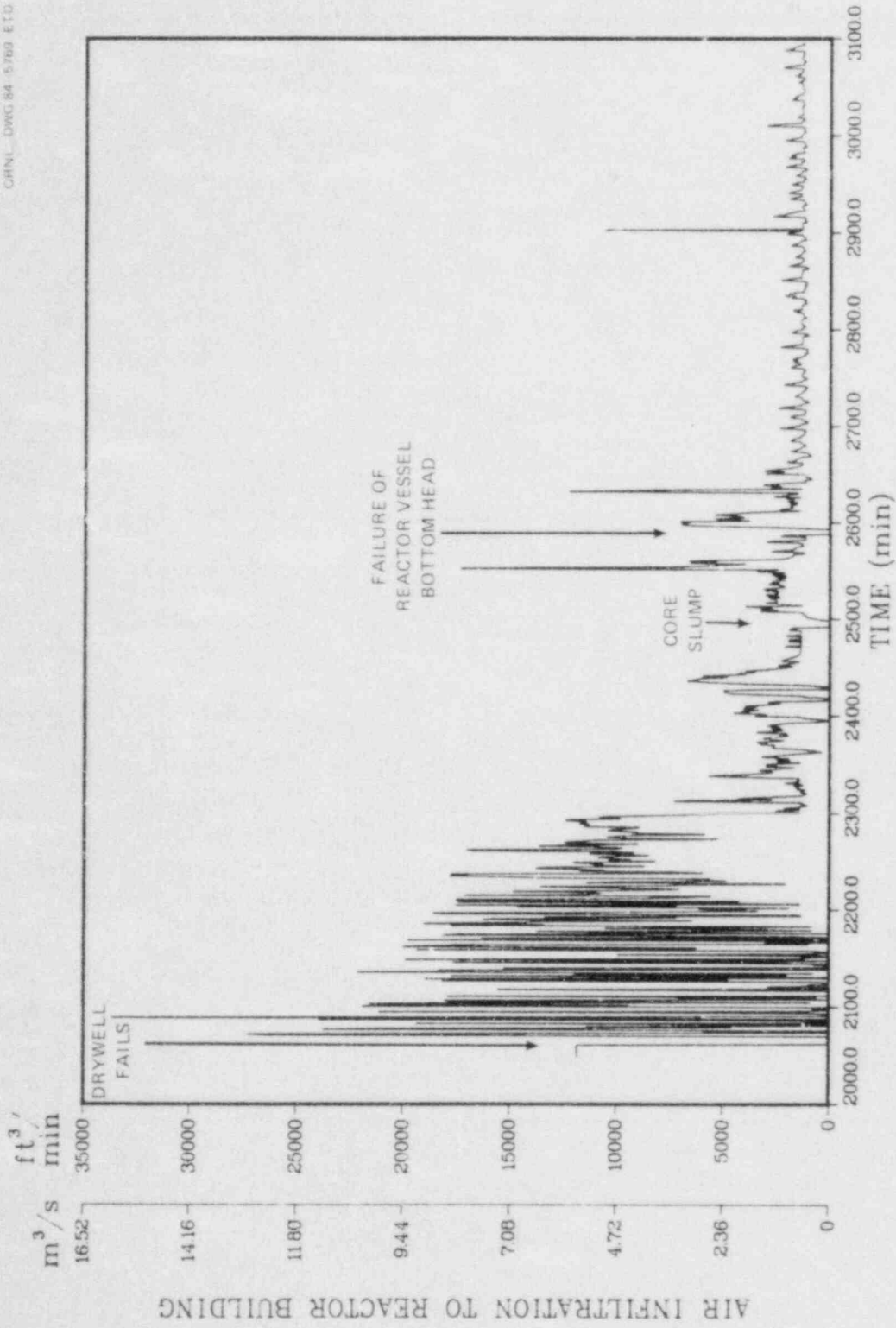
Fig. A.9. Infiltration of air to the reactor building.
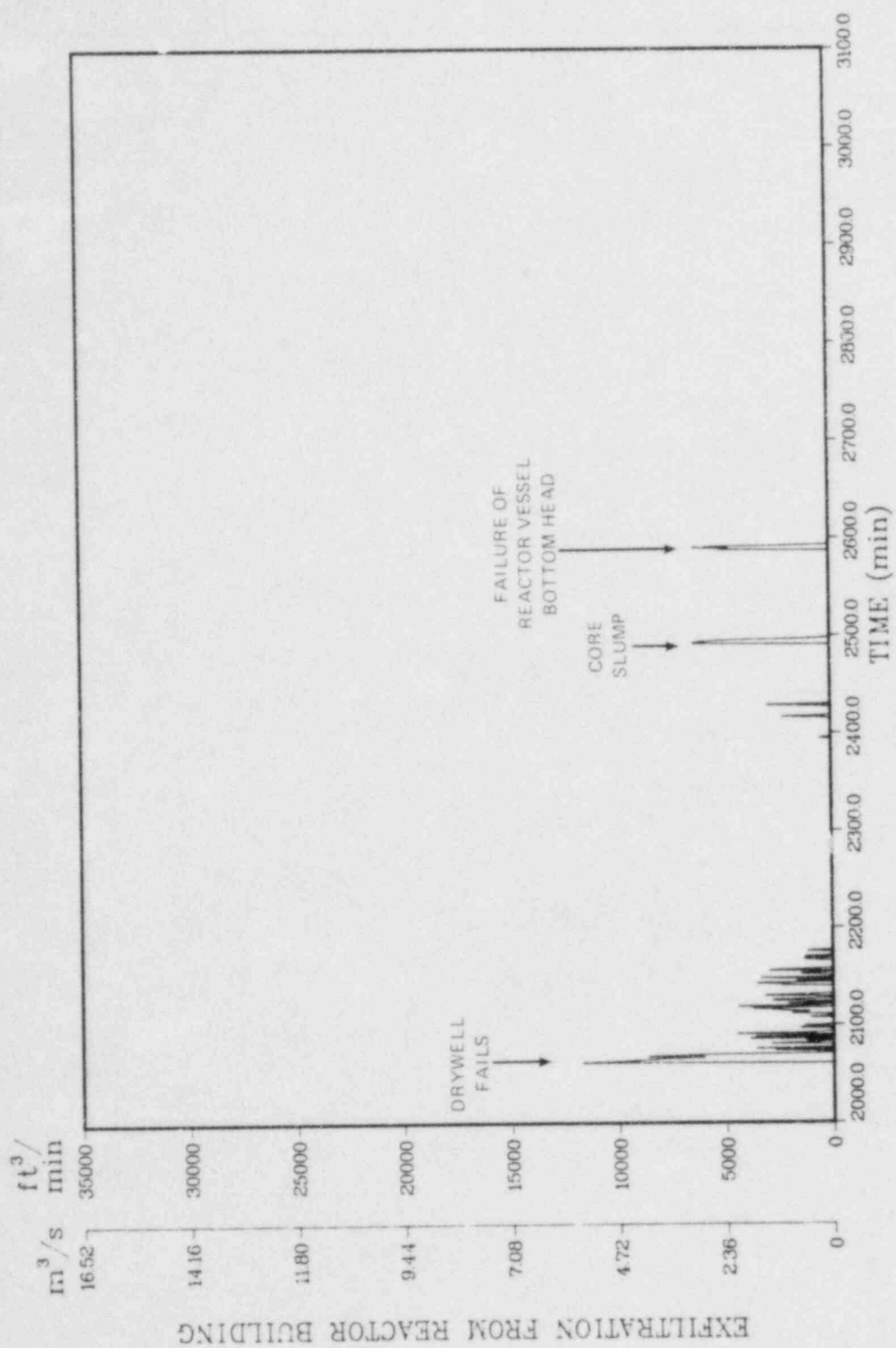
Fig. A.10. Exfiltration from the reactor building.
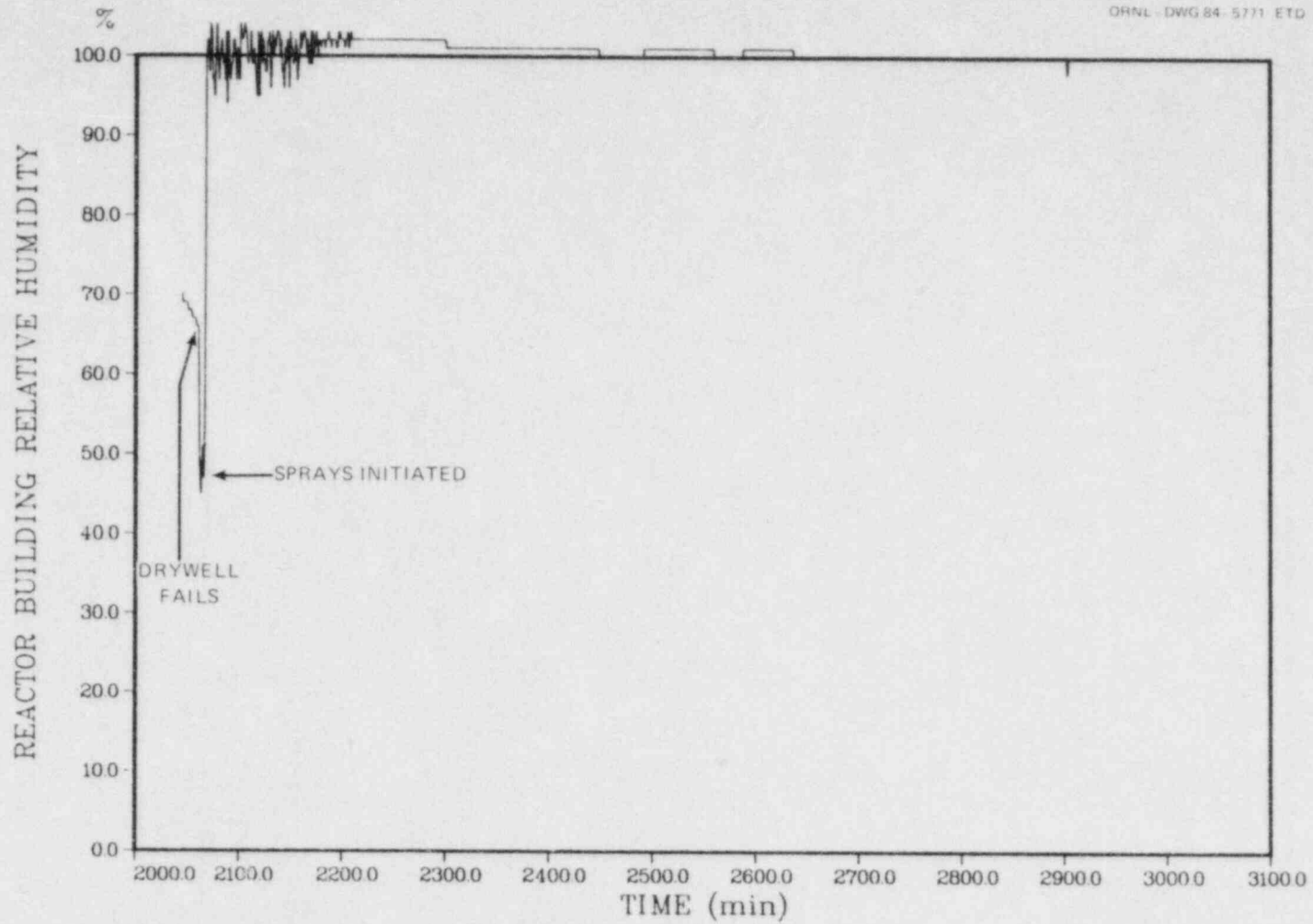
Fig. A.11. Relative humidity of the reactor building atmosphere.

REACTOR BUILDING FLOW TO REFUELING FLOOR
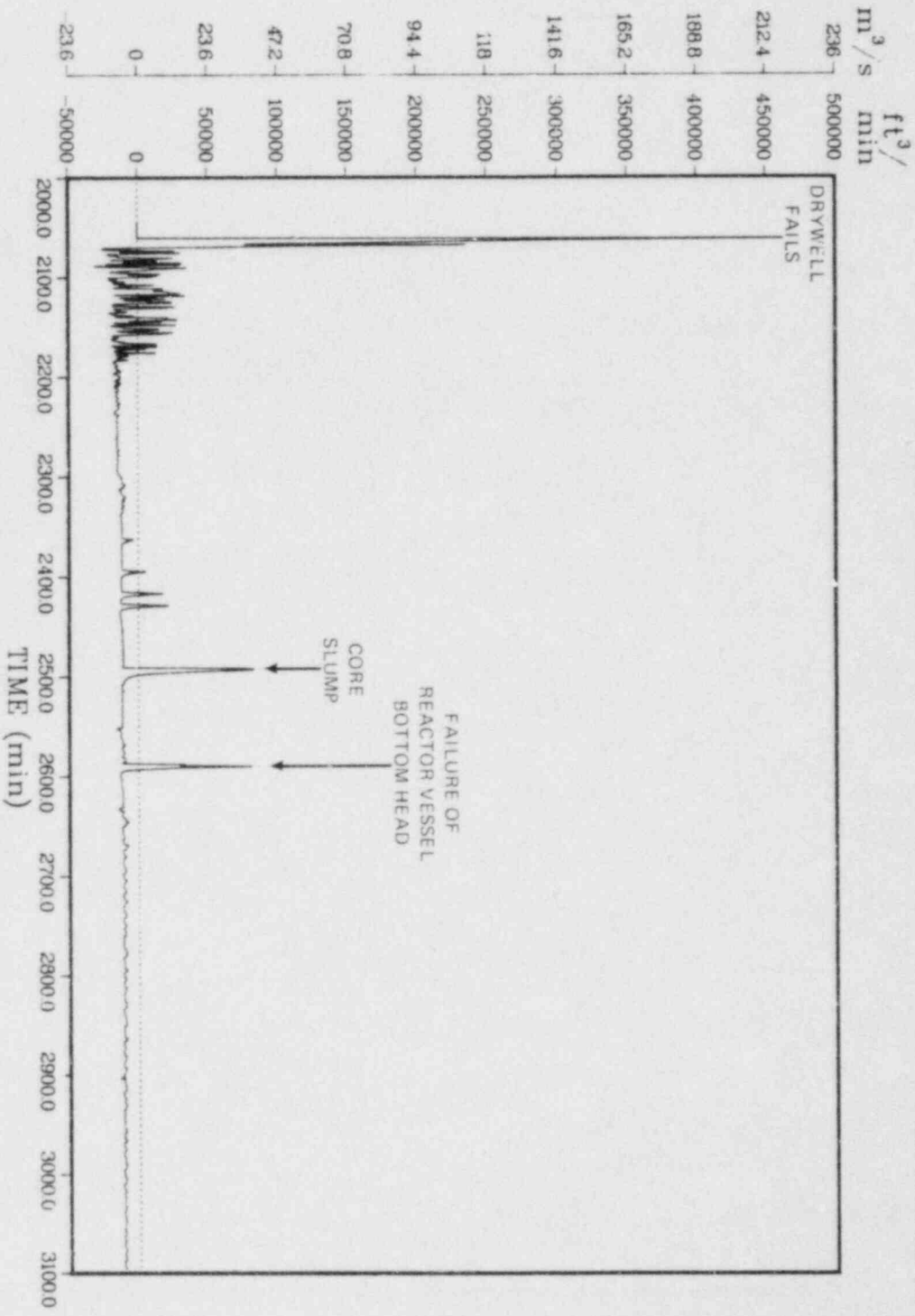
Fig. A.12. Volumetric flow from the reactor building to the re-
fueling floor.

ORNL DWG 84-5772 ETD

149
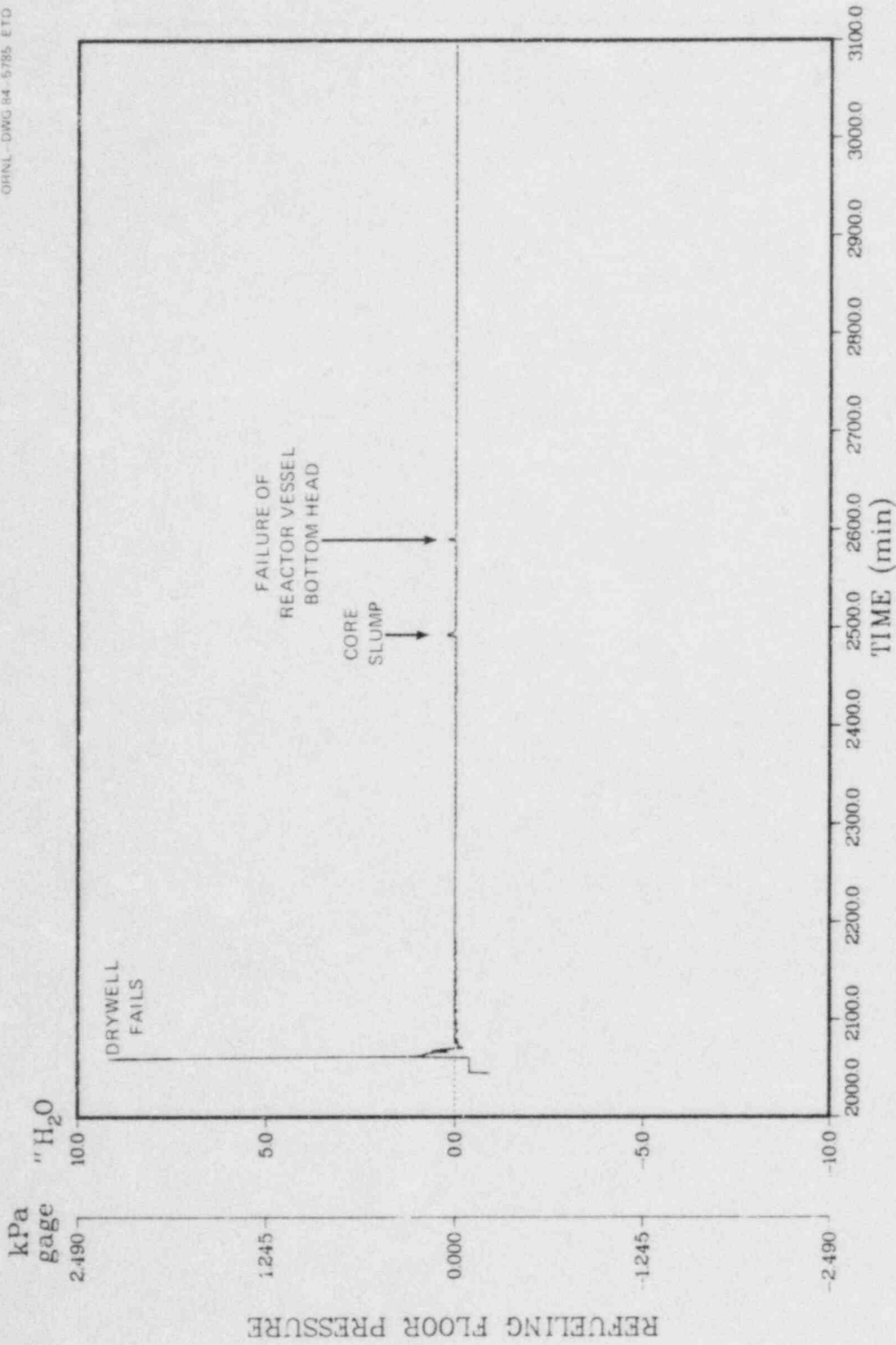
Fig. A.13. Refueling bay pressure.

REFUELING FLOOR TEMPERATURE
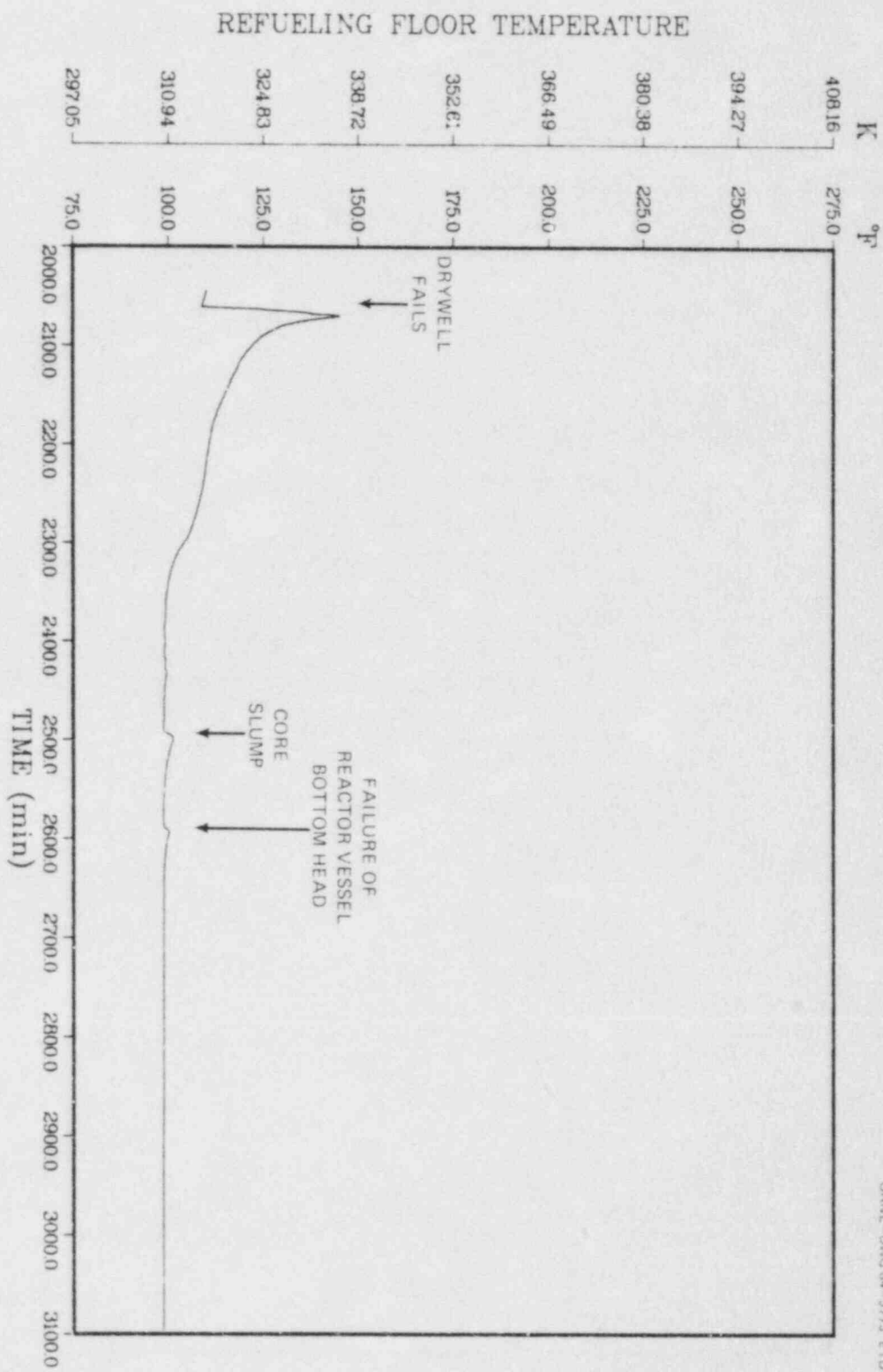
Fig. A.14. Refueling bay temperature.

151

152
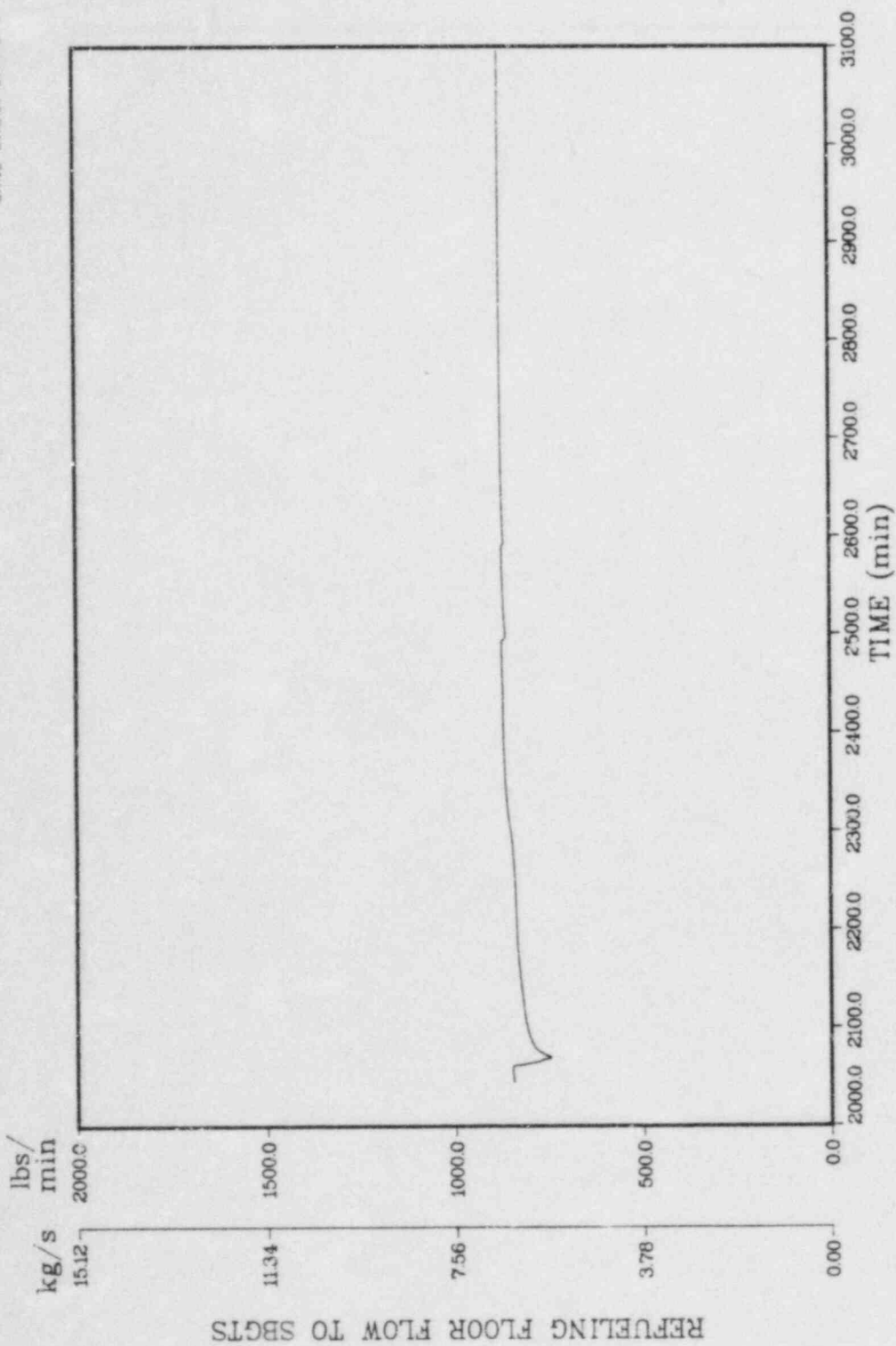
Fig. A.15. Mass flow from the refueling bay to the standby gas treatment system.

Fig. A.16. Infiltration of air to the refueling bay.
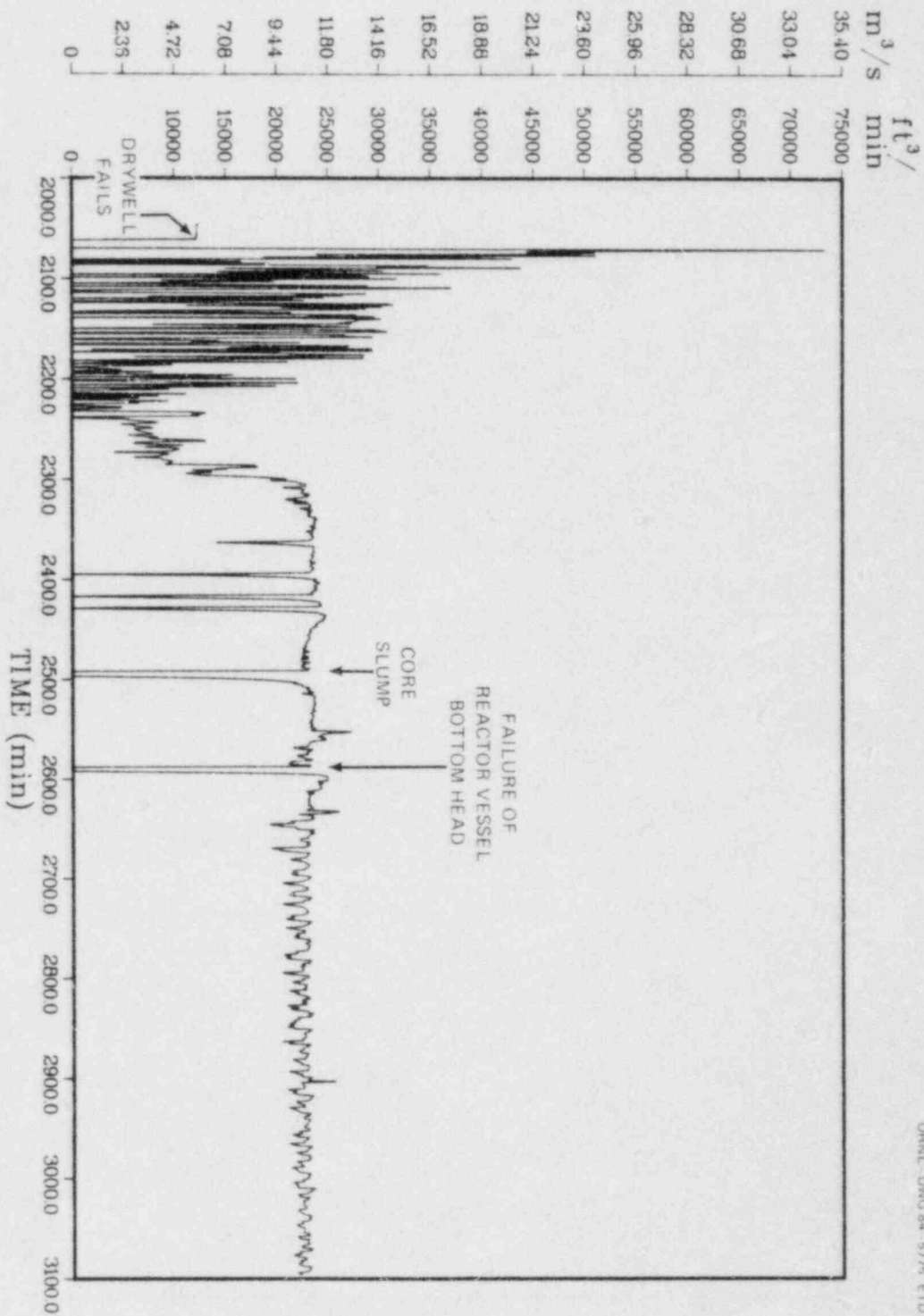
Fig. A.17. Exfiltration from the refueling bay.
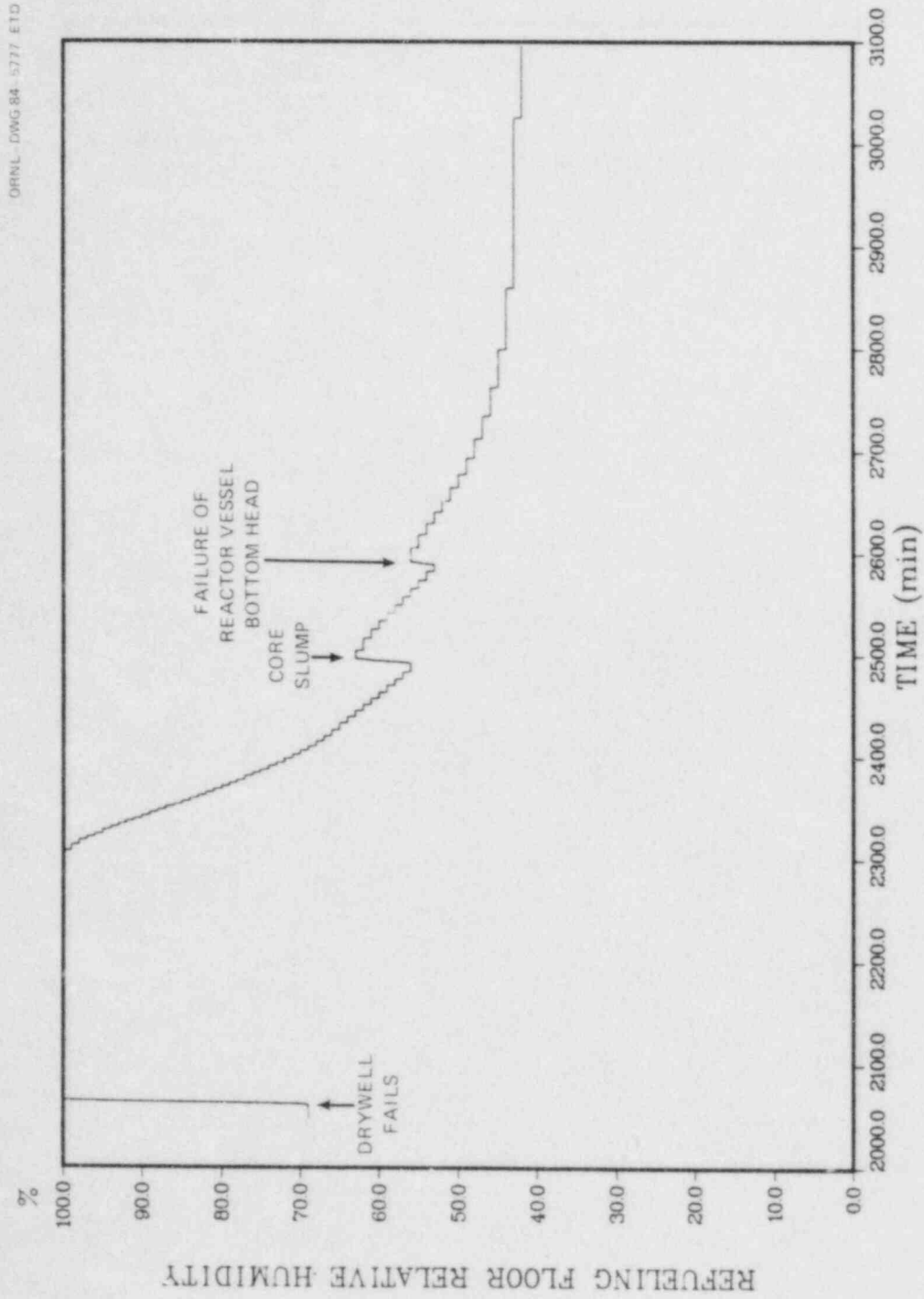
ORNL-DWG 84-5746 ETD

Fig. A.18. Relative humidity of the refueling bay atmosphere.
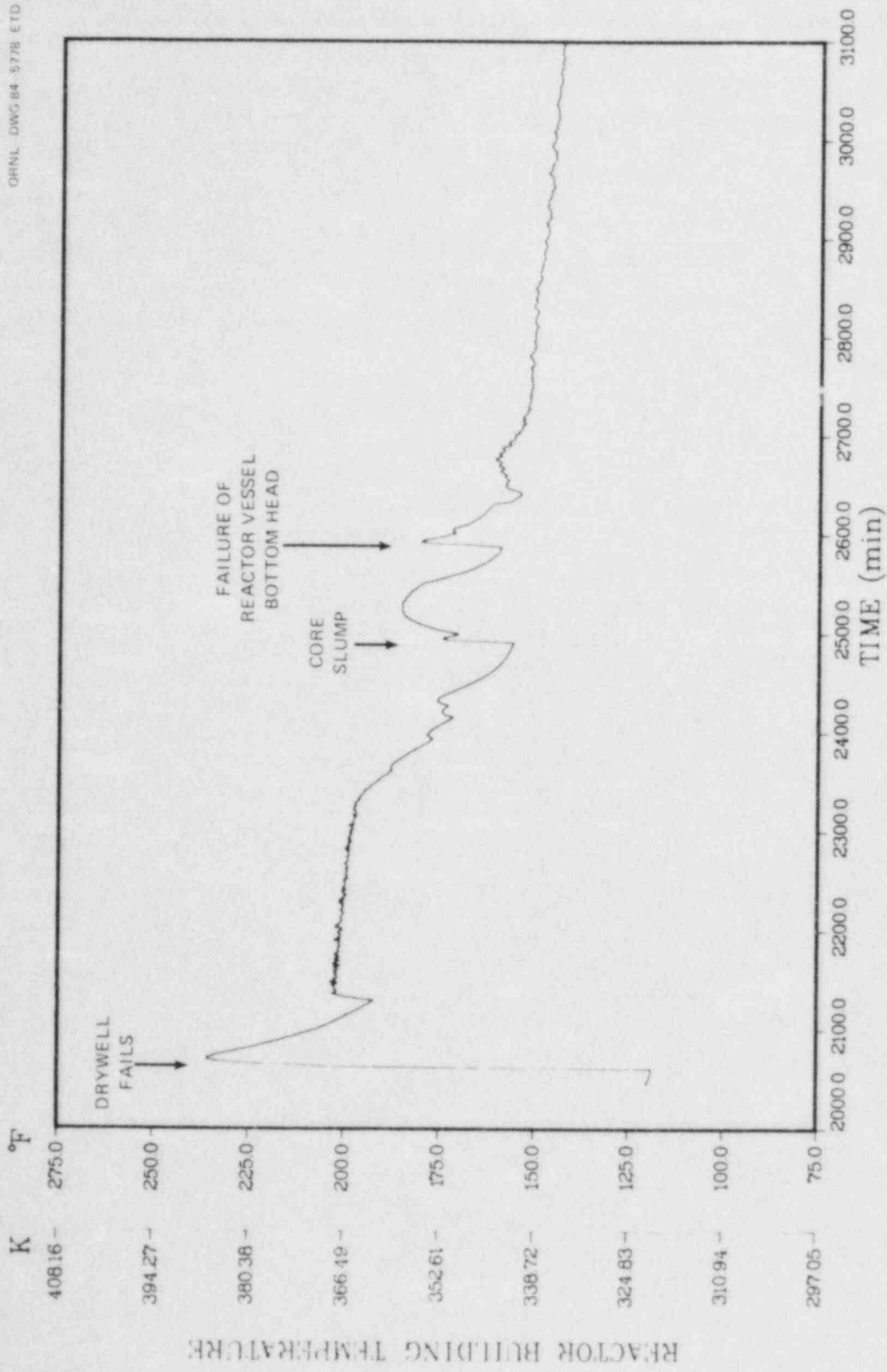
Fig. A.19. Reactor building temperature response without sprays.
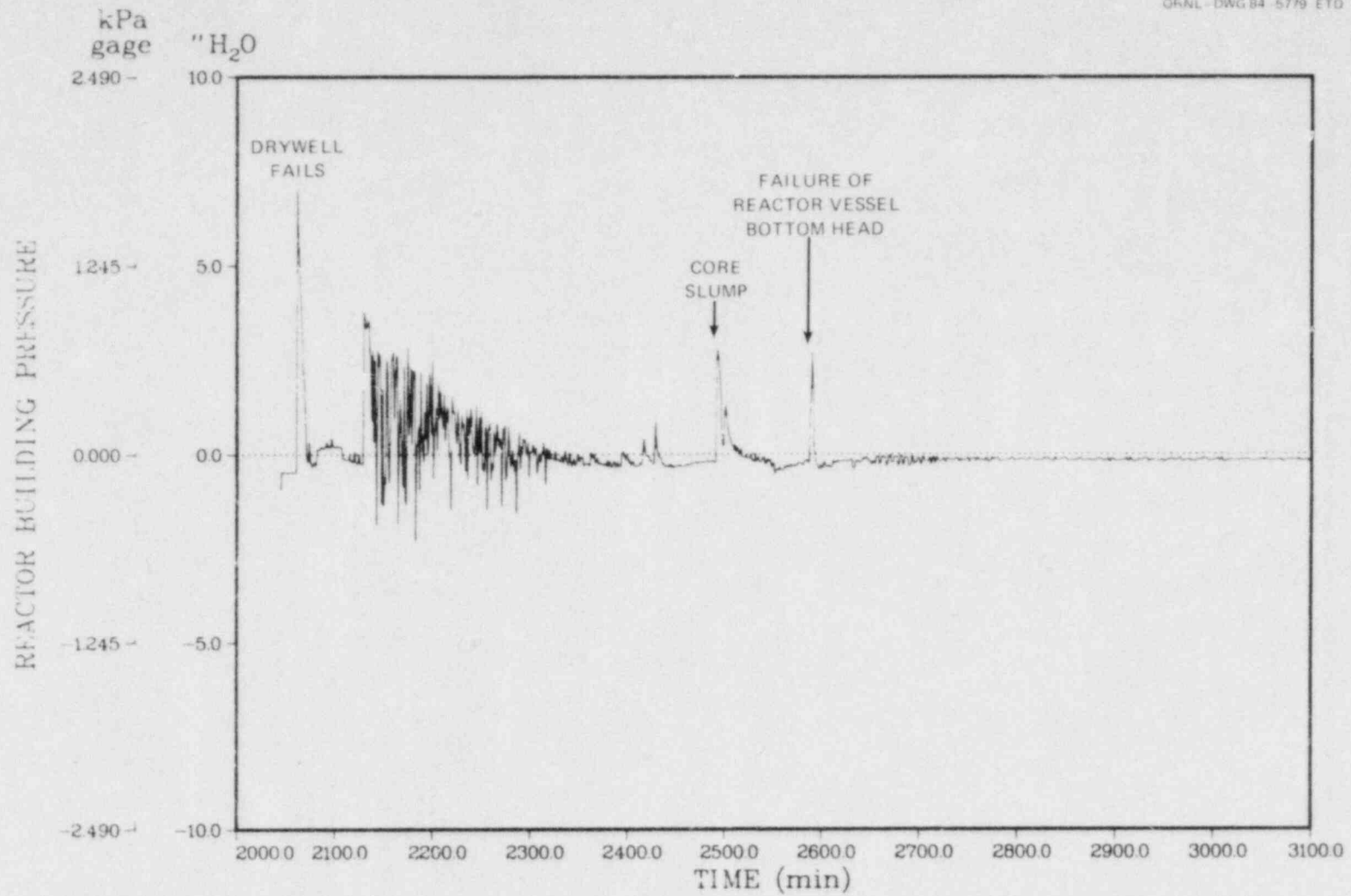
Fig. A.20. Reactor building pressure response without sprays.

157

Appendix B:

DETAILS OF CALCULATIONS FOR CORE-CONCRETE DEBRIS BED BEHAVIOR, CORE-CONCRETE AEROSOL PRODUCTION RATES, AND AEROSOL TRANSPORT IN THE DRYWELL AND REACTOR BUILDING

B.1 Introduction

The purpose of this Appendix is to describe the methods used to calculate the results presented in Chap. 4 of this report. This includes core-concrete debris bed behavior calculations performed using the CORCON-MOD1 code (Ref. B.1) and the INTER subroutine from the MARCH code, (Ref. B.2) aerosol production rate calculations performed using the VANESA code, (Ref. B.3) and aerosol transport calculations performed using the QUICK code (Ref. B.4). In addition to the results presented in Sect. 4, three additional CORCON calculations were performed so that the sensitivity of CORCON calculations to input parameters could be investiated in a limited way; these results are presented in Sect. B.2 of this Appendix. The VANESA code was used to predict aerosol generation rates vs time for all of the CORCON runs and for the INTER calculation; these results are presented in Sect. B.3.

B.2 Core-Concrete Debris Bed Behavior Calculations

As discussed in Sect. 4.2, the aerosol transport results predicted for the LDHR sequence are based on core-concrete gas evolution rates and rubble temperatures calculated with the CORCON-MOD1 code; for past Browns Ferry accident sequences the results calculated with the INTER subroutine of the MARCH code were used. In this section we present a comparison of the "base-case" CORCON results presented in Chap. 4 with calculated INTER results and also with results from three additional CORCON calculations.

Table 4.1 in Chap. 4 presents the major input parameters used for the base-case CORCON run ("CORCON1") and for the MARCH INTER calculation. Table B.1 presents a summary of the major parameters varied in the four CORCON runs and the INTER run. The MARCH code calculated that roughly 13% of the zircaloy cladding was oxidized before melt-through of the reactor vessel; this amount of oxidation was assumed in the CORCON1 and INTER calculations. The CORCON2 and CORCON3 calculations were performed to determine the influence of the initial amount of zircaloy oxidation on the calculated gas evolution rates and core debris temperatures. The initial amounts of zircaloy oxidation assumed in the CORCON2 and CORCON3 calculations were 50% and 90%, respectively. The CORCON4 calculation was performed to determine how an increase in the initial core-melt temperature would influence the calculated core-concrete interaction phenomena.

Tables B.2 through B.6 summarize the results from the CORCON and INTER calculations. Presented in the tables are metal and oxide layer temperature, cumulative releases of CO, CO_2, H_2, and H_2O, and cumulative amounts of SiO_2 mixed into the melt due to interaction of the core-melt

material with the concrete. A number of observations can be made relative to the information presented in these tables:

1. As discussed in Chap. 4, CORCON tends to predict lower gas releases and higher metal and oxide temperatures than INTER does.

2. The largest difference in gas evolution between the CORCON1 and INTER results was for CO; the CO release predicted in the CORCON1 results is roughly four orders of magnitude less than that predicted by INTER. It was stated in Chap. 4 that the low CO release in the CORCON1 run is due to "coking," or the reduction of CO to elemental carbon. Results from the CORCON2 and CORCON3 runs seem to indicate that the initial amount of oxidized zircaloy in the core melt has an influence on the calculated total amount of CO release. The total CO release predicted in the CORCON2 calculation (50% of the zircaloy initially oxidized) was roughly 9 times that predicted in the CORCON1 run, and the total CO release in the CORCON3 run (90% of the zircaloy initially oxidized) was more than 3500 times that predicted in CORCON1. It is interesting to note in Table B.4 that there is a rapid increase in CO release after 2830 min; this time corresponds exactly to the time when there is no more metallic zircaloy in the core melt.

3. The oxide layer temperatures predicted in the CORCON2 and CORCON3 runs tend to be lower, particularly near the end of the calculation, than the oxide temperatures predicted for the CORCON1 and CORCON4 runs. This may be due to the fact that a "layer flip" is predicted to occur in the CORCON2 and CORCON3 runs and not in the CORCON1 and CORCON4 runs. In CORCON calculations, the core-melt is segregated into oxide and metal layers; for the conditions in the LDHR CORCON runs the oxide layer is initially heavier and so is below the metal layer. CORCON assumes that all reactions in the metal layer after the start of core-concrete interaction produce oxides that form a separate oxide layer above the metal. As the lower oxide layer heats and changes composition, it may eventually become less dense and "flip" with the metal layer; if this happens, then all of the oxides mix together. A layer flip was predicted in the CORCON2 run at 2890 min, and was predicted in the CORCON3 run at 2760 min. This layer flip was most likely due to the fact that there initially is more oxidized zircaloy in the melt layers for the CORCON2 and CORCON3 runs. The mixing of the two oxide layers due to the layer flip probably results in the lower oxide temperatures predicted in CORCON2 and CORCON3.

4. The increase in the initial melt temperature in the CORCON4 run leads to increases in the release of CO, CO_2, H_2, and H_2O when compared to the CORCON1 run.

5. The total amount of SiO_2 predicted to be formed by INTER is a factor of 2 to 5 times that predicted from the CORCON runs. Within the CORCON runs themselves, the total SiO_2 produced varied by roughly a factor of 2.5. The amount of SiO_2 produced is an important output, because SiO_2 may make up a major portion of the core-concrete aerosol.

B.3 Core-Concrete Aerosol Production Rate Calculations

Core-concrete aerosol production rate calculations were performed for this accident sequence using the VANESA code; these calculations were performed at Sandia National Laboratories by Dana Powers, who developed VANESA. The required input for VANESA calculations include concrete specifications, the specification of fission product inventories and other materials in the core melt at the time of start of core-concrete interaction, and core-concrete interaction gas evolution rates, layer temperatures, and SiO_2 production rates. The data presented in Tables B.2 through B.6 provided a large portion of the input for the VANESA calculations. It should be noted that the concrete specifications used for the VANESA calculations were for "degassed" limestone concrete; these specifications are presented in Table B.7. As will be seen in discussing the VANESA results, some concrete components that are present in small amounts contribute significantly to the predicted aerosol source.

Tables B.8 through B.13 and Fig. B.1 present a summary of results from the VANESA calculations. Some of the important results from these calculations include the following:

1. Tables B.8 through B.12 and Fig. B.1 present aerosol release rates and cumulative aerosol production predicted by VANESA. The total amounts of core-concrete aerosol predicted by VANESA to be produced during the 8 h following the start of core-concrete interaction varied by roughly a factor of 4. However, the assumption used in the CORCON3 calculation that 90% of the zircaloy is oxidized at reactor vessel melt-through is probably unrealistic for this accident sequence; if the VANESA-CORCON3 results are ignored, the total predicted aerosol production for the other four calculations varies by only slightly greater than a factor of 2.
2. It is interesting to find that the VANESA run performed using the INTER data as input gave the highest total aerosol release of 2107 kg over the 8-h period. This was somewhat surprising since the predicted INTER temperatures are quite a lot lower than those predicted in the CORCON runs. At least a partial explanation for the high release predicted in the VANESA-INTER calculation is that the gas evolution rates from INTER calculations are significantly larger than those predicted in the CORCON runs.
3. The VANESA-CORCON4 predicted aerosol release was higher than that predicted for the VANESA-CORCON1 run. This was expected, since the initial melt temperature assumed for CORCON4 was more than 200 K higher than that assumed for CORCON1.
4. Table B.13 illustrates the predicted make-up of the core-concrete aerosol at 3070 min. The predicted make-up of the core-concrete aerosol varied significantly for the summarized calculations. It should be noted that although K_2O and Na_2O made up only 1.75% of the assumed concrete composition (Table B.7), because they are quite volatile they constituted a significant fraction of the aerosol composition in the VANESA calculations. In particular, for the VANESA-INTER calculation K_2O made up 93.8% of the predicted final aerosol mass.

B.4 QUICK Drywell Aerosol Transport Calculations

The results from the QUICK code aerosol transport calculations per-
formed for drywell conditions in the LDHR sequence were summarized in
Sect. 4.4. The purpose of this section is simply to summarize the input
data used for these calculations, and to present any results not
summarized in Sect. 4.4.

The input data for the QUICK drywell calculations fall into the
following categories: (1) "fixed" QUICK input parameters, (2) aerosol
production-rate data, (3) drywell leak-rate data, (4) drywell pressure
and temperature data, and (5) drywell geometric data. Input data used
for each of these categories is described in this section.

B.4.1 Fixed QUICK parameters

Table B.14 presents QUICK input parameters that do not vary during
the drywell and reactor building calculations.

B.4.2 Aerosol production-rate data

The VANESA-CORCON1 calculation was used to develop the aerosol pro-
duction-rate data for the LDHR sequence. Aerosol production rates for
QUICK calculations are input in the form of cumulative aerosol mass con-
centrations as a function of time. This data is obtained from the data
presented in Table B.8 by dividing the column labeled "total aerosol
produced" by the drywell volume which is 4,500 m^3. The drywell aerosol
production-rate input data is presented in Table B.15.

An aerosol particle size is input to QUICK. The particle size used
for this sequence is the same as that used in the SBLOCA sequence,[B.6]
and is based on data from experiments performed at Sandia.[B.7] The aer-
osol source parameters used, assuming that the core-concrete aerosol
density is 2.8 g/cm^3, are:

Geometric particle radius: $r_g = 0.113$ μm

Standard deviation:* $\sigma_g = 1.9$

B.4.3 Drywell leak-rate data

The MARCH code computes gas leak rates from the drywell; however,
at present MARCH uses INTER gas evolution rates to calculate the drywell
leak rates. For this accident sequence, as is described in Appendix A,
the MARCH-INTER drywell leak rates were modified by the ratio of the
CORCON1-to-INTER gas evolution rates; the modified drywell leak rates
were used in the QUICK calculations. The leak-rate data used for the

---

*84% size/50% size.

QUICK drywell calculations are presented in Table B.16; the fractional gas leakage rate is obtained by dividing the volumetric leakage rate by the drywell volume.

B.4.4 Drywell pressure and temperature data

Based on MARCH drywell calculations, a temperature of 530 K and a pressure of 1 atmosphere were used in the QUICK calculation.

B.4.5 Drywell geometric data

Table B.17 presents drywell geometric data used in the QUICK calculation.

B.4.6 QUICK drywell results

Table 4.4 and Figs. 4.4 through 4.6 present some of the results from the QUICK drywell calculations. Figures B.2 and B.3 present additional results for the aerodynamic aerosol radius and the aerosol standard deviation as a function of time.

B.5 QUICK Reactor Building Aerosol Transport Calculations

The input parameters used in the QUICK reactor building aerosol transport calculations are presented in this section.

B.5.1 Reactor building aerosol production-rate data

Aerosols that are leaked out of the drywell become the aerosol source to the reactor building. Table B.18 summarizes data related to the aerosol source to the reactor building. The aerosol source data used by QUICK are again the cumulative aerosol concentrations in the building; these data are obtained by dividing the total amount of aerosol released to the building by the building volume of 42,470 m^3.

In principle, the time variation of the agglomerate geometric radius and standard deviation, listed in Table B.18, can be input to QUICK for the building calculations. However, including this form of input makes the code calculations very long-running and expensive. Because of this, a time-average of the size data presented in Table B.18 was used as input for the reactor building calculations:

Average geometric radius: $r_g = 0.2154$ μm

Average standard deviation: $\sigma_g = 1.796$

B.5.2 Reactor building leak-rate data

Reactor building thermal-hydraulic calculations described in Appendix A indicate that for the first 4 min after the start of core-concrete interaction there is gas exfiltration to the refueling bay and to the environment in addition to the gas transport to the Stand-By Gas Treatment System (SGTS). However, after 2594 min all gas leakage in the reactor building is directly through the SGTS at a rate of 12,500 SCFM. Table B.19 presents the leak-rate data used in the QUICK building calculation; the fractional leakage rate is obtained by dividing the volumetric rate by the reactor building volume.

B.5.3 Reactor building pressure and temperature data

Based on secondary containment model calculations, a temperature of 283 K and a pressure of 1 atmosphere was used in the QUICK calculation.

B.5.4 Reactor building geometric data

Table B.20 presents reactor building geometric data used for the QUICK calculation.

B.5.5 QUICK reactor building results

Table 4.5 and Figs. 4.7 to 4.9 present some of the results from the QUICK reactor building calculations. Figures B.4 and B.5 present additional results for the aerodynamic radius and the aerosol standard deviation as a function of time. It should be noted that the predicted aerodynamic radius in the building is somewhat smaller than that predicted in the drywell; this is due to the fact that the aerosol source to the reactor building was assumed to have a time-independent averaged size.

References for Appendix B

B.1   J. F. Muir, R. K. Cole, Jr., M. L. Corradini, and M. A. Ellis, *CORCON-MOD1: An Improved Model for Molten Core/Concrete Interactions*, NUREG/CR-2142, SAND80-2415 (February 1982).

B.2   R. O. Wooten and H. I. Avci, *MARCH Code Description and User's Manual*, Battelle Columbus Laboratories, USNRC Report NUREG/CR-1711 (October 1980).

B.3   D. A. Powers and J. E. Brockman, "Status of VANESA Validation," in *Report of the Status of Validation of the Computer Codes Used in the NRC Accident Source Term Reassessment Study* (BMI-2104), prepared by T. S. Kress, ORNL/TM-8842 (to be published).

B.4   H. Jordan, P. Schumacher, and J. A. Gieseke, *QUICK User's Manual*, NUREG/CR-2015, BMI-2082 (April 1981).

B.5   Personal Communication, D. A. Powers, Sandia National Laboratories, January 1984.

B.6   R. P. Wichner et al., *SBLOCA Outside Containment at Browns' Ferry Unit One, Volume 2. Iodine, Cesium, and Noble Gas Distribution and Release*, NUREG/CR-2672, Vol. 2, ORNL/TM-8119/V2 (September 1983).

B.7   Letter from R. A. Lorenz to A. L. Wright, "Recent Communications from Sandia Laboratories Regarding Core Melt-Concrete Interaction Aerosol Sizes," July 12, 1982.

Table B.1. Summary of major parameters varied
for the CORCON and INTER calculations

Case	Initial temperature (K)	Initial FeO (kg)	Initial Fe (kg)	Initial ZrO_2 (kg)	Initial Zr (kg)
CORCONI	1737	5,150	116,100	11,530	56,960
CORCON2	1737	5,150	116,100	44,240	32,750
CORCON3	1737	5,150	116,100	79,620	6,550
CORCON4	1950	5,150	116,100	11,530	56,960
INTER	1737	0	120,100	11,530	56,960

Table B.2 CORCON1 results

Time (min)	Tmetal (K)	Toxide (K)	Total CO (kg)	Total CO2 (kg)	Total H2 (kg)	Total H2O (kg)	Total SiO2 (kg)
2590	1737	1737	.00	.0	.0	.0	0
2610	1745	1896	.00	78.9	.6	25.7	187
2630	1757	2000	.01	310.1	4.1	100.8	819
2650	1758	2046	.03	651.8	10.5	211.8	1826
2670	1759	2062	.06	979.9	18.5	318.1	2886
2690	1761	2068	.08	1310.0	26.9	425.8	3980
2710	1763	2069	.11	1648.0	35.5	535.7	5095
2730	1764	2070	.14	1987.0	44.2	645.8	6217
2750	1766	2070	.17	2330.0	52.8	757.4	7344
2770	1778	2071	.20	2681.0	61.2	871.2	8473
2790	1825	2065	.24	3034.0	68.5	986.0	9549
2810	1857	2067	.32	3431.0	75.5	1115.0	10694
2830	1882	2071	.44	3866.0	82.5	1257.0	11912
2850	1904	2079	.52	4290.0	89.7	1394.0	13116
2870	1912	2109	.76	4622.0	94.2	1502.0	14004
2890	1905	2166	.77	4811.0	94.7	1564.0	14396
2910	1899	2222	.79	4999.0	95.3	1625.0	14788
2930	1893	2275	.80	5183.0	95.8	1685.0	15176
2950	1889	2326	.82	5368.0	96.4	1744.0	15570
2970	1885	2376	.83	5551.0	97.0	1804.0	15951
2990	1882	2424	.84	5732.0	97.7	1863.0	16339
3010	1879	2470	.86	5913.0	98.4	1922.0	16722
3030	1877	2515	.87	6095.0	99.0	1981.0	17113
3050	1876	2558	.88	6275.0	99.8	2039.0	17560
3070	1874	2600	.90	6456.0	100.5	2098.0	17896

Table 8.3 CORCON2 results

Time (min)	Tmetal (K)	Toxide (K)	Total CO (kg)	Total CO_2 (kg)	Total H_2 (kg)	Total H_2O (kg)	Total SiO_2 (kg)
2590	1737	1737	.00	.0	.0	.0	0
2610	1745	1863	.00	64.5	.4	21.0	145
2630	1757	1964	.01	223.9	2.1	72.8	549
2650	1757	2025	.02	528.8	6.2	171.9	1357
2670	1759	2056	.04	873.4	12.1	283.9	2338
2690	1760	2070	.06	1218.0	18.9	395.9	3376
2710	1762	2076	.08	1580.0	26.3	513.5	3404
2730	1763	2078	.11	1953.0	33.9	634.7	5602
2750	1765	2079	.14	2326.0	41.6	755.9	6737
2770	1767	2078	.16	2704.0	49.3	878.8	7883
2790	1807	2079	.20	3086.0	57.1	1003.0	9035
2810	1854	2084	.28	3519.0	64.9	1144.0	10297
2830	1892	2081	.44	4013.0	73.3	1304.0	11700
2850	1919	2069	.70	4549.0	81.3	1478.0	13170
2870	1935	2063	.97	5097.0	88.5	1657.0	14618
2890	1944	2017	1.32	5637.0	96.4	1832.0	16090
2910	1940	2028	2.21	6133.0	123.6	1993.0	18510
2930	1935	2038	3.01	6639.0	150.2	2158.0	20910
2950	1933	2046	3.76	7172.0	176.4	2331.0	23340
2970	1932	2049	4.48	7761.0	202.5	2522.0	25880
2990	1934	2048	5.21	8416.0	228.7	2735.0	28550
3010	1932	2044	5.92	9155.0	254.1	2975.0	31340
3030	1931	2039	6.60	9913.0	279.3	3222.0	34160
3050	1933	2033	7.30	10680.0	304.8	3471.0	37020
3070	1934	2027	8.02	11458.0	330.8	3724.0	39920

Table B.4   CORCON3 results

Time (min)	Tmetal (K)	Toxide (K)	Total CO (kg)	Total CO_2 (kg)	Total H_2 (kg)	Total H_2O (kg)	Total SiO_2 (kg)
2590	1737	1737	.00	.0	.0	.0	0
2610	1746	1839	.00	56.1	.3	18.2	124
2630	1757	1928	.00	171.2	1.3	55.6	400
2650	1757	1994	.12	403.3	3.7	131.1	982
2670	1758	2035	.03	725.3	7.8	235.7	1822
2690	1760	2058	.04	1065.0	13.0	346.0	2759
2710	1761	2071	.06	1430.0	19.0	464.6	3787
2730	1763	2077	.08	1813.0	25.4	589.3	4875
2750	1765	2079	.11	2211.0	32.1	718.6	6002
2770	1766	2054	.13	2592.9	41.3	842.5	7234
2790	1767	2049	.16	2965.0	52.2	963.5	8543
2810	1780	2045	.19	3387.0	63.6	1091.0	9915
2830	1827	2036	.25	3828.0	78.2	1244.0	11610
2850	1797	2002	574.10	4393.0	93.7	1428.0	13530
2870	1768	1974	1147.00	4886.0	105.4	1588.0	15110
2890	1768	1955	1656.00	5336.0	115.8	1734.0	16540
2910	1767	1955	2168.00	5711.0	126.3	1856.0	17830
2930	1766	1979	2396.00	5912.0	136.7	1922.0	18770
2950	1766	1991	2579.00	6115.0	147.1	1988.0	19730
2970	1766	2003	2761.00	6322.0	157.4	2056.0	20680
2990	1765	2015	2929.00	6528.0	167.0	2123.0	21590
3010	1765	2027	3089.00	6734.0	176.1	2191.0	22480
3030	1765	2038	3250.00	6946.0	185.2	2260.0	23380
3050	1764	2049	3410.00	7164.0	194.3	2331.0	24290
3070	1764	2059	3570.00	7387.0	203.5	2404.0	25210

169

Table B.5 CORCON4 results

Time (min)	Tmetal (K)	Toxide (K)	Total CO (kg)	Total CO_2 (kg)	Total H_2 (kg)	Total H_2O (kg)	Total SiO_2 (kg)
2590	1950	1950	.00	.0	.0	.0	0
2610	1941	2044	.27	465.6	5.5	151.3	1199
2630	1951	2086	.70	1016.0	14.0	330.3	2722
2650	1966	2104	1.30	1625.0	24.2	528.2	4444
2670	1981	2112	2.09	2277.0	35.0	740.0	6285
2690	1993	2116	3.05	2967.0	45.9	964.2	8208
2710	2000	2111	4.11	3675.0	56.6	1195.0	10155
2730	2001	2100	5.09	4359.0	66.1	1417.0	11986
2750	1999	2097	6.00	5032.0	74.9	1635.0	13763
2770	1996	2099	6.85	5677.0	83.4	1845.0	15472
2790	1995	2107	7.68	6271.0	92.0	2038.0	17082
2810	1985	2137	8.15	6718.0	97.0	2183.0	18214
2830	1969	2195	8.19	6980.0	97.5	2269.0	18750
2850	1955	2250	8.23	7235.0	98.0	2351.0	19272
2870	1944	2303	8.26	7481.0	98.6	2431.0	19780
2890	1933	2354	8.28	7723.0	99.2	2510.0	20280
2910	1925	2403	8.31	7958.0	99.8	2586.0	20770
2930	1917	2451	8.33	8190.0	100.4	2662.0	21250
2950	1910	2497	8.35	8419.0	101.1	2736.0	21740
2970	1904	2541	8.37	8645.0	101.8	2810.0	22210
2990	1898	2584	8.39	8870.0	102.5	2883.0	22680
3010	1893	2626	8.41	9092.0	103.2	2955.0	23150
3030	1889	2666	8.43	9315.0	104.0	3027.0	23630
3050	1886	2724	8.45	9546.0	104.9	3102.0	24120
3070	1883	2791	8.47	9785.0	105.9	3180.0	24640

Table B.6 INTER results

Time (min)	Tmetal (K)	Toxide (K)	Total CO (kg)	Total CO₂ (kg)	Total H₂ (kg)	Total H₂O (kg)	Total SiO₂ (kg)
2590	1737	1737	0	0	0	0	0
2610	1690	1744	139	4555	10	1482	9253
2630	1649	1750	283	6557	19	2132	13570
2650	1643	1734	1023	7553	61	2456	17760
2670	1640	1707	2311	7957	134	2587	22460
2690	1631	1642	3162	9157	182	2977	27390
2710	1628	1638	3713	9849	213	3201	30400
2730	1628	1641	4275	10440	245	3391	33250
2750	1628	1643	4860	10990	278	3571	36110
2770	1628	1642	5457	11550	312	3753	39010
2790	1628	1641	6057	12100	346	3932	41910
2810	1628	1642	6670	12600	381	4093	44740
2830	1628	1641	7287	13110	416	4260	47610
2850	1627	1638	7896	13640	450	4432	50490
2870	1627	1633	8491	14190	484	4610	53360
2890	1627	1629	9066	14750	517	4792	56210
2910	1626	1624	9621	15330	548	4979	59010
2930	1626	1620	10150	15920	578	5170	61730
2950	1625	1616	10670	16520	608	5365	64500
2970	1625	1612	11160	17130	635	5563	67180
2990	1625	1609	11620	17740	662	5764	69800
3010	1624	1606	12070	18360	687	5965	72370
3030	1624	1603	12500	18980	712	6167	74870
3050	1623	1601	12910	19600	735	6369	77320
3070	1623	1598	13300	20240	757	6575	79740

Table B.7
"De-gassed" concrete
specifications used
for VANESA
calculations

Material	Total concrete mass (%)
CaO	43.0
Al_2O_3	4.9
Na_2O	0.1
K_2O	1.65
SiO_2	48.4
FeO	1.95

Table B.8.   VANESA aerosol generation
rate results, based on CORCON1

Time (min)	Aerosol generation rate (g/s)	Total aerosol produced (kg)
2590	6.70	.0
2610	22.69	17.6
2630	34.93	52.2
2650	40.92	97.7
2670	42.16	147.6
2690	43.32	198.9
2710	43.93	251.2
2730	44.19	304.1
2750	44.53	357.3
2770	44.21	410.6
2790	45.37	464.3
2810	49.24	521.1
2830	50.66	581.0
2850	44.22	637.9
2870	29.38	682.1
2890	20.91	712.3
2910	22.09	738.1
2930	22.13	764.6
2950	22.53	791.4
2970	22.93	818.7
2990	23.51	846.5
3010	25.13	875.7
3030	26.28	906.6
3050	27.74	939.0
3070	29.50	973.3

Table B.9. VANESA aerosol generation
rate results, based on CORCON2

Time (min)	Aerosol generation rate (g/s)	Total aerosol produced (kg)
2590	5.13	.0
2610	13.65	11.3
2630	35.44	40.7
2650	35.73	83.4
2670	39.69	128.7
2690	41.70	177.5
2710	43.57	228.7
2730	44.32	281.4
2750	44.63	334.8
2770	45.02	388.6
2790	47.64	444.2
2810	53.28	504.7
2830	58.00	571.5
2850	59.44	641.9
2870	59.22	713.1
2890	66.71	788.7
2910	75.54	874.1
2930	76.62	965.3
2950	79.94	1059.3
2970	85.25	1158.4
2990	91.28	1264.3
3010	94.91	1376.0
3030	95.69	1490.4
3050	96.45	1605.7
3070	96.69	1721.6

Table B.10. VANESA aerosol generation
rate results, based on CORCON3

Time (min)	Aerosol generation rate (g/s)	Total aerosol produced (kg)
2590	4.22	.0
2610	8.72	7.8
2630	21.95	26.2
2650	24.34	53.9
2670	34.48	89.2
2690	37.79	132.6
2710	40.41	179.5
2730	42.16	229.1
2750	43.41	280.4
2770	43.93	332.8
2790	39.83	383.1
2810	4.15	409.4
2830	6.39	415.8
2850	7.07	423.8
2870	5.75	431.5
2890	4.88	437.9
2910	3.61	443.0
2930	2.66	446.8
2950	2.64	450.0
2970	2.65	453.1
2990	2.63	456.3
3010	2.68	459.5
3030	2.78	462.8
3050	2.89	466.2
3070	2.98	469.7

Table B.11. VANESA aerosol generation
rate results, based on CORCON4

Time (min)	Aerosol generation rate (g/s)	Total aerosol produced (kg)
2590	40.26	.0
2610	57.46	58.6
2630	69.56	134.8
2650	77.48	223.1
2670	82.66	319.2
2690	85.63	420.1
2710	83.62	521.7
2730	79.33	619.4
2750	76.22	712.8
2770	71.96	801.7
2790	60.06	880.9
2810	39.56	940.7
2830	28.68	981.5
2850	29.44	1016.5
2870	29.29	1051.7
2890	29.11	1086.8
2910	29.25	1121.8
2930	30.65	1157.7
2950	31.59	1195.1
2970	32.84	1233.7
2990	34.27	1274.0
3010	36.30	1316.3
3030	39.71	1361.9
3050	44.57	1412.5
3070	53.68	1471.5

Table B.12. VANESA aerosol generation
rate results, based on INTER

Time (min)	Aerosol generation rate (g/s)	Total aerosol produced (kg)
2590	279.83	.0
2610	245.10	315.0
2630	152.41	553.5
2650	158.39	739.9
2670	167.91	935.7
2690	122.23	1109.8
2710	88.42	1236.2
2730	85.03	1340.3
2750	84.73	1442.1
2770	84.01	1543.4
2790	81.53	1642.7
2810	79.80	1739.5
2830	78.48	1834.5
2850	74.97	1926.5
2870	66.02	2011.1
2890	28.17	2067.6
2910	2.70	2086.2
2930	2.57	2089.3
2950	2.42	2092.3
2970	2.24	2095.1
2990	2.11	2097.7
3010	1.97	2100.2
3030	1.83	2102.4
3050	1.70	2104.6
3070	1.59	2106.5

Table B.13. Core-concrete aerosol components predicted by
VANESA based on CORCON and INTER data

Material	Total aerosol mass at 3070 min, (%)				
	CORCON1	CORCON2	CORCON3	CORCON4	INTER
SiO_2	26.6	23.5	1.15	19.8	0.11
CaO	20.4	21.9	6.12	18.3	2.06
K_2O	13.0	20.2	69.0	9.57	93.8
FeO	$1^.4$	21.5	1.1	9.31	0.05
Al_2O_3	7.32	$9(10^{-4})$	0.01	8.33	0.05
Na_2O	7.22	12.1	3.69	5.37	1.57
Mn	7.11	0.53	12.3	8.97	0.77
La_2O_3	1.87	$3(10^{-5})$	$6(10^{-4})$	5.10	$8(10^{-4})$
CeO_2	1.08	$1(10^{-3})$	$8(10^{-4})$	1.90	$1(10^{-3})$
Te	0.33	0.13	2.76	0.42	0.96
Sn	0.66	0.03	2.65	1.11	0.1
All other materials	2.0	0.1	1.2	11.8*	0.5

*For the VANESA-CORCON4 run, Nb_2O_5 made up 9.45% of the aero-
sol mass at 3070 min.

Table B.14. "Fixed"
QUICK input data

Parameter	Value
CASE	COMPL
LSTEP	20
NDIM	1500
DELR	0.001
RMAX	100.0
N	30
DELT	0.001
EPS	10^{-6}
MF	22
BMIN1	10^{-15}
BMIN2	10^{-4}
IRST	0
RG	0.0
SIG	0.0
NO	0.0
T	155400.0
TMAX	184200.0
TMASS	0.0
ENERGY	0.0
TNERG	0.0
PRESS	1.0
RHOP	2.8
CRATIO	0.0006
DELD	0.001
GEFF	-1.0
TS	184200.0
CHI	1.0
GAMMA	1.0
VF	0.0

Table B.15. Drywell
aerosol data

Time (min)	Cumulative aerosol concentration (g/m^3)
2590	.000
2610	3.919
2630	11.601
2650	21.715
2690	44.189
2710	55.823
2750	79.401
2770	91.233
2790	103.177
2810	115.792
2830	129.112
2850	141.763
2870	151.576
2890	158.281
2910	164.015
2950	175.865
2990	188.118
3010	194.604
3030	201.458
3070	216.293

Table B.16. Drywell leak-rate data

Time (min)	Volumetric leak rate (m^3/s)	Fractional leak rate $(1/s)$
2590	54.361	.0120802
2594	27.069	.0060153
2597	19.818	.0044041
2606	14.585	.0032412
2618	11.027	.0024504
2630	9.051	.0020114
2653	3.712	.0008248
2670	5.038	.0011196
2685	3.338	.0007419
2709	3.518	.0007817
2769	3.039	.0006752
2829	3.381	.0007512
2889	2.715	.0006034
2949	2.834	.0006298
3009	2.554	.0005675
3069	2.523	.0005606
3070	2.523	.0005606

Table B.17. Drywell
geometric data

Floor area/volume	$= 2.89(10^{-3})$ cm^{-1}
Wall area/volume	$= 9.49(10^{-3})$ cm^{-1}
Drywell volume	$= 4,500$ m^3

Table B.18. Reactor building aerosol data

Time (min)	Total aerosol to building (kg)	Cumulative concentration to building (g/m^3)	Aerosol geometric radius (μ)	Aerosol standard deviation
2590.0	.000	.000	.1130	1.900
2600.5	4.311	.102	.1468	1.810
2617.2	20.502	.483	.1756	1.739
2633.8	46.186	1.087	.1945	1.713
2667.2	105.110	2.475	.2406	1.740
2700.5	178.230	4.197	.2499	1.835
2733.8	255.810	6.023	.2284	1.880
2767.2	332.540	7.830	.2281	1.899
2800.5	411.240	9.683	.2260	1.912
2833.8	497.570	11.716	.2278	1.914
2850.5	539.710	12.708	.2308	1.914
2867.2	576.690	13.579	.2312	1.912
2883.8	606.670	14.285	.2288	1.905
2901.3	632.080	14.883	.2248	1.902
2933.8	673.750	15.864	.2218	1.875
2967.2	715.050	16.837	.2226	1.849
3000.5	755.670	17.793	.2238	1.846
3033.8	798.090	18.792	.2252	1.856
3070.0	848.120	19.970	.2402	1.847

Table B.19. Reactor building leak-rate data

Time (min)	Total volume leak rate (cfm)	Total volume leak rate (m^3/s)	Fractional volume leak rate (1/s)
2590	99139.8	46.788	.0011017
2591	50605.7	23.883	.0005623
2592	31281.0	14.763	.0003476
2593	13866.2	6.544	.0001541
2594	12500.0	5.899	.0001389
3070	12500.0	5.899	.0001389

Table B.20. Reactor building
geometric data

Floor area/volume	=	1.387 m^{-1}
Wall area/volume	=	1.334 m^{-1}
Reactor building volume	=	$42,470 \text{ m}^3$
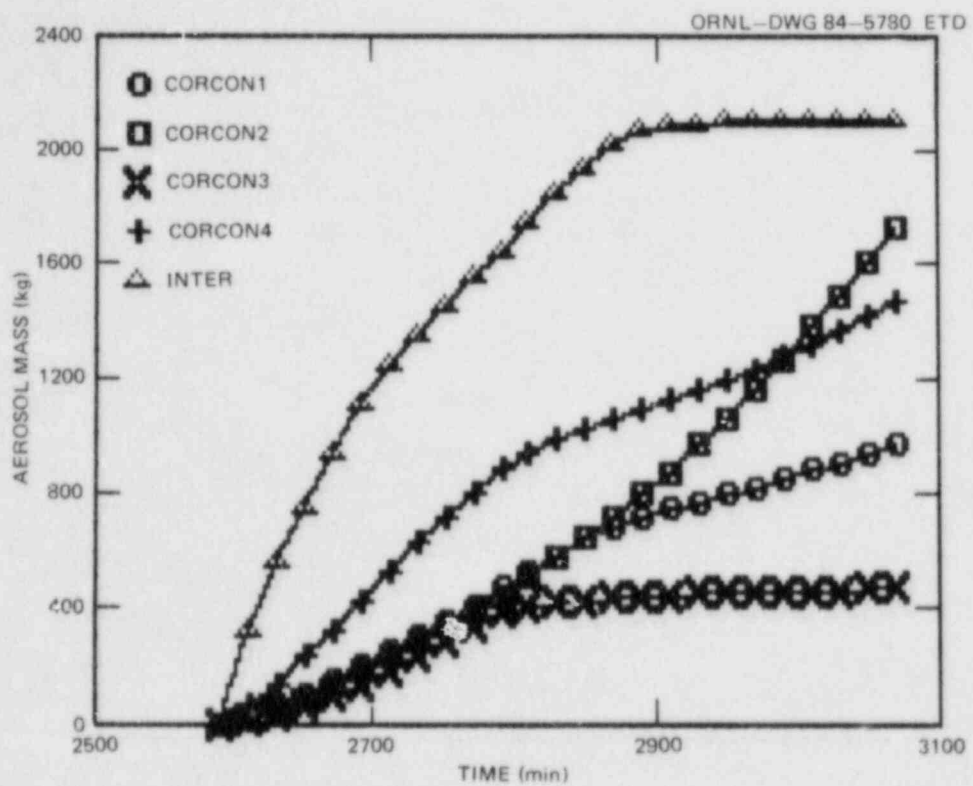
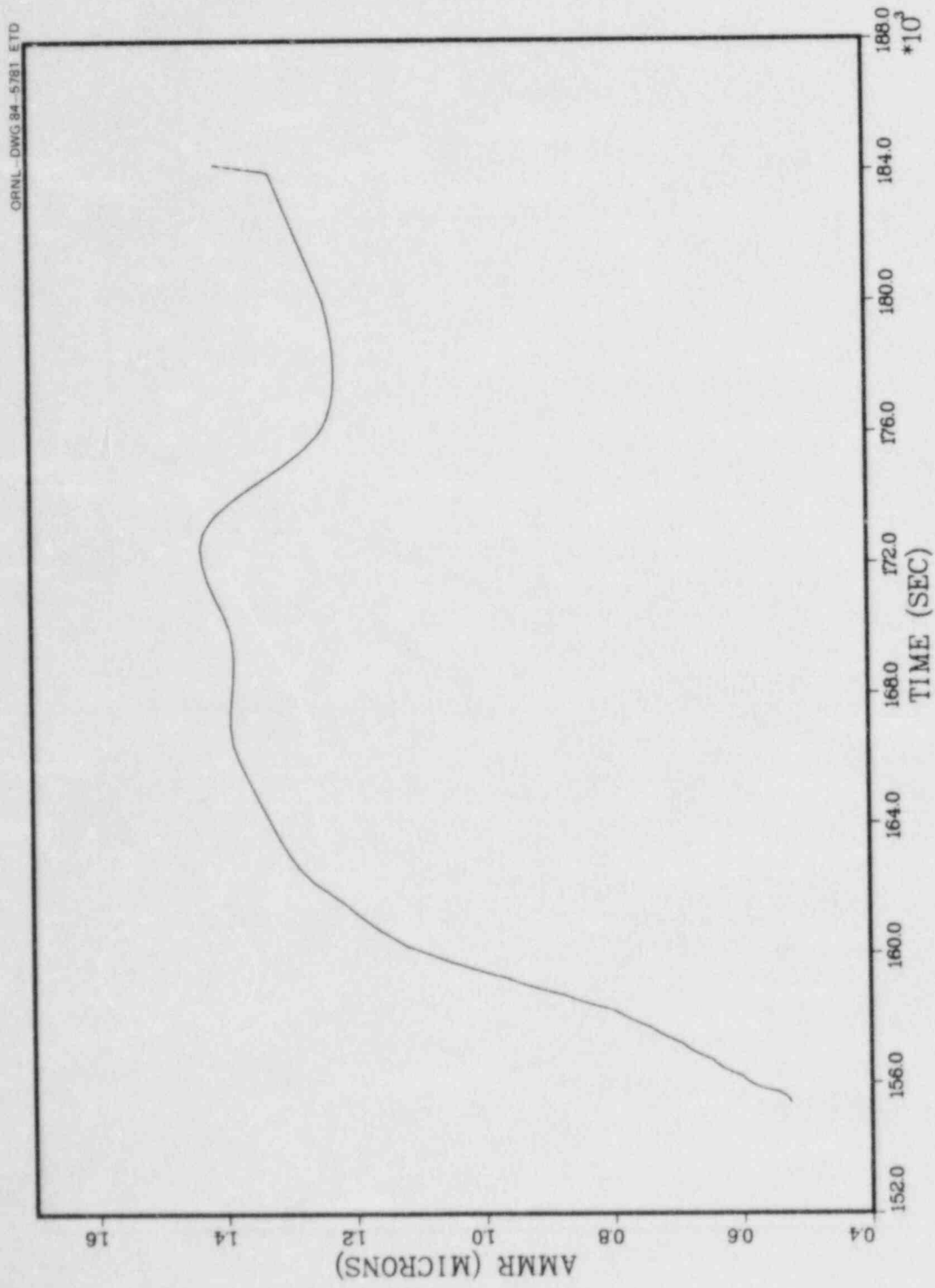Fig. B.1. Total aerosol mass vs. time from VANESSA calculations.

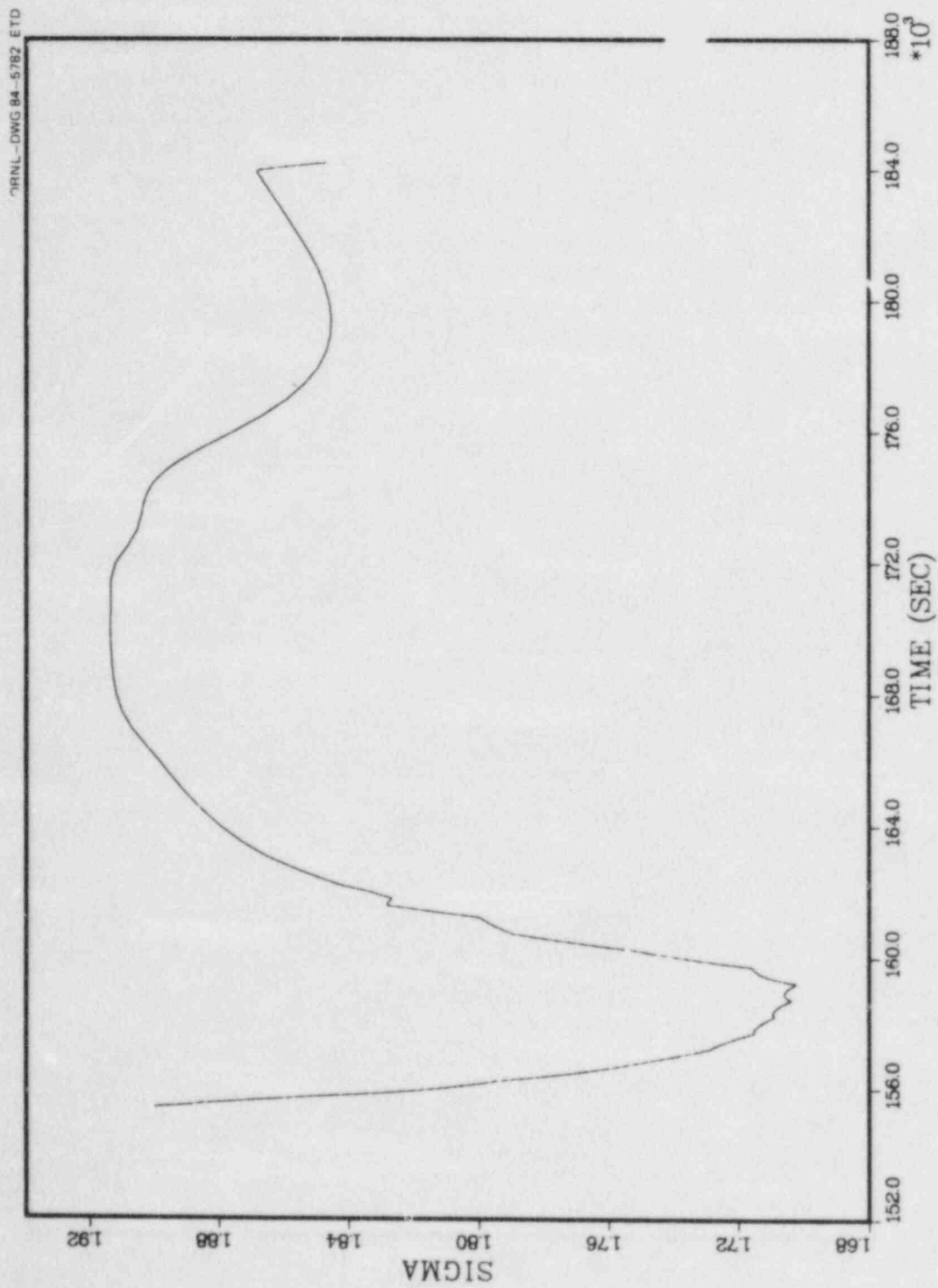Fig. B.2. Drywell aerosol aerodynamic radius vs. time.

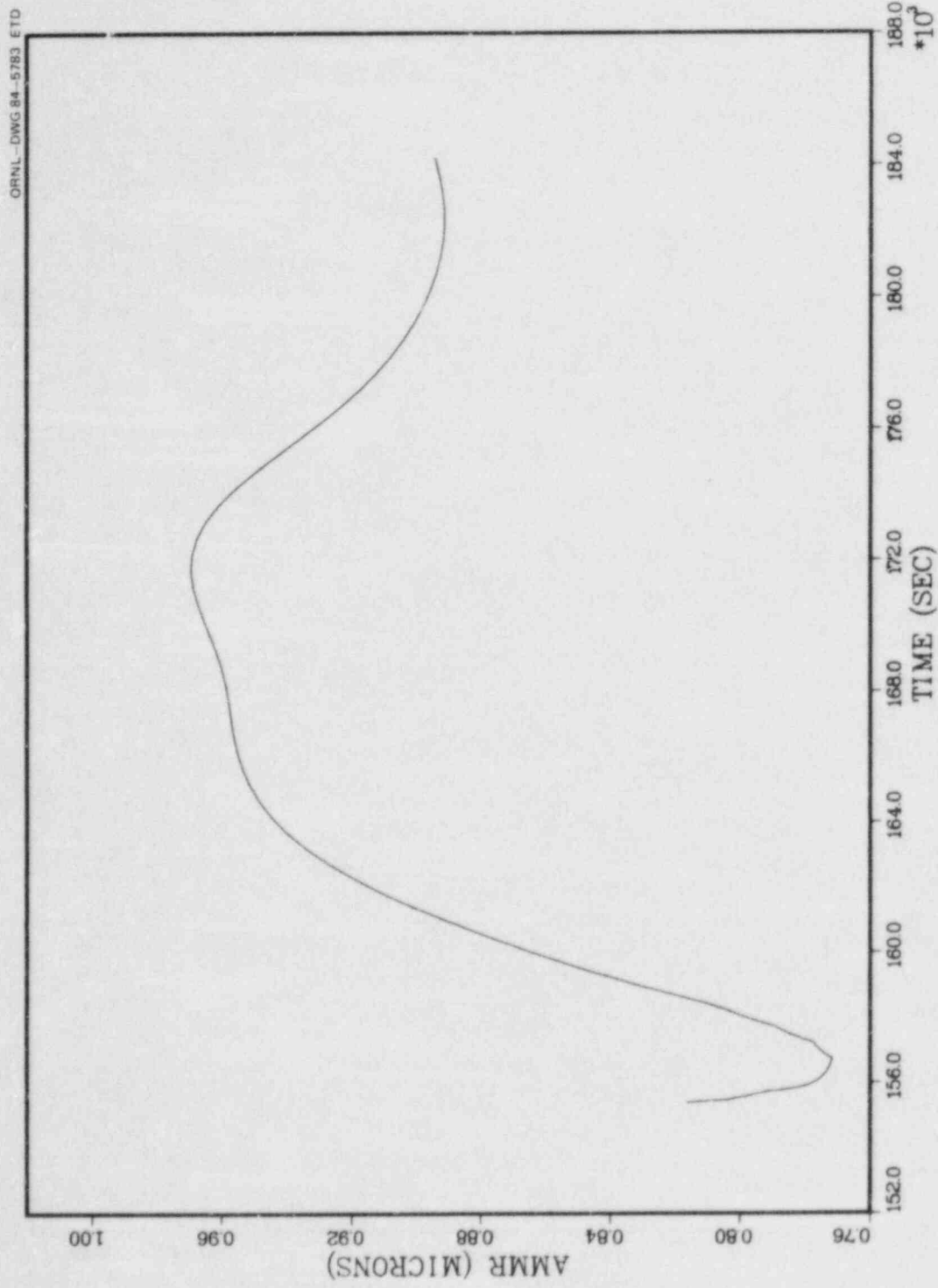Fig. B.3. Drywell aerosol standard deviation vs time.

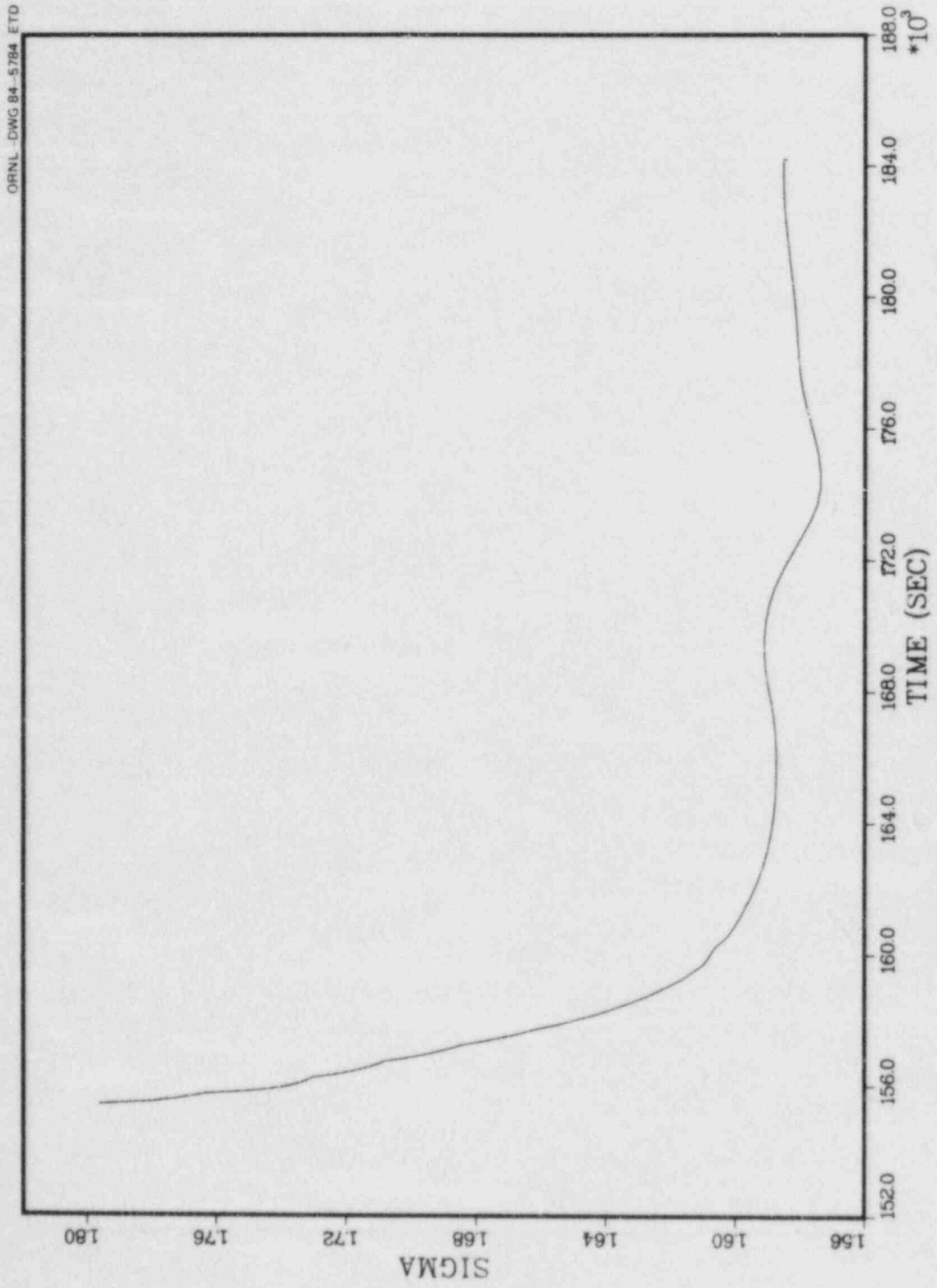Fig. B.4. Reactor building aerosol aerodynamic radius vs. time.

Fig. B.5. Reactor building aerosol standard deviation vs. time.

Appendix C

ACRONYMS AND SYMBOLS

ANS	American Nuclear Society
ANSI	American National Standards Institute
BAF	Bottom of Active Fuel
BCL	Battelle Columbus Laboratories
BFNP	Browns Ferry Nuclear Plant
Br	Bromine
BWR	Boiling Water Reactor
CBP	Condensate Booster Pump
Co	Cobalt
CP	Condensate Pump
Cr	Chromium
CRD	Control Rod Drive
CRDHS	Control Rod Drive Hydraulic System
Cs	Cesium
CSE	Containment Systems Experiment
CsOH	Cesium hydroxide
DF	Decontamination Factor
DW	Drywell
ECCS	Emergency Core Cooling System
EOI	Emergency Operating Instruction
EPA	Electrical Penetration Assembly
EPRI	Electric Power Research Institute
Fe	Iron
FSAR	Final Safety Analysis Report
GE	General Electric Company
HAARM	Heterogeneous Aerosol Agglomeration Revised Model
HEPA	High Efficiency Particulate Filter
HOI	Hypoiodous Acid
HPCI	High Pressure Coolant Injection
I	Iodine
$I_2(d)$	Dissolved molecular iodine
ID	Internal Diameter
Kr	Krypton
L	Liter
LDHR	Loss of Decay Heat Removal
LPECCS	Low Pressure Emergency Core Cooling System
LPCI	Low Pressure Coolant Injection mode of the RHR system
LOCA	Loss of Coolant Accident
LWR	Light Water Reactor
MARCH	Meltdown Accident Response Characteristics
Mn	Manganese
MPa	Megapascal
MSIV	Main Steam Isolation Valve
Ni	Nickel
NRC	Nuclear Regulatory Commission
O	Oxygen
ORNL	Oak Ridge National Laboratory

Pa	Pascal
PBq	Petabecquerel
PC	Partition Coefficient
PSP	Pressure Suppression Pool
PV	Pressure Vessel
PWR	Pressurized Water Reactor
RCIC	Reactor Core Isolation Cooling
RES	Office of Nuclear Regulatory Research
RHR	Residual Heat Removal
RPV	Reactor Pressure Vessel
RV	Reactor Vessel
SASA	Severe Accident Sequence Analysis
SBGTS	Standby Gas Treatment System
SBLOCA	Small-Break Loss of Coolant Accident
SGTS	Standby Gas Treatment System
Si	Silicon
SI	Systeme International
Sn	Tin
SNL	Sandia National Laboratories
SRV	Safety Relief Valve
TAF	Top of Active Fuel
Te	Tellurium
TVA	Tennessee Valley Authority
U	Uranium
WW	Wetwell
Xe	Xenon
Zr	Zirconium

Internal Distribution

1.	E. C. Beahm	17.	F. R. Mynatt
2.	S. D. Clinton	18.	L. J. Ott
3.	T. E. Cole	19.	R. D. Spence
4.	G. F. Flanagan	20.	H. E. Trammell
5.	S. R. Greene	21.	D. B. Trauger
6.	D. Griffith	22.	C. F. Weber
7.	W. O. Harms	23-24.	R. P. Wichner
8.	R. M. Harrington	25.	J. H. Wilson
9.	J. R. Hightower	26.	A. L. Wright
10-11.	S. A. Hodge	27.	R. G. Wymer
12.	C. R. Hyman	28.	Patent Office
13.	J. E. Jones	29.	Central Research Library
14.	T. S. Kress	30.	Document Reference Section
15.	R. A. Lorenz	31-32.	Laboratory Records Department
16.	A. P. Malinauskas	33.	Laboratory Records (RC)

External Distribution

34. Director, Division of Accident Evaluation, Nuclear Regulatory Commission, Washington, DC 20555

35-36. Chief, Containment Systems Research Branch, Nuclear Regulatory Commission, Washington, DC 20555

37. Chief, Fuel Behavior Branch, Nuclear Regulatory Commission, Washington, DC 20555

38. M. J. Jankowski, Fuel Behavior Branch, Nuclear Regulatory Commission, Washington, DC 20555

39. L. Chan, Fuel Behavior Branch, Nuclear Regulatory Commission, Washington, DC 20555

40. W. Pasedag, Accident Evaluation Branch, Division of Systems Integration, NRR, Washington, DC 20555

41. Director, Reactor Safety Research Coordination Office, DOE, Washington, DC 20555

42. Office of Assistant Manager for Energy Research and Development, DOE, ORO, Oak Ridge, TN 37830

43. L. O. Proctor, Tennessee Valley Authority, W10D199 C-K, 400 West Summit Hill, Knoxville, TN 37902

44. Wang Lau, Tennessee Valley Authority, W10C126 C-K, 400 West Summit Hill, Knoxville, TN 37902

45. J. A. Raulston, Tennessee Valley Authority, W10C126 C-K, 400 West Summit Hill, Knoxville, TN 37902

46-47. R. F. Christie, Tennessee Valley Authority, W10C125 C-K, 400 Summit Hill, Knoxville, TN 37902

48. H. L. Jones, Tennessee Valley Authority, W10A17 C-K, 400 West Summit Hill, Knoxville, TN 37902

194

49. J. D. Woolcott, Tennessee Valley Authority, 1530 Chestnut Street, Tower II, Chattanooga, TN 37902

50. Z. R. Rosztoczy, Research and Standards Coordination Branch, Office of Nuclear Reactor Regulation, U.S. Nuclear Regulatory Commission, Washington, DC 20555

51-52. Technical Information Center, DOE, Oak Ridge, TN 37830

53-577. Given distribution as shown under categories RX, 1S (NTIS-10)

2 TITLE AND SUBTITLE

Noble Gas, Iodine, and Cesium Transport in a Postulated
Loss of Decay Heat Removal Accident at Browns Ferry

3 LEAVE BLANK

4 DATE REPORT COMPLETED

MONTH	YEAR
July	1984

5 AUTHOR(S)

R. P. Wichner, C. F. Weber, A. L. Wright
S. A. Hodge, E. C. Beahm

6 DATE REPORT ISSUED

MONTH	YEAR
August	1984

7 PERFORMING ORGANIZATION NAME AND MAILING ADDRESS (Include Zip Code)

Oak Ridge National Laboratory
P. O. Box X
Oak Ridge, Tennessee 37831

8 PROJECT/TASK/WORK UNIT NUMBER

9 FIN OR GRANT NUMBER

B0452

10 SPONSORING ORGANIZATION NAME AND MAILING ADDRESS (Include Zip Code)

Division of Accident Evaluation
Office of Nuclear Regulatory Research
U.S. Nuclear Regulatory Commission
Washington, D. C. 20555

11a TYPE OF REPORT

Topical

b PERIOD COVERED (Inclusive dates)

N/A

12 SUPPLEMENTARY NOTES

13 ABSTRACT (200 words or less)

This report presents an analysis of the movement of noble gas, iodine, and cesium
fission products within the Mark-I containment BWR reactor system represented by Browns
Ferry Unit 1 during a postulated accident sequence initiated by a loss of decay heat
removal capability following a scram. This accident could be brought under control by
various means, but the sequence with no operator action ultimately leads to failure fol-
lowed by loss of water from the reactor vessel, core degradation due to overheating, and
reactor vessel failure with attendant movement of core debris onto the drywell floor.

The fission product transport analysis is based on the no-operator-action sequence
and provides an estimate of fission product inventories, as a function of time, within 14
control volumes outside the core, with the atmosphere considered as the final control
volume in the transport sequence. We find small barrier for noble gas ejection to air,
these gases being effectively purged from the drywell and reactor building by steam and
concrete degradation gases. In contrast, large degrees of holdup for iodine and cesium
are projected due to the chemical reactivity of these elements. Only about $2 \times 10^{-4}\%$
of the initial iodine and cesium activity are predicted to be released to the atmosphere.
Principal barriers for release are deposition on reactor vessel and containment walls.

14 DOCUMENT ANALYSIS - a KEYWORDS/DESCRIPTORS

BWR

Severe Accident Analyses

Fission Product Transport

b IDENTIFIERS OPEN-ENDED TERMS

15 AVAILABILITY STATEMENT

Unlimited

16 SECURITY CLASSIFICATION
(This page)
Unclassified

(This report)
Unclassified

17 NUMBER OF PAGES

18 PRICE